UNIVERSITY OF TURKU
Faculty of Science

Metallogeny of remobilised komatiite-associated Sika-aho nickel deposit, Kuhmo greenstone belt

Bedrock geology track
Master's thesis

Author:
Tuomas Gråsten

21.12.2022
Turku

Master's thesis

Subject: Bedrock geology
Author: Tuomas Gråsten
Title: Metallogeny of remobilised komatiite-associated Sika-aho nickel deposit, Kuhmo greenstone belt
Supervisors: Esa Heilimo & Tapio Halkoaho
Number of pages: 108 pages + 3 appendixes
Date: 21.12.2022

Growing demand of nickel requires new discoveries to be made, highlighting the need for better understanding of mineralisation processes. All Archaean nickel deposits are invariably metamorphosed and deformed, which has modified the geometry, textures, mineralogy, and metal content of the deposits. Remobilised komatiite-associated nickel deposits are scarcely studied in Finland, even though komatiites are highly potential targets for nickel(-copper-platinum group element) exploration. This study aims to define the source of nickel, resolve the reasons and mechanisms for nickel remobilisation, explain the atypical metal contents, and attempt to recognise geochemical haloes around the Sika-aho nickel deposit.

Drill core revision, geochemical analysis and petrographic study provide information about the geochemical and mineralogical compositions, textures, and alterations of all lithological units. Elevated Ni/Cu ratios and high Ni tenors in sulfides indicate that the source of Ni has been sulfides from a komatiitic source. Upgrading of the Ni content in sulfides during serpentinisation and talc-carbonate alteration is likely. Pentlandite, which hosts most of the Ni, can be found as individual grains, intergrown with other sulfides, and as inclusions and lamellae in pyrrhotite. Elongated and flattened sulfides with stretching lineations on the schistosity planes in the strongly sheared host rocks are evidence of mechanical remobilisation.

Replacement textures in sulfides indicate that the deposit has been affected by hydrothermal fluids, possibly causing redistribution of Fe, Cu, and S among other elements. However, geochemical analyses revealed that external remobilisation of Ni by hydrothermal fluids is unlikely. Ratios and total contents of platinum group elements as well as Ni and other siderophile and chalcophile elements evidence this. The host rocks of the deposit are highly heterogeneous: majority of the host rocks are strongly altered basalts, however the deposit is also partly hosted by altered komatiites and intermediate-felsic volcanic rocks.

Geochemical data from drill cores were used to create a numeric 3D-model that defines the extent and continuity of the Sika-aho Ni deposit. Numeric models were also created for other elements to detect possible geochemical haloes. A geological 3D-model of the host rocks and surrounding lithological units was created based on drill hole data, and it could be used in combination with numeric models to recognise depletion or enrichment of elements in different rock types. A combined 3D-model provided further evidence that the Ni sulfides have been remobilised and are not at their original volcanic position.

The results indicate that the source of Ni has been sulfides in a komatiitic cumulate unit, and the Ni contents of the sulfides have been upgraded during metamorphism. The remobilisation mechanisms have been dominantly mechanical, and the sulfides have undergone ductile plastic flow. Atypically high Cr contents of the deposit are attributed to both magmatic and hydrothermal processes, whereas the high Zn contents are hydrothermal in origin. Geochemical haloes were not detected in Sika-aho, however that alone should not be regarded as a negative indicator in Ni(-Cu-PGE) exploration.

Key words: metallogeny, nickel, remobilisation, Archaean, komatiite, exploration

Pro gradu -tutkielma

Oppiaine: Kallioperägeologia
Tekijä: Tuomas Gråsten
Otsikko: Kuhmon vihreäkivivyöhykkeellä sijaitsevan uudelleenmobiloituneen komatiittisen Sika-ahon nikkeliesiintymän metallogenia
Ohjaajat: Esa Heilimo & Tapio Halkoaho
Sivumäärä: 108 sivua + 3 liitettä
Päivämäärä: 21.12.2022

Nikkelin kasvavan kysynnän vuoksi uusia esiintymiä täytyy löytää, jolloin mineralisaatioprosessien ymmärtäminen on ensisijaisen tärkeää. Kaikki arkeeiset nikkeliesiintymät ovat metamorfoituneita ja deformoituneita, minkä seurauksena niiden geometria, tekstuurit, mineraloginen koostumus ja metallipitoisuudet ovat muuttuneet. Komatiitteihin liittyviä uudelleenmobiloituneita nikkeliesiintymiä on Suomessa tutkittu vain vähän, vaikka komatiitit ovat potentiaalisia nikkeli(-kupari-platinametalli) malminetsintäkohteita. Tämän tutkimuksen tarkoituksena on määrittää Sika-ahon esiintymän nikkelinlähde, selvittää syyt ja mekanismit nikkelin uudelleenmobiloitumiselle sekä löytää selitys esiintymässä nikkelin lisäksi havaituille epätyypillisen kohonneille metallipitoisuuksille. Näiden lisäksi pyritään havaitsemaan mahdolliset geokemialliset kehät esiintymän ympärillä.

Kairasydänten tarkastelulla, geokemiallisten analyysien tulkinnalla ja ohuthieiden petrografisella tutkimuksella saatiin tietoa tutkimusalueen kivien mineralogisista koostumuksista, tekstuureista ja muuttumisista. Koholla olevat Ni/Cu -suhdeluvut ja sulfidien korkeat nikkelipitoisuudet osoittavat, että nikkelinlähde on ollut komatiittisten kivien sulfidit, joiden nikkelipitoisuus on mahdollisesti kohonnut serpentinisaation ja talkki-karbonaattimuuttumisen vuoksi. Pentlandiitti sisältää suurimman osan esiintymän nikkelistä, ja sitä havaitaan yksittäisinä kiteinä, yhteenkasvettumana muiden sulfidien kanssa, sekä sulkeumina että erkaantumislamelleina magneettikiisussa. Voimakkaasti hiertyneiden isäntäkivien liuskeisuuspinnoilla on pitkänomaisia ja litistyneitä sulfideja venytyslineaatioineen, mikä todistaa sulfidien uudelleenmobiloituneen mekaanisesti.

Sulfidien korvautumistekstuurien perusteella esiintymään ovat vaikuttaneet hydrotermiset fluidit, jotka ovat vaikuttaneet ainakin raudan, kuparin ja rikin jakautumiseen. Geokemiallisten analyysien tuloksista voidaan todeta, että nikkelin ulkoinen uudelleenmobiloituminen hydrotermisissä fluideissa on kuitenkin epätodennäköistä. Muun muassa suhdeluvut platinametallien sekä nikkelin ja muiden siderofiilisten ja kalkofiilisten alkuaineiden välillä eivät tue kyseistä uudelleenmobilaatiomekanismia. Esiintymän isäntäkivistä suurin osa on voimakkaasti muuttuneita basaltteja ja komatiitteja, mutta myös intermediäärisissä ja felsisissä vulkaanisissa kivissä esiintyy paikoin mineralisoitumista.

Kairasydänten geokemiallisia analyysejä käytettiin nikkeliesiintymän ulottuvuuksien ja jatkuvuuden rajaavan numeerisen 3D-mallin tekemiseen. Numeerisia malleja tehtiin myös muille alkuaineille, jotta mahdolliset geokemialliset kehät voitaisiin havaita. Geologista 3D-mallia pystyttiin käyttämään yhdessä numeeristen mallien kanssa eri alkuaineiden rikastumisen tai köyhtymisen havaitsemisessa eri kivilajiyksiköissä. Yhdistetty 3D-malli osoittaa sen, että nikkelipitoiset sulfidit ovat uudelleenmobiloituneita.

Tulokset viittaavat siihen, että nikkelinlähteenä ovat olleet komatiittisissa kumulaateissa sijainneet sulfidit, joiden nikkelipitoisuudet ovat kohonneet metamorfoosin aikana. Uudelleenmobiloitumismekanismit ovat olleet mekaanisia, ja sulfidit ovat liikkuneet duktiilin plastisen virtauksen seurauksena. Epätyypillisen korkeat kromipitoisuudet esiintymässä ovat määritetty magmaattisten ja hydrotermisten prosessien aiheuttamiksi, kun taas korkeat sinkkipitoisuudet ovat alkuperältään hydrotermisiä. Geokemiallisia kehiä ei havaittu Sika-ahossa, mutta niiden puuttuminen ei yksinään ole negatiivinen indikaattori Ni(-Cu-PGE) -malminetsinnän kannalta.

Avainsanat: metallogenia, nikkeli, uudelleenmobiloituminen, arkeeinen, komatiitti, malminetsintä

Contents

1 Introduction

Nickel is used in variety of applications crucial for modern society, such as infrastructure, buildings, industrial machinery, transportation, appliances, and metals goods (Elshkaki et al. 2017). Global primary production of Ni has more than doubled in the last 20 years: in 1999, the estimated production was 1.12 Mt, while in 2019 it was 2.61 Mt (U.S. Geological Survey 2001, 2021). Demand for Ni has been estimated to keep growing significantly in the coming decades (e.g., Elshkaki et al. 2017; Watari et al. 2021), hence new primary sources of Ni are required. According to Elshkaki et al. (2017), industrial machinery, infrastructure, and buildings are the sectors that will continue to be the main fields of Ni use as they employ stainless steel products. However, the demand for Ni, for example, in electrification of transportation sector will also create substantial pressure on geological reserves of Ni (Habib et al. 2020). Thus, it is necessary to explore for new Ni deposits, improve our understanding of the deposits for better exploitation, as well as to develop new and advanced exploration techniques.

Archaean greenstone belts are typically endowed with mineral deposits that have formed in varying geodynamic settings and due to versatile processes (e.g., Hanski 2015; Ganguly & Yang 2018). Komatiite-associated nickel-copper-platinum group element (Ni-Cu-PGE) deposits are only one of the many deposit types found in Archaean greenstone belts, but their exploration potential in Finnish context is significant (Konnunaho et al. 2015). The target of this study, the Sika-aho Ni deposit, is located in Kuhmo Greenstone Belt. According to Luukkonen et al. (2002), the Kuhmo greenstone belt is very prospective for komatiite-hosted Ni deposits.

Luukkonen et al. (2002) and Heino (1998) state that the Sika-aho Ni deposit is mainly hosted by SiO_2-rich, chlorite±carbonate±sericite schist. The source of Ni is most likely komatiitic, and the remobilisation of Ni from its primary volcanic position is widely agreed upon (Heino 1998; Luukkonen et al. 1998, 2002; Makkonen & Halkoaho 2007). The ore minerals found in Sika-aho are pentlandite, pyrrhotite, and Ni-Fe arsenides (Heino 1998; Makkonen & Halkoaho 2007). Sika-aho also has unusually high Cr and Zn contents for an Archaean Ni deposit (Makkonen & Halkoaho 2007).

During ore-forming processes, elements are dispersed in the rocks depending on the conditions in and around the deposit. As a result, geochemical haloes that are either enriched

or depleted in different elements are formed (Haldar 2013). Study of primary geochemical haloes is an invaluable tool used in exploration of mineral deposits near or below the surface (Wang et al. 2013) as the haloes are nearly invariably larger than the deposit itself (Haldar 2013) and they reflect the processes of mineral formation and metal precipitation (Tao et al. 2021). Geochemical haloes have been found from komatiite-associated Ni deposits before (e.g., Barnes et al. 2004; Le Vaillant et al. 2015, 2016a, 2016b), but the recognition has been quite recent compared to other ore deposit types. Since the studies of komatiite-associated geochemical haloes are limited, the study of Sika-aho Ni deposit will improve our understanding of the phenomenon.

Generally, transfer mechanisms in mobilisation and remobilisation can be divided into three different groups: mechanical (solid-state), chemical (liquid-state), and mixed-state processes, which consists of both mechanical and chemical mechanisms (e.g., Marshall & Gilligan 1987; Marshall et al. 1998). Mobilisation can potentially create new deposits from originally dispersed constituents, whereas remobilisation can modify pre-existing concentrations of elements (Marshall & Gilligan 1987). Remobilisation has been proven to have modified numerous Ni sulfide deposits of different origin, including komatiite-associated, mafic-ultramafic orthomagmatic, as well as astrobleme-associated deposits (e.g., McQueen 1987; Mancini & Papunen 1998; Stone et al. 2005; Hoatson et al. 2006; Mukwakwami et al. 2014), thus they are critical in understanding mineralisation processes in places where metamorphism and deformation have been prevalent.

Drill core revision logging, petrographic examination, geochemical analysis, and 3D-modelling are used to study the topic. The aim is to improve the understanding of the metallogeny of Sika-aho Ni deposit, and possibly other remobilised Ni deposits, by answering to the following questions: **1)** What is the source of Ni in the Sika-aho deposit? **2)** What are the reasons and mechanisms for Ni remobilisation in Sika-aho? **3)** What is the host rock of the Sika-aho Ni deposit, and why does it contain atypical metal contents compared to other Archaean Ni deposits? **4)** Can geochemical haloes be detected around the Sika-aho Ni deposit? **5)** What are the implications for exploration of similar komatiite-associated Ni deposits?

2 Background

2.1 Komatiites

Komatiites are high-magnesium ultramafic rocks with a volcanic or subvolcanic origin (Arndt et al. 2008). Komatiites were first described in 1969 from the Barberton greenstone belt in Kaapvaal Craton in South Africa (Viljoen & Viljoen 1969). According to Dostal (2008), komatiites are found mainly in Archaean and Palaeoproterozoic greenstone belts and are characterised by olivine-rich composition and spinifex textures. Spinifex textures are defined as platy or skeletal olivine crystals in a glassy matrix.

Based on a revised definition by Le Bas (2000), komatiites are classified with the following geochemical characteristics: MgO > 18 wt%, SiO_2 30–52 wt%, $Na_2O + K_2O$ < 2 wt%, and TiO_2 < 1 wt%. Komatiites have the highest concentrations of PGEs in mantle-derived melts (Barnes et al. 2015). Also, compatible elements, such as Ni and Cr, have elevated concentrations in komatiites, whereas incompatible elements, such as Al, Si, Ti, and Zr, are typically low in concentration.

Common petrological classifications of komatiites are based on the Al_2O_3 content relative to TiO_2 and CaO, as well as on the heavy rare-earth element (HREE) patterns (e.g., Nesbitt et al. 1979; Arndt et al. 2008; Sossi et al. 2016). Komatiites are usually divided into Al-undepleted (chondritic Al_2O_3/TiO_2 with flat HREE patterns) and Al-depleted (low Al_2O_3/ TiO_2 with depleted HREE patterns) komatiites (e.g., Nesbitt et al. 1979). Arndt et al. (2008) have also included a third type: komatiites with high Al_2O_3/ TiO_2. Additionally, komatiites that are enriched in Fe+Ti and are typically found in the Karasjok greenstone belt, Fennoscandian shield, Norway, could constitute their own Karasjok-type komatiite.

Komatiites are considered to form by high degree, about 30–50 %, of partial melting of the deep anhydrous mantle (e.g., Herzberg 1992; Arndt et al. 2008). Komatiites are also thought to have high liquidus and eruption temperatures of ~1360–1600 °C (Herzberg 1992; Williams et al. 1998; Arndt et al. 2008). The eruptions of komatiite lavas have formed large and broad flow fields with very low thickness to area ratios (e.g., Hill et al. 1995) due to the exceptionally low viscosities of the lavas (Hill 2001, and references therein).

Even though the origin of komatiites from an anhydrous magma source has been generally accepted, opposing ideas of origin from subduction-related hydrous magma source have been

presented, for example, by Brooks & Hart (1974), De Wit (1998), and Parman et al. (2004). Arndt et al. (2008) have comprehensively discussed both hypotheses and their strengths and weaknesses, and state that the best arguments against hydrous komatiite models are that spinifex textures do not require water to form, geochemical characteristics indicate a deep anhydrous source rather than shallow hydrous source related to subduction, and that Barberton komatiites have erupted as submarine lava flows rather than intruded as sills or dikes.

The mineralogy of an unaltered komatiite depends on the chemical composition and the cooling rate of the lava, however the first mineral to always crystallise in large amounts is olivine. Minor chromite and Ni-Fe sulfides start to crystallise early as well. Once the crystallisation proceeds further, augite usually crystallises in the matrix with chromite. In some cases, orthopyroxene, pigeonite, plagioclase, amphibole, quartz, and Fe-Ti oxides can crystallise as well, and if the cooling rate is rapid, glass will form. (Arndt et al. 2008).

All komatiites are altered to some degree (Arndt et al. 2008; Barnes & Liu 2012), however the alteration mineralogy is heavily depended on the metamorphic temperatures, bulk-rock chemistry, and the X_{CO_2} (partial pressure of CO_2) of the metamorphic fluid (Barnes & Hill 1998). In almost all cases, the komatiites are at least partially serpentinised, altered to talc-carbonate assemblages, or to high temperature metamorphic equivalents of them. Serpentine and carbonate minerals are stable at low temperatures with or without chlorite and talc. Metamorphic olivine becomes a significant mineral at higher temperatures, and it can coexist with chlorite, tremolite, talc, anthophyllite, or enstatite depending on the conditions mentioned previously (Barnes & Hill 1998).

2.2 Komatiite-associated Ni-Cu-PGE deposits

Komatiites are in many cases associated with Ni-Cu-PGE sulfide deposits. To form such deposit, multiple factors need to be realised (e.g., Naldrett 2004; Arndt et al. 2005, 2008): 1) Metal-bearing ultramafic parental magma forming in the mantle as a result of high-degree partial melting that ascends through the mantle and erupts on the surface or intrudes into the crust; 2) Incorporation of external S from wall rocks by thermomechanical erosion processes, consequently generating or segregating an immiscible sulfide melt; 3) Interaction of the sulfide melt with a much greater volume of silicate melt that leads to upgrading of ore metal tenors in the sulfides; 4) Accumulation of metal-rich sulfide melt in sufficient quantities. A

simplified model of komatiite flow fields and associated Ni-Cu-PGE deposit formation is shown in Figure 1.

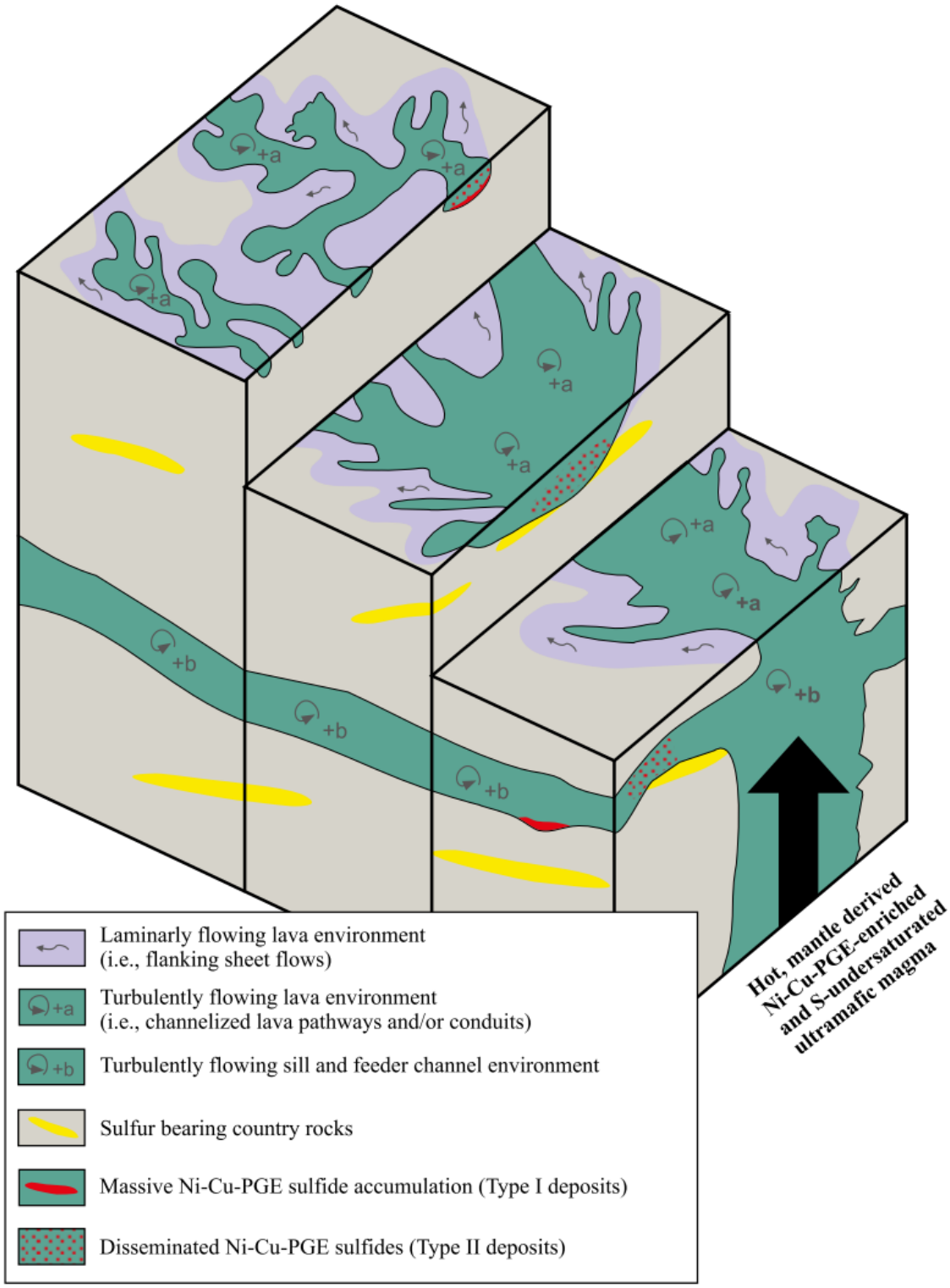

Figure 1. Magmatic and volcanic setting of komatiites with associated Ni-Cu-PGE deposits. Konnunaho (2016), after Fiorentini et al. (2012).

Globally, komatiite-associated Ni-Cu-PGE deposits accounted for approximately 18 % of the world's Ni resources in 2006 (Hoatson et al. 2006), thus being a significant source of Ni. In Finland, several komatiite-associated deposits have been found in the greenstone belts of eastern and northern Finland, however the deposits are generally dispersed and small in size with low Ni concentrations (Konnunaho et al. 2015). However, a medium-sized high-grade Cu-Ni-PGE deposit called Sakatti was discovered in 2009, but its komatiitic origin is still under debate (e.g., Makkonen et al. 2017). So far, only one komatiite-hosted Ni-Cu-PGE deposit has been briefly mined in Finland: the Tainiovaara deposit in eastern Finland was partly mined in 1989, for a total of ~0.02 Mt of ore with 1.40 % Ni and 0.12 % Cu (Puustinen et al. 1995). Konnunaho et al. (2015) state that the komatiite-hosted Ni-Cu-PGE deposits in Finland are mostly similar to their counterparts found elsewhere in the world, however some deposits that have formed from less Mg-rich parental magmas are considerably enriched in Cu and PGE.

Komatiite-associated Ni-Cu-PGE deposits can be classified based on, for instance, their sulfide distribution and textures, ore tenors, timing, as well as paragenesis. The majority of komatiite-associated deposits can be divided into two different types by their sulfide distribution and textures: Type I, where high-grade massive and net-textured sulfides occur near or at basal contact of the komatiite unit; or Type 2, where low-grade disseminations of sulfides occur in the cores of thick dunite bodies (Arndt et al. 2008). A more detailed classification system is presented by Lesher & Keays (2002), where the deposits have been classified into five different main types (I, II, III, IV, V) and further to several subtypes (I, Ib, IIa, IIb, IIc, IVa, IVb) based on sulfide distribution and textures, ore tenor, as well as timing and paragenesis. Type III deposits are stratiform reef mineralisations, type IV deposits are hydrothermal-metamorphic mineralisations, and type V deposits are offset mineralisations that have been mobilised in syn-tectonic processes (Lesher & Keays 2002). The significance of type III, IV, and V deposits in total metal budget of Archaean deposits is small compared to type I and II deposits (Arndt et al. 2008).

The effects of metamorphism on different types of komatiite-hosted Ni sulfide deposits vary. In type I deposits the modal proportion of sulfides to silicates is usually high, meaning that most of the Ni is in sulfide minerals. Mineral grain sizes and silicate-sulfide intergrowths can however be affected by metamorphism. On the other hand, substantial proportion of Ni in type II deposits resides in both sulfides and silicates. Under favourable conditions, the Ni tenor of disseminated sulfides can be substantially increased during metamorphism. For

example, serpentinisation of olivine cumulates can result in very Ni-rich assemblages due to uptake of originally silicate-hosted Ni by sulfides, usually forming pentlandite and possibly heazlewoodite or millerite. Talc-carbonate metamorphism, however, produces more S-rich sulfides such as pyrite, millerite, vaesite, and polydymite. This is due to the more oxidizing nature of the fluid, converting serpentine to talc and carbonate. Also, Ni contents of disseminated sulfides at higher metamorphic grades might be influenced by redistribution of Ni and Fe between olivine and monosulfide solid solution (MSS). (Barnes & Hill 1998).

Formation, redistribution, and upgrading of Ni sulfides can also occur in barren or weakly mineralised ultramafic rocks. According to Donaldson (1981), serpentinisation of barren and weakly mineralised dunites of the Yilgarn craton, Western Australia, in relatively low temperatures resulted in approximately 30 % of original silicate-hosted Ni to be redistributed to newly formed sulfides. Serpentinisation at higher temperature when lizardite-bearing assemblage metamorphosed to antigorite serpentinite caused about 60 % of the Ni to reside in sulfides. In case of complete CO_2 metasomatism, talc-carbonate rocks with even more redistributed Ni in sulfides were found. If the sulfur activity was low, sulfides could not form and Ni was enriched in talc in talc-carbonate rocks, and in magnetite in serpentinites. It is mentioned that about half of the sulfide contents could have been metamorphically derived from olivine in deposits that were originally magmatic Ni-sulfide deposits but were later metamorphosed. It was also found that up to 30 % of sulfidic Ni in ores averaging 0.7 wt% Ni is of metamorphic origin, with possibly even higher values assumed for talc-carbonate ores.

2.3 Remobilisation processes and mechanisms

The terminology and concepts of mobilisation and remobilisation of ore-forming compounds have been studied by several authors (e.g., Mookherjee 1976; Hobbs 1987; Marshall & Gilligan 1987, 1993; Marshall et al. 1998). A definition by Marshall & Gilligan (1987) is as follows: “Mobilization involves the translocation and concentration of originally dispersed metallic constituents; remobilization is the translocation resulting in modified concentration and distribution of pre-existing metalliferous concentrations.”. A simple illustration of the concept is shown in Figure 2.

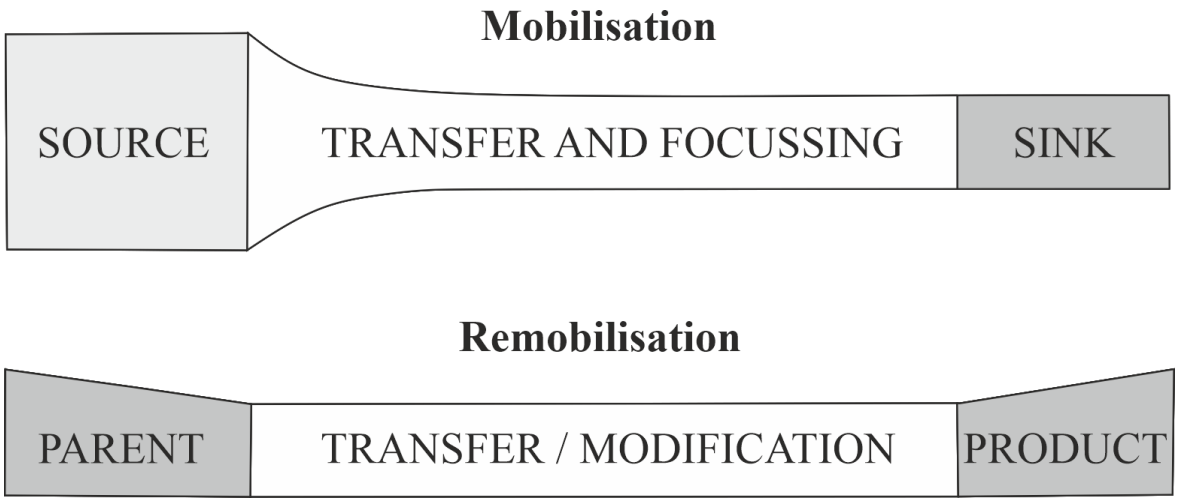

Figure 2. Basic concept of mobilisation and remobilisation of ore-forming compounds (modified after Marshall & Gilligan, 1993).

Marshall & Gilligan (1987, 1993) have proposed terminology for remobilisation processes and mechanisms. They state that remobilisation must be divided into internal and external remobilisation, because otherwise even micro-scale translocation fits into the definition of remobilisation, causing every metamorphosed deposit to be remobilised. Thus, internal remobilisation occurs when gross relationships between the deposit and its host rock are retained, and external remobilisation occurs when the gross relationships undergo substantial modification, with the possibility of forming new deposits. Extent of remobilisation is defined as the distance over which the ore body has been translocated, whereas degree is defined as the amount of impact on the ore body that remobilisation has caused. Sometimes the higher the degree and the larger the extent of external remobilisation is, the more difficult it is to actually substantiate; this is referred to as the paradox of remobilisation (Marshall & Gilligan 1987).

A widely used way to classify different remobilisation mechanisms is by separating them to chemical (liquid-state), mechanical (solid-state), and concurrent mechanical and chemical (mixed-state) processes (Table 1; Marshall & Gilligan 1987, 1993; McQueen 1987). The solid-state remobilisation mechanisms can be divided into different groups: cataclastic flow, dislocation flow, diffusive mass transfer, and grain-boundary sliding (Marshall & Gilligan 1993). Cataclastic flow includes the brittle failures that result in inter- and intragranular microfracturing, where sliding and rotating of fragments causes the flowing. Dislocation flow consists of several mechanisms, including translocation gliding (or translocation slip), kinking, mechanical twinning, and dislocation creep. Diffusive mass transfer consists of

Nabarro-Herring creep (lattice diffusion) and Coble creep (grain boundary diffusion), where atoms are transferred through lattice and around grain boundaries from high to low normal stress sites, respectively. Grain boundary sliding constitutes sliding on grain boundaries without cohesion loss (Marshall & Gilligan 1987).

Liquid-state chemical transfer can be divided into solution transfer and magmatic transfer (Marshall & Gilligan 1993). Solution transfer includes pressure solution around grain boundaries (a wet-state, stress-controlled diffusive mass transfer; Durney 1972) and advective mass transfer (Etheridge et al. 1984). In case of remobilisation, magmatic transfer means metamorphic sulfide anatexis where a sulfide(-sulfosalt) melt forms (e.g., Tomkins et al. 2007), sulfides are dissolved by a migrating silicate melt, or sulfide components are directly incorporated to a silicate melt (e.g., Marshall et al. 1998), and eventually translocated forming a new deposit. The liquid-state chemical mechanisms together with solid-state physical mechanisms constitute the mixed-state (re)mobilisation mechanisms, and in nature most remobilisation is indeed achieved by mixed-state processes (e.g., Marshall & Gilligan 1987, 1993; Marshall et al. 1998).

Different classifications of sulfide/metal mobilisation mechanisms have also been proposed (Mukwakwami et al. 2014; Table 1). Classification to three types is following: 1) ductile plastic flow of sulfides with strain preferentially partitioning into low-strength sulfides. Compared to Table 1, it basically covers the solid-state mechanical transfer mechanisms; 2) Metamorphic-hydrothermal mobilisation involving liquid-state transport in solutions and wet diffusion. This corresponds to the solution transfer mechanisms shown in Table 1; 3) Metamorphic partial anatexis that involves production of a partial sulfide melt, and/or dissolution of ore minerals by a moving silicate partial melt which is subsequently mobilised. The corresponding mechanism in Table 1 is magmatic transfer.

Table 1. Mechanisms of mobilisation and remobilisation (modified after Marshall & Gilligan 1993).

<table>
<tr><th colspan="2">Solid-state mechanical transfer</th><th colspan="2">Liquid-state chemical transfer</th></tr>
<tr><td colspan="2">Cataclastic flow</td><td rowspan="2">Solution transfer</td><td>Fluid-assisted diffusion</td></tr>
<tr><td rowspan="2">Dislocation flow</td><td>Dislocation glide</td><td>Advective transfer</td></tr>
<tr><td>Dislocation creep</td><td colspan="2">Magmatic transfer</td></tr>
<tr><td rowspan="2">Diffusive mass transfer</td><td>Grain boundary diffusion</td><td colspan="2" rowspan="2">Mixed-state transfer</td></tr>
<tr><td>Lattice diffusion</td></tr>
<tr><td colspan="2">Grain boundary sliding</td><td colspan="2">Concurrent chemical & mechanical processes</td></tr>
</table>

2.3.1 Evidence of mechanical remobilisation

Different textural evidence for remobilisation can be observed on micro-, meso-, and macroscale. Micro- and mesoscale textures alone can only attest to the degree of the remobilisation, whereas macroscale textures together with mesoscale textures can attest to the extent of remobilisation. Microscale evidence of remobilisation that can be observed in sulfides depends on the species and metamorphic grade. Mechanically remobilised pyrite tends to show grain fracture, brecciation, and annealing recrystallisation at low metamorphic grade, but at increasing grades pyrite shows coarsening and porphyroblastic, poikiloblastic, and helictic structures. At higher metamorphic grades, pyrite can also deform ductilely, forming elongate grains by dislocation-flow or diffusive mass transfer, however similar textures can be formed by pressure solution in lower metamorphic grade environment, as well. Arsenopyrite and magnetite are also high-strength minerals that show similar cataclastic textures as pyrite in lower metamorphic grade settings. (Gilligan & Marshall 1987, and references therein).

Mechanically remobilised pyrrhotite typically shows textural evidence of ductile behaviour, such as undulose extinction, flattening, elongation, kinking, and twinning. However, because pyrrhotite usually acts ductilely even in low grade metamorphic environments, it can overprint other deformation fabrics, especially in massive aggregates. Chalcopyrite is also a sulfide that typically displays textures formed by ductile deformation, such as undulose extinction, grain flattening and elongation, lattice-preferred orientation, and deformation and bent annealing twin lamellae. Annealing crystallisation of chalcopyrite can destroy evidence of ductile deformation. Chalcopyrite is also usually seen in healing fractures in pyrite. Sphalerite shows evidence of ductile deformation in lattice-preferred orientation and spindle-like and lanceolate deformation twins. Often sphalerite grains are not flattened or elongated though, but rather equant, which could be due to annealing recrystallisation and sub-grain development even in low metamorphic grades. Galena, which is the most ductile of the common sulfide minerals, usually displays evidence of ductile deformation. That includes flattening and grain elongation, lattice-preferred orientation, slip planes, bent cleavage pits, deformation twinning, and kinking. (Gilligan & Marshall, 1987).

Mesoscale textures provide information about local remobilisation and deformation in the deposit. Important internal fabrics (i.e., within sulfide bodies) observed include elongation lineations and pressure shadows in disseminated sulfides. Massive sulfides can show

lineations, foliations, folded layering, dislocation features (e.g., attenuation on fold limbs or thickening in fold hinges), and different fault fabrics. External fabrics (i.e., outside the sulfide bodies) include attenuation and nose thickening (due to folding of layers with varying rheologies), cusps, piercement cusps, piercement veins, and boudinage. Macroscopic evidence can be observed in structures of layers, such as nose thickening, attenuation, boudinage, and local piercement effects, and in structure encompassing layers as folding, elongation, transposition, gross ductile piercement, and associated vein systems. (Gilligan & Marshall 1987).

The capacity of mechanical remobilisation to form new deposits is heavily affected by the high ductility contrasts between sulfides and silicate- or carbonate-rich host rocks, and also between different sulfide species (Cox 1987; Gilligan & Marshall 1987; Marshall & Gilligan 1987, 1993; McQueen 1987; Pesquera & Velasco 1993). Deformation of sulfides can happen by a range of different flow mechanisms, and they vary significantly based on, for example, temperature, applied stress difference, confining pressure, grain size, and presence of fluids (Cox 1987). Based on experimental studies, the strength of major sulfides in dry metamorphic conditions is usually in following order (from weakest to strongest): galena < pyrrhotite < chalcopyrite < sphalerite < pyrite, however variation in the relative positions of the three sulfides in the middle has been observed (Marshall & Gilligan 1987). The strength of carbonate rocks can be similar to the middle three sulfides, and in some cases silicate rocks can be weaker than pyrite. It is also important to note, that the presence of an aqueous phase modifies the mechanical behaviour of minerals (Marshall & Gilligan 1987).

Mechanical internal remobilisation can effectively upgrade a deposit at microscopic scale, and external remobilisation can cause localised upgrading, however formation of daughter deposits other than in shear zone-induced offsets is unproven (Marshall et al. 1998). Examples of mechanical remobilisation can be found, for example, in volcanic-associated Ni deposits in Western Australia. McQueen (1987) states that many deposits there are clearly metamorphosed (not metamorphic/metamorphogenic) and their initial Ni concentrations are due to igneous-related processes, however majority of the present features have formed due to deformation, recrystallisation, and remobilisation during later tectonism and medium- to high-grade regional metamorphism. In Finland, modification of a mafic-ultramafic Sääksjärvi complex in Vammala nickel belt, Fennoscandian shield, was caused by recrystallisation, solid-state flow during deformation, and low-temperature alteration. A sulfide matrix breccia exhibiting durchbewegt textures formed due to mixed-state remobilisation of sulfide into

shear zones and faults, and then overprinted by solid-state remobilisation developing tectonised planar zones of sulfides and rock fragments (Mancini & Papunen 1998).

2.3.2 Remobilisation by hydrothermal fluids

There has existed a common belief that Ni would be an extremely immobile element in hydrothermal fluids (e.g., Le Vaillant et al. 2015). Most of the mined Ni occurring in sulfide deposits owes the elevated concentration to magmatic processes (Liu et al. 2012), however there is evidence that several of them have been extensively hydrothermally altered (e.g. Molnár et al. 2001; Ripley et al. 2005; Barnes & Liu 2012; Benkó et al. 2015). In some deposits, such as Sudbury in Canada, hydrothermal alteration has caused mobilisation of Ni (e.g., Tuba et al. 2014). Some Ni deposits even have primarily hydrothermal origins, such as Avebury in Australia (Keays & Jowitt 2013) or Enterprise in Zambia (Capistrant et al. 2015). As Le Vaillant et al. (2015) state, it has been shown that specific fluids in appropriate environments could remobilise Ni from a massive sulfide source despite the common belief that Ni is extremely immobile.

Since remobilisation and transportation of Ni can occur via hydrothermal fluids, it is highly important to understand the thermodynamic properties and aqueous speciation of Ni: unfortunately, the studies concerning this topic are few and far between (Liu et al. 2012). Even though the studies are still limited on behaviour of Ni (Co, Pd, and Pt, too) in hydrothermal fluids, it has been shown that the solubility increases with S contents and formation of bisulfide complexes, as well with chloride contents and formation of chloride complexes (Le Vaillant et al. 2015, and references therein).

Behaviour of PGE (Pt, Pd, Rh, Ru, Ir, Os) in hydrothermal fluids has been shown to vary greatly between the six elements: combined, the studies by Wood (2002), Hanley et al. (2005), Barnes & Liu (2012), and Le Vaillant et al. (2015) indicate that Pd is the most mobile element, second is Pt, and lastly the iridium-group PGEs (IPGE; Ru, Ir, Os) and Rh. This means that if a hydrothermal fluid with the capability to dissolve PGE has altered the composition of a rock, decoupling between the elements should be detectable. PGE and Ni have a close relationship in hydrothermal processes, which is why the hydrothermal remobilisation of Ni can be studied by the behaviour of different PGEs (e.g., Le Vaillant et al. 2014).

2.4 Geochemical haloes

2.4.1 Formation of geochemical haloes

Geochemical dispersion haloes or often simply geochemical haloes are elemental anomalies, either enrichments or depletions, that can form around deposits during mineralisation processes (e.g., McQueen 2005; Carranza & Sadeghi 2012; Cohen & Bowell 2013; Haldar 2013). Geochemical haloes are classified depending on their formation environment and the stage of element dispersion (Figure 3): generally, the terms used in literature are primary and secondary geochemical haloes. Primary haloes form during or close to the time of mineralisation, whereas secondary haloes form later when surficial processes, such as weathering, erosion, and hydrological processes modify the dispersion of elements (McQueen 2005). However, some deposits form due to only surficial processes, meaning that they can have primary and secondary dispersion patterns that both formed in surficial environments (e.g., supergene and placer deposits). Since the study is not focused on surficial processes affecting the deposit, only primary haloes are reviewed thoroughly.

The primary dispersion halo is essentially a result of migration of elements during a mineralisation process, such as formation and crystallisation of magmas or hydrothermal activity (Cohen & Bowell 2013). According to McQueen (2005), primary dispersion pattern comprises two components: the sub-ore grade portion of the deposit and the deposit-related zones of non-ore depletion or enrichment. An example of the sub-ore grade portion in magmatic Ni-Cu-PGE sulfide deposit could be a low-grade halo of disseminated sulfides around the massive/semi-massive sulfides. An example of the non-ore enrichment or depletion, which in many cases can be more obvious and extensive than the sub-ore portion, could be a certain type of alteration that is associated with mineralising fluids. The mineralisation processes along with physicochemical conditions during transportation and deposition, nature of the host rocks, as well as the controlling structures dictate the intensity, extent, and shape of primary dispersion patterns (McQueen 2005).

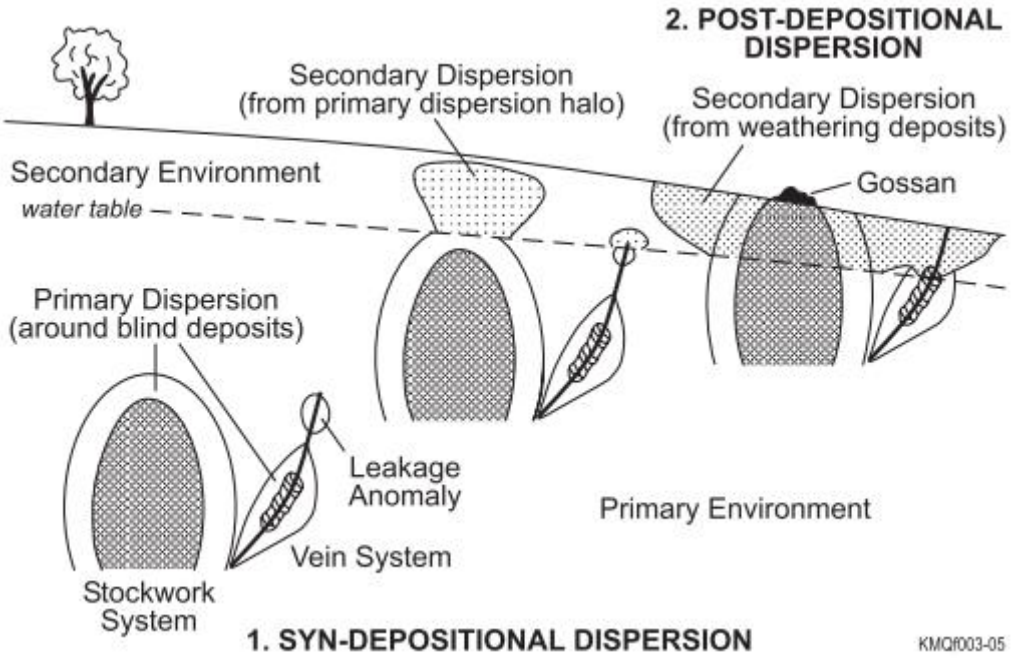

Figure 3. Sketch of primary and secondary geochemical haloes around ore deposits (McQueen 2005).

Elements that occur in close geochemical association with the element(s) being searched for are called pathfinder or indicator elements (Haldar 2013). These elements are more easily found because they can form a geochemical halo larger than the deposit itself, and/or they are more readily detected. The indicator elements must occur in primary association with the element that is being sought for. Element associations with Ni, Cu, Co, S, and PGE, and in some cases As and Te are typical for komatiite-associated Ni deposits (e.g., McQueen 2005; Le Vaillant et al. 2015, 2016c).

Mechanical, solid-state remobilisation can potentially have large extents as presented in Chapter 2.3, however the ability to form a geochemical halo is limited because in purely mechanical remobilisation no chemical reactions occur between the mineralised rocks and the country rocks. The presence of low-grade disseminated sulfides (e.g., McQueen 2005) can be used as an exploration guide, however in case of mechanical remobilisation, the lower grade sulfides would be found spatially between the parent and daughter deposit as a result of deformation, not dispersed around the deposit (i.e., there would not be a halo sensu stricto).

2.4.2 Geochemical haloes associated with Ni-Cu-PGE deposits

According to McQueen (2005), ore minerals can crystallise or exsolve from a silicate melt or a sulfide-oxide phase during the formation of magmatic deposits by variety of mechanisms,

such as gravity settling, convective accumulation, dynamic flow, or filter pressing. Sulfide immiscibility or oxide crystallisation can be caused by, for example, mixing of magmas or contamination of magmas with felsic crust and/or external S. These processes can produce a halo of disseminated sulfides around a massive sulfide deposit, or elevated S contents indicating possible S-saturation of the unit. Indications of magma mixing, S-saturation, and/or scavenging of chalcophile elements can be detected in variations of, for instance, Ni, Co, Cr, Cu, PGE, and Mg contents and ratios. Anomalies of light rare-earth elements (LREE), Zr, and Y in host rocks are possible indicators of contamination processes. Brand (1999) states that elevated Ni/Cr ratios can indicate suitable environments for mineralisation and vice versa. However, McQueen (2005) states that the most reliable lithogeochemical indicator is elevated Ni above the expected linear Ni-MgO trend for komatiites, usually indicated by the presence of low-grade disseminated sulfides.

Hydrothermal geochemical haloes around magmatic Ni sulfide deposits have been detected in several areas (e.g. Barnes et al. 2004; Barrie et al. 2007; Hanley & Bray 2009; Le Vaillant et al. 2015, 2016b), however the recognition has been relatively recent and studies concerning them are limited in number. During the last decade, a few studies were conducted in the Archaean Norseman-Wiluna greenstone belt, Yilgarn craton, Western Australia, presented in full length in Le Vaillant (2014) and reviewed in Le Vaillant et al. (2016c). In total, they studied five different komatiite-hosted Ni-Cu-PGE deposits in detail: Miitel, Sarah's Find, Otter-Juan, Durkin, and Perseverance. All these deposits have undergone numerous phases of alteration and deformation, however only Miitel and Sarah's Find deposits showed evidence of hydrothermal geochemical haloes.

The Sarah's Find Ni deposit is largely positioned at a basal contact between a komatiite unit and a dacite footwall, containing massive sulfides (pyrrhotite-pentlandite assemblage with minor amounts of chalcopyrite) as very small lenses (1–2 metres wide) or stringers (0.1–0.2 metres). A large geochemical halo along a shear zone at Sarah's Find extending up to 1780 metres away from massive sulfides was detected. Elevated levels of Ni and Pd were associated with high As, Co, Cu, and S. The Ni-Co-As-Pd geochemical halo was interpreted to have formed syn-deformation by As-rich hydrothermal fluids that had the capacity to dissolve base metals, Pt, and Pd from the orebody, and eventually redeposit them along a sheared footwall contact parallel to the prominent stretching lineation. The results indicate that a combination of physical and hydrothermal remobilisation was the reason for formation

of the geochemical halo, and that similar haloes could form around any magmatic Ni deposits that have undergone As metasomatism. (Le Vaillant et al. 2016b).

The Miitel Ni deposit is hosted by komatiites at a basal contact between the komatiite unit and basalt or a thin veneer of sulfidic sediments (Le Vaillant et al. 2015). At the Miitel deposit, Le Vaillant et al. (2015) detected a Ni-As-Pd-Pt geochemical halo extending at least 250 metres away from the ore body. Late circulation of hydrothermal fluids rich in As have scavenged Ni and PGE, transported them largely along footwall contact and shallow-dipping crosscutting splay structures, and redeposited them within small carbonate and/or quartz veins close to the contact with the footwall. The enrichment in Ni and PGE is associated with the presence of Ni arsenides, and the connection between remobilisation of Ni and PGE is strong. Similarly to the findings from Sarah's Find deposit (Le Vaillant et al. 2016b), As metasomatism could produce a geochemical halo around any type of magmatic Ni sulfide deposit.

Hanley & Bray (2009) report elevated Ni concentrations in vein-hosted amphiboles up to 700 metres away from the deposit in the footwall of Sudbury Igneous Complex, Ontario, Canada. Wide-scale Ni mobility in sodium- and halogen-rich hydrothermal fluids is indicated, and the anomalous Ni concentration in amphiboles could be detected even from samples that had no visible sulfides in hand samples or thin sections and showed no bulk rock anomalies either. Barrie et al. (2007) have studied geochemical and mineralogical haloes around several magmatic sulfide deposits: River Valley deposit in Sudbury Area, Ontario, Canada, Ferguson Lake deposit in Nunavut, Canada, and Kabanga deposit in western Tanzania. Their results indicate that the country rocks show slight anomalies in several different elements including PGEs up to several hundreds of metres from the deposits.

2.4.3 Altered and deformed Ni-Cu-PGE deposits without geochemical haloes

The Perseverance deposit is one of the largest komatiite-hosted Ni-Cu(-PGE) deposits in the world (Barnes et al. 2011). It has been metamorphosed at low- to mid-amphibolite facies conditions and undergone high-strain polyphase deformations (Duuring et al. 2010). There are indications of hydrothermal fluid circulation, and the geological setting is similar to the Sarah's Find deposit: however, no evidence of chemical remobilisation of sulfides or hydrothermal haloes is present (Le Vaillant et al. 2016c). Anomalous but relatively low As concentrations occur inside the extents of mechanical remobilisation (200–300 m). However, the hydrothermal fluids that circulated in the system might not have carried As, as the As is interpreted to be of magmatic origin, thermomechanically eroded and incorporated to the

komatiitic melt during its emplacement. The absence of Ni-PGE hydrothermal halo could be explained by the composition of this hydrothermal fluid (Le Vaillant et al. 2016c).

The Otter-Juan and Durkin deposits, both located in the Kambalda mining district, are geologically similar to the Miitel deposit. According to Le Vaillant et al. (2016c), neither of these deposits show evidence of geochemical haloes or anomalous Ni or PGE concentrations around the deposit. Analyses of Pd and Pt reveal that they have positive correlation. If the deposits would have been hydrothermally altered with fluids that could mobilise Pd and/or Pt, there would be signs of decoupling between them (Barnes & Liu 2012). The As concentrations of collected samples are low and no apparent interaction with As-rich fluids can be detected (Le Vaillant 2014).

The role of arsenic as well as the redox conditions of the hydrothermal fluids and the country rocks are crucial for Ni and PGE remobilisation and consequently for the formation of geochemical haloes. However, the absence of a Ni-Co-PGE-As geochemical halo does not necessarily mean that there is no Ni sulfide deposit, and it shouldn't be regarded as a negative indicator for exploration. (Le Vaillant 2014).

2.4.4 Sulfidation-oxidation haloes

In addition to purely geochemical haloes, certain mineralogical haloes that have formed as a result of sulfidation and oxidation reactions in metamorphosed rocks have been detected (e.g., Spry 1998). Sulfur and oxygen from a sulfide deposit can react with Fe component in ferromagnesian silicates and produce more Mg- or Zn-rich silicates or Zn-rich oxides with proximity to the sulfides, thus creating a halo around the deposit. Spry (1998) states that the ferromagnesian silicates where the reaction has been detected include garnet, staurolite, chlorite, biotite, and amphibole, whereas the oxides were gahnite and högbomite. The distribution members and compositions of Fe-Mg silicates and Zn-rich minerals were dependent, for instance, on bulk-rock composition, temperature, pressure, and fugacity of S, O, and H_2O. A large f_{S_2}-f_{O_2} gradient produces the most prominent halo, and it was found that abundant graphite-bearing rocks (low f_{O_2}-conditions) around pyrrhotite-pyrite-magnetite assemblage (high f_{S_2}-f_{O_2}-conditions) created such gradient. Sulfidation-oxidation haloes can be used as exploration tools, as they can be recognised at least 40 metres away from the sulfide deposit in some cases (Spry 1998).

3 Regional geology

3.1 Karelia province

The Karelia province, located in the Precambrian Fennoscandian shield, largely consists of an Archaean basement that is partly covered by Paleoproterozoic supracrustal rocks (Figure 4; Luukas et al. 2017). Different subdivisions of Karelia province to terranes or subprovinces based on geochemistry, lithology, structures, metamorphism, and geochronology have been suggested by several authors: Slabunov et al. (2006) and Hölttä et al. (2008) have divided the Karelia province into Vodlozero, Central Karelia, and Western Karelia terranes, whereas Hölttä et al. (2012a) use the same subdivision but rather call terranes subprovinces. A further division of subprovinces of the Finnish part of the Archaean Karelia province into nine separate complexes has been suggested by Hölttä et al. (2012a): Lentua, Rautavaara, Iisalmi, Kuopio, Kalpio, Manamansalo, Siurua, Ranua, and Ilomantsi complexes.

All Archaean complexes in Finland belong to the Western Karelia subprovince aside from the Ilomantsi complex (Hölttä et al. 2012a). The Ilomantsi complex (Figure 4), which belongs to the Central Karelia subprovince, is chiefly composed of Neoarchaean plutonic and volcanic sequences with relatively abundant sanukitoids (e.g., Hölttä et al. 2012b; Huhma et al. 2012). The Ilomantsi complex also includes Kovero and Ilomantsi greenstone belts. Hölttä et al. (2012a) state that the Vodlozero subprovince in the south-eastern part of the Karelia province is dominated by Mesoarchaean 3.2–3.0 Ga tonalite-trondhjemite-granodiorites (TTG) and migmatitic amphibolites. Additionally, there are several groups of greenstone belts with ages of 3.01–2.95 Ga, 2.9–2.85 Ga, and ≤ 2.85 Ga.

In the Finnish Western Karelia subprovince, Lentua complex is the largest one and it covers most of eastern Finland (Figure 4). It is largely comprised of Meso- and Neoarchaean migmatitic and gneissic TTGs, which can be divided into three groups based on their age: ca. 2.95 Ga, 2.83–2.78 Ga, and 2.76–2.73 Ga. Sanukitoid intrusions with the age of 2.72 Ga are common in the Lentua complex. Lentua complex also includes the Suomussalmi-Kuhmo-Tipasjärvi greenstone belt, as well as some narrow greenstone interlayers in the TTGs. Adjacent to the Lentua complex in the southwest, the Rautavaara complex is separated from it by a Proterozoic shear zone. (Hölttä et al. 2012a).

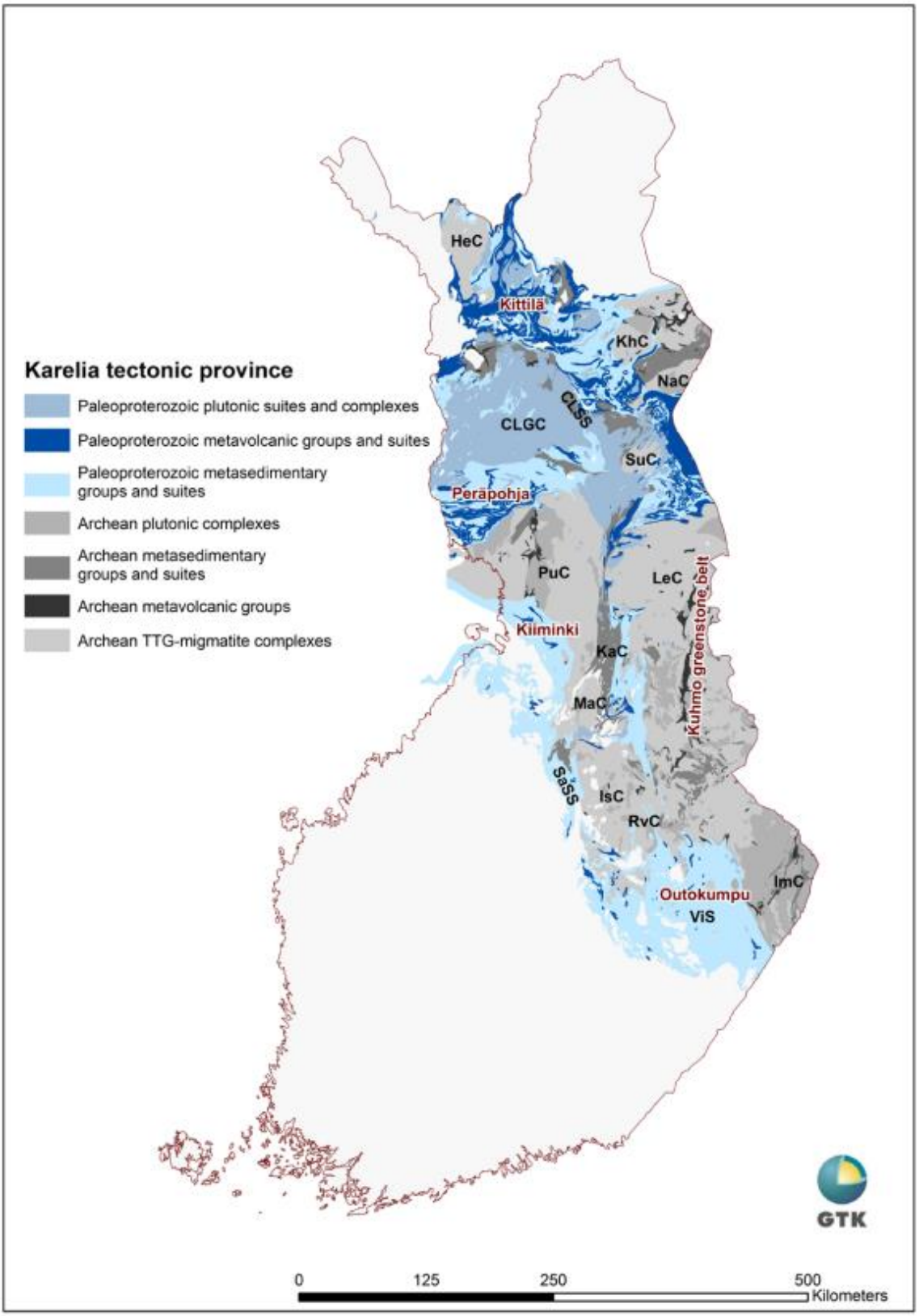

Figure 4. Karelia province according to Finstrati database with the Archaean basement and Palaeoproterozoic cover complexes, groups, and suites. CLGC = Central Lapland granitoid complex, HeC = Hetta complex, KhC = Kemihaara complex, NaC = Naruska complex, SuC = Suomujärvi complex, PuC = Pudasjärvi complex, KaC = Kalpio complex, MaC =Manamansalo complex, LeC = Lentua complex, IsC = Iisalmi complex, RvC = Rautavaara complex, ImC = Ilomantsi complex, CLSS = Central Lapland supersuite, SaSS = Savo supersuite, and ViS = Viinijärvi suite. Luukas et al. (2017).

The Rautavaara complex is predominantly composed of Neoarchaean TTG gneisses with amphibolite and biotite-plagioclase paragneiss schlierens and enclaves, and it is characterised by the abundance of ultramafic to felsic rocks that have been chemically altered (Hölttä 2012a; Figure 4). To the west from the Rautavaara complex is the Iisalmi complex, and they have been interpreted to be separated by a boundary that is a suture between two terranes (Hölttä et al. 2012a). The Iisalmi complex is mainly composed of Mesoarchaean gneisses and Neoarchaean orthopyroxene-bearing quartz diorites (Mänttäri & Hölttä 2002). To the south of the Iisalmi complex, there is the Kuopio complex which includes Archaean gneiss tectonic slivers and/or domes in Proterozoic metasediments (Hölttä et al. 2012a). To north from Iisalmi and Rautavaara complexes is the Manamansalo complex that is composed of TTG gneisses with micaceous paragneiss and amphibolite layers (Hölttä et al. 2012a). On the northern side of the Manamansalo complex is the Kalpio complex that is characterised by abundant metasediments, such as mica schists, mica gneisses, arkosic gneisses, and gneissic quartzites (Hölttä et al. 2012a). Metaplutonic and metavolcanic rocks, as well as zones of TTGs, are also found.

The Siurua complex is to the northwest from the Kalpio complex, and it contains the oldest rocks (trondhjemitic gneisses) found in the Karelia Province so far (Mutanen & Huhma 2003). However, the Palaeoarchaean rocks are not abundant, and they are surrounded by Mesoarchaean TTG orthogneisses and amphibolites, with paragneisses in the vicinity that are generally Neoarchaean (Huhma et al. 2012). On the northern side of the Siurua complex is the Ranua complex which consists of Meso- and Neoarchaean TTG rocks and granites (Huhma et al. 2012), as well as quartz diorites/monzonites (Mutanen & Huhma 2003). Oijärvi greenstone belt, which consists of amphibolite facies mafic and ultramafic volcanic rocks and sedimentary rocks, is also located in the Ranua complex (Sorjonen-Ward & Luukkonen 2005). In addition to the complexes described above, there are some poorly studied and defined complexes in northern Finland, such as the Kemihaara, Naruska, Suomujärvi, Hetta, Pomovaara, and Porttikoski complexes (e.g., Sorjonen-Ward & Luukkonen 2005; Luukas et al. 2017).

After the amalgamation of the Archaean nucleus of the Fennoscandian shield, the tectonism quieted down for approximately 200 Ma before large mafic layered intrusions, mafic dikes, A-type granitoids, and extrusive rocks started to form in the early Palaeoproterozoic (Lauri et al. 2012, and references therein). Dominantly extensional settings prevailed for possibly as long as 500 Ma evidenced by, for example, dolerite dike swarms (Vuollo & Huhma 2005;

Lauri et al. 2012). Later, during the Svecofennian orogeny, the Karelia province was reworked, deformed, and metamorphosed (e.g., Hölttä et al. 2012a, 2012b; Hölttä & Heilimo 2017).

3.2 Kuhmo greenstone belt

Kuhmo greenstone belt (KGB) constitutes the central part of the Tipasjärvi-Kuhmo-Suomussalmi greenstone belt, which is part of the Lentua complex (Huhma et al. 2012; Figure 4). The KBG is ca. 100 kilometres long and up to 16 kilometres wide (Figure 5). The lithological units consist mostly of mafic and ultramafic volcanic rocks, while felsic volcanic rocks and volcaniclastics along with pelitic sediments and banded iron formations are less abundant (e.g., Sorjonen-Ward & Luukkonen 2005; Papunen et al. 2009; Ranta et al. 2015). The belt likely represents a regional scale synclinorial structure (Papunen et al. 2009) where the margins are dominated by tholeiitic mafic and calc-alkaline volcanic rocks with komatiite cumulates and lava flows in the central part (Ranta et al. 2015).

3.2.1 Formation and age of Kuhmo greenstone belt

The tectonic evolution of Kuhmo greenstone belt is ambiguous and several different models have been proposed. The tectonic settings suggested for the formation include a continental rift (Papunen et al. 2009), oceanic plateau setting (Maier et al. 2013), failed rift followed by subduction (Piirainen 1988), and possible combination of more than one tectonic setting (Huhma et al. 2012; Lehtonen et al. 2016). Even though different lithological units have been extensively dated and lithostratigraphic interpretations have been made (e.g., Piirainen 1988; Papunen et al. 2009; Huhma et al. 2012; Lehtonen et al. 2016), the understanding of the geological evolution of KGB is still incomplete. Nevertheless, the mafic-ultramafic lithologies, including the Moisiovaara komatiites of the study area (Figure 7), show evidence that they have erupted subaqueously (Hanski 1980; Luukkonen et al. 1998; Maier et al. 2013).

Based on the data presented in Huhma et al. (2012), the majority of volcanic rocks in Kuhmo greenstone belt have formed approximately 2840–2800 Ma. The mafic-ultramafic magmatism that produced komatiites has occurred, at least locally in the central part of the KGB, prior to 2798 Ma when felsic rocks of Kellojärvi area formed. The upper age limit of komatiites is 2823±6 Ma based on the age determination from Moisiovaara gabbro (Huhma et al. 2012) and stratigraphic scheme presented in Papunen et al. (2009). Lehtonen et al. (2016) have divided the volcanism to two time periods, where the older volcanism occurred at ca. 2847–2836 Ma

and younger volcanism at ca. 2799–2792 Ma. Huhma et al. (2012) state that there are sedimentary rocks in KGB that have been deposited over 50 Ma after recorded volcanism; youngest sediments that have been found are in the Arola area where 2700 Ma detrital zircons are contained in a deformed quartzite (Figure 6).

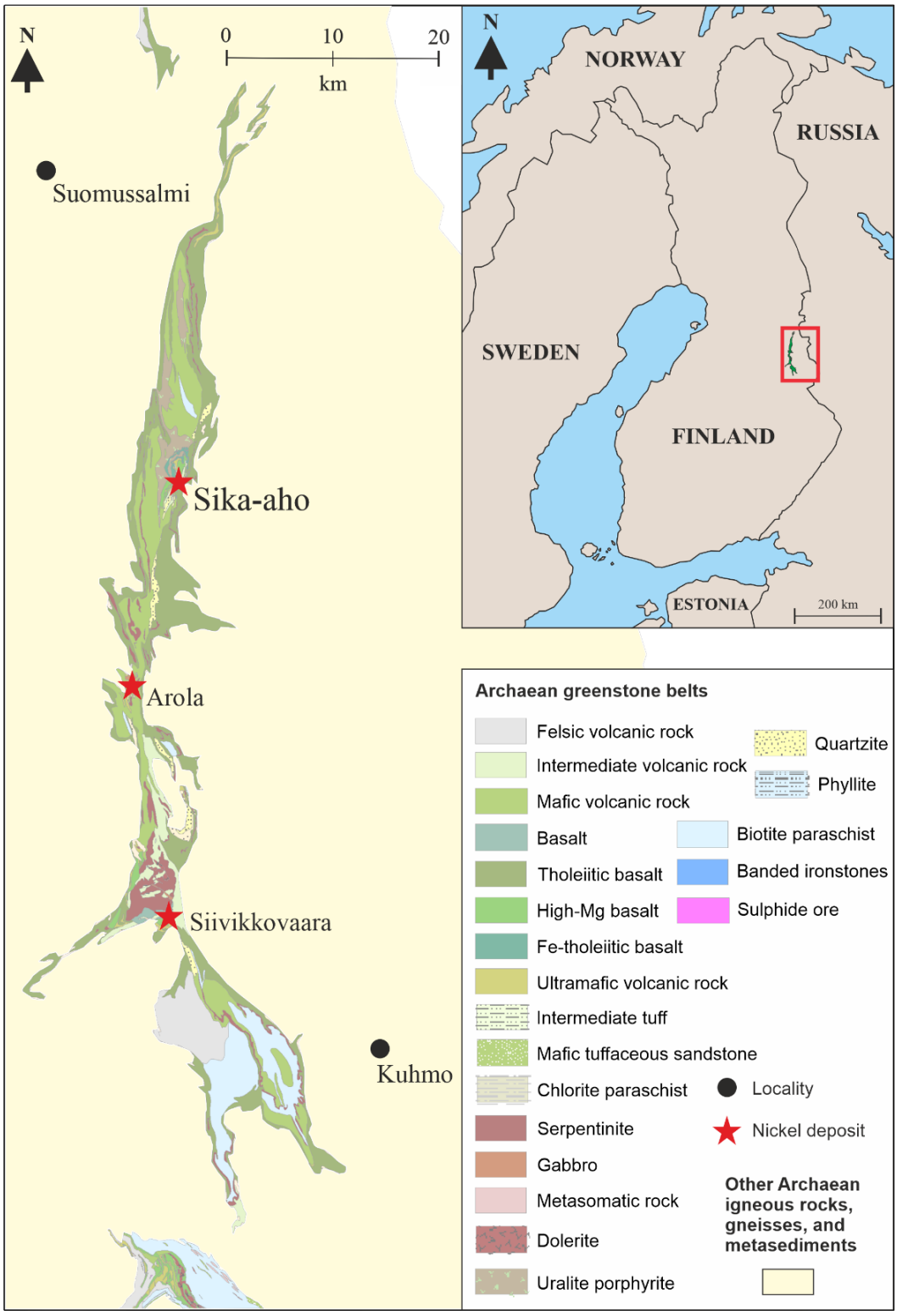

Figure 5. Lithological map of Kuhmo greenstone belt with notable Ni deposits (modified after GTK open licence CC BY 4.0, including GTK's Bedrock of Finland 1:200 000 data).

3.2.2 Stratigraphy of Kuhmo greenstone belt

The stratigraphy of Kuhmo greenstone belt has been interpreted by several different authors before, for example, Piirainen (1988), Papunen et al. (2009), Huhma et al. (2012), and Lehtonen et al. (2016). The stratigraphy presented here is according to Lehtonen et al. (2016; Figure 6). With new zircon U-Pb age data, they have refined and re-interpreted the chronostratigraphy of Kuhmo greenstone belt by proposing a division to three different major units with two major volcanic phases: the Nuolikangas unit (ca. 2847–2836 Ma), the Siivikkovaara unit (ca. 2799–2792 Ma), and the Ronkaperä unit (≤2750 Ma).

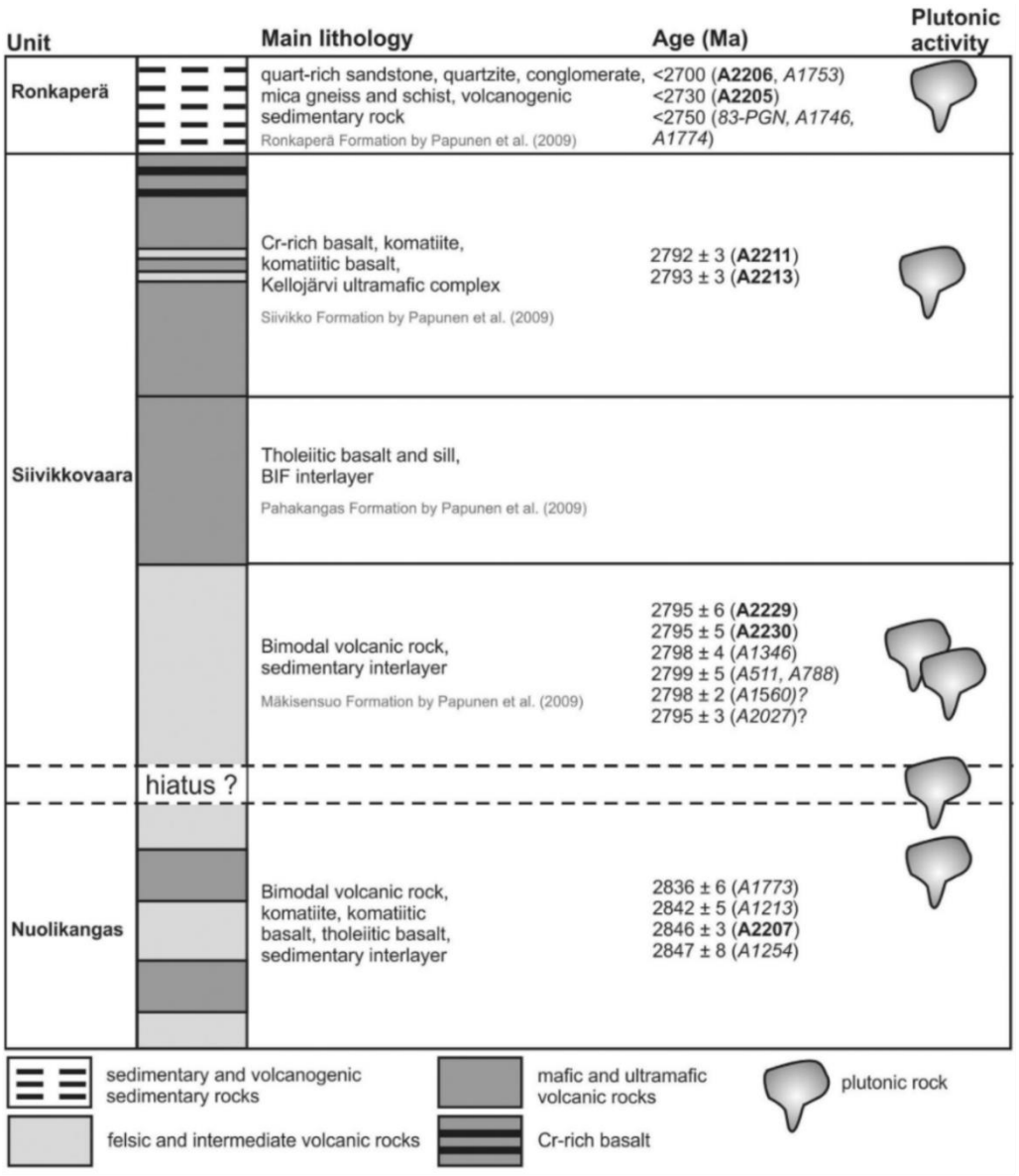

Figure 6. Chronostratigraphic interpretation of Kuhmo greenstone belt by Lehtonen et al. (2016), based on data from their own study, Huhma et al. (2012), and Käpyaho et al. (2006). Modified after Lehtonen et al. (2016).

Lehtonen et al. (2016) state that the Nuolikangas unit is mainly composed of bimodal volcanic rocks, where intermediate volcanic rocks, tholeiitic basalts, komatiitic basalts, and komatiites are spatially connected (Figure 6). The Nuolikangas unit contains some sedimentary interlayers, as well as plutonic rocks which are temporally close to the extrusive rocks and share similar chondrite-normalised rare-earth element (REE) patterns. In earlier lithostratigraphic interpretations, the andesite sample which marks the Nuolikangas unit in Lehtonen et al. (2016) has been described to represent the Ontojärvi Group (Piirainen 1988) or the Mäkisensuo Formation (Papunen et al. 2009).

Rocks in Siivikkovaara unit have been formed during a significant volcanic phase in the evolution of Kuhmo greenstone belt based on interpretation by Lehtonen et al. (2016; Figure 6). They also interpret that there has been a hiatus in volcanism between the formation of Nuolikangas and Siivikkovaara units. The rocks in Siivikkovaara unit can be subdivided into three different Formations: Siivikko, Pahakangas, and Mäkisensuo (e.g., Papunen et al. 2009). The oldest Formation of the three, Mäkisensuo Formation, is comprised of bimodal volcanic rocks and sedimentary interlayers, which are overlain by mainly massive and pillowed tholeiitic basalts with banded iron formation (BIF) interlayers of Pahakangas Formation (Papunen et al. 2009; Lehtonen et al. 2016). The uppermost Formation in the Siivikkovaara unit is the Siivikko Formation that contains the Kellojärvi ultramafic complex, komatiitic spinifex-textured lava flows, komatiitic basalts, pillow basalts, Cr-basalts, and high-Cr basalts (Lehtonen et al. 2016). Intrusive rocks that are coeval with supracrustal rocks are found in the Siivikkovaara unit, however the crosscutting relationships are still ambiguous (Lehtonen et al. 2016).

In the interpretation proposed by Lehtonen et al. (2016), the Ronkaperä unit is interpreted to the youngest unit in Kuhmo greenstone belt. It is largely comprised of sedimentary and volcanogenic sedimentary rocks. They consider the deposition of detritus to have occurred in fluvial to shallow marine basins, with the youngest zircon populations found in quartz sandstones to have an age of 2.70 Ga (Huhma et al. 2012), with the detritus being younger than that. The oldest detrital zircons have ages of over 3.0 Ga (Lehtonen et al. 2016), which implies that older crustal material was exposed or retained in the older sedimentary record during deposition of the Ronkaperä unit.

3.2.3 Structural and metamorphic evolution of Kuhmo greenstone belt

The most comprehensive field study of structural evolution of Kuhmo greenstone belt has been conducted by Luukkonen (1992), and no belt-scale revision of structural evolution has been done since. The KGB has been intensively deformed in six successive deformational phases during the late Archaean. Structures predating the KGB formation (S_1, F_1, and S_2) that formed during the first two deformational phases (D_1 and D_2) can be seen in the banded amphibolites and tonalite-trondhjemite gneisses of the Archaean basement. The structures that formed during later deformational phases in the Archaean (D_3, D_4, D_5, and D_6) can be encountered in all units of KGB and surrounding granitoids. (Luukkonen 1992).

Luukkonen (1992) states that the D_3 deformational phase followed the extrusion of bimodal volcanic rocks. The D_3 deformational phase has a complex history where early recumbent folding and thrusting occurred from E to W, followed by an oblique transpressional regime trending in NNE-NE direction that resulted in extensive strike-slip faulting and dextral folding. Large-scale dislocations and dextral F_3 folds occurred simultaneously with crustal shortening, which Luukkonen (1992) has interpreted to be a part of a system of regional scale strike-slip duplexes. He states that the complex lithostratigraphy is rather a result of volcanic rocks and sediments that have been tectonically repeated by overthrusting, folding, and faulting rather than polycyclic volcanism and sedimentation. Late D_3 fault bounded basins and extensional duplexes related to early D_3 boundary faults are associated with the formation of sedimentary rocks that lie in the upper part of KGB stratigraphy, with the detritus being sourced from pre-F_2 sialic crust.

Going from D_3 to D_4 deformation phase, the strike-slip system enabled the siliceous, carbonaceous, and potassic alteration of rocks in the KGB. Regional folding and faulting from D_3 to D_6 deformation phases record the change from ductile to brittle deformation conditions. The cratonisation of the late Archaean crust occurred simultaneously. The Archaean structures were reactivated during later deformational phases in the Proterozoic, when shearing occurred along older planes of weaknesses, and new material, mainly alkaline granites and diabase dykes, intruded into the crust. Indications of Svecofennian thermal resetting were also found. (Luukkonen 1992).

The Kuhmo greenstone belt has been metamorphosed at mid-amphibolite facies and medium pressures, even though pressures of 10 kbar or higher might have been possible (Hölttä & Heilimo 2017). Geothermometric calculations by Tuisku (1988) suggest that the metamorphic

grade increases from inner to outer parts of the belt. The lowest temperatures in the inner parts have been around 500 °C, whereas the outer parts could have reached temperatures up to 660 °C. The amount of strain observed in Kuhmo greenstone belt varies greatly. In high-strain areas, the primary structures and textures of supracrustal rocks have been destroyed due to intense deformation, however some low-strain areas, such as Siivikkovaara-Kellojärvi area, still contain well-preserved primary structures and textures (Papunen et al. 2009).

3.2.4 Mineral deposits in Kuhmo greenstone belt

Kuhmo greenstone belt contains several small and currently subeconomic Ni(-Cu), Au, and Zn-Pb(-Ag) deposits, as well as very small Fe deposits (Luukkonen et al. 2002; GTK 2022). The prospectivity of KGB has been studied, for example, by GTK and different state-owned companies during the 1900's, as well as by private companies since the 1990's. Notable Ni(-Cu) deposits include Sika-aho, Arola (e.g., Lehtinen 1983; Halkoaho & Papunen 1998; Juurela 2013), and Siivikkovaara (e.g, Hanski 1980; Ioannou 2020) deposits (Figure 5), however no Ni mining has been done in Kuhmo greenstone belt. Several small structurally controlled Au deposits have been identified (Luukkonen et al. 2002). Small BIF-associated Fe deposits and VMS- or magmatic-associated Zn-Pb-(Au) deposits are also found (GTK 2022), however they are poorly studied.

3.3 Moisiovaara and Sika-aho areas

3.3.1 Evolution and stratigraphy of Moisiovaara area

In the Moisiovaara area, Kuhmo greenstone belt is approximately 6 kilometres wide, and tectonic contacts with Archaean granitoids and migmatites border it from east and west (Luukkonen et al. 1998; Figure 7). The outermost and simultaneously stratigraphically lowest unit in Kuhmo greenstone belt consists of banded tholeiitic amphibolites that are strongly altered. Interlayers of felsic to intermediate volcanic rocks are observed in the amphibolites. This sequence is interpreted to be the oldest in Kuhmo greenstone belt (Luukkonen et al. 1998).

On top of the oldest sequence, mafic to ultramafic, massive and pillow lava textured volcanic rocks have erupted, and they account for the majority of rock units in the KGB. The composition of the volcanic rocks changes from tholeiitic to komatiitic when going upwards in stratigraphy. Felsic to intermediate volcanic rocks and sedimentary rocks are found as thin

interlayers in tholeiitic rocks and between tholeiitic and komatiitic rocks. On top of these are the most extensive felsic and intermediate volcanic and sedimentary rock units that are tectonically bounded within the Tammasuo shear zone, and they are considered to represent the youngest rock units in the KGB stratigraphy. (Luukkonen et al. 1998, 2002).

According to Luukkonen et al. (1998), the lithostratigraphical sequence in Moisiovaara (Figure 7), which continues from tholeiitic basalts all the way to komatiites and includes banded iron formations, mica schists, or felsic volcanic rocks in between, is analogous with the Pahakangas-Siivikkovaara sequence in Siivikkovaara lithostratigraphic unit (cf. interpretation of Lehtonen et al. (2016) presented in Chapter 3.2). Based on field observations and diamond drilling, the komatiites in Moisiovaara area have erupted subaqueously.

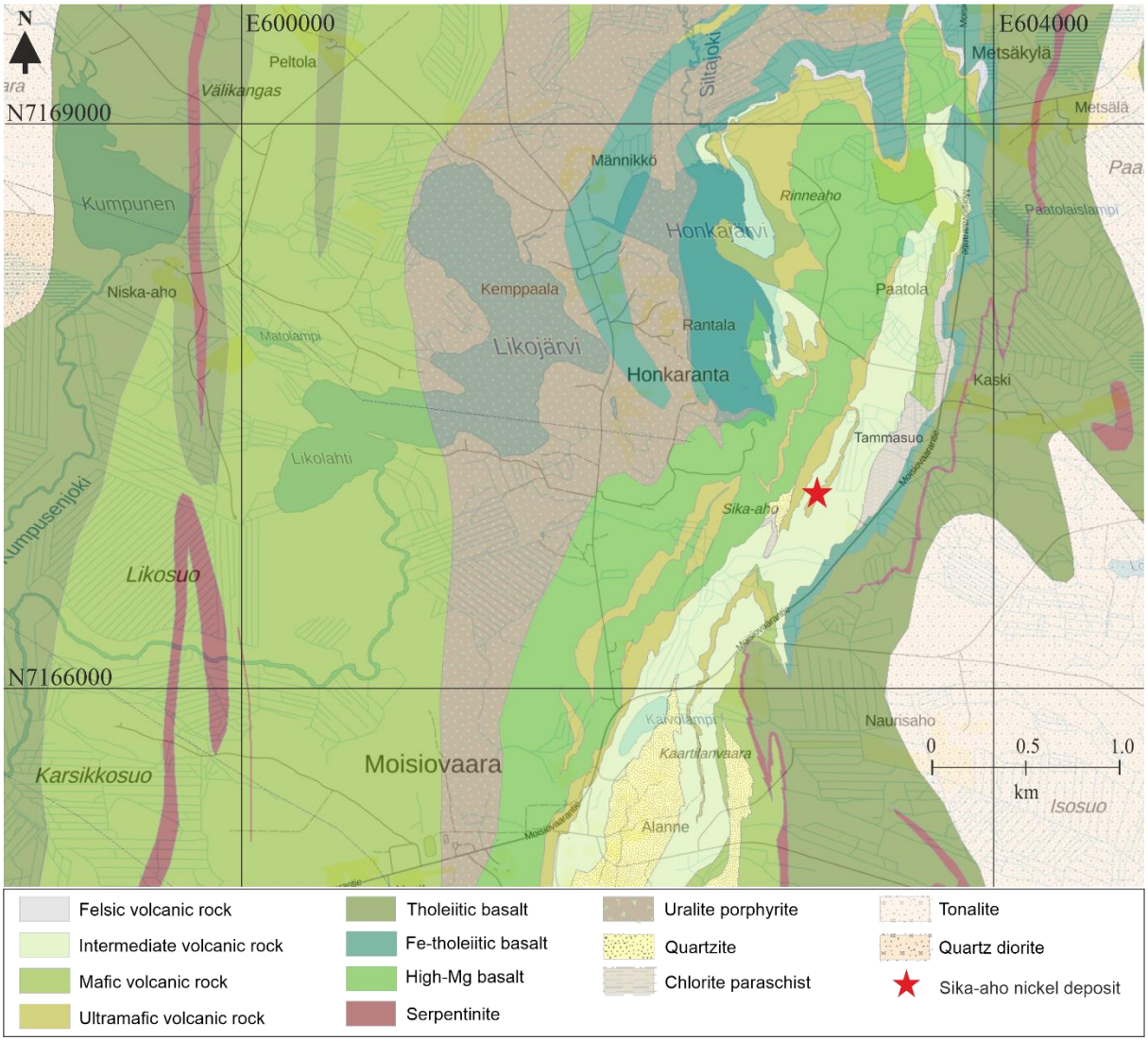

Figure 7. Generic map of Moisiovaara, Sika-aho, and Tammasuo areas with a partly transparent lithological map on top (modified after GTK open licence CC BY 4.0, including GTK's Bedrock of Finland 1:200 000 data). Coordinates are in ETRS-TM35FIN coordinate system.

3.3.2 Sika-aho nickel deposit

The Sika-aho Ni deposit is about 1 kilometre north from Moisiovaara village in Kainuu, eastern Finland (Figures 7 and 8). The deposit is largely hosted by SiO_2-rich and carbonated chlorite(±sericite) schist that is located along the western margin of a carbonate-altered and sheared komatiitic cumulate sequence (Figure 8; Heino 1998; Luukkonen et al. 1998, 2002). According to Luukkonen et al. (2002), the width of the deposit is between 1 and 9 meters and the length along strike is approximately 80 meters at present erosion level. They state that in the northeast of the deposit exists an additional, less mineralised extension with a width of 2–10 meters and strike length of 150 meters. The Ni deposit has a dip of approximately 85 degrees to the SE (Heino 1998).

The ore minerals found in Sika-aho are pentlandite, pyrrhotite, and Ni-Fe arsenides. Pentlandite is found as individual grains, intergrown with pyrrhotite, and as inclusions and exsolution lamellae in pyrrhotite (Heino 1998; Makkonen & Halkoaho 2007). Luukkonen et al. (1998) state that the Ni/Cu ratios are in range of 15.4–116.8 and Ni in sulfide fraction (Nisf) is high, varying between 7.2 and 30.1 wt.%. Heino (1998) reports that the average Ni/Cu ratio is 60.4 and average Nisf is 15.6 wt.% in the mineralised rocks. They all state that the high Ni/Cu ratio and Ni content in sulfides are typical for an Archaean komatiite-associated Ni deposit.

The formation of the Sika-aho Ni deposit has been discussed by Heino (1998), Luukkonen et al. (1998, 2002), and Makkonen & Halkoaho (2007). The deposit has been interpreted to be hosted by a hydrothermally altered pyroxenitic basal part of a komatiitic lava flow (Heino 1998; Luukkonen et al. 1998, 2002). The location along komatiitic cumulates is characteristic for Kambalda-type Ni deposits, but the deposit could have also been tectonically remobilised as it is located near a major deformation zone, the Tammasuo shear system. Based on outcrop observations, geophysics, and deep drilling results the mineralised rocks and associated komatiite unit have probably been translated to their present locations within Tammasuo shear system along an Archaean D_3-faulting with dextral sense of movement. An almost compositionally analogous komatiite unit exists close by to the west (Luukkonen et al. 1998, 2002; Figure 8).

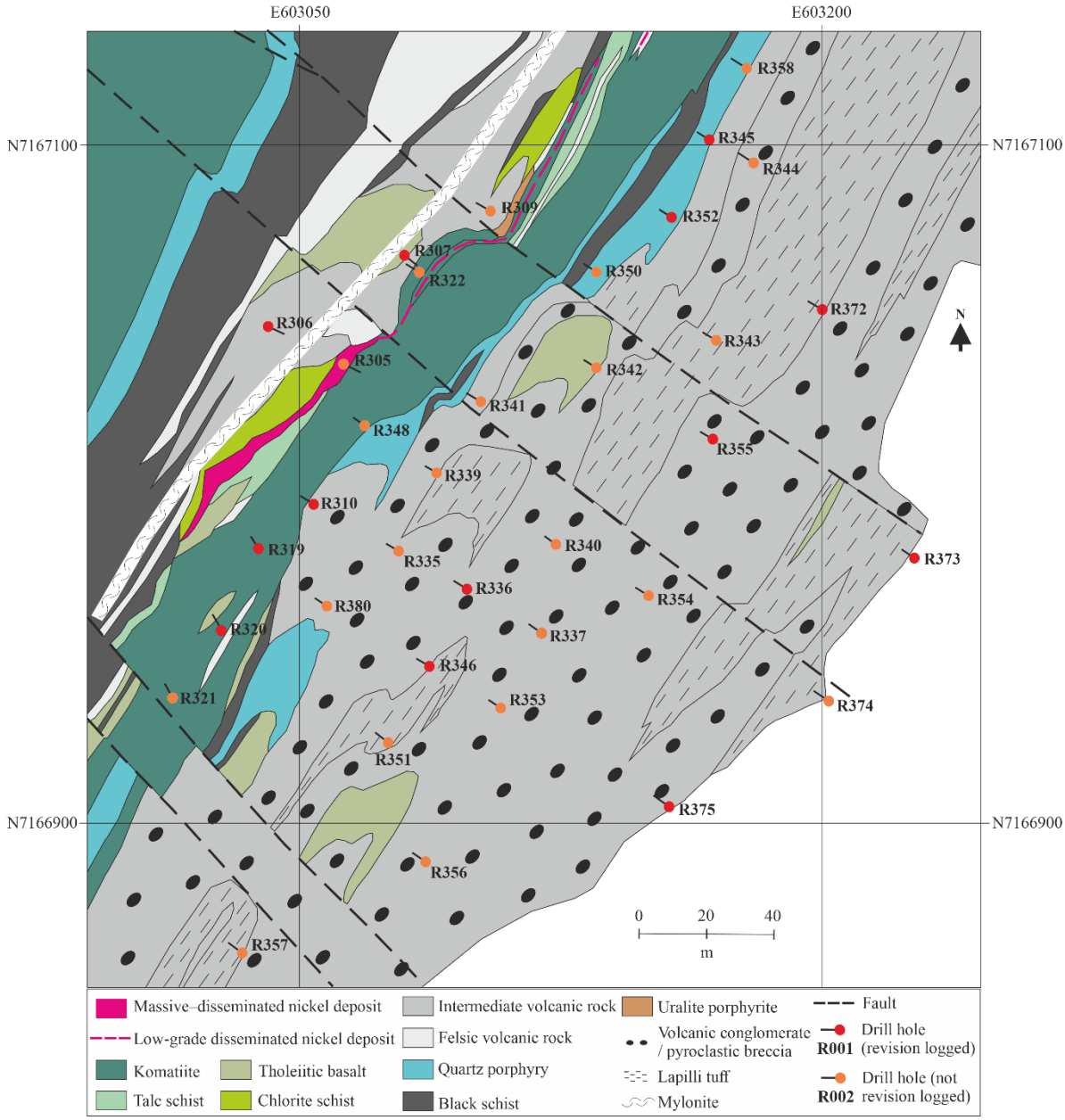

Figure 8. Lithological map of Sika-aho area (modified after Luukkonen et al. 2002). Coordinates are in ETRS-TM35FIN coordinate system.

Makkonen & Halkoaho (2007) have interpreted that the host rock of the deposit has been an intermediary rock based on elevated SiO_2 and Zn contents, and that the deposit has most likely been created by tectono-metamorphic processes. All authors agree that the deposit has been remobilised from its original location, which has been interpreted to be komatiitic, but the remobilisation mechanisms have not been defined. Luukkonen et al. (1998) state that the degree of remobilisation is at maximum a couple hundred metres, however it is very uncertain. It is unlikely that there has been substantial translocation from the primary formation environment (Luukkonen et al. 2002).

According to Luukkonen et al. (1998, 2002), komatiites that are chemically and lithologically similar to the Ni-critical Sika-aho komatiites have been detected elsewhere in the Moisiovaara area as up to several kilometres long and hundreds of metres wide arcuate and lenticular bodies (Figure 7). The Ni-critical komatiite unit is tightly folded and continues all the way from Kaivolampi to Paatola, after which it turns to NE corner of Honkajärvi and once again turns towards south along the eastern margin of Honkajärvi. The western branch of the unit is interpreted to extend towards Kaivolampi as a discontinuous and thin unit, from where both branches extend as a relatively thin units towards south.

The structure of the mineralised rocks and Ni-critical komatiite unit in their entirety has been interpreted to be a multiply folded synform structure that closes from its northern end and plunges steeply towards north, possibly forming an interference pattern caused by F_3 and F_4 folds. In the core of the synform are the Mg- and Cr-rich basalts and komatiitic basalts, which are overlaid by komatiites. Based on structural observations and SAMPO-probing (multifrequency electromagnetic method, 2–20 000 Hz) the limbs of the synform are subvertical or vertical and the synform hinge is below the depth of 500 metres. (Luukkonen et al. 2002).

3.3.3 Tammasuo gold deposit

Along with the Sika-aho Ni deposit in Moisiovaara area, there are anomalous Au contents found in Tammasuo nearby to the northeast of Sika-aho (Figure 7). Luukkonen et al. (1998, 2002) state that a small Au deposit was found by till geochemical surveys, induced polarisation (IP) surveys, and diamond drilling. The drilling results indicate that there are a few one metre wide intervals with max. 2.0–2.5 ppm Au, and some additional intervals with clearly elevated Au contents between 0.5–2.0 ppm. The highest contents were found from till geochemical samples with approximately 2.3–8.8 ppm of Au, however they are interpreted to be at least partly enriched by supergene processes. The Au in Tammasuo deposit is structurally controlled and associated with narrow cataclastic and strongly carbonate-, quartz-, and sericite-altered discontinuous zones, as well as with felsic dykes. The Au contents correlate well with S and As, as well as occasionally with Te.

3.3.4 Earlier studies in Sika-aho area

The first sign of Sika-aho Ni deposit was discovered in 1994 during one of GTK’s research and exploration projects in eastern Finland when a sample from till geochemical profile

showed anomalous Ni. The mineralised bedrock had been intersected by drill hole R306 by the end of same year, and the drilling continued until 1996 to trace the mineralised zone and Ni-critical komatiitic unit. (Luukkonen et al. 1998; Figure 8).

Based on conducted geophysical measurements, Sika-aho Ni deposit has a relatively low magnetic susceptibility (< 0.005 SI) and density varies between 2700–3100 kg m^{-3}, however Ni content has no detectable correlation with increasing density. The gravity anomalies are relatively subtle (Bouguer-anomaly of only 0.05–0.08 mgal). Some conductive horizons were detected, and they were utilised in misé-a-la-masse surveys that aided in determining the dimensions of the deposit. (Luukkonen et al. 2002).

After the exploration campaign ended, a mineral resource estimation of the Sika-aho deposit was done by Heino (1998). He estimated that there exists 175 085 tons of mineralised rock with a mean Ni concentration of 0.665 %, when the cut-off value is 0.35 % and the calculation extends to a depth of 150 meters. There is no available information about reporting in accordance with any reporting codes or standards.

Archaean Ni deposits in eastern Finland can be divided into different genetic groups based on the metal contents found in the deposits. Makkonen & Halkoaho (2007) divided the deposits into three genetic groups: 1) remobilised type deposits, where nickel is not at its primary magmatic position; 2) polymetallic hydrothermal deposits; and 3) magmatic komatiitic nickel deposits with “normal” characteristics. Sika-aho Ni deposit was determined to belong to the group 1 of remobilised type deposits.

The latest Sika-aho mineral deposit report shows that GTK’s exploration permit expired in 1998, and afterwards there have been two private companies that have held an exploration permit in the area: Polar Mining Oy in 2004–2005 and Kuhmo Metals Oy in 2005–2013 (GTK 2021). Kuhmo Metals Oy was sold to Boliden in late 2014, and the combined work of the companies consisted of mobile metal ions (MMI) sampling, aerogeophysics, diamond drilling, and in-house 3D-modelling. They drilled 17 new diamond drill holes for a total of 1043.6 metres and extended the current deposit some 20 m to the south. New mineral resource estimates have not been conducted (Juurela 2017). Currently, the area has been reserved by Magnus Minerals Oy starting from May 2021 with the reservation expiring in January 2023.

4 Materials and methods

4.1.1 Drill core revision logging and sampling

Drill cores from 13 Sika-aho drill holes were revised at GTK's national drill core archive in Loppi in January 2021. The drill cores were drilled between 1993 and 1997 during "The activities of the Archean Terrains in Eastern Finland" -project conducted by GTK (Heino 1998).

Various lithologies, including volcanic, subvolcanic, and sedimentary lithologies were observed and initially named based on their field characteristics. The collected data consisted of rock type, mineralogy, colour, α-angle of foliation (if applicable), and any relevant comments on lithology, mineralogy, or alterations. The drill cores did not contain any orientation information. During the drill core revision logging, 45 samples were collected from key locations for further analysis, however a few of them were deemed unnecessary, thus discarded later.

4.1.2 Petrographic analysis materials and methods

In total, 36 polished thin sections were made by Arto Peltola in the laboratory of Geohouse, University of Turku. In petrographic examination, the polished thin sections were studied with transmitted and reflected light. Different minerals were identified and their modal abundances (vol%) were approximated. Textures, grain sizes, alterations, and any other relevant features were documented. The protolith takes precedence over mineralogical/structural terms in the classification scheme as it better describes the original nature of the rock, and it has been extensively used in earlier studies of the area. However, descriptive names of the lithologies are given as well, as they provide necessary information about the current characteristics. All of the rocks have been metamorphosed under amphibolite facies conditions (Maier et al. 2013; Hölttä & Heilimo 2017), which makes the use of "meta-" prefix fairly redundant in the context of this study. Abbreviations for mineral names used in the figures are according to the list presented in Whitney & Evans (2010).

4.1.3 Geochemical analysis materials and methods

In total, 284 analyses were used for the study. The number of new samples for the study that were analysed by ALS laboratory in Outokumpu, Finland, was 43. The major rock-forming elements (Al_2O_3, BaO, CaO, Cr_2O_3, Fe_2O_3, K_2O, MgO, MnO, Na_2O, P_2O_5, SO_3, SiO_2, SrO,

and TiO_2) were analysed with ME-XRF26 method, which is a fused disc X-Ray fluorescence analysis. Majority of trace elements (Ba, Ce, Cr, Cs, Dy, Er, Eu, Ga, Gd, Hf, Ho, La, Lu, Nb, Nd, Pr, Rb, Sm, Sn, Sr, Ta, Tb, Th, Tm, U, V, W, Y, Yb, and Zr) were analysed with ME-MS81 method, which consists of lithium borate fusion prior to acid dissolution and ICP-MS analysis. Other trace elements (Ag, As, Cd, Co, Cu, Li, Mo, Ni, Pb, Sc, Tl, and Zn) were analysed with ME-4ACD81 method, which consists of four acid digestion and ICP-AES analysis. Nickel was also analysed as a sole analyte with a four-acid Ni-OG62 method, that is used to detect "ore-grade" (Ni > 1 wt%) contents, however only one sample exceeded the detection limit of ME-4ACD81 method. Platinum, Pd, and Au were analysed with PGM-MS23L method, which is a standard lead oxide collection fire assay finished with ICP-MS analysis. Loss On Ignition (LOI) was measured with OA-GRA05x method by a furnace or a thermogravimetric analyser (TGA). (ALS Geochemistry 2021).

A total of 229 earlier analyses used by Luukkonen et al. (1998) and Heino (1998) were provided by GTK, of which 51 were whole-rock analyses done by Labtium using X-Ray fluorescence (method 175X) and 178 were weak leach analyses (method 511U) that detected Ni, Co, Cu, Cr, and S. In addition, 12 whole-rock analyses from mineralised zone in Sika-aho were reported by Makkonen & Halkoaho (2007), making the total amount of earlier analyses 241. Samples with missing metadata and/or overlapping intervals (newer data were prioritised over older data) had already been omitted from the total. Ultimately, after omitting unsuitable data for the geochemical study, a total of 98 whole-rock analyses were considered. Nine of these analyses were from black schists, thus they were examined separately from volcanic rocks.

The analysis results were plotted with GCDkit 6.0 IN R 3.6.0 (Janoušek et al. 2006). Values below detection limit were replaced with half of detection limit value. Because the analyses were from different laboratories using different methods, some elements were not reported uniformly. Iron was reported as Fe_2O_3 and FeO, thus they had to be converted to correspond with each other. Using a stoichiometric factor of 0.89981, Fe_2O_3 was converted to FeO. Sulfur was reported as both SO_3 and S, thus SO_3 values had to be multiplied by 0.4 to convert them to S.

The major element abundances were normalised to volatile-free (for Al_2O_3, CaO, FeO, K_2O, MgO, MnO, Na_2O, P_2O_5, SiO_2, and TiO_2) and are written with an n-suffix (e.g., MgOn). Normalisation was done by calculating the sum of the major elements (those listed before,

with Cr_2O_3 for the new analyses as well) and consequently determining the factor by dividing 100 with the sum. Then, the factor was used to multiply each value, which resulted in the normalised value. Additionally, the bulk-rock chemistry of a sulfide deposit can be better defined if the Fe content in sulfides is removed: If the S content is > 0.3 wt%, then the sulfidic Fe can be calculated with Equations 1 and 2 (T. Halkoaho, personal communication, 7.10.2022).

$$1.7936 \times S = Fe\ in\ sulfide\ phase \quad (1)$$

$$Fe\ in\ sulfide\ phase \times 1.28648 = FeO \quad (2)$$

Thus, the calculated FeO content in sulfides is removed from the total FeO content of the mineralised rocks. Nevertheless, it is important to note that this assumes the sulfide assemblage to consist of typical magmatic sulfide phases, i.e., pyrrhotite, pentlandite, and chalcopyrite. Therefore, the presence of additional sulfur as pyrite, for example, would skew the values, but the Sika-aho deposit contains only minor pyrite locally. The exact sulfide mineralogy and elemental concentrations in each sulfide species are not known accurately for Sika-aho. The normalisation and subtraction of sulfidic Fe are only estimations that aid to better constrain the host rocks.

The existence of geochemical haloes around Sika-aho Ni deposit was studied by examining the results of chemical analyses in multiple formats. This includes tables, variety of plots in GCDkit (binary, ternary, xyz plots with circles), and numeric 3D-models in Leapfrog Geo.

4.1.4 Numeric and geological 3D-modelling materials and methods

Before starting the modelling, the available data had to be collected, checked, filtered, and corrected. The two necessary data files for drill hole importing, collar and survey, were made based on collar coordinate, elevation, drill hole azimuth and dip, as well as drill hole depth data presented by Luukkonen et al. (1998). The analysis data was compiled from new analyses made for the thesis (n=43), older data provided by GTK (Heino 1998; Luukkonen et al. 2002) (n=229), and data presented by Makkonen & Halkoaho (2007) (n=12). The lithological data from 13 drill holes that was used is presented in Chapter 5.1 and in Appendix 1. Geophysical and geological maps from Luukkonen et al. (1998) were introduced to the model as photos and georeferenced to match the topography. 3D-modelling was done in its entirety with Seequent's modelling software Leapfrog Geo, with some preparatory photo, map, and file editing done in ArcMap 10.5.1 and CorelDRAW 2019.

In total, 26 drill holes were imported to Leapfrog: **R306**, **R307**, **R310**, **R319**, **R320**, **R336**, **R345**, **R346**, **R352**, **R355**, **R372**, **R373**, **R375**, R308, R309, R311, R312, R313, R314, R315, R321, R322, R323, R349, R351, and R354 (examined drill holes in **bold**). Some assays had no interval (e.g., 17.80 m): for that reason, they were changed to have an interval of 0.02 m (17.79 – 17.81 m) as otherwise an error would have occurred. When importing the analytical data, assays below detection limit were replaced with half the value in Leapfrog.

The topography for the model was created using the elevation model from National Land Survey of Finland (NLS). The dataset is based on laser scanning data with point density of at least 0.5 points per square meter with a grid size of 2x2 meters (Open licence CC BY 4.0, acquisition of data on 01/2022).

The geological model was built using the lithological data imported in the drill hole directory. For the model, the lithologies had to be grouped and simplified as there were many thin and irregular units with limited continuity, causing major challenges for creating the surfaces and volumes that would respect the actual geology. The procedure contains the following simplifications that were done before building the final model (Figure 9): 1) Carbonate-quartz veins, quartz veins, and fractures were dismissed due to narrowness and little apparent spatial continuity over longer distances; 2) Tholeiitic basalts and komatiitic basalts were grouped as basalt; 3) Intermediate volcanic conglomerates, intermediate lapilli tuffs, and intermediate – felsic volcanic rocks were grouped as intermediate – felsic volcanic rocks. To be accurate, the group should have been named as intermediate – felsic volcanic and volcaniclastic rocks, however later on renaming could not be done without resplitting the lithological units and reprocessing the models, thus it was kept as the shorter and simpler, though slightly inaccurate name; 4) Black schists were originally named as black shales, thus they are called black shales in the 3D-model. The interval R310 107.9 – 114.2 m of phyllite was combined to black shale as it occurred only in one hole and surface could not be built only from it.

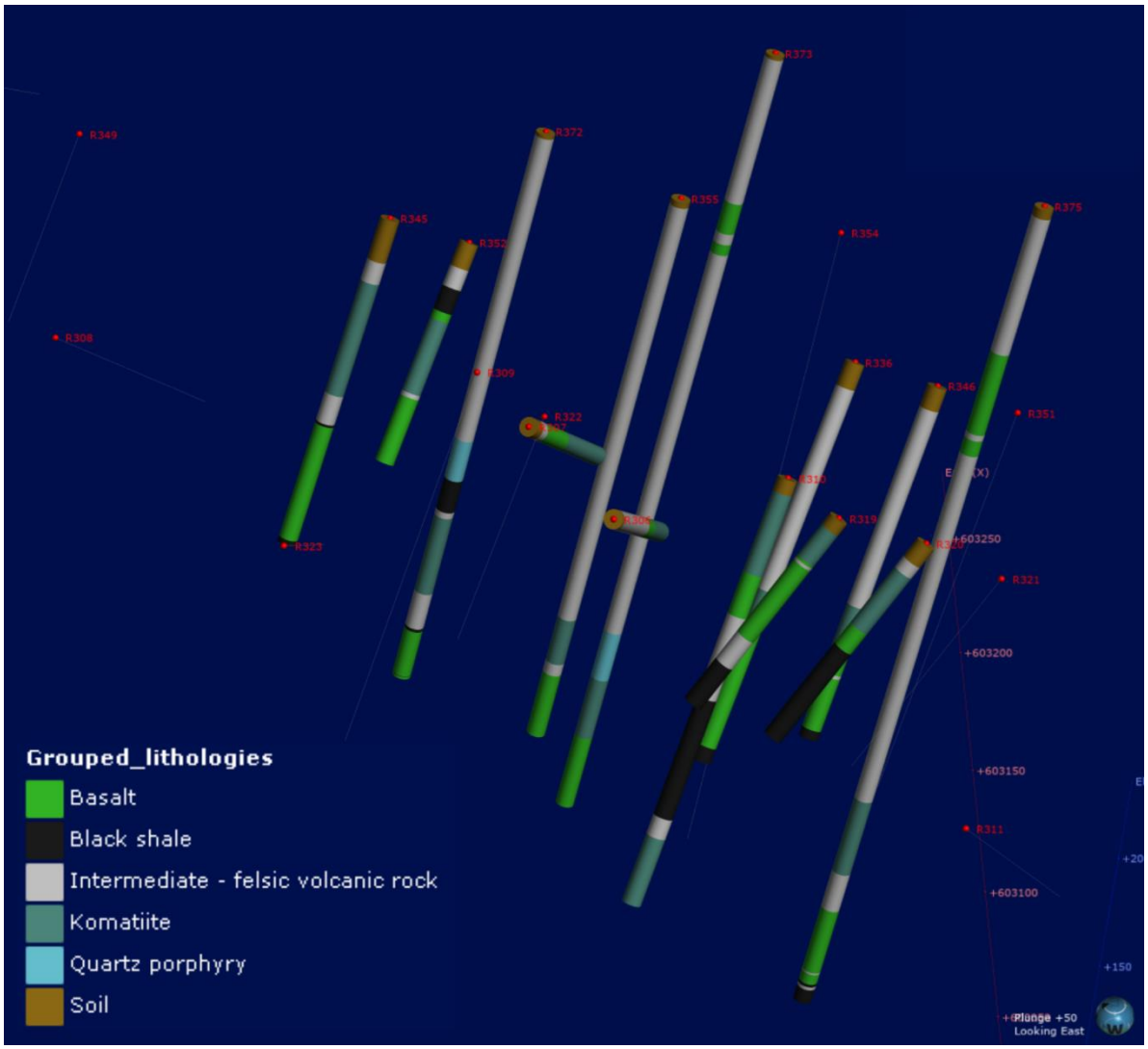

Figure 9. Grouped and simplified lithological units from Sika-aho shown in drill holes. Plunge is 50 degrees, looking towards east.

To improve the accuracy of created surfaces, polylines were used: lithology contacts were traced over the bedrock map of Luukkonen et al. (2002). The model extents were created so that the geological model would not continue too far outside the available data points as it would have created unnecessarily large “unknown lithology” volumes. Also, the deposit surfaces related to the numeric model were created: polylines were traced over map contacts and earlier cross sections by Heino (1998) (Figure 10), and connecting polylines were created between vertical cross section polylines.

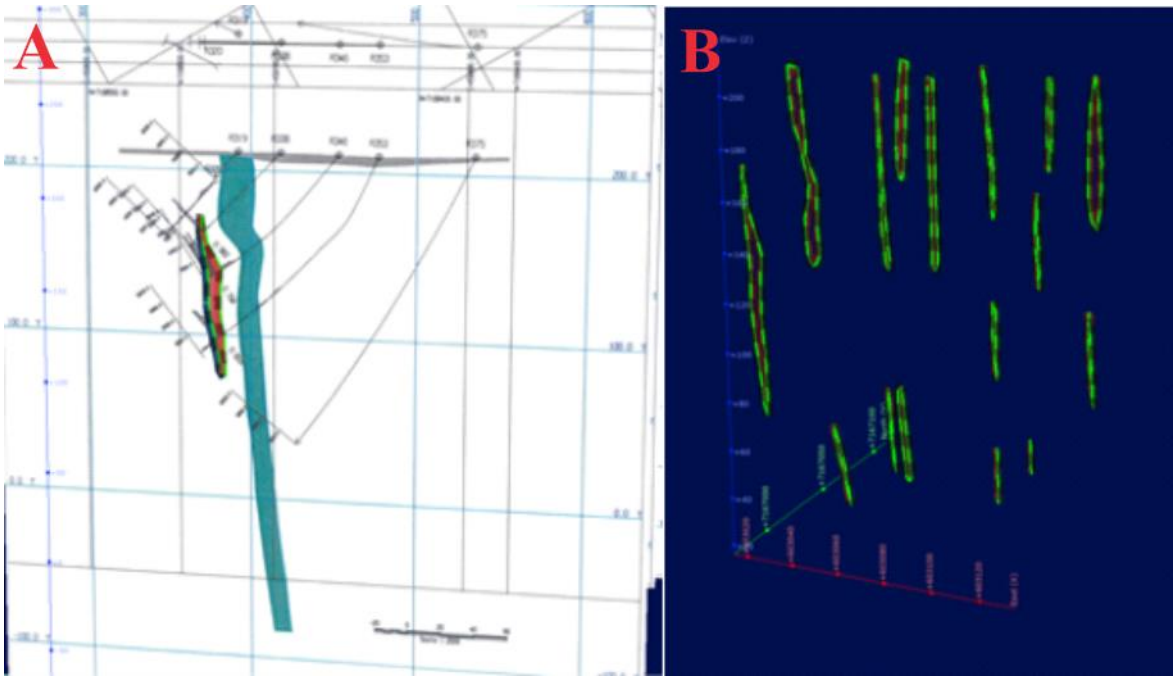

Figure 10. a) Example of creating polylines from cross sections (Heino 1998) by tracing over the deposit outlines. b) The created polylines that better constrain the Sika-aho Ni deposit.

Two different geological models were built. The “Deposit GM” and the “Stratigraphy GM” were created: the difference between these two models is that the model surfaces have been built as deposits versus stratigraphies, which results in different surface geometries. It was attempted to have the stratigraphic surface order of “Stratigraphy GM” follow the interpretations by Luukkonen et al. (1998) and Lehtonen et al. (2016), but it was not possible to build an entirely correct stratigraphical model: the banded amphibolites and tholeiites to the east of the study area are the oldest rocks and they are overlain by komatiites and mafic volcanic rocks seen in northwest corner of Figure 8, however the volcaniclastic rocks between those two sequences have been interpreted to be the youngest rocks in the stratigraphy. Yet, uncertainty still exists, and the result is a pseudo-stratigraphic model that should not be treated as a true representation of the stratigraphy.

Numeric modelling was used to create interpolants that allowed to estimate the elemental contents for intervals where no geochemical data was available. The numeric modelling tool in Leapfrog Geo utilises the FastRBF™ (Radial Basis Function) algorithm. To create the numeric model, a spheroidal interpolant function was used rather than the linear interpolant function. Linear interpolant function works better for categorical data, such as lithology, but not as well for values with a distinct finite range of influence because it heavily extrapolates values outside the data (Seequent Limited 2019). The parameters that define the interpolant were chosen based on information provided in Seequent Limited (2019) and other Seequent

tutorials and webinars, as well as the author's interpretation of continuity and extent for the deposit.

In the final model, no compositing has been done. Compositing with different values and settings were experimented with, however the result usually was exaggerating the volume of the deposit. Compared to the mineral resource estimation by Heino (1998), the volume was already significantly larger [105 893 m^3, which corresponds to 328 268 tons if the density is approximated as 3100 kg/m^3 per Heino (1998)]. One thing that distorts the isosurfaces of the deposit is that the drill holes were imported as straight lines with no available data for the deviation along depth, however the cross sections that were used had been adjusted for the deviation. This caused the deposit to be wider than in reality, especially in the southern end: the deeper you go, the larger the error will become.

A global trend was set as 85/135 (dip/dip direction) with pitch = 90, and the ellipsoid ratios were 3:3:1 (Max-Int-Min). The orientation was based on the reported dip and dip direction by Heino (1998). The interpolant properties are presented in Table 2.

Table 2. Interpolant properties for the numeric Ni model.

	Alpha	**Total sill**	**Nugget**	**Base range**	**Drift**	**Accuracy**
Value	9	0.01	0.0	50.0	None	2.0

The alpha value was simply left as the default option of 9, because it is closest in shape to a spherical variogram (Seequent Limited 2019). No justification for a higher or lower value was made.

According to Seequent Limited (2019), the total sill determines the upper limit of the spheroidal interpolant function. Beyond the upper limit, there ceases to be correlation between values. It was set as 0.01 for the interpolant, however different values do not affect the interpolant when nugget is 0, because the shape of the interpolant is determined by the total sill to nugget ratio.

Nugget value was kept at 0 as default. If there were local anomalies, a positive nugget value would have placed more emphasis on the average values around the anomalous sample (Seequent Limited 2019). In case of Sika-aho, there were not too many anomalous samples present, even though the usage of a low total sill to nugget ratio could be justified to reduce the noise from possibly erroneous values from geochemical analyses.

The base range was set as 50.0 m. This is based on the distance between drill holes, which is usually about 25 m or more in Sika-aho. As mentioned in manual by Seequent Limited (2019), twice the average distance between drill holes is an optimal range in many cases.

Drift was set as None, because Linear and Constant drift would give unreasonable values away from data points, as the interpolant boundary is larger than extent of the data.

Accuracy was set at 2.0 as a default, as Leapfrog estimates it by taking a fraction of the smallest difference between two data values. Lower value for accuracy would not influence the interpolant in this case, as the errors for Ni values are higher than that.

In addition to numeric and geological 3D-models, a combined model was created. Combined models can show, for example, what the host rocks of the deposit are. The combined model uses the Ni-interpolant and the “Stratigraphy GM” geological model.

5 Results

For the study of geochemical analyses and thin sections, the mineralised zone is considered to contain at least 2000 ppm of Ni. The cut-off value of 2000 ppm for the mineralised zone was selected due to geochemical reasons: the highest Ni value observed in non-mineralised komatiites was 1780 ppm, thus values over 2000 ppm in mostly basaltic and intermediate-felsic volcanic rocks can be reasonably attributed to remobilisation of Ni. The higher cut-off value selected for the numeric 3D-model is 3500 ppm because it was used by Heino (1998) in the mineral resource estimation, thus allowing the usage of earlier cross sections and better comparability between the model and the estimation. Also, there would have been only one thin section from a sample interval that exceeds 3500 ppm Ni, whereas there are four that exceed 2000 ppm Ni.

5.1 Drill core revision logging results

The drill core revision logging results are presented in two forms: simplified drill core profiles in Figures 11 and 12, and revised version of the original logging book as a table in Appendix 1. The rocks found in the study area are mostly volcanic and volcaniclastic with composition varying from ultramafic to felsic, but minor subvolcanic and sedimentary rocks are also encountered (Figures 11 and 12). The thickness of intermediate-felsic volcanic rocks varies heavily between tens of centimetres to tens of metres, whereas tholeiitic basalts, komatiitic basalts, and komatiites usually form thicker layers from metres to tens of metres. The eastern part of the study area is dominated by volcanic conglomerates/pyroclastic breccias and lapilli tuffs, as well as intermediate-felsic volcanic rocks (Figures 8, 11, and 12). In two of the drill holes (Figure 12), quartz porphyry is observed. Black schists are found as thin to thick interbeds with thickness varying from tens of centimetres to tens of metres (Figures 11 and 12).

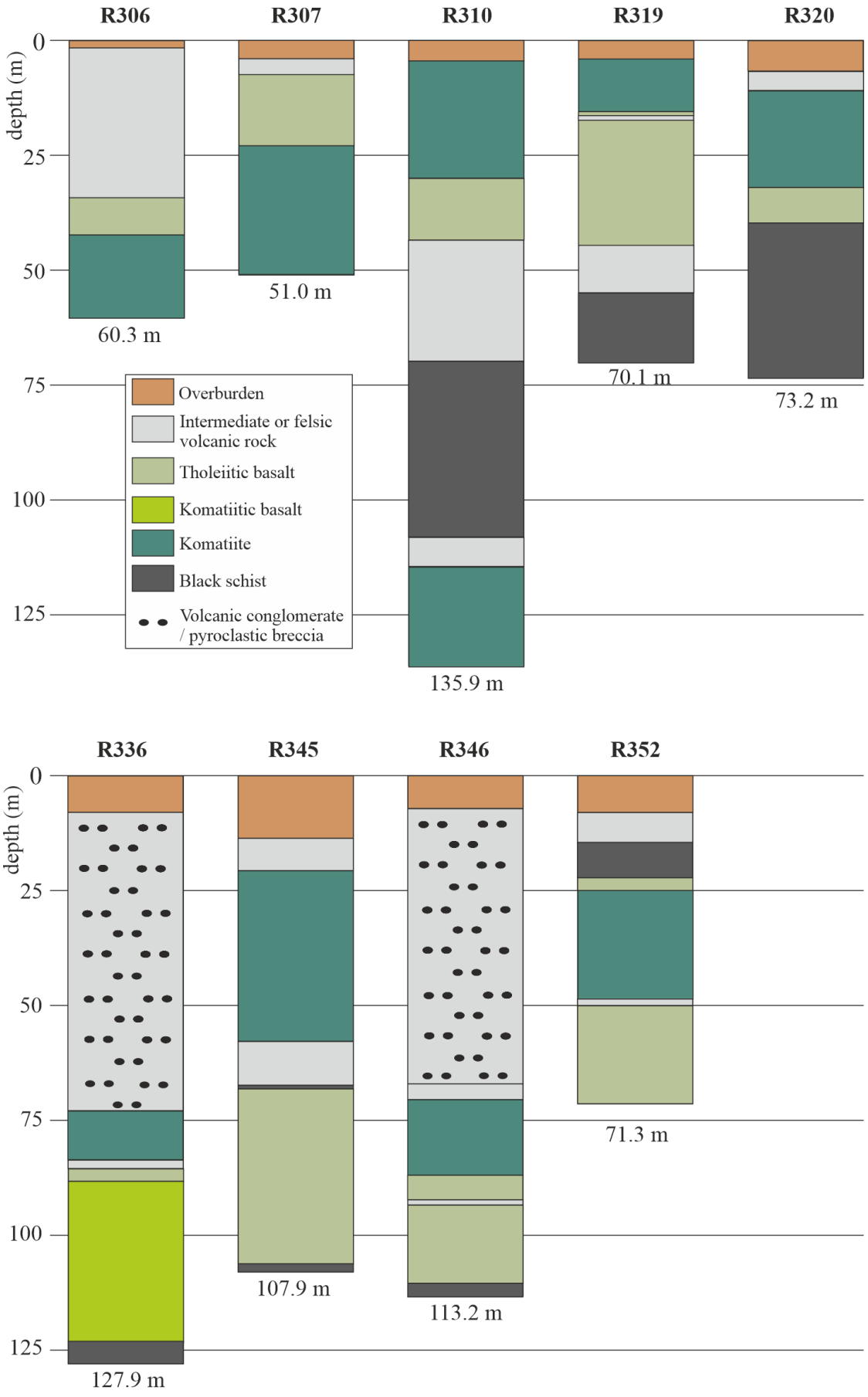

Figure 11. Simplified profiles for drill holes R306, R307, R310, R319, 320, R336, R345, R346, & R352.

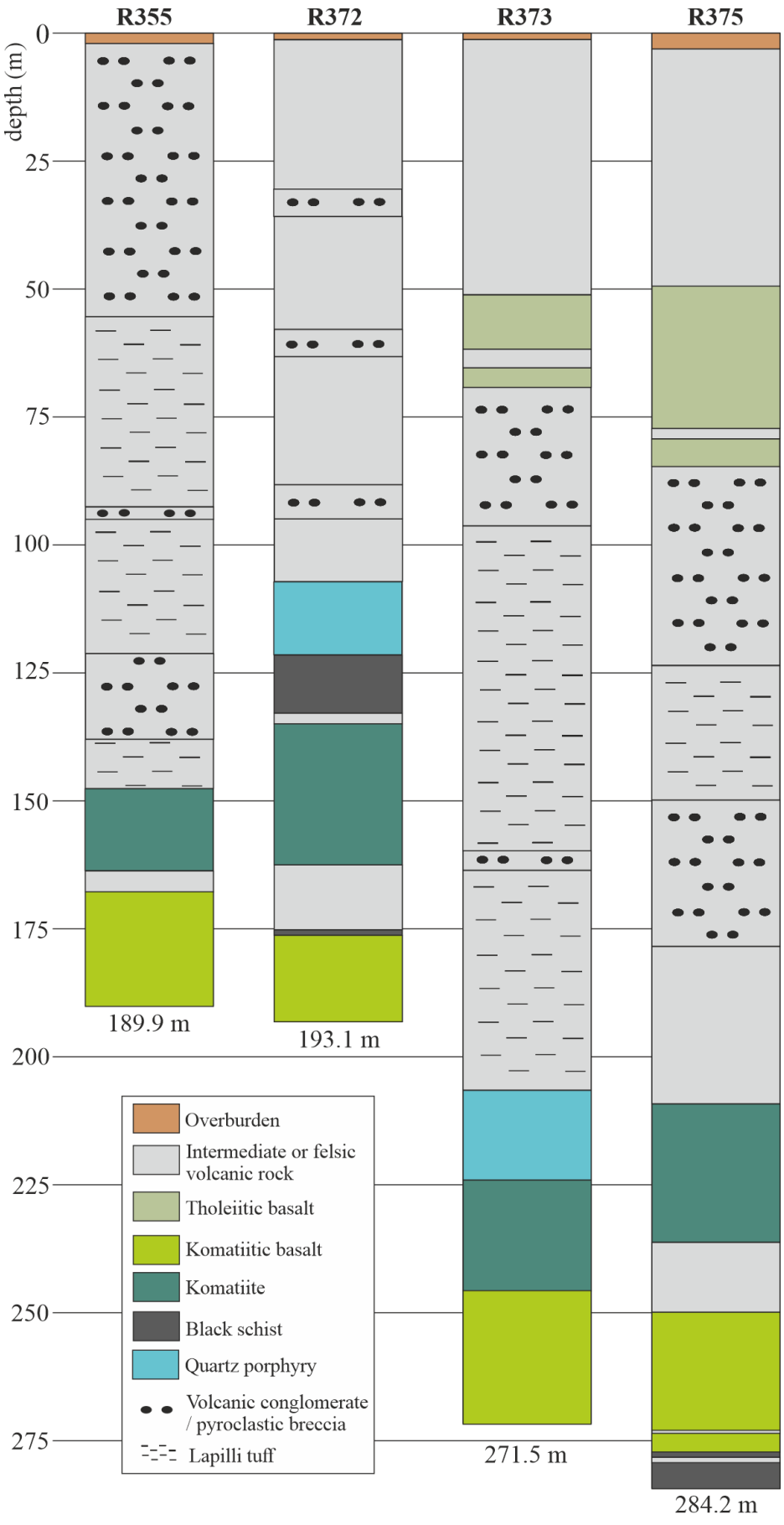

Figure 12. Simplified drill core profiles for drill holes R355, R372, R373, & R375.

5.1.1 Description of nickel mineralised zone

The mineralised zone was observed in 9 out of 13 drill holes, and it was typically a few metres thick. Characteristic features were strong schistosity and presence of sulfides (pyrrhotite, pentlandite, chalcopyrite) along schistosity planes as well as disseminated in the matrix (Figure 13a and 14a). Stretching lineations in sulfides can be observed on schistosity planes, especially in the very strongly schistose mineralised rocks. Massive vein-like sulfides were also observed (Figure 13b). The host rock appeared to consist of at least of chlorite, quartz, and carbonate, and based on the examination, the most probable protolith for the mineralised zone rocks were determined to be mafic or intermediate volcanic rocks.

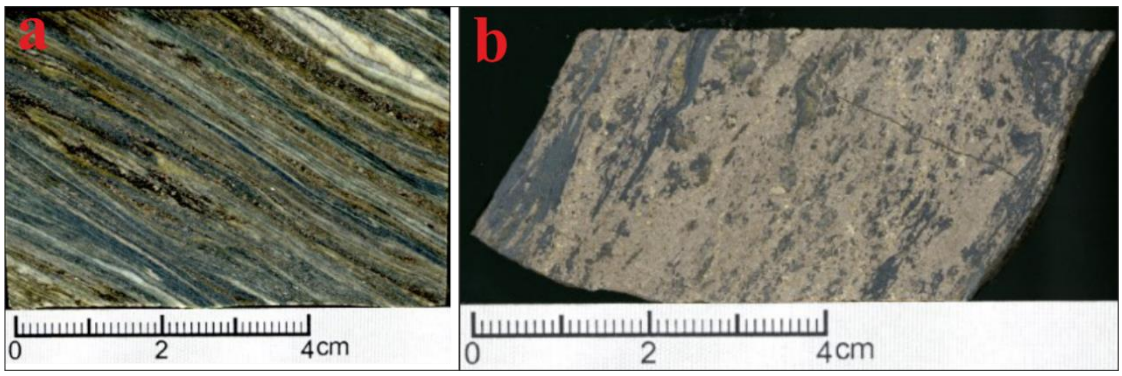

Figure 13. a) Typical mineralised zone in Sika-aho (R310-39.40). b) Massive pyrrhotite-pentlandite(-chalcopyrite) vein (R336-89.60). Photos by Markku Laaksonen, GTK.

5.1.2 Description of komatiites

Komatiites were easily distinguished from other rocks due to abundant talc, and komatiites were found in each of the studied drill holes. Other identified minerals were serpentine and carbonates, and possibly minor tremolite. The schistosity of komatiites varied from non-schistose (massive) to moderately schistose. Oxides and sulfides were typically too small to identify. The colour was usually light grey with greenish shade (Figure 14b).

5.1.3 Description of mafic volcanic rocks

Generally, mafic volcanic rocks were moderately to strongly schistose (Figures 14c and 14d). This lithology was observed in all drill holes. The colours were different shades of green and grey on the fresh surface. Observed minerals included chlorite, quartz, carbonates, and sulfides. Reliable differentiation between tholeiitic basalt and komatiitic basalt was not possible without chemical analyses, however, it was usual that fuchsite could be seen in komatiitic basalts.

5.1.4 Description of intermediate-felsic volcanic and volcaniclastic rocks

The intermediate to felsic rocks comprise a larger group of rocks, and they were the most abundant lithologies found in the study area. The major minerals observed in the rock were quartz, carbonates, and sericite, along with minor sulfides. The schistosity varied from moderate to strong, but certain intermediate interlayers were massive. The colour was typically light grey. All pyroclastic rocks showed similar mineralogy: the volcanic conglomerates/pyroclastic breccias and lapilli tuffs were distinguished from each other by the amount of blocks, bombs, lapilli, and ash. The pyroclasts were invariably flattened/elongated (Figures 14e and 14f)

5.1.5 Description of other lithologies

Two quartz porphyry intervals were distinguished (Figure 12): the rocks were characterised by rounded quartz grains in a moderately schistose, very fine-grained groundmass. The quartz porphyries were typically light grey in colour.

Only rocks with sedimentary origin observed were black schists, and they were found above and below the eastern komatiite unit. They were quartz-rich and had a strongly foliated, very fine-grained matrix consisting of graphite and sericite (Figure 14d). Sulfide grains up to 3 cm in diameter, mainly pyrrhotite, were observed. The colour of the black schist was dark grey to black.

There were quartz-carbonate veins which occasionally contained sulfides and fragments of surrounding rocks. However, they were narrow and the volume of them was very low, hence they were not addressed in this study. Furthermore, some very narrow, strongly fractured intervals were identified, but they were scattered and not spatially connected.

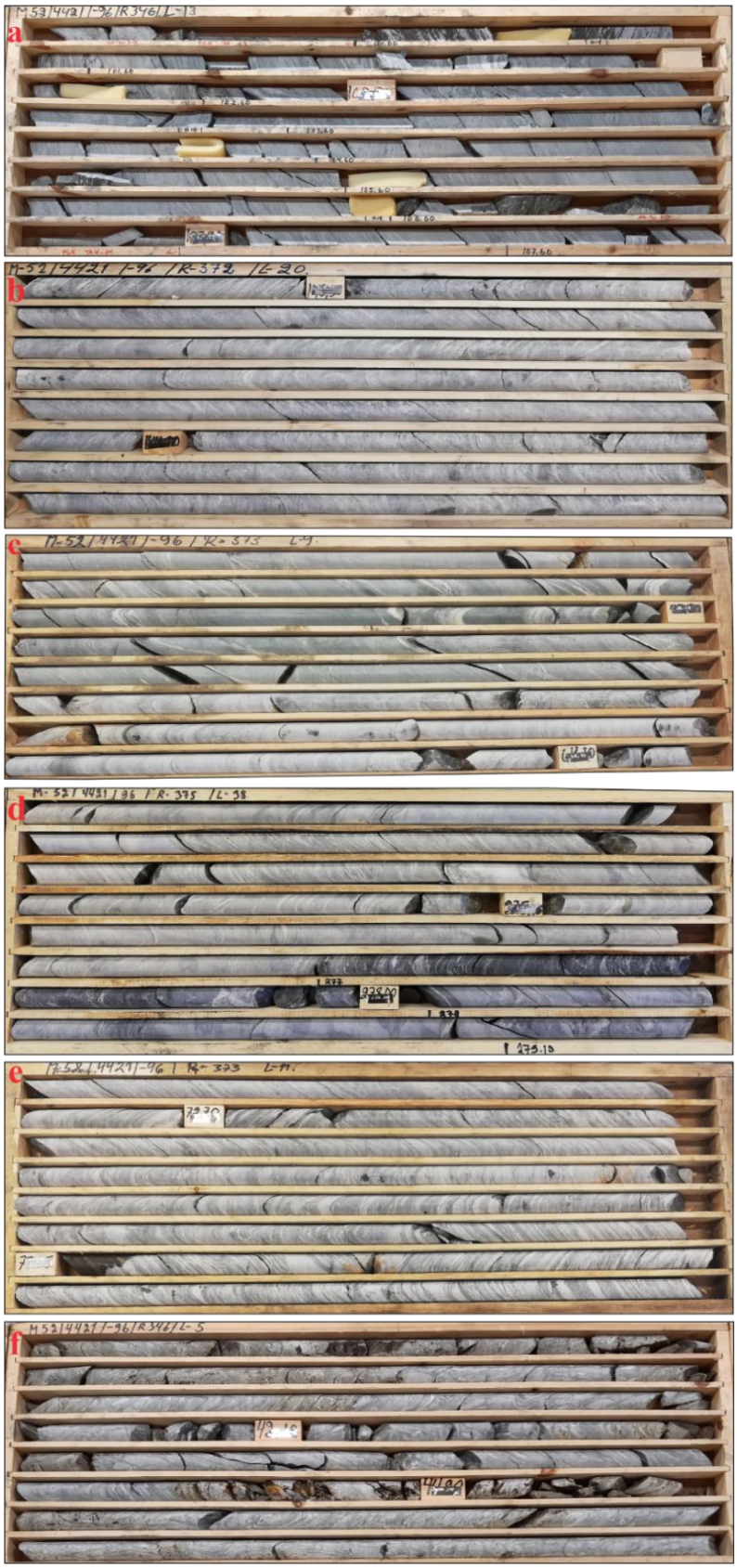

Figure 14. Drill core pictures of different rocks in the Sika-aho study area, see text for further explanation. a) Mineralised tholeiitic basalt (R346, box 13), b) Altered komatiite (R372, box 20), c) Mafic and intermediate-felsic volcanic rocks (R373, box 9), d) Tholeiitic basalt, intermediate-felsic volcanic rock, and black schist (R375, box 38), and e) & f) Intermediate volcanic pyroclastic rocks (R373, box 11 and R346, box 5).

5.2 Petrography

5.2.1 Petrography of nickel mineralised zone

All mineralised samples contain quartz, carbonate, chlorite, sulfides, and oxides in varying abundances. Descriptive name for the host rocks in Ni mineralised zone is sericite-carbonate-chlorite-quartz schist. The mineralised rocks are strongly schistose, and the sulfides were almost invariably elongated and flattened along schistosity planes (Figure 15). Occasionally, crenulation cleavage can be observed in the mineralised rocks (Figure 16).

The abundance of carbonates can vary between few singular crystals (< 1 vol%) in R375-246.45 up to approximately 50 vol% in R306-36.10, with R307-22.15 and R352-58.00 having values of 5 vol% and 25 vol%, respectively. Quartz is inversely proportional to carbonates, accounting for 15–50 vol% of the samples. Both carbonates and quartz are found mostly as granular recrystallised grains, with grain sizes commonly varying between 0.1 mm and 0.01 mm in diameter. R375-246.45 contains only few chlorite crystals (~1 vol%), whereas R306-36.10 has 20 vol% of chlorite, and both R307-22.15 and R352-58.00 have up to about 50 vol% of chlorite. Chlorite generally has a foliated or massive crystal habit with grain sizes up to a couple millimetres. The only sample containing sericite is R375-246.45 with approximately 25 vol% of foliated sericite. Also, minor biotite was observed in thin section R306-36.10.

Opaque minerals (sulfides, oxides, hydroxides) account for approximately 5–25 vol% of the samples. Sulfides are mostly pyrrhotite and pentlandite, with minor chalcopyrite, bravoite, sphalerite, and covellite. Pyrrhotite is observed as anhedral, elongated crystals along schistosity, disseminated in the matrix, or as intergrowths with pentlandite and chalcopyrite (Figure 15). Pentlandite can be found as lamellae in pyrrhotite, as anhedral crystals disseminated in the matrix, or as intergrowths with pyrrhotite and chalcopyrite. Chalcopyrite is observed mostly as intergrowths with pyrrhotite and pentlandite. In one of the samples, R307-22.15, some chalcopyrite crystals have altered to covellite on crystal boundaries. In samples R306-36.10, R375-246.45, and R307-22.15, an alteration mineral in fracture planes and crystal boundaries of pentlandite was identified as a mineral that is most likely bravoite (and magnetite+goethite) (Figure 17). Sphalerite intergrowths with other sulfides were observed in sample R352-58.00. Sulfide grain sizes vary greatly, from 0.01 mm to several tens of mm in diameter.

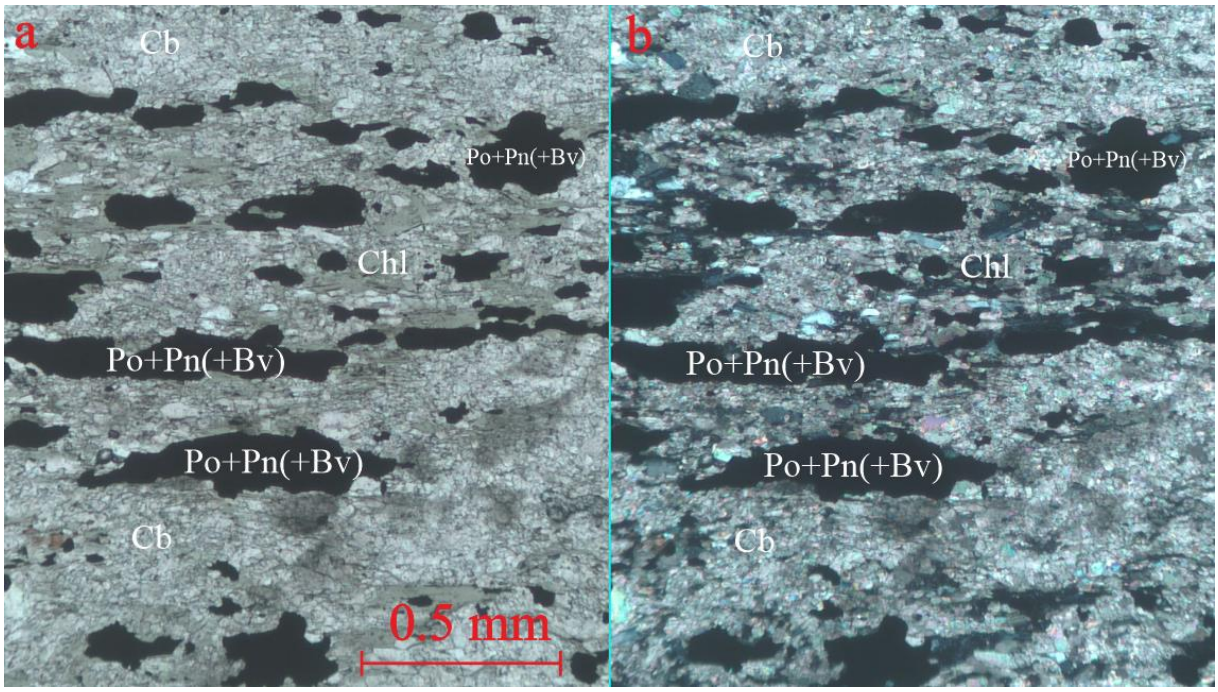

Figure 15. Elongated sulfides, mainly pyrrhotite (Po) and pentlandite (Pn) with minor bravoite (Bv) along schistosity in carbonate (Cb) and chlorite (Chl) groundmass. R306-36.10. a) Plane polarised light, 5x magnification, b) Cross polarised light, 5x magnification.

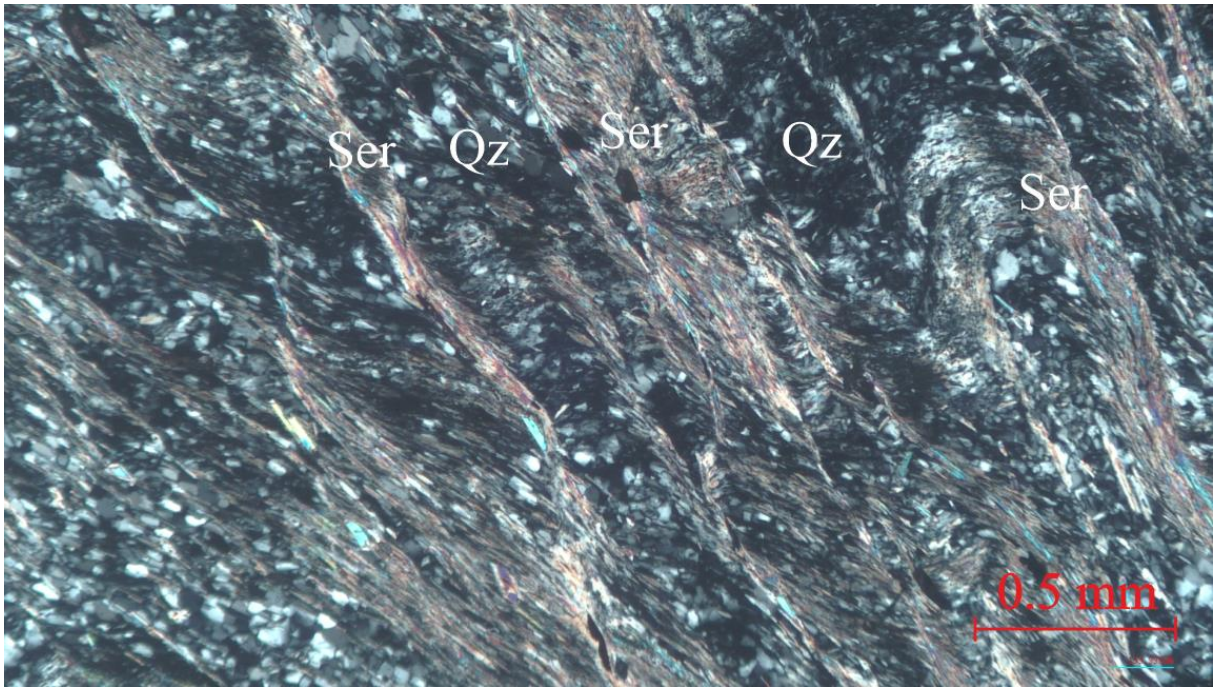

Figure 16. Crenulation cleavage in a mineralised intermediate-felsic volcanic rock containing mainly quartz (Qz) and sericite (Ser) in the groundmass. R375-246.45. Cross polarised light, 5x magnification.

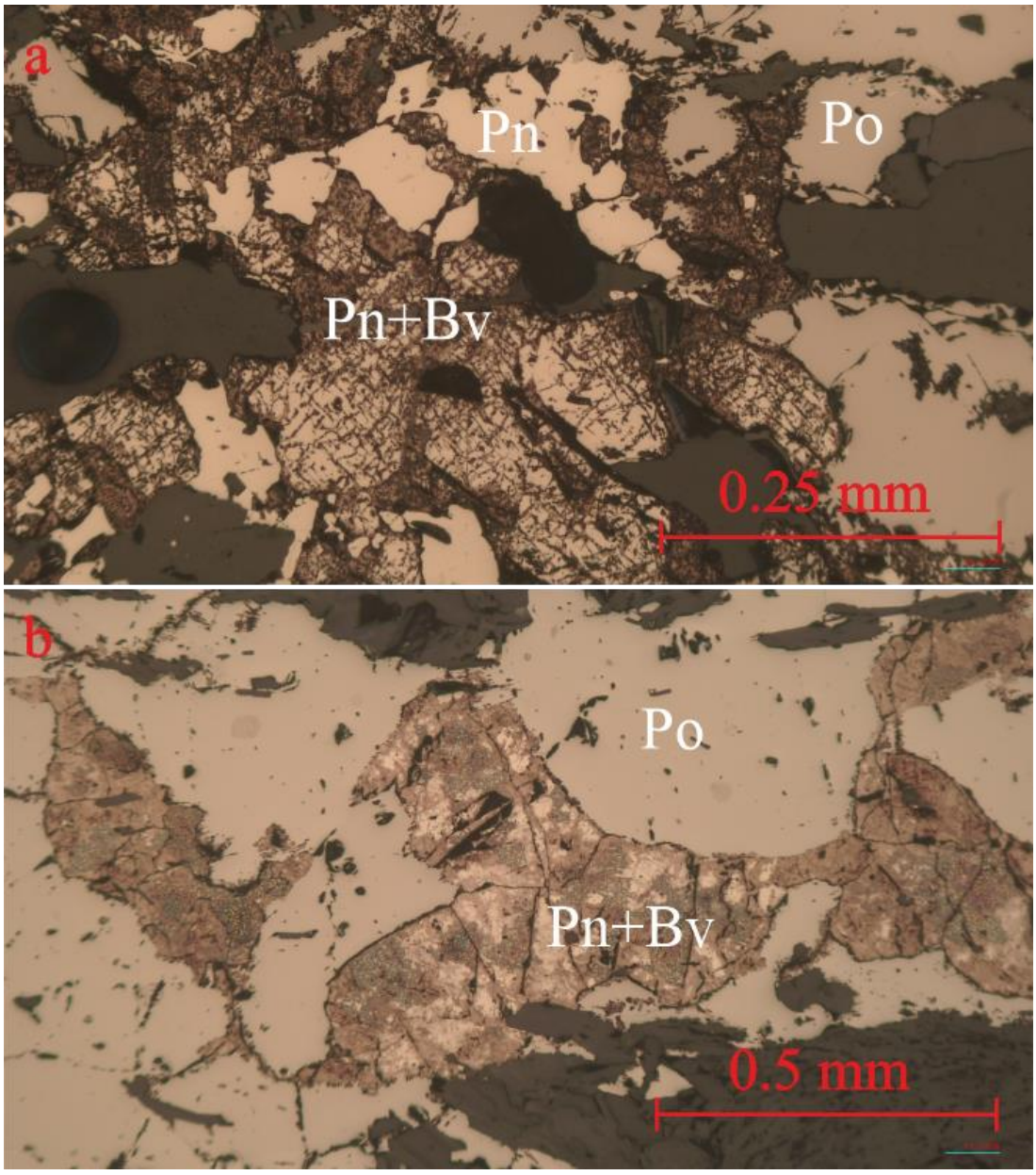

Figure 17. Pyrrhotite (Po) and pentlandite (Pn) intergrowth with some pentlandite grains that have been altered to bravoite (Bv) and (hydr)oxides along fracture planes. a) R306-36.10, reflected plane polarised light, 20x magnification, b) R375-246.45, reflected plane polarised light, 10x magnification.

The most common oxide observed in each sample is magnetite. It is found as disseminated grains in the matrix or as intergrowths with sulfides or ilmenite. Another oxide is ilmenite, which occurs similarly to magnetite. Generally, the oxide grain sizes were below 0.1 mm in diameter, often even too small to identify with the highest magnification. One mineral that was not reliably identified was an isotropic or weakly anisotropic mineral with similar reflectivity as magnetite, grey colour, distinct yellowish to brownish and sometimes reddish internal reflections, and often broken up with non-opaque minerals. It was observed as intergrowth and fracture filling in oxides and sulfides, and as very small individual grains

disseminated in the matrix. Based on its optical properties and occurrence it was identified as goethite, however sphalerite can also have similar optical properties. Some of the sulfides were replaced with quartz, carbonate, chlorite, and (hydr)oxides. Pyrrhotite with minor pentlandite flames and intergrown chalcopyrite was replaced with mainly carbonate and quartz, evidenced by caries texture and spotted alteration (Figure 18).

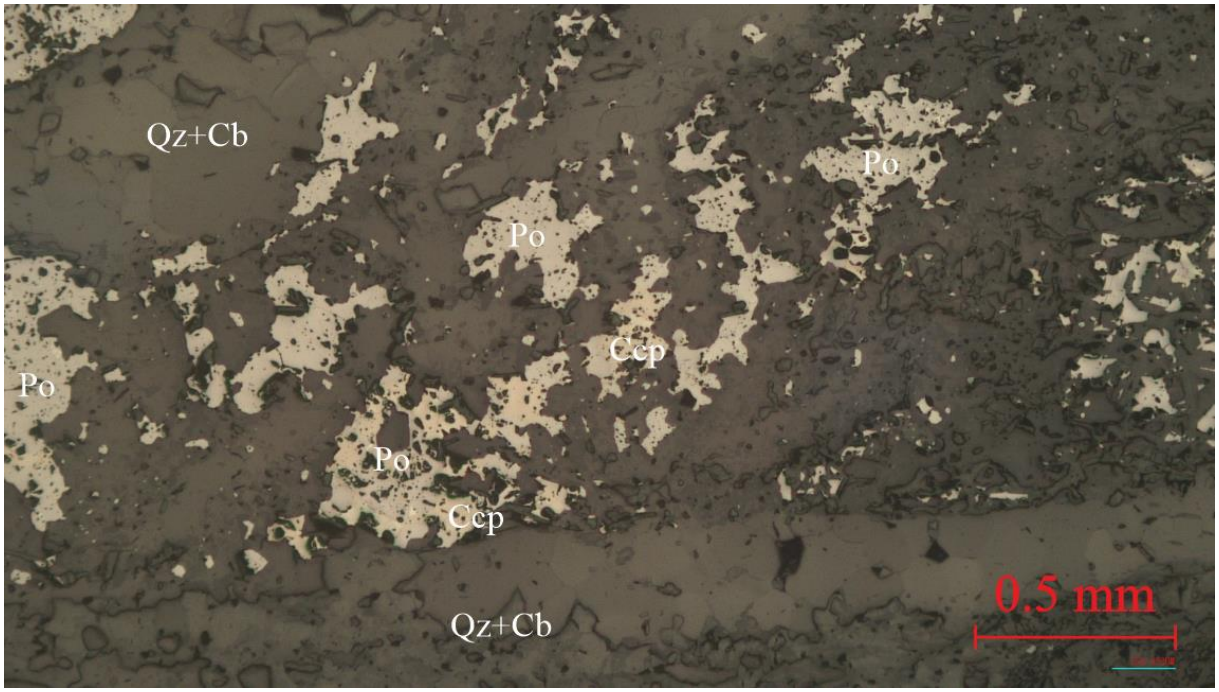

Figure 18. Pyrrhotite (Po) and chalcopyrite (Ccp) intergrowth, micrometre scale pentlandite flames in pyrrhotite (not distinguishable in the picture). Caries textures and spotted alteration of sulfides. R345-73.60. Reflected plane polarised light, 5x magnification.

5.2.2 Petrography of komatiites

The descriptive name for the komatiites is carbonate-talc-serpentine schist. Hence, the main constituents are serpentine, talc, and carbonates, however some tremolite can also be found. Occasionally, few sericitised plagioclase grains can be observed. Schistosity varies from non-schistose to strongly schistose. Serpentine is fibrous and foliated, sometimes platy. Talc is mainly bladed or massive. Generally, the grain size is fine- to very fine-grained, but some larger 1–3 mm in are observed. Carbonate grains are larger, usually 1–5 mm in diameter, and they are eu- to subhedral. Example of typical komatiite from Sika-aho is shown in Figure 19.

Sulfides and oxides account for approximately 1–10 vol% of the rocks. Sulfide phases observed by reflected light microscopy in decreasing abundance were pyrrhotite, pentlandite, chalcopyrite, and pyrite. Pentlandite is observed as individual mineral grains disseminated in

the matrix, intergrown with pyrrhotite and chalcopyrite, or as exsolution lamellae in pyrrhotite. Pyrrhotite is observed as individual mineral grains disseminated in the matrix or intergrown with pentlandite and chalcopyrite. Chalcopyrite is found mainly intergrown with pentlandite and pyrrhotite. Pyrite is found as euhedral cubes. The sulfide and oxide grain sizes are generally from fine to very fine (1–0.01 mm in diameter). Oxide phases observed were chromite, magnetite, and ilmenite. They are found as bladed or anhedral grains disseminated in the matrix, or sometimes as inclusions in carbonate grains.

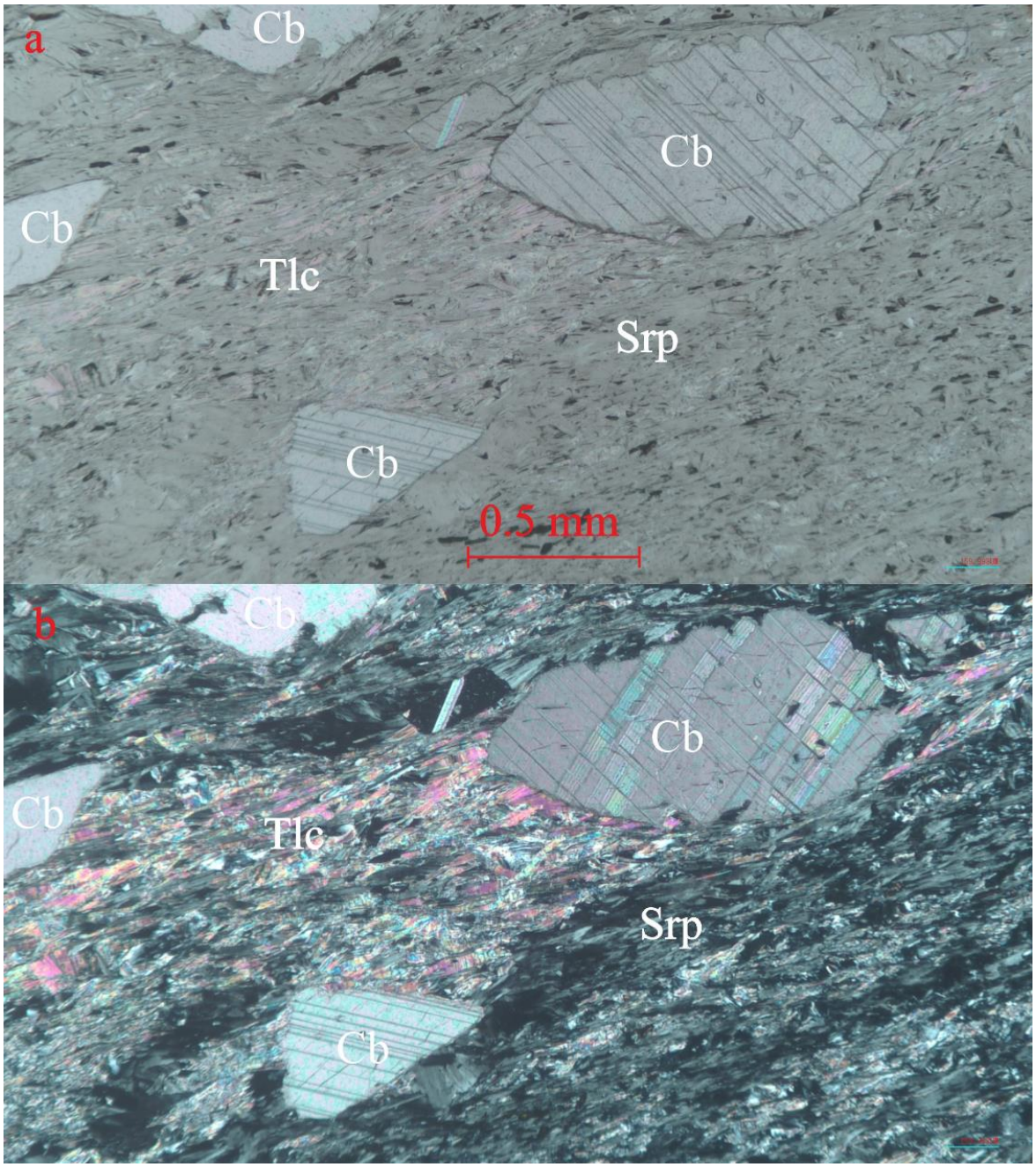

Figure 19. Altered komatiite with carbonate (Cb), serpentine (Srp), and talc (Tlc). R310-12.50. a) Plane polarised light, 5x magnification, b) Cross polarised light, 5x magnification.

5.2.3 Petrography of mafic volcanic rocks

The mafic volcanic rocks, which are not included in the Ni mineralized zone, are largely comprised of quartz, carbonates, chlorite, sericite, and variety of sulfides and oxides. A generalised, descriptive name for the mafic volcanic rocks is sericite-carbonate-chlorite-quartz schist. The mafic volcanic rocks are characterised by moderate to strong schistosity. Only minerals that were present in every thin section are quartz and carbonate. Quartz can be observed as fine- to very fine-grained (0.1–0.01 mm in diameter) crystals, usually recrystallised. Sometimes, there are larger quartz crystals in quartz-carbonate-sulfide veinlets. Carbonate has similar grain size as quartz in the groundmass, with larger crystals up to 2 mm in diameter, however the abundance varies greatly from just few individual crystals to approximately 50 vol%. Banded texture with chlorite- or sericite-rich and recrystallised quartz-carbonate bands are frequently observed (Figure 20). Generally, chlorite and sericite have an inverse relationship meaning that chlorite-rich samples are sericite-poor and vice versa. They are foliated or massive, and usually account for 1–50 vol% of the rocks, heavily depended on how strongly silicified and/or carbonatised the rocks are. Plagioclase can be observed in some thin sections accounting for < 5 vol%, and they are invariably sericitised.

The most common sulfides are pyrrhotite and pentlandite, however pyrite, chalcopyrite, bravoite, sphalerite, and covellite were observed, as well. Common oxide phases are magnetite and chromite, with possible ilmenite in a few samples. Sulfides and oxides are generally very fine-grained and are disseminated in the groundmass. Sulfides are usually elongated along schistosity or as irregular disseminated grains in groundmass. Oxides very often have bladed crystal habit.

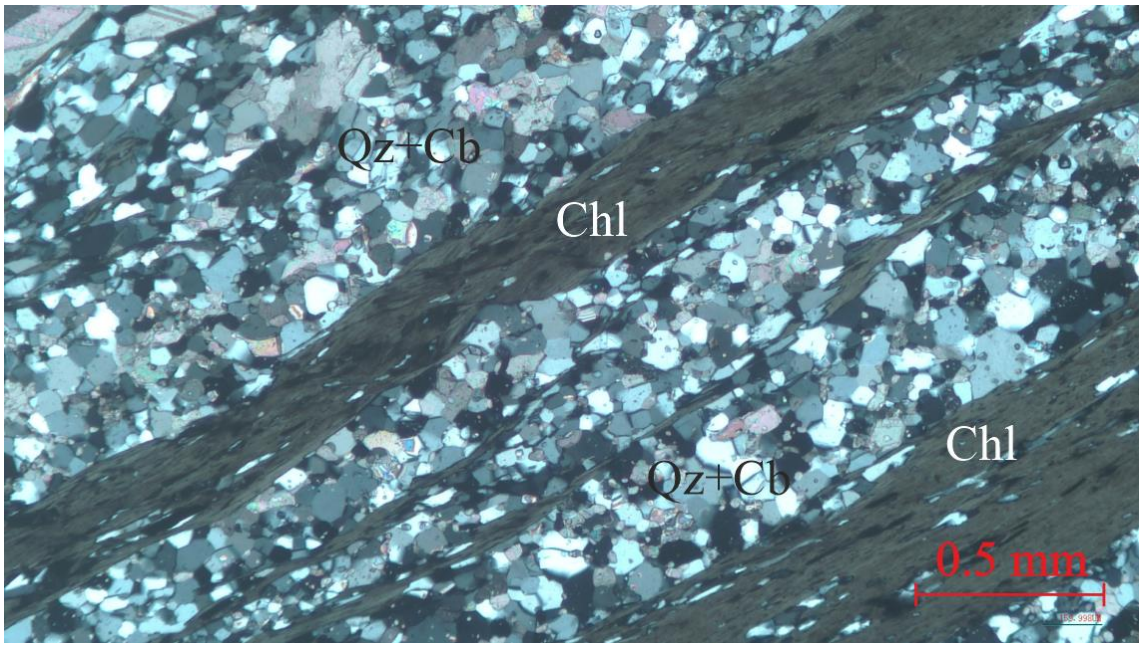

Figure 20. Mafic volcanic rock with quartz (Qz) and carbonate (Cb) groundmass with bands of chlorite (Chl). R346-94.95. Cross polarised light, 5x magnification.

5.2.4 Petrography of intermediate to felsic volcanic and volcaniclastic rocks

Intermediate to felsic volcanic rocks including pyroclastic rocks (lapilli tuffs and volcanic conglomerates/pyroclastic breccias) of the study area are mineralogically very similar. They are characteristically quartz-rich (~40–70 vol%) with strongly varying carbonate abundances (Figure 21). The grain size is generally 0.01–0.1 mm in diameter in the groundmass with individual crystals up to 1 mm, and the textures are similar as in mafic volcanic rocks. Usually, sericite accounts for 5–30 vol% and chlorite for 0–20 vol%. Occasionally, plagioclase that has been sericitised is found. Generally, the rocks are moderately to strongly foliated, however some non-foliated, massive rocks are also observed. The groundmass of pyroclastic rocks is microscopically very similar to other intermediate volcanic rocks, and the clasts could not be studied in more detail as the thin sections covered mostly the groundmass.

Sulfides and oxides in intermediate to felsic volcanic rocks account for only about 1–5 vol%. Pyrrhotite, pentlandite, chalcopyrite, pyrite, and sphalerite were the identified sulfide species, of which pyrrhotite was clearly the most abundant. The sulfides are disseminated in the groundmass with similar intergrowth and lamellae textures as in mafic volcanic rocks. Magnetite is the most abundant mineral out of all oxides and hydroxides; however, goethite and possibly minor ilmenite were also observed. Oxides are found disseminated in the

groundmass as anhedral, rounded, or bladed grains, and intergrown with other oxides or sulfides.

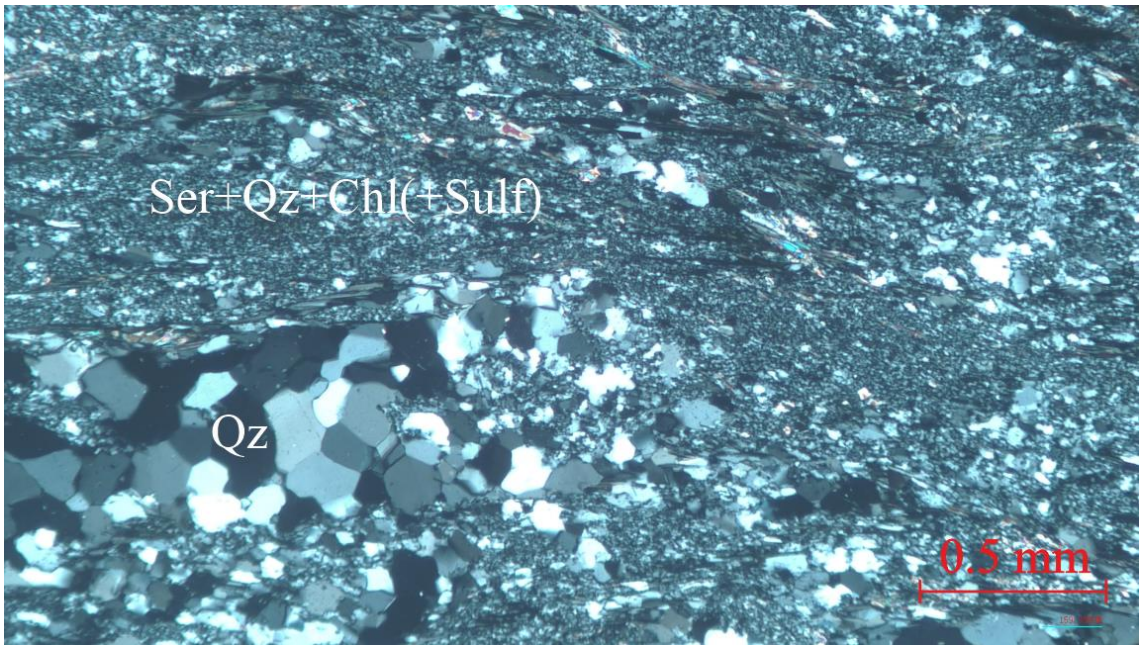

Figure 21. Intermediate volcanic rock with sericite (Ser), quartz (Qz), chlorite (Chl), and minor sulfide (Sulf) groundmass. Bands of recrystallised quartz. R346-68.50. Cross polarised light, 5x magnification.

5.2.5 Petrography of quartz porphyries

Volume of quartz porphyries in the study area is low, thus only one thin section was made. The quartz porphyry is characterised by rounded quartz crystals and crystal clusters with sizes up to 5 mm in diameter set in a very fine-grained (~0.01 mm in diameter) groundmass. It is common for the larger quartz crystals to have smaller quartz crystals around the crystal boundaries (Figure 22). Quartz porphyries are moderately foliated. Sericite is the main constituent of the groundmass, with plagioclase, carbonates, chlorite, and minor sulfides and (hydr)oxides accounting for the rest of the rock. Plagioclase crystals have undergone sericite alteration. The sulfides are pyrrhotite, pentlandite, and chalcopyrite, and they are found as individual crystals, intergrown with each other, and intergrown with magnetite and goethite. Minor pentlandite is also observed as lamellae in pyrrhotite.

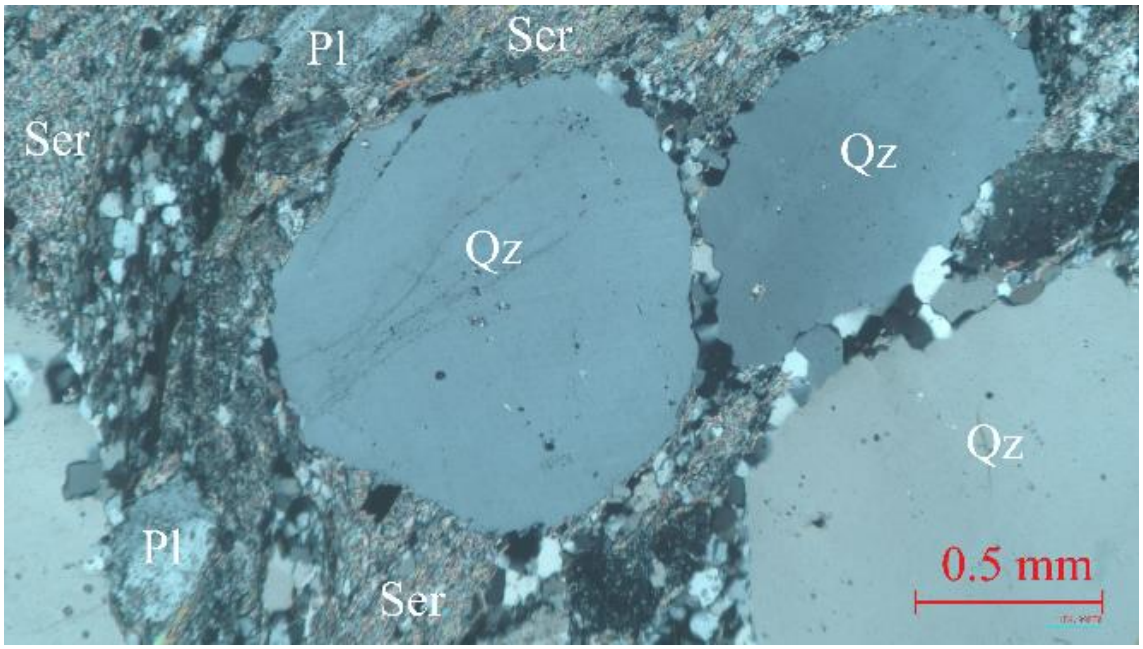

Figure 22. Quartz porphyry with quartz (Qz) phenocrysts in sericite-rich (Ser) groundmass with sericitised plagioclase (Pl) grains. R373-221.90. Cross polarised light, 5x magnification.

5.2.6 Petrography of black schists

The only non-volcaniclastic sedimentary rocks in the study area were black schists, however there are also sericite-quartzites nearby to the west and south-west of the area (Luukkonen et al. 2002). The descriptive name for the black schists is graphite-sericite-quartz phyllite. Typically, the black schists are strongly phyllitic (Figure 23). All three thin sections from the black schists contain quartz, sericite, graphite, sulfides, and minor carbonates in varying abundances. Quartz is found as granular recrystallised grains, with grain sizes commonly varying between 1.0 mm and 0.01 mm in diameter, accounting for 40–60 vol% of the rock. Carbonates have similar occurrence as quartz, but the modal abundance is between 5 and 15 vol%. Sericite is observed as foliated crystals in the matrix. Graphite is microcrystalline and individual crystals cannot be distinguished; it is only seen as a black mass with dirty appearance under the microscope. A few individual plagioclase crystals are found. Chlorite is a minor constituent, observed in two thin sections.

Sulfides present in every sample include pyrrhotite and chalcopyrite, whereas abundance of pentlandite and sphalerite vary. Pyrrhotite is observed as anhedral, elongated crystals along schistosity, disseminated in the matrix, and intergrown with other sulfides. In pyrrhotite, there are inclusions of sphalerite and chalcopyrite, along with silicates and carbonates. Pentlandite is found as lamellae in pyrrhotite, as anhedral crystals disseminated in the matrix, or as

intergrowths with pyrrhotite and chalcopyrite. Chalcopyrite is intergrown with pyrrhotite, pentlandite, and sphalerite. In sphalerite, there is chalcopyrite disease. There are very little oxides or hydroxides in the black schists, however in two samples the previously mentioned goethite can be observed.

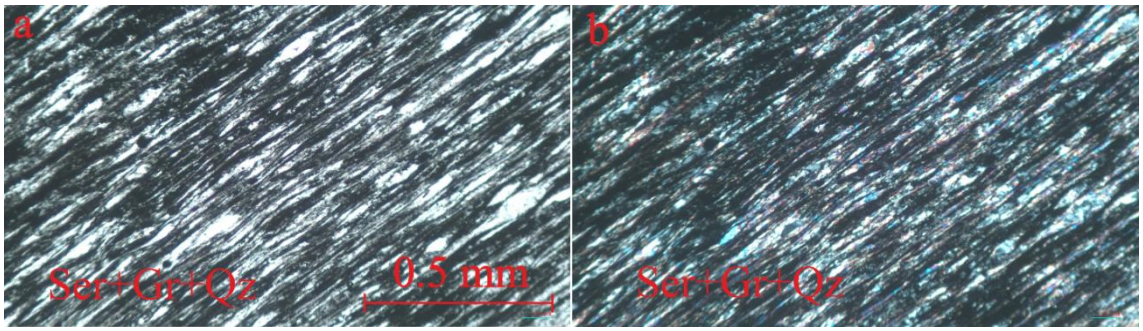

Figure 23. Black schist with very fine-grained matrix consisting of sericite (Ser), graphite (Gr), and quartz (Qz). R372-129.65. a) Plane polarised light, 10x magnification, b) Cross polarised light, 10x magnification.

5.3 Geochemistry

5.3.1 Major and trace element characteristics

The geochemistry of volcanic and subvolcanic rocks in Sika-aho are all presented together, where different trends and elemental variations between rock types can be seen the best. The most suitable classification diagram for the rock types found in Sika-aho was determined to be the cation plot from Jensen (1976) shown in Figure 24a. From the mineralised rocks, the approximated sulfidic Fe has been subtracted: otherwise almost all of them would plot in the high-Fe tholeiitic basalt field. Generally, the komatiites and komatiitic basalts plot accordingly to their composition, even though some komatiites are in the komatiitic basalt field. Rest of the volcanic rocks are plotted into tholeiitic basalts, andesites, and dacite fields, with quartz porphyries being in the rhyolite field. Mineralised rocks show a lot of variation, and they are classified from dacite to komatiitic basalt. On the CaO-MgO-Al_2O_3 diagram, the volcanic rocks plot expectedly: komatiites are close to the MgO apex, komatiitic basalts in the middle, tholeiitic basalts and intermediate-felsic volcanic/volcaniclastic rocks converging towards the Al_2O_3 apex, and quartz porphyries at or close to the Al_2O_3 apex (Figure 24b). Mineralised rocks again show large variation, with most of them plotting together with tholeiitic basalts and intermediate-felsic volcanic rocks, however two outliers that are clearly poorer in Al_2O_3 and richer in CaO are found.

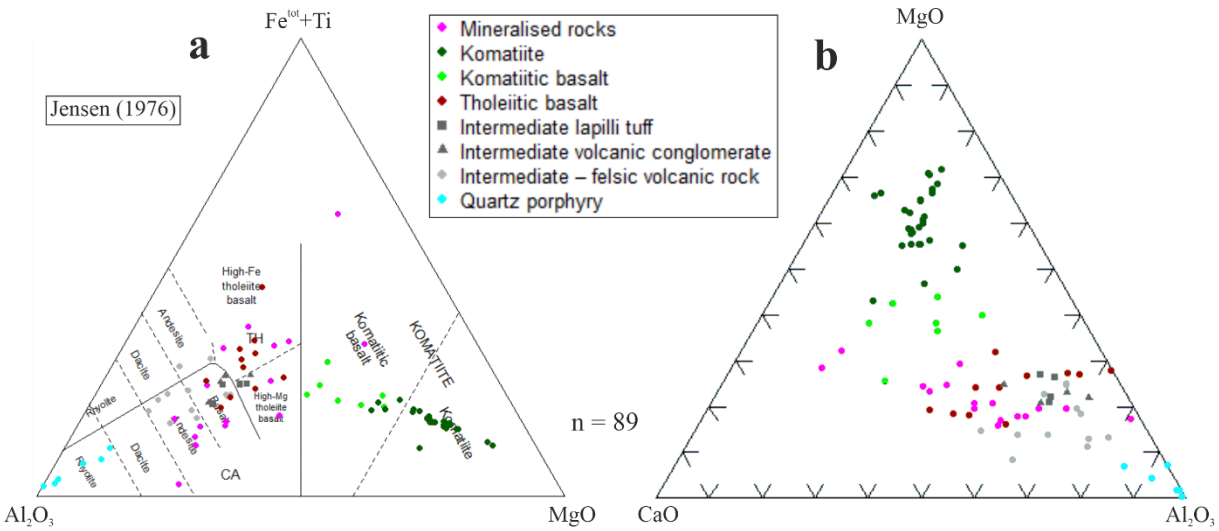

Figure 24. Geochemistry of volcanic, subvolcanic, and volcaniclastic rocks from Sika-aho. a) Jensen (1976) cation diagram. b) Ternary CaO-MgO-Al_2O_3 diagram.

Aluminium is the most petrologically important element in komatiites, with essential role in all komatiite classifications (e.g., Arndt et al. 2008). Other important elements include Ti, Ca, and HREEs, however Ca is more mobile than Ti, thus more unreliable (especially in Sika-aho where the rocks are carbonatised). The normalised, volatile-free contents of MgO and Al_2O_3 are shown in a binary plot in Figure 25, where clear negative correlation between MgO and Al_2O_3 is observed. Variations in Al_2O_3 and TiO_2, both of which are relatively immobile elements, are integrated in basically all komatiite classifications. Globally, komatiites usually have close to chondritic Al_2O_3/TiO_2 contents, with a ratio of about 20 (Arndt et al. 2008). In Figure 26, the komatiites from Sika-aho are very close to the chondritic ratio with one TiO_2-rich outlier. From Figures 24 and 25, it can also be seen that basalts have similar trends with komatiites.

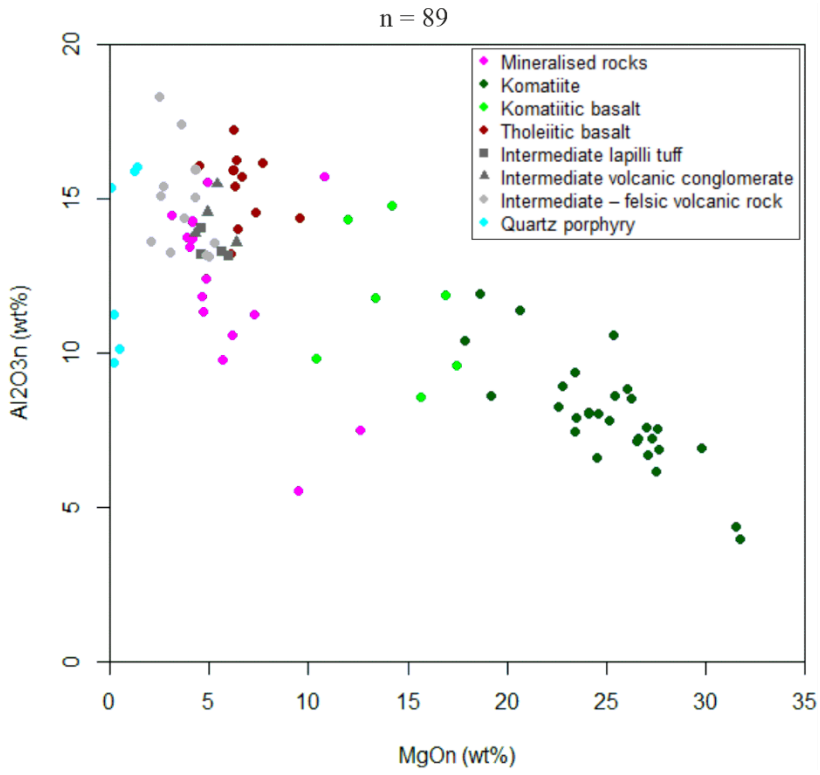

Figure 25. Binary diagram of MgO vs. Al_2O_3 (volatile-free) from the rocks of Sika-aho study area.

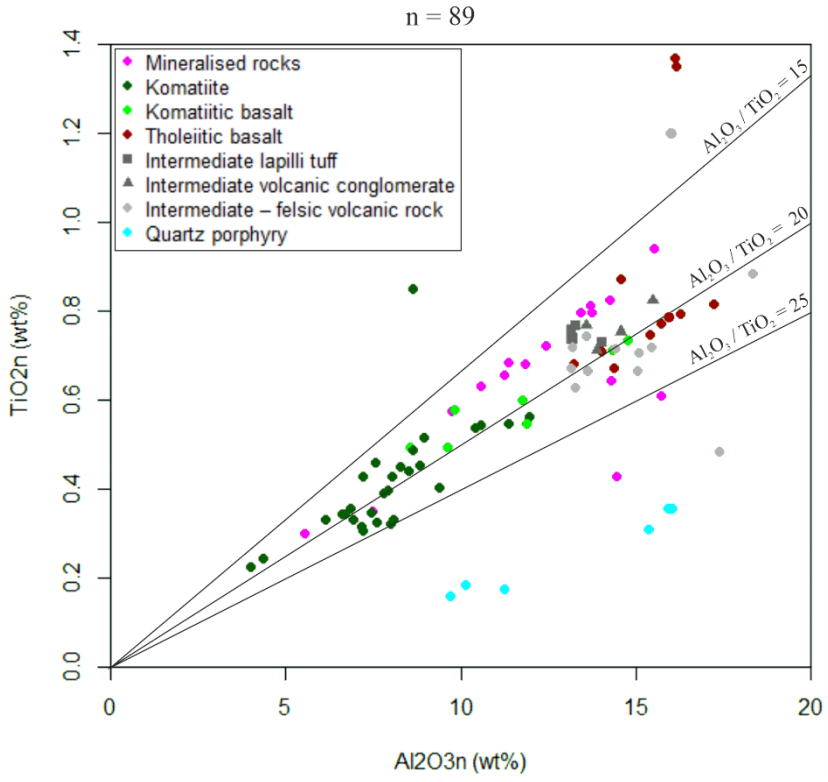

Figure 26. Binary diagram of Al_2O_3 vs. TiO_2 (volatile-free) from the rocks of Sika-aho study area, with lines marking ratios between the two compounds.

Zirconium has been plotted against TiO_2 on a binary diagram in Figure 27. A clear trend can be seen in komatiites and basalts, where Zr and TiO_2 correlate positively. The diagram can efficiently reveal characteristics, for example, of the host rocks of the deposit, because Zr is often considered as a very immobile element (Arndt et al. 2008). Majority of the mineralised rocks plot with the tholeiitic and komatiitic basalts, with a few of them together with intermediate-felsic volcanic rocks and komatiites.

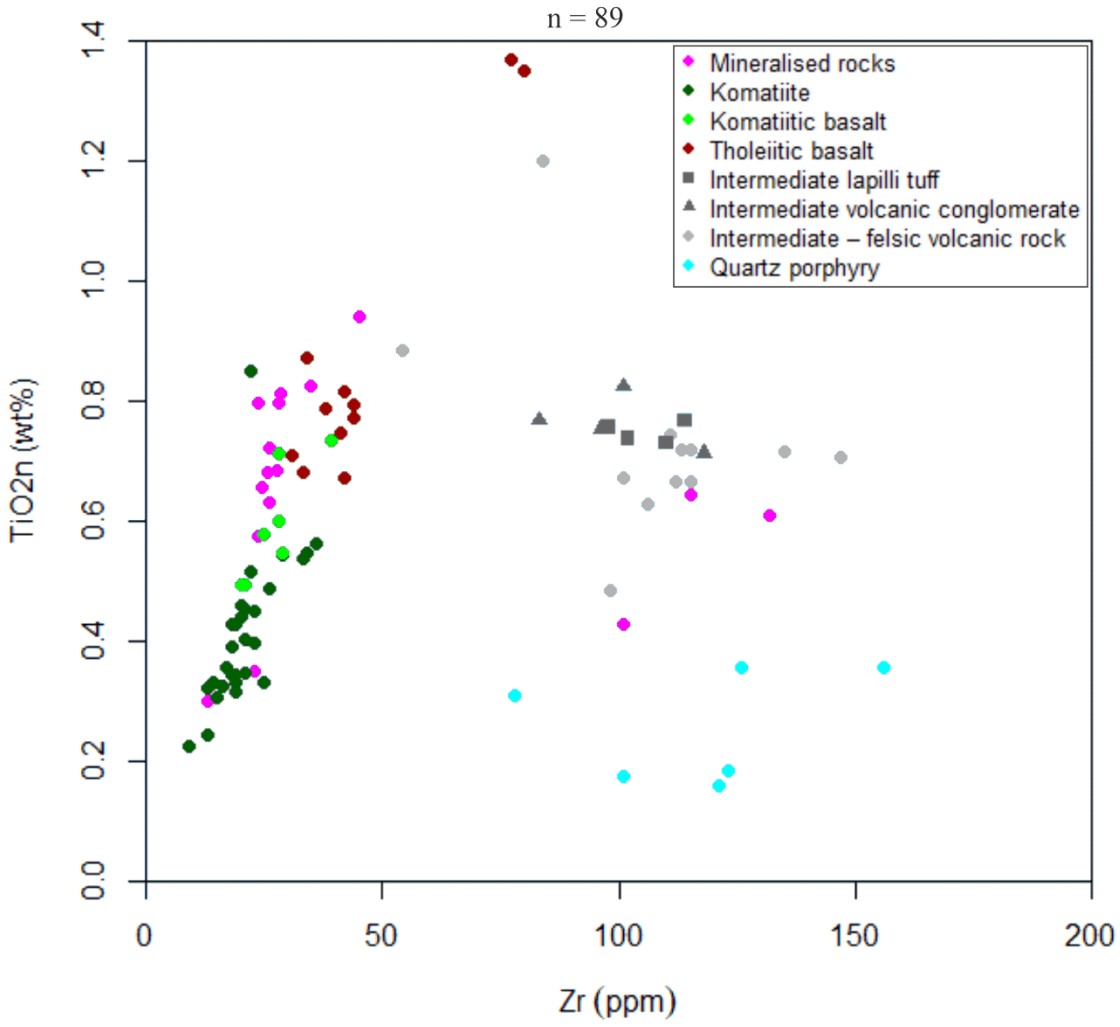

Figure 27. Binary diagram of Zr vs. TiO_2 (volatile-free) from the rocks of Sika-aho study area.

The rocks in Sika-aho are almost invariably Cr-rich. The average crustal abundance of Cr in peridotites is 2300 ppm, in gabbros 250 ppm, and in granites 10 ppm (Koljonen 1992). The Cr contents of komatiites are not unusually high, however the komatiitic basalts, tholeiitic basalts, and even intermediate-felsic volcanic and volcaniclastic rocks in Sika-aho are very enriched in Cr (Figure 28). Quartz porphyries are the Cr-poorest out of all rocks in the study area, but they still contain 32–70 ppm of Cr.

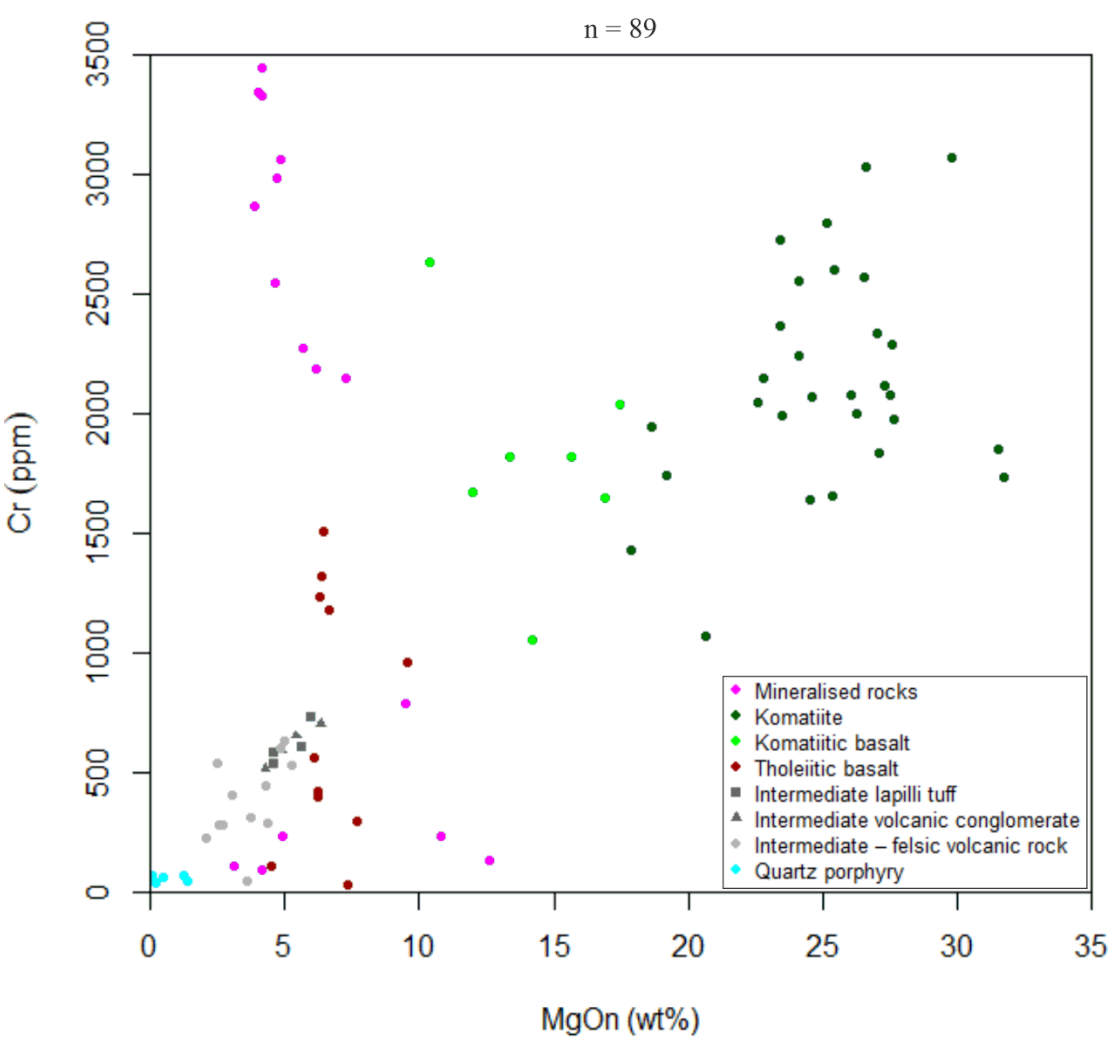

Figure 28. Binary diagram of MgO vs. Cr (volatile-free) from the rocks of Sika-aho study area.

The REE abundances are shown with profiles and fields in chondrite-normalised diagrams (Boynton 1984). The LREE patterns observed in mineralised rocks vary heavily due to the heterogeneous nature of the host rocks, however the HREE patterns are quite flat (Figure 29). Komatiites have slightly depleted LREE patterns with flat HREE patterns (Figure 29). Basalts generally have flat or slightly depleted LREE patterns and flat HREE patterns, whereas intermediate-felsic volcanic rocks are enriched in LREE and sometimes depleted in HREE (Figure 30). The intermediate volcaniclastic rocks have coherent patterns, whereas more variation was observed in intermediate-felsic volcanic rocks. The single quartz porphyry analysis showed the strongest enrichment in LREE and depletion in HREE.

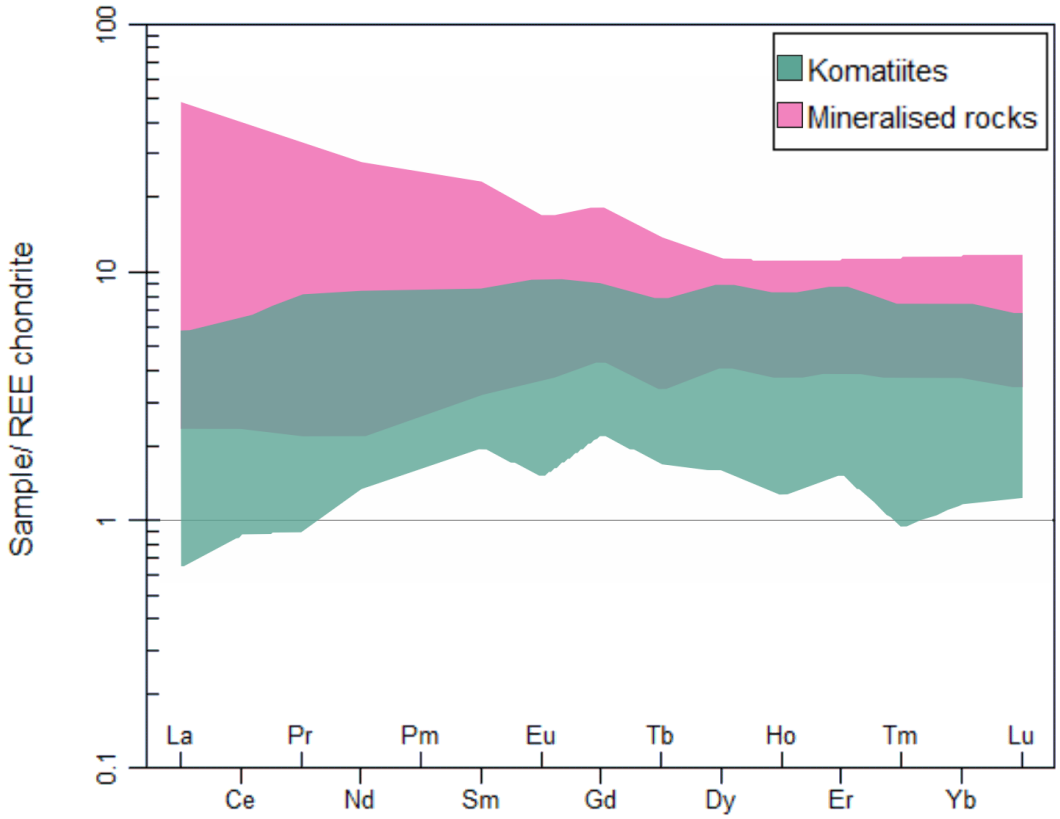

Figure 29. REE patterns of mineralised rocks and komatiites from Sika-aho, chondrite-normalised (Boynton 1984).

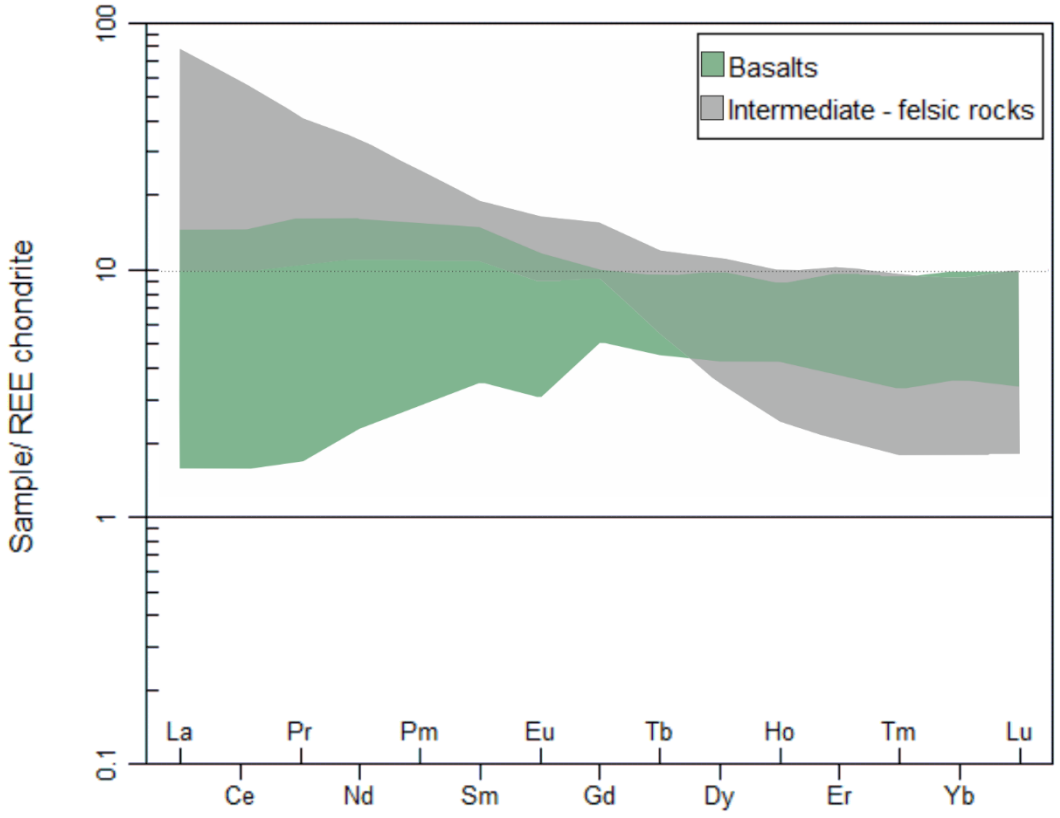

Figure 30. REE patterns of basalts and intermediate-felsic rocks from Sika-aho, chondrite-normalised (Boynton 1984).

5.3.2 Comparison of nickel to different major and trace elements

The Ni contents found in mineralised rocks and surrounding lithological units in comparison to major elements (Figures 30 and 31) and trace elements (Figures 32 and 33) are presented. In Figure 31a, the variation between Ni and MgO shows that the deposit is MgO-poor on average, with a mean content of 5.91 wt%. The MgO contents follow a very straightforward trend with komatiites and komatiitic basalts having the highest MgO contents, then tholeiitic basalts, and lastly the intermediate-felsic volcanic and volcaniclastic rocks as well as quartz porphyries. Al_2O_3 contents of the deposit vary more, equivalent to what is found from komatiites to felsic volcanic rocks (Figure 31b). Al_2O_3 contents are generally lowest in komatiites, whereas higher contents are found in intermediate-felsic volcanic rocks and tholeiitic basalts. Majority of the deposit has SiO_2 contents in range of 55–70 wt%, however the lowest content is below 30 wt%. The variation in SiO_2 contents is the largest in the mineralised rocks as well as mafic volcanic rocks (Figure 31c). The TiO_2 contents do not correlate with Ni contents and are distributed in the "normal" range relative to other rocks in the study area (Figure 31d).

The CaO contents in mineralised rocks vary greatly, with 0.35 wt% being the minimum and 24.2 wt% being the maximum (Figure 32a). In the non-mineralised rocks, it can be seen that ultramafic and mafic rocks contain more CaO than intermediate-felsic rocks. The K_2O contents, however, show an inverse trend, where the intermediate-felsic rocks have higher contents and the more mafic, especially komatiites, have very low K_2O contents (Figure 32b). In the mineralised rocks, the K_2O contents vary heavily and do not correlate with Ni. Abundance of Na_2O is quite similar to K_2O, as the intermediate-felsic rocks tend to have higher Na_2O contents, komatiitic basalts and komatiites have very low contents, and the mineralised rocks have a sporadic distribution (Figure 32c). Na and K are both alkali metals, thus some degree of resemblance is expected. Compared to K_2O, more variation in the Na_2O contents in quartz porphyries can be detected, though. In the Ni vs. P_2O_5 diagram, it can be seen that the distribution in mineralised rocks is tighter and that the intermediate-felsic volcanic rocks generally have higher P_2O_5 contents (Figure 32d).

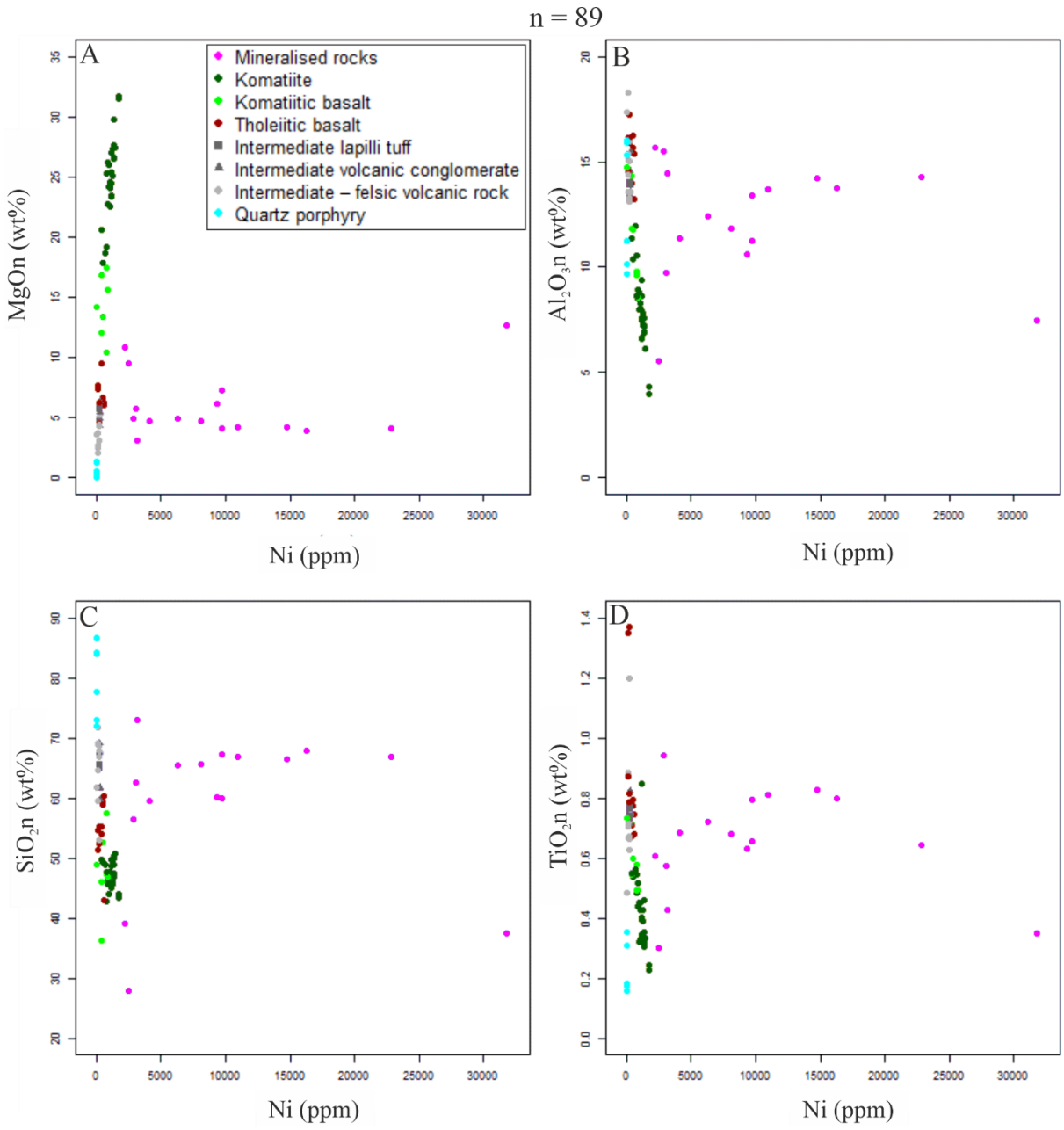

Figure 31. Binary diagrams of Ni vs. major elements (volatile-free) from the rocks of Sika-aho study area: a) Ni vs. MgO, b) Ni vs. Al_2O_3, c) Ni vs. SiO_2, d) Ni vs TiO_2.

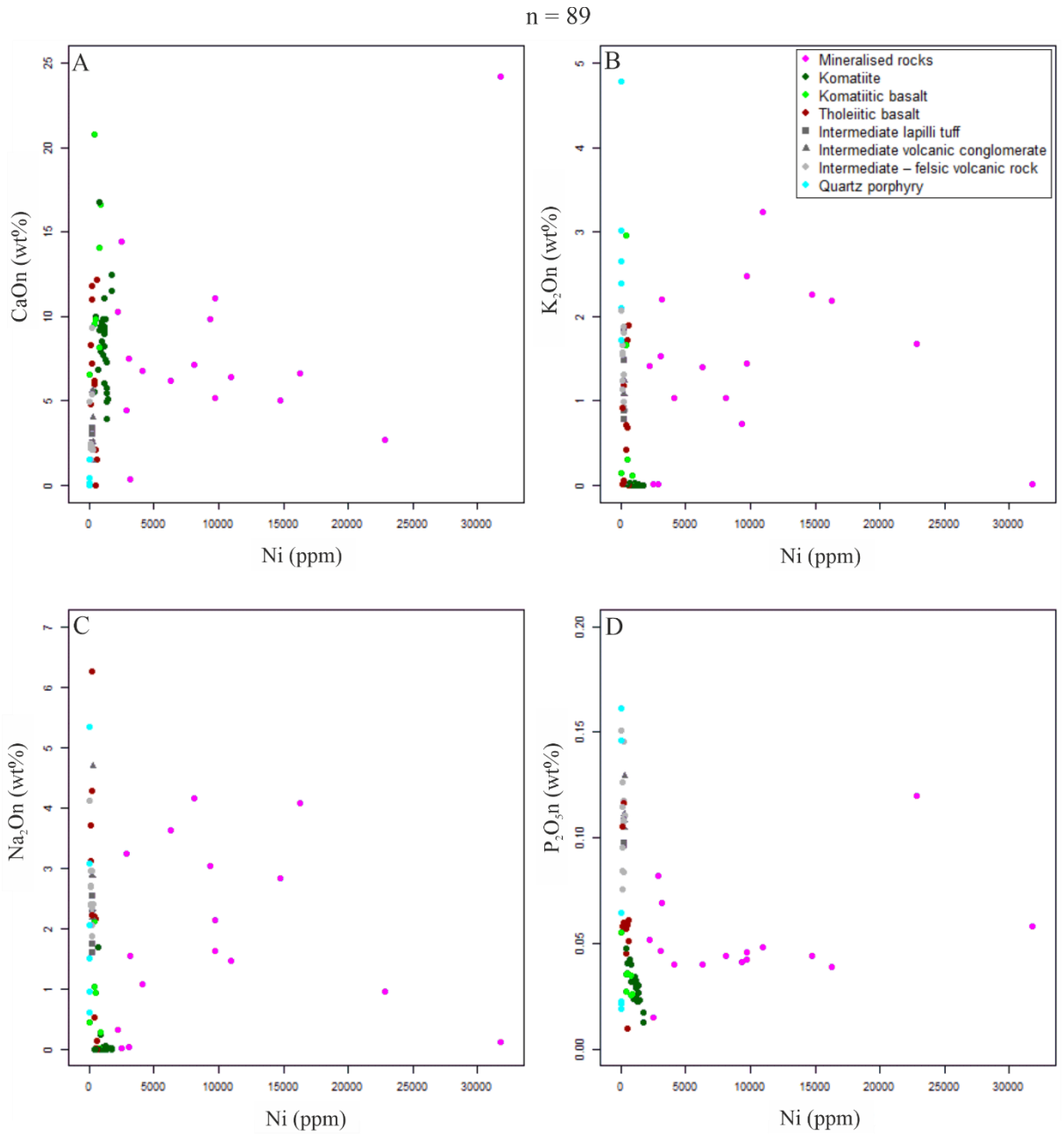

Figure 32. Binary diagrams of Ni vs. major elements (volatile-free) from the rocks of Sika-aho study area: a) Ni vs. CaO, b) Ni vs K_2O, c) Ni vs. Na_2O, d) Ni vs. P_2O_5.

In Figure 33a, Cu is observed to vary significantly from Ni in mineralised rocks. The Pearson correlation coefficients (R-values) were computed accordingly to formulas presented by Morton-Thompson & Woods (1992). The R-value for Ni and Cu is 0.47 with $p > 0.05$, thus showing statistically insignificant relationship. A subset of 9 mineralised rocks seems to linearly have higher Cu contents with increasing Ni. Relatively high Cu contents are observed in basalts and komatiites that do not have high Ni contents. The average Ni/Cu ratio in the komatiites is 79.8 and in mineralised rocks 82.0. It can be observed in the Ni vs. Co diagram

(Figure 33b) that the contents correlate in mineralised rocks: the calculated R-value is 0.86 ($p < 0.01$), which means that there is a strong positive correlation between Ni and Co. In komatiites the R-value is 0.61, showing moderate positive correlation, however it is statistically insignificant ($p > 0.05$). The Ni/Co ratio in komatiites is 15.4, and in mineralised rocks it is 50.5. The ratios and R-values are also presented in Table 3.

Ni and Cr do not seem to correlate in the mineralised rocks, as majority of them have > 2000 ppm Cr with moderate Ni contents, however there are 6 samples that are relatively poor in Cr (92–790 ppm), even though 2 of those 6 samples are the most Ni-rich (Figure 33c). The average Ni/Cr ratio in the komatiites is 0.53, whereas the mineralised rocks have a ratio of 36.2. The Ni vs. Zn is presented in Figure 33d, where it can be seen that the contents do not seem to correlate in the mineralised zone (R-value = 0.21). In the surrounding lithologies there does not seem to be any correlation either and the Zn abundances are almost invariably lower everywhere outside the mineralised zone.

The As contents are low for the majority of the mineralised rocks (Figure 33e). A couple outliers can be observed, however they are in no way correlated to Ni contents. Arsenic contents also do not seem to be correlated with rock type either, as low and high As contents can be found in all types of rocks, from quartz porphyries to komatiites. The S contents do correlate with Ni in the mineralised zone (Figure 33f): R-value is 0.74 ($p < 0.01$), therefore there is a moderate positive correlation (Table 3). In other rocks, there does not seem to be much correlation between Ni and S.

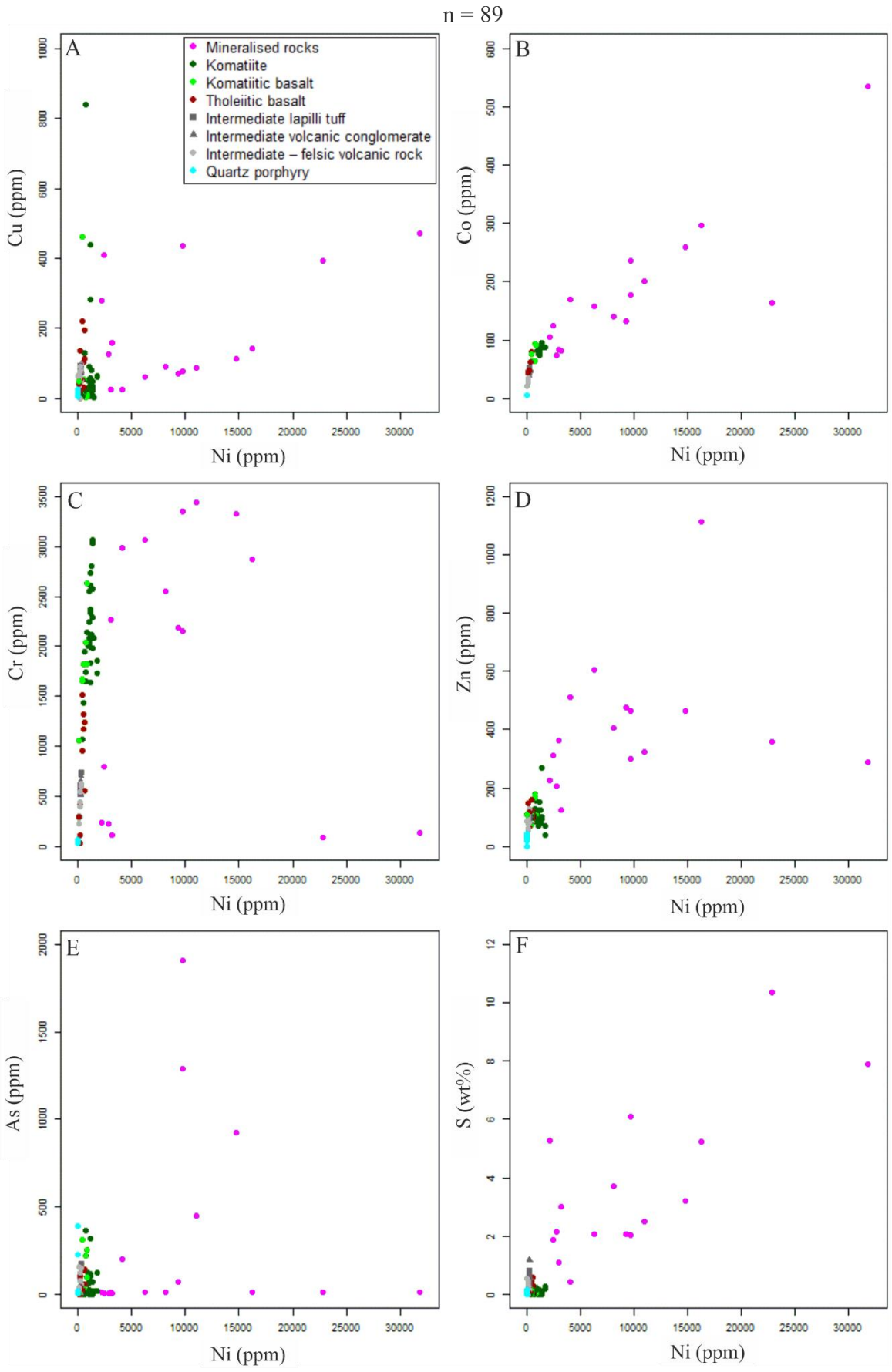

Figure 33. Multiple binary diagrams from the rocks of Sika-aho study area: a) Ni vs. Cu, b) Ni vs. Co, c) Ni vs. Cr, d) Ni vs. Zn, e) Ni vs. As, f) Ni vs. S.

The Ni, Co, Cu, Cr, and S concentrations were also examined based on the aqua regia weak leach analysis values and the results compared to the whole-rock XRF analyses are shown in Table 3. The ratios are similar between the different analysis methods, however weak leach analyses show poorer correlation. Based on the weak leach analysis results, there is a moderate positive correlation between Ni and Co (R-value = 0.52, $p < 0.01$), even though the R-value is heavily affected by one outlier with significantly anomalous Co content. Ni and S also have moderate positive correlation (R-value = 0.61, $p < 0.01$), but Ni and Cu do not correlate (R-value = 0.18, $p > 0.05$). There is one distinctly anomalous concentration observed for each Cr, Cu, and Co, but none of those are from the same samples.

Table 3. Ratios and R-values between Ni and Cu, Co, and S in the mineralised zone based on XRF and weak leach analysis results. N = number of pairs.

	Ni/Cu (XRF)	**Ni/Cu (weak leach)**	**Ni/Co (XRF)**	**Ni/Co (weak leach)**	**Ni/S (XRF)**	**Ni/S (weak leach)**
Ratio	82.0	70.0	50.5	44.6	0.32	0.30
R-value	0.47 ($p > 0.05$)	0.18 ($p > 0.05$)	0.86 ($p < 0.01$)	0.52 ($p < 0.01$)	0.74 ($p < 0.01$)	0.61 ($p < 0.01$)
N	16	37	16	37	16	37

5.3.3 Platinum group element and gold characteristics

The Au contents found in Sika-aho are generally low and heterogeneous (Figure 34a). In total, there are four samples with Au > 50 ppb, with the highest content being 702 ppb. The highest Au content is found in the Ni-richest sample, however no correlation between Ni and Au contents exists. In non-mineralised rocks, the Pt+Pd contents are usually low in intermediate-felsic rocks with increasing contents in basalts and komatiites (Figure 34b). On average, komatiitic and tholeiitic basalts have the highest Pt+Pd contents. Out of the mineralised rocks, 11 of them have Pt+Pd contents of 20–35 ppb, similar what is found in basalts. Surprisingly, five samples have very low Pt+Pd contents, including the two most Ni-rich samples. Based on major and trace element geochemistry, three of these samples are basalts and two are intermediate-felsic volcanic rocks.

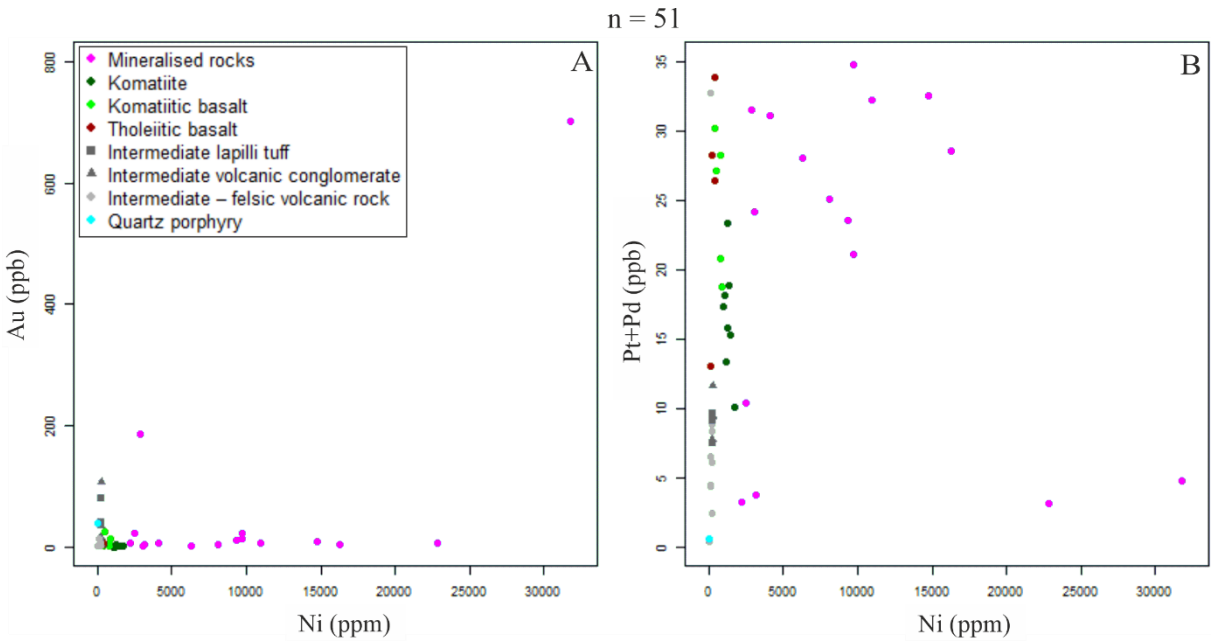

Figure 34. Binary diagrams from the rocks of Sika-aho study area: a) Ni vs. Au and b) Ni vs. Pt+Pd.

Pt was plotted against other PGE elements, however Ir, Ru, Rh, and Os analyses were only available for mineralised rocks from study by Makkonen & Halkoaho (2007; Figure 35). Pt and Pd correlate very strongly (R-value = 0.9651, $p < 0.01$), with an average Pt/Pd ratio of 1.06 for all samples (Figure 35a). For the other PGEs in the mineralised zone, the ratios and R-values (with $p < 0.01$) are the following: 1) Pt/Ir = 15.8, R-value = 0.9828 (Figure 35b); 2) Pt/Rh = 6.8, R-value = 0.9339 (Figure 35c); 3) Pt/Ru = 2.6, R-value = 0.9663 (Figure 35d). These results indicate very strong correlations between the PGEs, although unfortunately no data for Os, Ir, Rh, and Ru was available outside the mineralised zone.

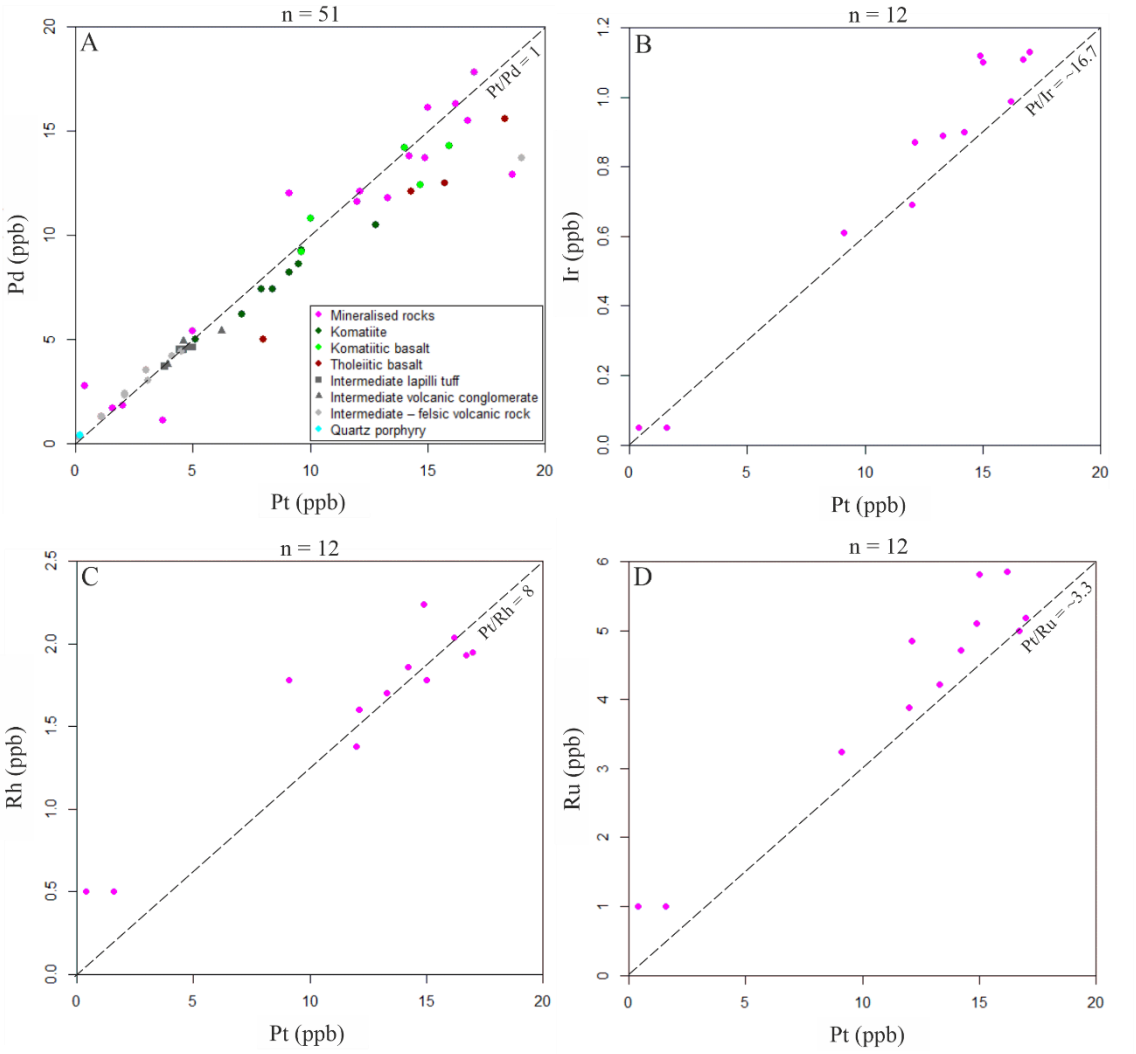

Figure 35. Variation of PGEs in Sika-aho. The data in diagram A is from this study and Makkonen & Halkoaho (2007), whereas the diagrams B, C, and D only contain data from Makkonen & Halkoaho (2007).

5.3.4 Geochemistry of black schists

The black schists from the study area were not plotted in the diagrams as they were examined separately from the volcanic and volcaniclastic rocks. The examination revealed that they are SiO_2-rich (58.0–73.4 wt%, non-normalised) with varying abundances of mobile elements (e.g., S, Fe, Na, K, and Ca). Aside from Zn and to some degree Cr, the trace element patterns were not anomalous. It was observed that there were two anomalous Zn contents of 1240 and 953 ppm. The background contents of Zn in black schist varies between 28 and 173 ppm. As for Cr, black schists have Cr contents between 60 and 421 ppm. Ni contents were low (≤ 200 ppm in all black schists) as were the Cu contents (≤ 145 ppm). Cobalt and Pt+Pd were only

analysed from the new samples (n = 4), and the contents varied between 5 and 36 ppm for Co, and between 2.2 and 5.0 ppb for Pt+Pd.

5.3.5 Classifications of Sika-aho nickel deposit and surrounding lithologies

The komatiite-associated Ni-Cu-PGE deposits in Finland can be classified to two groups based on geochemistry: 1) deposits enriched in PGE (Pd+Pt > 500 ppb) and Cu (Ni/Cu < 13), and 2) deposits with low PGE and enrichment in Ni (Ni/Cu > 15; Konnunaho et al. 2015). Based on the presented data, Sika-aho clearly belongs to the second group with low PGE and high Ni/Cu ratios (Figures 33a and 34b), rather representing the more extreme end of the second group deposits. Other classifications of Ni(-Cu-PGE) deposits usually include types of information, such as sulfide distribution and textures (e.g., Lesher & Keays 2002), that cannot be determined from geochemistry alone.

The information from major and trace element data presented indicates that the Sika-aho komatiites belong to the Al-undepleted (AUK) type of Nesbitt et al. (1979) or to the corresponding Munro-type of Arndt et al. (2008). The basalts can be divided into komatiitic and tholeiitic basalts, however a further division into (high-Cr) komatiitic basalts, high-Cr basalts, and tholeiitic basalts could be justified. The intermediate-felsic volcanic rocks were not further classified based on geochemistry, as the differences in major and trace elements are in many cases quite small and classification based on SiO_2 contents is not reliable in Sika-aho due to strong silicification. The intermediate volcaniclastics have relatively uniform geochemical compositions and are better classified by mesoscale textures.

5.4 Numeric and geological 3D-modelling

Numeric modelling produced a volume that matches reasonably well with the contents from chemical analyses as well as the earlier cross sections (Figure 36). Discontinuities in the volume can be observed, but it is expected as the Ni contents are heterogeneous even inside the deposit. The sharpish edges are partly the result of low data density, as there can be tens of metres without any analysis data, and partly due to the spacing between the cross sections. The comparison of the actual deposit (Ni > 3500 ppm) to lower-grade part of the deposit (Ni = 2000–3500 ppm) is shown in Figure 37, however, the lower-grade part is not very well constrained due to poor drill hole density and lack of cross sections that could be used to delineate those parts.

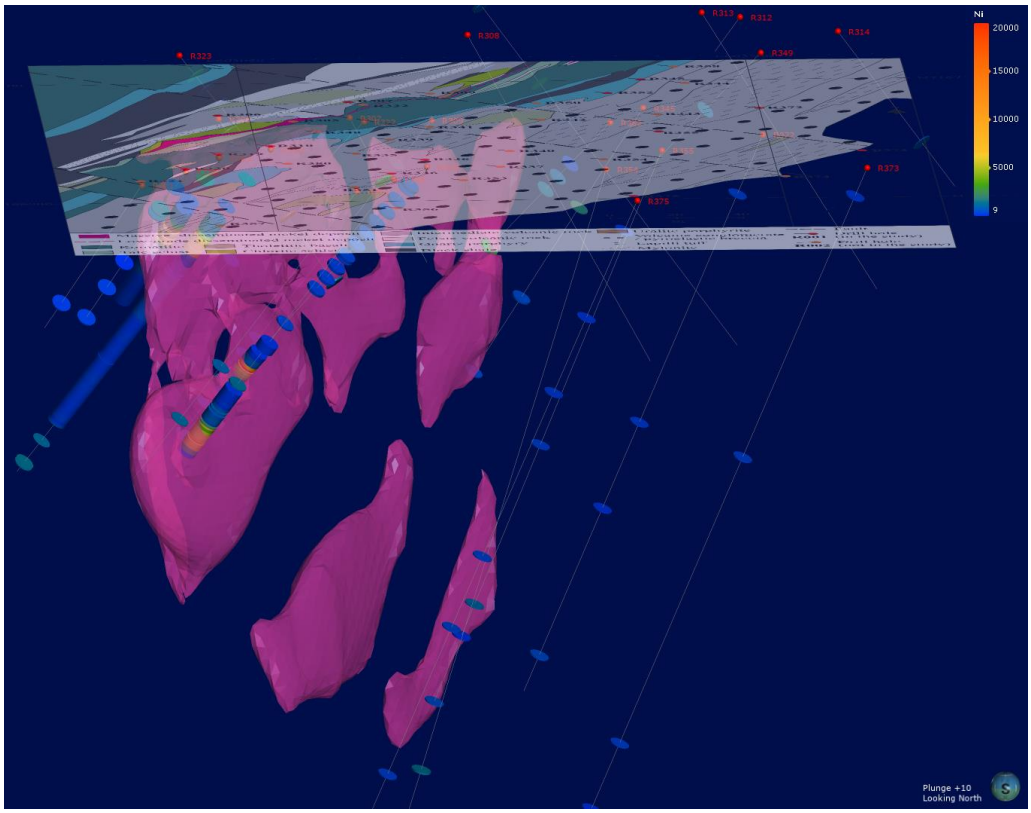

Figure 36. Snapshot of Leapfrog Geo numeric 3D-model showing the Sika-aho Ni deposit in pink (cut-off value 3500 ppm), drill holes with Ni contents from geochemical analyses, and partly transparent bedrock map. Looking towards north, plunge is 10 degrees.

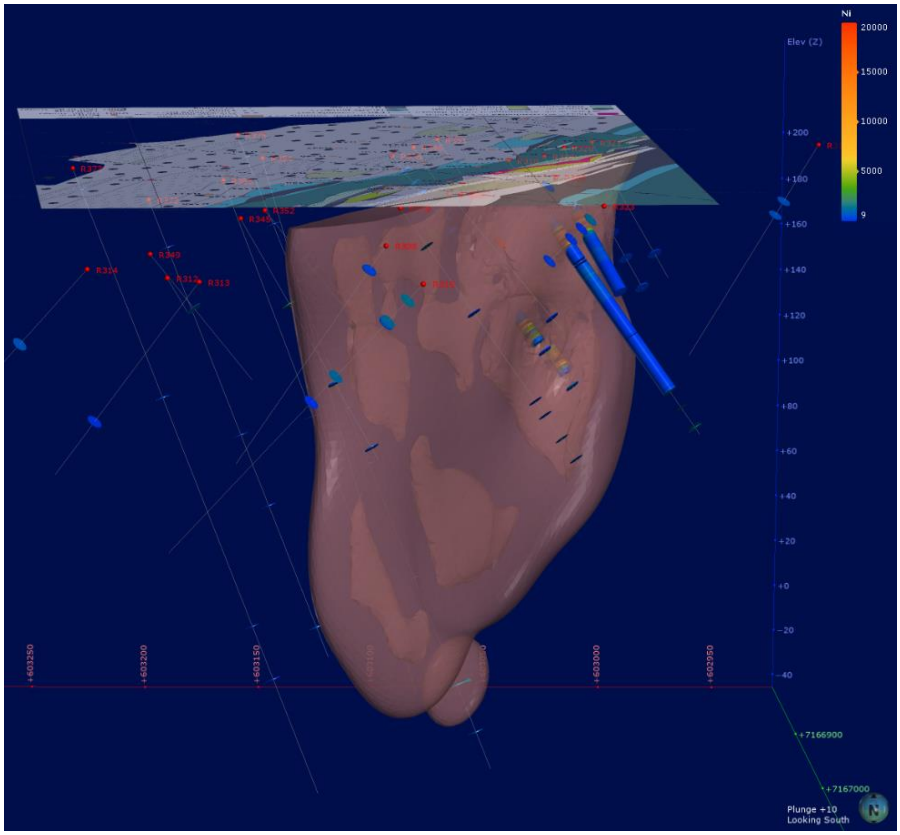

Figure 37. Snapshot of Leapfrog Geo numeric 3D-model showing the Sika-aho Ni deposit in light brownish red (cut-off value 2000 ppm), drill holes with Ni contents from geochemical analyses, and partly transparent bedrock map. Looking towards south, plunge is 10 degrees.

A numeric model that has the same resolution but no trend has been set, no delineation with cross sections has been conducted, and the default interpolant settings are used is shown in Figure 38. The difference to the model that was created with additional geological data and more suitable interpolant settings is stark, and shows how large influence they have.

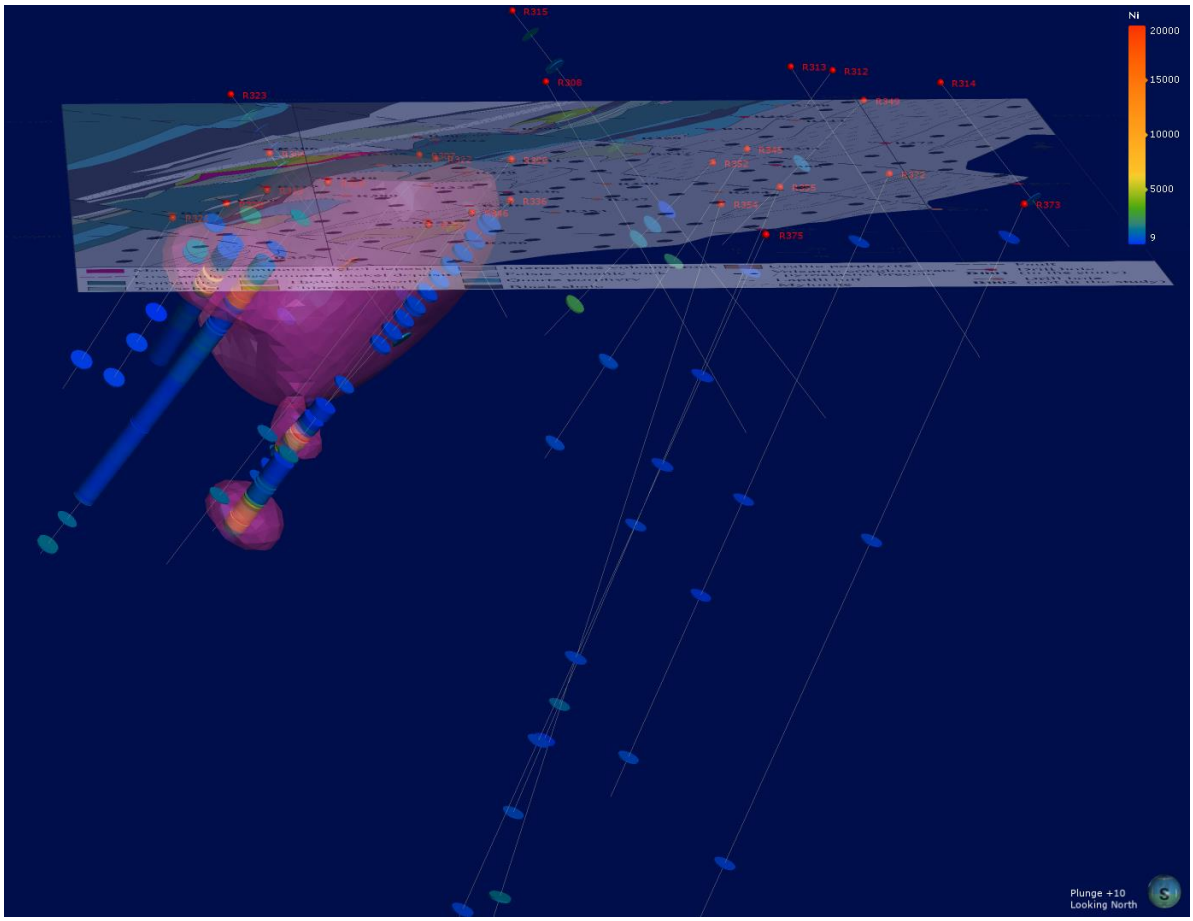

Figure 38. Snapshot of Leapfrog Geo numeric 3D-model showing the Sika-aho Ni deposit in pink (cut-off value 3500 ppm) created without any external modification, drill holes with Ni contents from geochemical analyses, and partly transparent bedrock map. Looking towards north, plunge is 10 degrees.

The geological modelling results were compared between the deposit and stratigraphic models, and the more consistent results from stratigraphic model are shown in Figures 39 and 40 along with the outline of the Ni deposit. The lithological units are subvertical, dipping mainly towards SE similarly to the deposit. Quartz porphyry was modelled as a vein, which is why it can be seen cutting through other units.

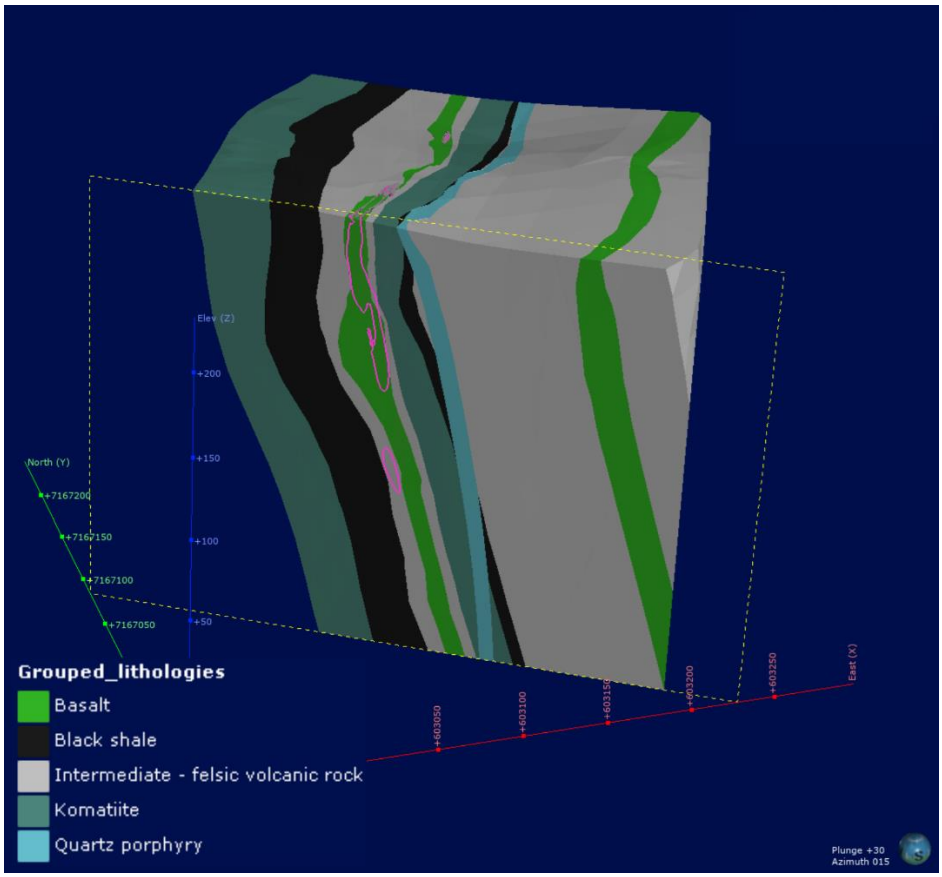

Figure 39. Snapshot of Leapfrog Geo geological 3D-model with simplified lithological units along with the outline of the Sika-aho Ni deposit in pink. The viewing angle azimuth is 015, plunge is 30 degrees.

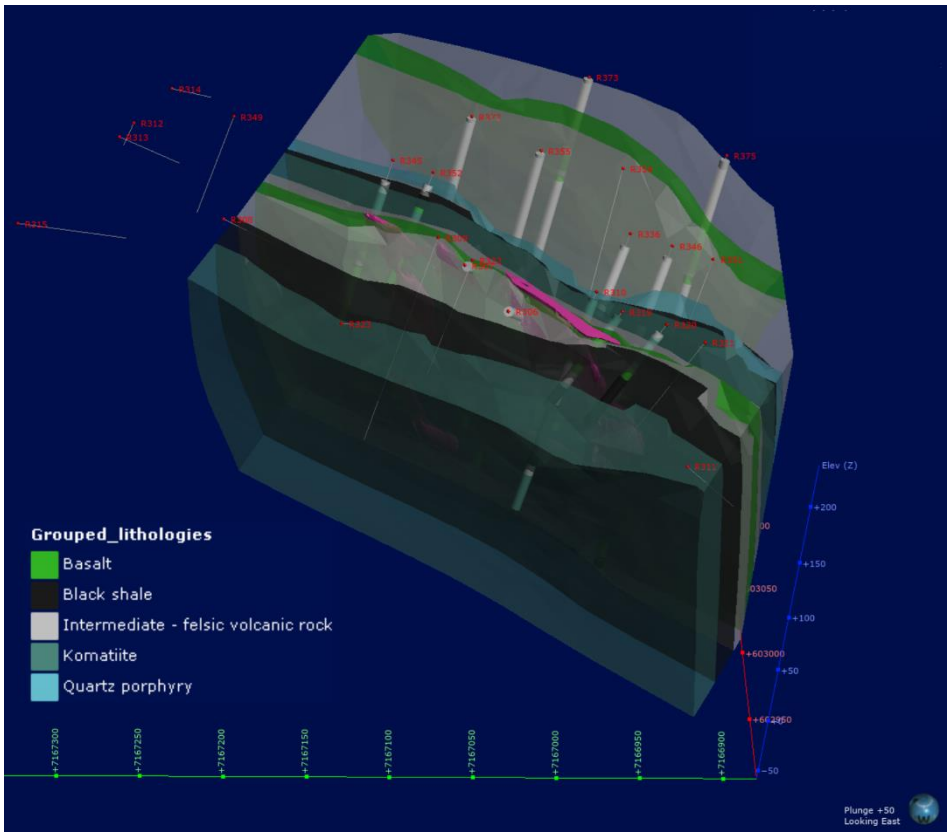

Figure 40. Snapshot of Leapfrog Geo geological 3D-model showing the different simplified lithological units along with the Sika-aho Ni deposit and drill holes. Looking towards east, plunge is 50 degrees.

In addition to numeric and geological models, a combined model could be produced based on them. It shows how high Ni contents (>3500 ppm) are distributed among different lithological units (Figure 41). Albeit not entirely accurate, the combined model shows how the deposit is hosted by a variety of rocks, including intermediate-felsic volcanic rocks, basalts, and komatiites. The small parts where the deposit seems to be hosted by black schists cannot be confirmed as the drill holes do not go through it, even if the interpolant does. Nevertheless, this model helps in visualisation of the results that were received from geochemical analyses and drill core revision logging, and it confirms that the nature of the host rocks is very heterogeneous.

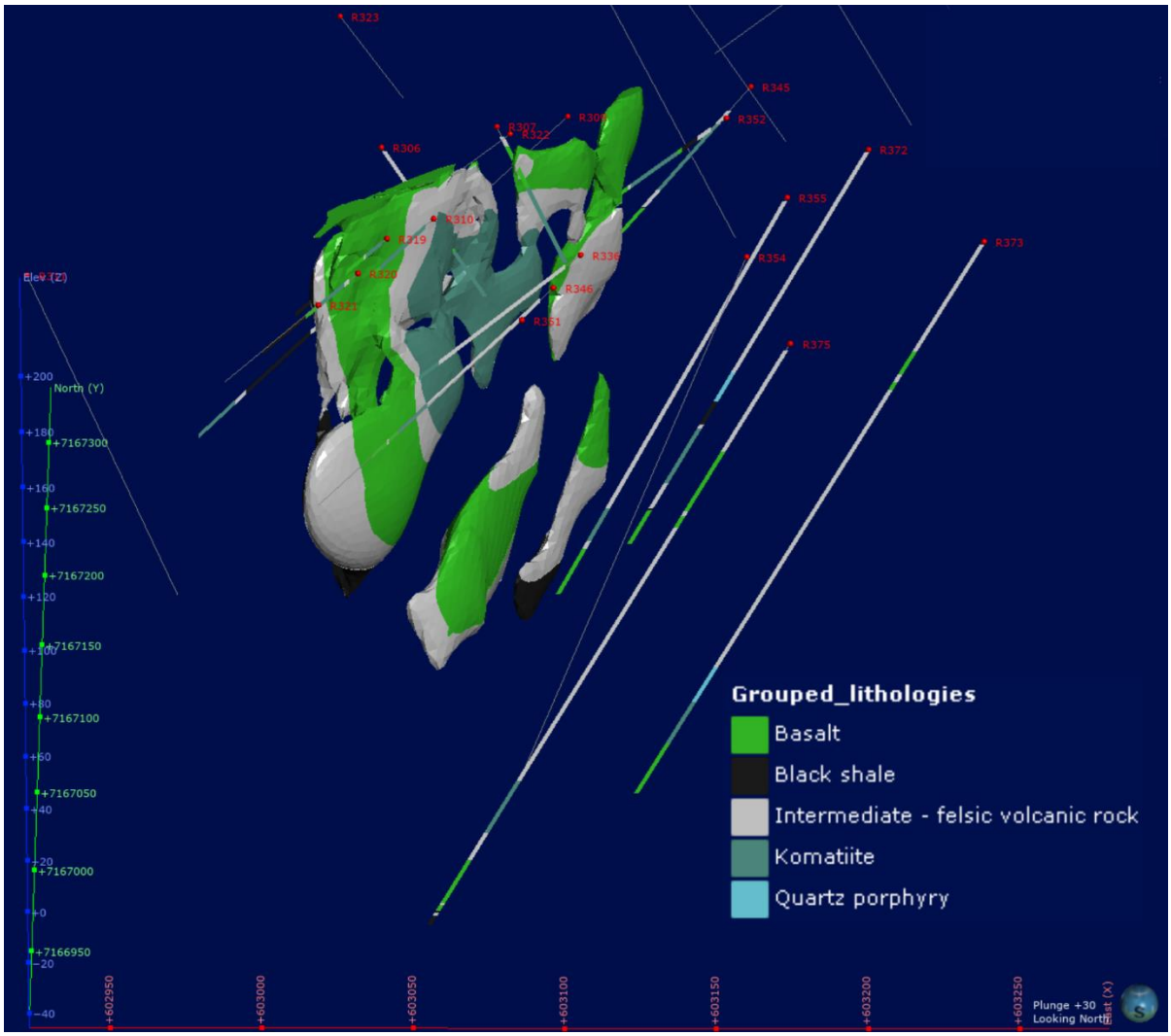

Figure 41. Snapshot of Leapfrog Geo combined 3D-model showing how the Sika-aho Ni deposit is hosted by a variety of rock types. Looking towards north, plunge is 30 degrees.

6 Discussion

6.1 Metallogeny of the Sika-aho nickel deposit

6.1.1 Source of nickel

The source of Ni in Sika-aho deposit is komatiitic cumulate rocks. Earlier studies (Heino 1998; Luukkonen et al. 1998, 2002; Makkonen & Halkoaho 2007) have also proposed that the source of Ni in Sika-aho deposit is komatiitic. The average Ni/Cu ratios in both komatiites and mineralised rocks are very high (Figure 33a; Table 3), even higher than is typical for an Archaean komatiite-associated Ni deposit, however the Ni and Cu contents do not necessarily correlate well in the mineralised rocks. The Ni in sulfide fraction is also high, varying between 7.2 and 30.12 wt.% (Luukkonen et al. 1998), with the average being 15.61 wt% (Heino 1998). These ratios and tenors strongly indicate that the source is komatiitic (e.g., Luukkonen et al. 1998; Konnunaho et al. 2015), however later post-deposition modification has likely occurred.

There are indications that upgrading of sulfidic Ni content during metamorphism has occurred in Sika-aho. The mineralogy of Sika-aho komatiites reveals that they have undergone serpentinisation and talc-carbonate alteration (Chapter 5.2.2), which have been proven to upgrade Ni content in sulfides. This holds true especially for disseminated deposits, as Ni is released from olivine and partitioned into sulfides almost entirely in some cases (Donaldson 1981; Barnes & Hill 1998; Arndt et al. 2008). The high Ni tenors reported from Sika-aho with a maximum of 30.12 wt% Ni in sulfides (Luukkonen et al. 1998) is clearly above what would form in a komatiitic environment (e.g., Arndt et al. 2008), thus suggesting upgrading of Ni in sulfides or preferential loss of other elements (Fe, Cu, S). Also, the deposit is characterised by very low PGE concentrations and total absence of olivine, which suggest that some of the Ni currently residing in sulfides has been liberated from olivine.

For a komatiitic Ni(-Cu-PGE) deposit to form, an external sulfur source is generally required as komatiites are almost always undersaturated in sulfur when they erupt (Fiorentini et al. 2010). Black schists are found in Sika-aho area both below and above komatiites stratigraphically (Figure 8), and they are a potential source of abundant S. If the komatiites were S-deficient during metamorphism, high Ni tenor sulfides would not have been able to form as Ni would be enriched in talc in talc-carbonate rocks, or in magnetite in serpentinites (Donaldson 1981). Also, taking the geochemical signatures of Ni, Cu, Co, and PGE as well as

the major elements abundances into account, it is most likely that the source of Ni in Sika-aho have been massive to disseminated sulfides in a komatiitic cumulate unit, however the production of nickeliferous sulfides during metamorphism could have had an effect on the production of PGE-poor sulfides.

The nickeliferous sulfide source in Sika-aho might have been outside the study area, in which case mineralised komatiite trends could be identified further away assuming the sulfides have been remobilised next to barren komatiites to their present position and the remobilisation processes have not been completely exhaustive. The Ni vs. Cr trends in komatiites can be indicative of barren or mineralised komatiites, forming an L-shape distribution in a binary diagram where increasing Cr and constant Ni indicate increase of chromite accumulation (barren komatiites), and constant Cr with increasing Ni indicates sulfide accumulation (mineralised komatiites) (Barnes & Brand 1999; Brand 1999; Figure 33c). In Sika-aho, the komatiites do not really plot on either trend, even if the relative abundance of the elements is slightly skewed towards the Cr-rich barren trend. Nevertheless, Ni/Cr element ratio has limited applicability in Sika-aho because the deposit is not largely komatiite-hosted presently.

6.1.2 Remobilisation of nickel

The dominant remobilisation mechanisms of Ni have been mechanical in Sika-aho. The principal mechanisms have been shear zone transfer and dislocation flow (Figure 42), however purely solid-state transfer with zero influence from fluids is difficult to prove and unlikely in metamorphic conditions, thus some degree of fluid involvement is likely (e.g., Marshall et al. 1998). Dislocation flow, which is one of the solid-state transfer mechanisms (Table 1), has been determined to be an important deformation mechanism in sulfides at medium-grade metamorphic environments (e.g., McQueen 1987; Marshall & Gilligan 1987). Dislocation flow causes plastic deformation of material; the resulting textures can be used as evidence of mechanical remobilisation of sulfides (e.g., Gilligan & Marshall, 1987). The petrographic study of Ni mineralised zone in Sika-aho showed that the sulfides are elongated and flattened along the schistosity planes (Chapter 5.2.1), which indicates that the sulfides have been ductile during the formation of the dominant schistosity. This, however, is not unequivocal evidence of ductile external remobilisation of sulfides since later deformation events can in some cases also cause lattice-preferred orientation of pyrrhotite-dominated assemblages parallel to the fabric of the host rock (Gilligan & Marshall, 1987). The original deformation fabrics are better preserved in disseminated sulfides compared to massive

sulfides, though. In Sika-aho, stretching lineations in sulfides in the mineralised zone were observed from drill core samples, which is interpreted to have been caused by shearing (e.g., Tikoff & Greene 1997) associated with the major Tammasuo shear zone. Thus, the textural evidence from sulfides indicates that mechanical remobilisation has likely occurred.

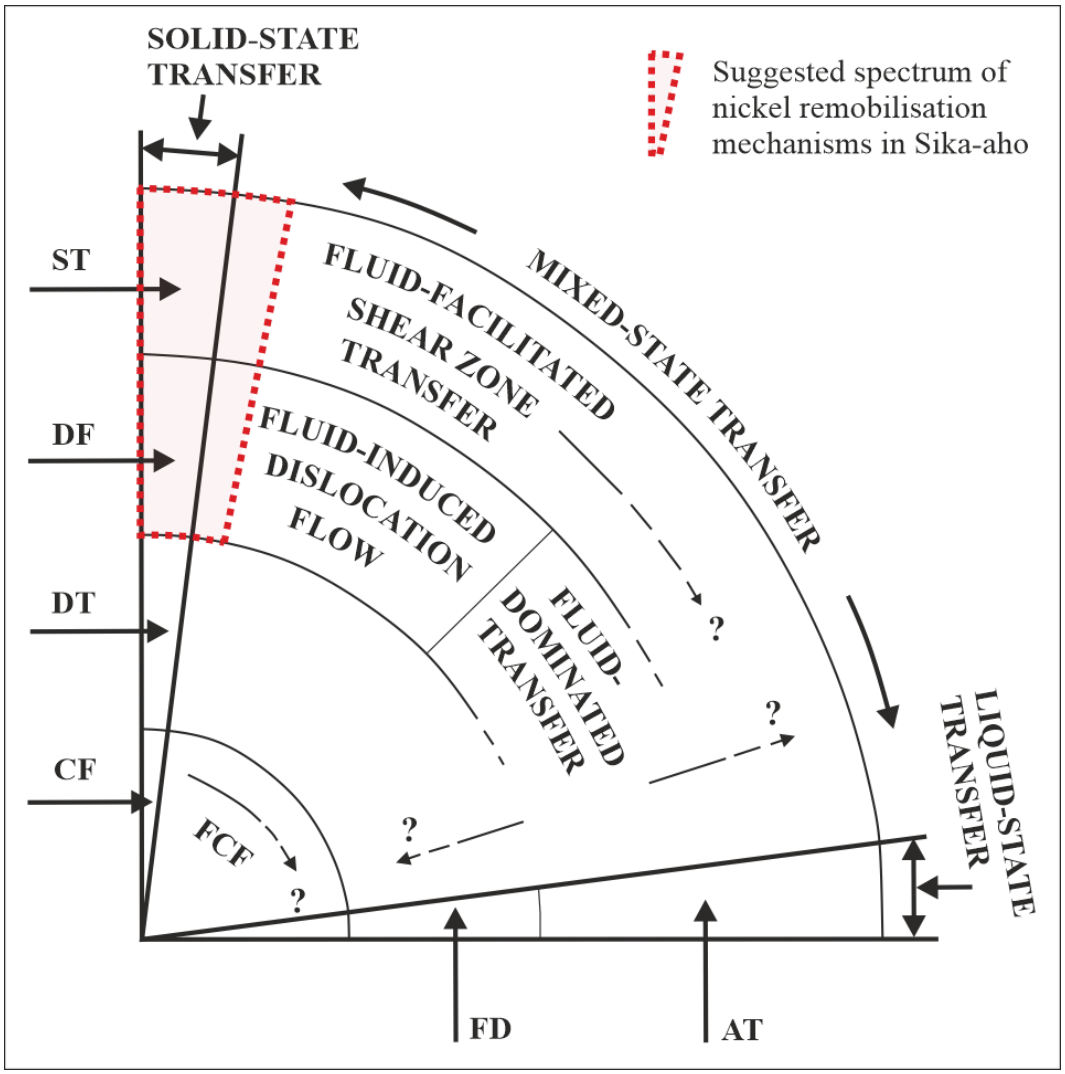

Figure 42. Spectrum of transfer mechanisms with interpreted external remobilisation mechanisms for Sika-aho Ni deposit. ST = shear zone transfer, DF = dislocation flow, DT = diffusive mass transfer, CF = cataclastic flow, FCF = fluid-controlled cataclastic flow, FD = fluid-assisted diffusion, AT = advective transfer. Not to scale (modified after Marshall et al. 1998).

The peak metamorphic temperatures reached in Kuhmo greenstone belt have been 500–660 °C with increasing temperatures towards the margins (Tuisku 1988), indicating that the nickeliferous sulfide phase in Sika-aho has most likely been deformed as a monosulfide solid solution (MSS). Based on experimental data and observations from elsewhere, pentlandite in massive ores transforms to MSS at temperatures between 350 and 550 °C, and it behaves similarly to homogeneous pyrrhotite with dislocation processes being dominant (McQueen

1987). Pentlandite-rich ores require temperatures from the higher end of the range, with diffusion processes becoming more important at temperatures above 550 °C (McDonald & Paterson 1980, after McQueen 1987). Further evidence of this could attained by, for example, analysing the Fe, Ni, and Cu ratios and tenors in sulfides, as the range would be limited in sulfide assemblages that have been remobilised as a homogeneous MSS, whereas large-scale variations would be expected if the remobilisation occurred as a polymineralic pyrrhotite-pentlandite-chalcopyrite aggregate (Mukwakwami 2012, and references therein). However, this does not take post-remobilisation processes into account, which can have significant effect on, for instance, Ni/Cu ratios (e.g., Makkonen et al. 2017).

Any new interpretations for the extent of remobilisation in Sika-aho cannot be provided in this study due to inadequate data and overall challenges that are faced when trying to determine the extent of remobilisation. The extent of remobilisation has been found to be very difficult to determine in most remobilised ores, as it requires a vast amount of macroscale and mesoscale observations for a reliable interpretation (Gilligan & Marshall 1987; Marshall & Gilligan 1993). Also, the more extensive remobilisation is, the harder it is to quantify (paradox of remobilisation). The Sika-aho Ni deposit does not outcrop and there are no underground openings where one could map the textures. All observations are made from drill cores and thin sections, thus limiting the textural interpretation to mostly microscale and some mesoscale observations. Luukkonen et al. (1998) state that the Sika-aho Ni deposit has translocated from its original magmatic position to “some extent”, however no one has been able to determine the true extent. They mention that based on the knowledge from similar Australian Ni deposits, the extent is probably a couple hundred metres at maximum. Ductile plastic flow has remobilised massive sulfides of many deformed Ni-Cu-PGE deposits at the scale of tens of metres to a hundred metres (e.g., McQueen 1987; Marshall et al. 1998), however larger extents have been reported from, for example, Sudbury, where the remobilisation distance in the sulfide ore of Garson mine was about 450 metres (Mukwakwami et al. 2014).

The Sika-aho Ni deposit has undergone very high degree of remobilisation. The degree of remobilisation can be determined based on the micro- and mesoscale textures seen in the rocks. The whole deposit is hosted by strongly schistose, sheared rocks that have disseminated sulfides that are elongated and flattened along the schistosity planes. Only small part of the deposit has been interpreted to be hosted by strongly altered komatiites (Chapter

6.1.3), which means that even in the most conservative case the deposit has been almost completely remobilised.

It is most likely that the remobilisation of Ni sulfides occurred syn- or post-D_3 Archaean deformation phase of Luukkonen (1992) within the Tammasuo shear zone, similarly to what Luukkonen et al. (1998, 2002) have interpreted. This phase was interpreted to be the first deformation phase after volcanism and deposition of sediments ceased, while also reaching the highest metamorphic grade (amphibolite facies) in the evolution of Kuhmo greenstone belt with temperatures up to 660 °C (Tuisku 1988; Luukkonen 1992). Mechanical remobilisation of sulfides, and especially pyrrhotite-dominated sulfide assemblage, does not necessarily require that high of a temperature, since external ductile remobilisation is most effective during pro- and retrograde metamorphism in approximately 350–500 °C (Marshall & Gilligan, 1993). Based on the interpretation by Luukkonen (1992), the pressure-temperature conditions decreased during D_4 deformation phase with cataclastic deformation occurring. The temperatures continued to decrease during D_5 deformation phase. However, it is not known when the temperatures decreased to levels when ductile flow of sulfides would have been ineffective. The hydrothermal fluids that produced, for example, anomalous Au contents in the Tammasuo shear zone are associated with altered cataclastic rocks (Luukkonen 1998, 2002), thus they have likely formed syn- or post-D_4 deformation phase.

Assessment of other possible transfer mechanisms of Ni in Sika-aho results to a conclusion that they are not feasible compared to ductile plastic flow based on the results from this and earlier studies. Metamorphic sulfide anatexis is not plausible as the pyrrhotite-pentlandite(-chalcopyrite) dominated mineralogy would require temperatures exceeding 900 °C (Kullerud et al. 1969, after Mukwakwami et al. 2014) and the volume of sulfide melt produced would be very low (Tomkins et al. 2007). External remobilisation of sulfides by solid-state diffusive mechanisms has so far been interpreted to only have occurred in sulfide-rich metasedimentary rocks adjacent to magmatic ores in magmatic temperatures (e.g., Lesher & Keays 2002), thus being improbable in Sika-aho.

The rocks in the study area are hydrothermally altered, however the sulfides do not show evidence of external remobilisation by fluids, as decoupling between Pt, Pd, and other PGEs would be observed in that case (e.g., Keays & Jowitt 2013; Le Vaillant et al. 2015). It is suggested that the fluids in Sika-aho area have not had the capacity to remobilise Ni, Co, Pt, or Pd in any significant amounts. Generally, the salinity of the fluids has been determined to

be important to dissolve and transport base metals (Yardley 2005). To remobilise Ni, Co, Pt, and Pd, the fluids typically have to be acidic, with oxidation states as well as sulfide and chloride complexation being crucial for the mobility of these metals (Liu et al. 2011, 2012; Barnes & Liu 2012; Jansson & Liu 2020). Most of the rocks in Sika-aho are carbonatised, which would make the fluids less acidic, thus limiting the ability for them to dissolve base metals (Barnes & Liu 2012). Arsenic, which has been reported to be important for Ni mobility by Le Vaillant (2014), does not correlate with Ni at all in Sika-aho. Other PGEs aside from Pt and Pd were not analysed in this study, thus the IPGE and Rh data available from Sika-aho only covers the mineralised rocks (Makkonen & Halkoaho 2007). PGEs correlate strongly with each other (Figure 35), which is further evidence that they have not been hydrothermally remobilised. However, lack of IPGE and Rh analyses from komatiites creates some uncertainty, as the ratios and abundances cannot be compared with the source and the product.

Fluids that have the capacity to remobilise other base or precious metals do not necessarily have the capacity to remobilise Ni and PGE. The mobility of base metals and PGE in Kevitsa magmatic Ni sulfide deposit during low temperature carbonation and hydration of the mineralised mafic-ultramafic intrusion has varied between different metals: Ni and PGE have been remobilised only on millimetre scale, whereas Cu and Au have been remobilised on centimetre to kilometre scale (Le Vaillant et al. 2016a). Evidently, anomalous Au concentrations can be found in Sika-aho and Tammasuo areas (Luukkonen et al. 2002; this study), and the Au in Tammasuo is structurally controlled in cataclastic and strongly altered zones. Luukkonen et al. (1998) state that this Au-critical shear zone extends over 10 km to north and south based on geophysics. Metamorphic fluids could therefore have also remobilised Cu (e.g., Luukkonen et al. 2017), which could explain the varying Cu contents and Ni/Cu ratios in the mineralised rocks, even if the average is close to the ratios found in komatiites. The Ni tenors in sulfides are variable as well (Heino 1998; Luukkonen et al. 1998), however heterogeneity in the ratios and tenors could be caused by differences in sulfide grain sizes and textures inside the Sika-aho Ni deposit: smaller, disseminated sulfide grains have comparably more surface area that can react with hydrothermal fluids, whereas larger, massive sulfides do not react with hydrothermal fluids as efficiently.

6.1.3 Host rock characteristics

The host rock characteristics of Sika-aho Ni deposit strongly favour the interpretation presented in previous chapter that Ni has been remobilised and is not at its original volcanic

position. MgO is quite constant among the mineralised rocks with an average of 5.91 wt% (Figure 31a), which implies that the host rocks are mainly mafic and intermediate in composition. The abundance of immobile elements, such as Zr and TiO_2, in mineralised rocks indicate that small part of the deposit is hosted by rocks that were originally komatiites but are now altered (Figure 27). Three of the samples in the Figure 27 clearly plot into the same field as intermediate-felsic rocks. This combined with, for example, Al_2O_3 contents (Figure 31b) and REE-patterns (Figure 29) indicate that the host rocks of the Sika-aho Ni deposit are highly variable: majority of them are strongly altered tholeiitic basalts and high-Cr basalts, however, some parts of the deposit are hosted by altered komatiites, komatiitic basalts, and intermediate–felsic volcanic rocks. The combined 3D-model (Figure 41) shows similar results and confirms that the deposit is hosted by a variety of lithologies.

The already heterogeneous host rocks were affected by later hydrothermal activity that potentially caused redistribution of at least Fe, Cu, and S. The petrographic study of the mineralised rocks revealed that the mineralogy and alteration intensity vary heavily. Even though all thin sections contained at least some quartz, the amount of carbonates, chlorite, and sericite were very heterogeneous, which indicates that there is a lot of internal variation in the host rock lithology and alteration types. Secondary alteration of sulfides was evident from, for example, pentlandite grains altering to bravoite along fracture planes (Figure 17) and chalcopyrite grains altering to covellite along grain boundaries. Replacement of sulfides by silicate and carbonate minerals was also observed (Figure 18).

Considering the other indications favouring mechanical remobilisation of sulfides, it is likely that the correlation between Ni and Co is the result of them residing in pentlandite. Nickel and cobalt correlate strongly in the mineralised zone (Figure 33b; Table 3), which could either indicate that the fluids that have dissolved Ni have also dissolved Co and they have been deposited in similar manner, or that Co is residing in pentlandite and/or pyrrhotite, which are the major sulfides present in Sika-aho capable of incorporating Ni and Co in the crystal lattice.

Compared to other Archaean Ni deposits in eastern Finland, Sika-aho deposit is relatively rich in Zn (Makkonen & Halkoaho 2007) with an average concentration of ~409 ppm in the mineralised zone: the elevated Zn contents are most likely a result of hydrothermal activity. The distribution of Zn is sporadic and Zn doesn’t correlate well with any chalcophile or major elements, and the relationship is weak even with Co that shows a slight positive correlation.

Makkonen & Halkoaho (2007) state that the host rock of Sika-aho Ni deposit has been an intermediate rock because of high SiO_2 and Zn contents, but the average Zn content is very similar for all lithologies outside the deposit (~108 ppm for komatiites, ~117 ppm for mafic volcanic rocks, and ~91 ppm for intermediate and felsic volcanic rocks) except black schists and quartz porphyries, which show relatively high (~294 ppm) and low (~25 ppm) average Zn contents, respectively. However, the average content for black schists is heavily affected by two anomalous contents (1240 and 953 ppm).

Numeric and geological 3D-modelling with Leapfrog Geo confirm that elevated Zn contents are mainly found in and close to the mineralised zone. These findings combined with previously mentioned results from geochemical analyses suggest that the high Zn in the Sika-aho deposit is rather a result of remobilisation of Zn from another source than a characteristic feature of the host rock. Zinc can be mobilised in variety of different geological environments, and hydrothermal fluids have the capacity to dissolve, transport, and deposit Zn (e.g., Brugger et al. 2003; Mei et al. 2015). Ultramafic rocks, including komatiites, are quite Zn-poor (e.g., Sossi et al. 2018), thus Zn must have a different source compared to Ni. Brugger et al. (2003) state that precipitation of Zn-sulfides will trigger if a metal-rich, sulfide-free fluid interacts with a reducing and/or sulfide-rich rock. The anomalous Zn contents in Sika-aho are found in the deposit or close by in the black schists: these rocks are more reduced compared to surrounding rocks and could therefore act as deposition sites for Zn-bearing fluids.

Magmatic enrichment of basaltic volcanic rocks in Sika-aho area could partly explain the anomalous Cr contents of the deposit. Tectonically remobilised ores have been found to be variably depleted in Cr, with the depletion being due to presumed ductility contrast between sulfides and spinel (Lesher & Keays 2002, and references therein). For the majority of the mineralised rocks in Sika-aho, this is not the case as the Cr contents are abnormally high in many samples (Figure 28). Unusually Cr-rich basalts are very uncommon globally, as the Cr abundances in terrestrial basaltic rocks typically range from 200 to 400 ppm, however some exceptionally Cr-rich basalts have been found, for example, in Tipasjärvi and Kuhmo greenstone belts in Finland (Halkoaho et al. 2000, and references therein). According to Halkoaho et al. (2000), Cr is mainly hosted by amphiboles that have formed from breakdown of chromian clinopyroxenes, and the Cr enrichment is due to low f_{O_2} in the magma, preventing the crystallisation of chromite. Similar magmatic processes could therefore have caused the enrichment of Cr in the basaltic rocks of Sika-aho area.

The high Cr contents in the Sika-aho deposit and around it are also partly a result of hydrothermal activity. In the MgOn vs. Cr binary plot (Figure 28), it can be seen that the Cr contents are very high in the mineralised rocks even though they are not as MgO-rich as the komatiitic basalts and komatiites. The MgO content is largely closer to tholeiitic basalts and intermediate volcanic rocks. Even the volcaniclastic rocks to the east of the deposit show very high Cr contents of over 500 ppm (Figure 28), which indicates later enrichment. In the petrographic study, chromite or spinel were not observed in the mineralised zone. During drill core revision logging, however, fuchsite (chrome-bearing mica) was observed especially in the mineralised rocks. Ni and Cr do not correlate at all in the mineralised rocks, thus different remobilisation mechanisms are to be expected.

6.1.4 Comparison of Sika-aho to other similar nickel deposits

The komatiite-associated Arola Ni deposit, which is approximately 20 km to S-SW from Sika-aho, shows many similarities with the Sika-aho Ni deposit and has very likely formed by comparable processes (Makkonen & Halkoaho 2007). The mineralised rocks in Arola are intensively sheared, and the Ni-sulfides are found in bands parallel to the schistosity in strongly schistose quartz-carbonate-chlorite schist (Lehtinen 1983). According to Makkonen & Halkoaho (2007), the average of Pt/Pd ratios in four samples from Arola deposit is 1.14. Both Arola and Sika-aho have similar stratigraphy as found in Siivikko-Kellojärvi area. Anomalous Au contents are found along the shear zone with intense silicification, carbonatization, and turmalinisation, thus being analogous with the Tammasuo Au deposit except for the turmalinisation. Halkoaho & Papunen (1998) have interpreted that the Arola Ni deposit has formed as a result of tectono-metamorphic redistribution of magmatic sulfides in a shear zone, while considering hydrothermal accumulation of Ni-sulfides implausible due to the spatial association to only mafic host rocks and not beyond them. In future studies of remobilised komatiite-associated Ni deposits it would be worthwhile to compare Sika-aho and Arola in more detail.

In the Yilgarn craton in Western Australia, several mechanically remobilised komatiitic Ni(-Cu-PGE) deposits have been identified, such as the ore shoots around Widgiemooltha and Kambalda domes, as well as at Nepean and Windarra (McQueen 1987; Stone et al. 2005). The ores owe their elevated concentrations to igneous-related processes; however, their current features are due to remobilisation, deformation, and recrystallisation in tectono-metamorphic environments. McQueen (1987) states that, for example, in the Durkin Deeps area the

extensive ore bodies are completely enclosed within metabasalts as a result of tight folding and overthrusting. Many ore shoots at Kambalda have been mesoscopically remobilised along high-angle reverse faults and shear zones. The processes have involved movement of ductile high-temperature sulfides in a relatively higher-strength and less ductile host rocks, akin to what this study suggests for the formation of Sika-aho Ni deposit.

6.2 Apparent lack of geochemical haloes in Sika-aho

Examination of geochemical analyses combined with numeric and geological 3D-modelling did not show indications of geochemical haloes around the Sika-aho Ni deposit. Nickel has been found to correlate with Co, Cu, Pd, Pt, S, and As (+Te, which was not analysed in this study) in some hydrothermally altered Ni sulfide deposits (e.g., Le Vaillant 2014), and in some cases forming geochemical haloes. Geochemical haloes were not detected with other analysed chalcophile or siderophile elements, either.

Ni-Cu-PGE deposits that have undergone several phases of deformation and alteration still do not necessarily form geochemical haloes, as has been the case, for example, in Perseverance, Otter-Juan, and Durkin ore bodies in the Yilgarn craton (Le Vaillant et al. 2016c). The Perseverance deposit has been deformed and elongated along a major shear zone that could have enabled circulation of hydrothermal fluids, but still no evidence of chemical transfer of sulfides could be detected. Also, similarly to Sika-aho, the Pt/Pd ratio in Perseverance is consistently close to 1 and the IPGE have strong correlation between one another. Le Vaillant et al. (2016c) have determined that the remobilisation was mechanical rather than chemical. Perseverance shares a lot of similar characteristics with Sika-aho, which indicates that alike processes have affected both deposits, but no distinguishable geochemical haloes have formed.

The presence of As-bearing fluids has been determined to be important for the formation of geochemical haloes associated with Ni sulfide deposits by Le Vaillant (2014), however the rocks in Sika-aho are largely very As-poor outside of few singular anomalies (Figure 33e). Minor arsenopyrite and Ni-Fe arsenides have been detected sporadically in Sika-aho Ni deposit (Luukkonen et al. 2002), both of which are usually found in hydrothermal deposits (e.g.,Pokrovski et al. 2002; Scharrer et al. 2019). The sporadic occurrence of As-bearing minerals in Sika-aho, correlation of As with Au, S, and to some extent Te in adjacent Tammasuo Au deposit (Luukkonen et al. 2002), and prevalence of As-phases in hydrothermal fluids indicate that As-bearing hydrothermal fluids have been present at some point. The

studies by Hanley & Bray (2009) and Barrie et al. (2007), even though they are related to intrusive Ni-Cu-PGE deposits, also show promising results for detecting geochemical haloes in veins. Thus, there is a possibility that faint geochemical haloes could be detected in Sika-aho if the veins are analysed, even if the current results indicate that Ni has been largely immobile.

The structures in Sika-aho could be possible channels where even faint geochemical haloes could potentially be detected with more detailed study. Whether a deposit has formed because of chemical, mechanical, or mixed-state remobilisation processes, understanding of structural geology of the deposit is important in any case. Mineralising fluids from ore depositional environments that have penetrated structural or permeability channels have the capability to produce elemental leakage anomalies far away from the deposit (McQueen 2005). For example, in Sarah's Find Ni-Cu-(PGE) deposit in Yilgarn craton, a Ni-Co-As-Pd geochemical halo extending along a shear zone was identified up to 1780 metres away from the massive sulfides (Le Vaillant et al. 2016b). A dominant stretching lineation was observed parallel to the geochemical halo. Another example from Yilgarn craton is the Miitel Ni sulfide deposit, which has a Ni-As-Pd-Pt geochemical halo extending at least 250 metres away from the ore, and the fluid flow is suggested to have been structurally controlled (Le Vaillant et al. 2015).

6.3 Implications for exploration

Many widely utilised exploration techniques for komatiite-associated Ni(-Cu-PGE) deposits have limited applicability in Sika-aho due to the remobilisation of Ni from its magmatic position, absence of primary volcanic textures, and strong alteration. Le Vaillant et al. (2016c, 2017) state that camp to prospect scale tools include identifying channelised volcanic environments, evidence of crustal contamination, and evidence of sulfide accumulation and/or extraction. The deposit scale methods which could be potential in Sika-aho and/or similar Ni deposits elsewhere seem to be largely restricted to detection of geochemical haloes and/or low-grade disseminations around the deposit. Other methods, such as detecting evidence of sulfide extraction/accumulation by identifying positive or negative anomalies of chalcophile elements (e.g., PGE) in whole-rock analyses or Ni in olivine are not plausible methods in Sika-aho because the Ni sulfides have been externally remobilised away from the original volcanic position, and olivine cannot be found due to total serpentinisation and talc-carbonate alteration. Delineation of ore-related channels with, for example Ni/Cr ratios, cannot be done reliably as there are no primary volcanic textures to observe. Methods such as Ru depletion in

chromite grains can be used in highly altered terrains (Fiorentini et al. 2008), and it could be used to find prospective areas where sulfide-saturated komatiites have occurred, however it would not lead to the location of where the sulfides reside currently in the case of a remobilised deposit.

Luukkonen et al. (1998, 2002) state that a less mineralised, low-grade extension of disseminated sulfides along the margin of the komatiite unit and along the strike of the deposit can traced for about 150 m to northeast from the Sika-aho Ni deposit (Figure 8). The deposit also continues along its dip as a narrower low-grade dissemination of pyrrhotite and can be detected below 200 metres of depth. McQueen (2005) states that a halo of low-grade disseminated sulfides where Ni content is above the expected linear Ni-MgO trend are the best lithogeochemical indicators for komatiite-hosted Ni deposits. In Sika-aho, the original magmatic low-grade halo has undoubtedly been remobilised, and is most likely found in the current state as low-grade extensions along the strike and dip of the deposit.

The exploration of komatiite-associated Ni(-Cu-PGE) deposits that have been remobilised continue to be challenging exploration targets, especially if they have been remobilised by dominantly mechanical processes. In addition to elevated Ni contents found in soil and boulders in direct vicinity of the deposit, the extension of low-grade disseminated sulfides is currently the only clearly identifiable indicator of the Sika-aho Ni deposit. There is no single method that could be reliably used to find any komatiite-associated Ni(-Cu-PGE) deposit, but the combination of lithogeochemical and geophysical tools with comprehensive regional and local geological understanding seem to provide the best chances for discovering new deposits (e.g., McQueen 2005; Le Vaillant et al. 2016c).

6.4 Future studies

The study of veins and vein systems in Sika-aho could provide necessary information about the hydrothermal behaviour of different elements as well as provide a tool to study possible geochemical haloes in more detail. The composition of sulfides in the deposit compared to the sulfides in komatiites and carbonate-quartz veins should be compared, as similarity in them would provide strong evidence for mechanical transfer as opposed to chemical transfer (e.g., Barnes et al. 1988). Proof of hydrothermal remobilisation could be seen in possible enrichment or depletion of IPGE (Ru, Os, and Ir) relative to Pt and Pd, thus more extensive PGE analyses would reveal further evidence about the effect that hydrothermal fluids have had on the deposit: for example, the use of Ni/Ir and Pd/Ir ratios were key to determining the

hydrothermal origin of the Avebury Ni deposit (Keays & Jowitt 2013). The Ni contents in different silicates and oxides, specifically talc and magnetite, could also be analysed to determine how strongly Ni has been partitioned to sulfides during metamorphism, while also providing indications of sulfur activity in komatiites during metamorphism.

Considering the results and concepts of sulfidation-oxidation haloes around metamorphosed sulfide deposits in the vicinity of black schists presented by Spry (1998), the compositions of chlorites and possibly other ferromagnesian silicates could be studied to assess the applicability of sulfidation-oxidation haloes in Ni exploration. Interestingly, the presence of Fe-Mg chlorite (pennine) in mineralised zone and Mg-Fe chlorite (clinochlore) in non-mineralised zone in the Arola Ni deposit was observed by Lehtinen (1983), which contradicts the idea of Spry (1998) that generally ferromagnesian minerals are Mg-rich in metamorphosed sulfide deposits as Fe is taken by sulfides in greater quantities. More studies should be conducted to determine the controlling factors and processes related to formation of sulfidation-oxidation haloes in these environments.

Fluid inclusion studies, for example, of quartz or carbonate grains could be used to constrain the temperature, timing, and composition of metamorphic and possibly mineralising fluids (e.g., Nyman et al. 1990; Lahaye & Arndt 1996; Molnár et al. 1997; Farber et al. 2016). They have been used gather information about the fluids that have altered komatiites or have remobilised base and precious metals, such as Ni, Cu, PGE, and Au. The information gained from fluid inclusion studies could be especially helpful for determining the origin of anomalous Cr, Zn, and Au contents found in Sika-aho and Tammasuo, as well as help solve the reason for sporadic distribution of Cu contents in Sika-aho Ni deposit.

Studies of regional structural geology would be key to better understanding of, for example, the deformation history of the deposit and adjacent lithologies. Barnes et al. (2018) state that the geometry of a remobilised deposit is determined by the orientation of the stress field during deformation rather than emplacement. This highlights the importance for the recognition of deformation structures in the deposit and surrounding rocks. The direction of stretching lineations on the schistosity planes could be measured if oriented drill cores were drilled, thus providing further evidence for possible shear zone transfer. Structural data would also be highly important for improving the accuracy of the 3D-model, as the complex geology of Sika-aho area (or whole KGB, for that matter) inevitably requires vast amounts of structural data on top of lithological and analytical data to be modelled in detail.

7 Conclusions

The source of Ni in Sika-aho has been sulfides in a komatiitic cumulate unit. The Ni content of sulfides has been upgraded during serpentinisation and talc-carbonate alteration.

The remobilisation mechanisms of nickeliferous sulfides in Sika-aho have been dominantly mechanical. Sulfides in the mineralised zone are found as flattened and elongated grains on the schistosity planes and they show stretching lineations, which indicate that sulfides have undergone ductile plastic flow. Uniform PGE ratios in komatiites and mineralised rocks support mechanical remobilisation.

The nickeliferous sulfide phase in Sika-aho has likely been remobilised as a monosulfide solid solution. The degree of sulfide remobilisation by solid-state mechanisms is very high, and the remobilisation has occurred syn- to post-D_3 deformation phase of Luukkonen (1992) within the Tammasuo shear zone. However, the extent of remobilisation remains ambiguous.

The Sika-aho Ni deposit is largely hosted by strongly schistose, sheared, and altered basalts, however it is also partly hosted by altered komatiites and intermediate-felsic volcanic rocks. Most of the Ni is in pentlandite, which is found as individual grains, intergrown with other sulfides, and as lamellae and inclusions in pyrrhotite.

Strong correlation between Ni and Co indicates that Co has been simultaneously remobilised with Ni. It is suggested that both magmatic and hydrothermal processes have contributed to the unusually high Cr contents of the deposit. High Zn contents, however, are hydrothermal in origin. Replacement textures observed in sulfides in the mineralised zone indicate that the deposit has undergone later hydrothermal alteration that has most likely affected the distribution of Fe, Cu, and S.

Based on the geochemical analyses and numeric 3D-models, geochemical haloes cannot be detected around the Sika-aho Ni deposit. In Ni(-Cu-PGE) exploration, the lack of geochemical haloes should not be regarded as a negative indicator for prospectivity, though. A low-grade extension of disseminated sulfides is found up to about 150 metres to the northeast, and it can be used as a vector towards the deposit. However, further study of carbonate-quartz(-sulfide) veins is required to determine the nature of hydrothermal processes that occurred in Sika-aho.

Acknowledgements

I would like to thank my supervisors Associate Professor Esa Heilimo and Docent Tapio Halkoaho for continued support, productive discussions, and helpful feedback throughout the study process. I would also like to thank laboratory technician Arto Peltola for preparing the polished thin sections for the study. Geological Survey of Finland is thanked for funding the project and providing me the chance to study this topic, as well as for sponsoring me to present the results in LITO22 symposium in Turku, November 15–17, 2022.

References

ALS Geochemistry, 2021. Schedule of services & fees, 52 pp.

Arndt, N., Lesher, C.M., & Czamanske, G.K., 2005. Mantle-derived magmas and magmatic Ni–Cu–(PGE) deposits. Economic Geology, 100th Anniversary Volume, 5–24.

Arndt, N., Lesher, C.M., & Barnes, S.J., 2008. Komatiite. Cambridge University Press, New York, 488 pp.

Barnes, S.J., Gole, M.J., & Hill, R.E.T., 1988. The Agnew nickel deposit, Western Australia: Part I. Structure and stratigraphy. Economic Geology, 83 (3), 524–536. DOI: 10.2113/gsecongeo.83.3.524.

Barnes, S.J. & Hill, R.E.T., 1998. Metamorphism of Komatiite-Hosted Nickel Sulfide Deposits. Reviews in Economic Geology, 11, 205–217.

Barnes, S.J. & Brand, N.W., 1999. The distribution Cr, Ni, and chromite in komatiites, and application to exploration for komatiite-hosted nickel sulfide deposits. Economic Geology, 94 (1), 129–132.

Barnes, S.J., Hill, R.E.T., Perring, C.S., & Dowling, S.E., 2004. Lithogeochemical exploration for komatiite-associated Ni-sulfide deposits: Strategies and limitations. Mineralogy and Petrology, 82, 259–293. DOI: 10.1007/s00710-004-0051-7.

Barnes, S.J., Fiorentini, M.L., Duuring, P., Grguric, B.A., & Perring, C.S., 2011. The Perseverance and Mount Keith Nickel Deposits of the Agnew-Wiluna Belt, Yilgarn Craton, Western Australia. Reviews in Economic Geology, 17, 51–88.

Barnes, S.J. & Liu, W., 2012. Pt and Pd mobility in hydrothermal fluids: Evidence from komatiites and from thermodynamic modelling. Ore Geology Reviews, 44, 49–58. DOI: 10.1016/j.oregeorev.2011.08.004.

Barnes, S.J., Mungall, J.E., & Maier, W.D., 2015. Platinum group elements in mantle melts and mantle samples. Lithos, 232, 395–417. DOI: 10.1016/j.lithos.2015.07.007.

Barnes, S.J., Staude, S., Le Vaillant, M., Piña, R., & Lightfoot, P.C., 2018. Sulfide-silicate textures in magmatic Ni-Cu-PGE sulfide ore deposits: Massive, semi-massive and sulfide-matrix breccia ores. Ore Geology Reviews, 101, 629–651. DOI: 10.1016/j.oregeorev.2018.08.011.

Barrie, T., Samson, I., Price, M., Campos-Alvarez, N., & Fryer, B., 2007. Camiro Project 04E01 - Chemical and Mineralogical Halos Around Magmatic Sulfide Deposits. Canadian Mining Industry Research Organization. 216 pp. DOI: 10.13140/RG.2.1.5123.2167.

Le Bas, M.J., 2000. IUGS reclassification of the high-Mg and picritic volcanic rocks. Journal of Petrology, 41 (10), 1467–1470. DOI: 10.1093/petrology/41.10.1467.

Benkó, Z., Mogessie, A., Molnár, F., Krenn, K., Poulson, S.R., et al., 2015. Hydrothermal alteration and Cu-Ni-PGE mobilization in the charnockitic rocks of the footwall of the South Kawishiwi intrusion, Duluth Complex, USA. Ore Geology Reviews, 67, 170–188. DOI: 10.1016/j.oregeorev.2014.11.010.

Boynton, W. V., 1984. Cosmochemistry of the Rare Earth Elements: Meteorite Studies. In: Henderson, P. (ed.), Rare Earth Elements Geochemistry. Elsevier Science Publishing Company, Amsterdam, 63–114. DOI: 10.1016/b978-0-444-42148-7.50008-3.

Brand, N.W., 1999. Element ratios in nickel sulphide exploration: vectoring towards ore environments. Journal of Geochemical Exploration, 67 (1–3), 145–165. DOI: 10.1016/S0375-6742(99)00063-1.

Brooks, C. & Hart, S.R., 1974. On the Significance of Komatiite. Geology, 2 (2), 107–110.

Brugger, J., McPhail, D.C., Wallace, M., & Waters, J., 2003. Formation of willemite in hydrothermal environments. Economic Geology, 98 (4), 819–835. DOI: 10.2113/gsecongeo.98.4.819.

Capistrant, P.L., Hitzman, M.W., Wood, D., Kelly, N.M., Williams, G., et al., 2015. Geology of the Enterprise Hydrothermal Nickel Deposit, North-Western Province, Zambia. Economic Geology, 110, 9–38.

Carranza, E.J.M. & Sadeghi, M., 2012. Primary geochemical characteristics of mineral deposits - Implications for exploration. Ore Geology Reviews, 45, 1–4. DOI: 10.1016/j.oregeorev.2012.02.002.

Cohen, D.R. & Bowell, R.J., 2013. Exploration Geochemistry. In: Turekian, K. & Holland, H., 2013. Treatise on Geochemistry: Second Edition. Elsevier Ltd., 623–650 pp. DOI: 10.1016/B978-0-08-095975-7.01127-X.

Cox, S.F., 1987. Flow mechanisms in sulphide minerals. Ore Geology Reviews, 2 (1–3), 133–171. DOI: 10.1016/0169-1368(87)90026-6.

Donaldson, M.J., 1981. Redistribution of ore elements during serpentinization and talc-carbonate alteration of some Archean dunites, Western Australia. Economic Geology, 76, 1698–1713. DOI: 10.2113/gsecongeo.76.6.1698.

Dostal, J., 2008. Komatiites. Geoscience Canada, 35 (1), 21–31.

Durney, D.W., 1972. Solution-transfer, an important geological deformation mechanism. Nature, 235 (5337), 315–317. DOI: 10.1038/235315a0.

Duuring, P., Bleeker, W., Beresford, S.W., & Hayward, N., 2010. Towards a volcanic-structural balance: Relative importance of volcanism, folding, and remobilisation of nickel sulphides at the Perseverance Ni-Cu-(PGE) deposit, Western Australia. Mineralium Deposita, 45 (3), 281–311. DOI: 10.1007/s00126-009-0274-y.

Elshkaki, A., Reck, B.K., & Graedel, T.E., 2017. Anthropogenic nickel supply, demand, and associated energy and water use. Resources, Conservation and Recycling, 125, 300–307. DOI: 10.1016/j.resconrec.2017.07.002.

Etheridge, M.A., Wall, V.J., Cox, S.F., & Vernon, R.H., 1984. High Fluid Pressures During Regional Metamorphism and Deformation: Implications for Mass Transport and Deformation Mechanisms. Journal of Geophysical Research, 89 (B6), 4344–4358. DOI: 10.1029/jb089ib06p04344.

Farber, K., Dziggel, A., Meyer, F.M., & Harris, C., 2016. Petrology, geochemistry and fluid inclusion analysis of altered komatiites of the Mendon Formation in the BARB4 drill core, Barberton greenstone belt, South Africa. South African Journal of Geology, 119 (4), 639–654. DOI: 10.2113/gssajg.119.4.639.

Fiorentini, M.L., Beresford, S.W., & Barley, M.E., 2008. Ruthenium-chromium variation: A new lithogeochemical tool in the exploration for komatiite-hosted Ni-Cu-(PGE) deposits. Economic Geology, 103 (2), 431–437. DOI: 10.2113/gsecongeo.103.2.431.

Fiorentini, M.L., Barnes, S.J., Lesher, C.M., Heggie, G.J., Keays, R.R., & Burnham, O.M., 2010. Platinum group element geochemistry of mineralized and nonmineralized komatiites and basalts. Economic Geology, 105 (4), 795–823. DOI: 10.2113/gsecongeo.105.4.795.

Fiorentini, M.L., Barnes, S.J., Maier, W.D., Burnham, O.M., & Heggie, G., 2011. Global variability in the platinum-group element contents of komatiites. Journal of Petrology, 52 (1), 83–112. DOI: 10.1093/petrology/egq074.

Fiorentini, M.L., Beresford, S., Barley, M., Duuring, P., Bekker, A., et al., 2012. District to camp controls on the genesis of komatiite-hosted nickel sulfide deposits, Agnew-Wiluna greenstone belt, Western Australia: Insights from the multiple sulfur isotopes. Economic Geology, 107 (5), 781–796. DOI: 10.2113/econgeo.107.5.781.

Ganguly, S. & Yang, Q.Y., 2018. Greenstone belts and their mineral endowment: Preface. Geoscience Frontiers 9, 599–601. DOI: 10.1016/j.gsf.2017.11.001.

Gilligan, L.B. & Marshall, B., 1987. Textural evidence for remobilization in metamorphic environments. Ore Geology Reviews, 2 (1–3), 205–229. DOI: 10.1016/0169-1368(87)90029-1.

GTK, 2021. Sika-aho Mineral Deposit Report. 31 pp. https://tupa.gtk.fi/karttasovellus/mdae/raportti/48_Sika-aho.pdf [Accessed: 12.01.2022].

GTK, 2022. GTK open licence CC BY 4.0, including 'GTK's Mineral Deposits and Exploration' and 'Bedrock of Finland 1:200 00' data, imported from Hakku service and accessed online [October 2022].

Habib, K., Hansdóttir, S.T., & Habib, H., 2020. Critical metals for electromobility: Global demand scenarios for passenger vehicles, 2015–2050. Resources, Conservation & Recycling, 154, 104603.

Haldar, S.K., 2013. Mineral Exploration: Principles and Applications. Elsevier, 372 pp.

Halkoaho, T. & Papunen, H., 1998. Geology and Mineral Deposits of the Arola Area, Kuhmo. Technical Report 6.3, Turku University, 14 pp.

Halkoaho, T., Liimatainen, J., Papunen, H., & Välimaa, J., 2000. Exceptionally Cr-rich basalts in the komatiitic volcanic association of the Archaean Kuhmo greenstone belt, eastern Finland. Mineralogy and Petrology, 70, 105–120. DOI: 10.1007/s007100070016.

Hanley, J.J., Pettke, T., Mungall, J.E., & Spooner, E.T.C., 2005. The solubility of platinum and gold in NaCl brines at 1.5 kbar, 600 to 800°C: A laser ablation ICP-MS pilot study of synthetic fluid inclusions. Geochimica et Cosmochimica Acta, 69 (10), 2593–2611. DOI: 10.1016/j.gca.2004.11.005.

Hanley, J.J. & Bray, C.J., 2009. The trace metal content of amphibole as a proximity indicator for Cu-Ni-PGE mineralization in the footwall of the Sudbury Igneous Complex, Ontario, Canada. Economic Geology, 104 (1), 113–125.

Hanski, E., 1980. Komatiitic and tholeiitic metavolcanics of the Siivikkovaara area in the Archean Kuhmo greenstone belt, eastern Finland. Bulletin of the Geological Society of Finland, 52, 67–100. DOI: 10.17741/bgsf/52.1.004.

Hanski, E., 2015. Synthesis of the Geological Evolution and Metallogeny of Finland. In: Maier, W.D., Lahtinen, R., & O'Brien, H., (eds.), Mineral Deposits of Finland. Elsevier, 39–72.

Heino, T., 1998. HYRYNSALMI, Puistola 1 (kaivosrekisteri No 5657/1) ja Paatola 1 (kaivosrekisteri No 5619/1) nikkeliesiintymän mineraalivarantoarvio. Geological Survey of Finland, Archive report, M19/4421/-98/1/10, 33 pp.

Herzberg, C., 1992. Depth and degree of melting of komatiites. Journal of Geophysical Research, 97 (B4), 4521–4540. DOI: 10.1029/91JB03066.

Hill, R.E.T., Barnes, S.-J., Gole, M.J., & Dowling, S.E., 1995. The volcanology of komatiites as deduced from field relationships in the Norseman-Wiluna greenstone belt, Western Australia. Lithos, 34, 159–188.

Hill, R.E.T., 2001. Komatiite volcanology, volcanological setting and primary geochemical properties of komatiite-associated nickel deposits. Geochemistry: Exploration, Environment, Analysis, 1 (4), 365–381. DOI: 10.1144/geochem.1.4.365.

Hoatson, D.M., Jaireth, S., & Jaques, A.L., 2006. Nickel sulfide deposits in Australia: Characteristics, resources, and potential. Ore Geology Reviews, 29 (3–4), 177–241. DOI: 10.1016/j.oregeorev.2006.05.002.

Hobbs, B.E., 1987. Principles involved in mobilization and remobilization. Ore Geology Reviews, 2 (1–3), 37–45. DOI: 10.1016/0169-1368(87)90022-9.

Hölttä, P., Balagansky, V., Garde, A.A., Mertanen, S., Peltonen, P., Slabunov, A., Sorjonen-Ward, P., & Whitehouse, M., 2008. Archean of Greenland and Fennoscandia. Episodes, 31 (1), 13–19. DOI: 10.18814/epiiugs/2008/v31i1/003.

Hölttä, P., Heilimo, E., Huhma, H., Juopperi, H., Kontinen, A., Konnunaho, J., Lauri, L., Mikkola, P., Paavola, J., & Sorjonen-Ward, P., 2012a. Archaean complexes of the Karelia province in Finland. Geological Survey of Finland, Special Paper 54, 9–20.

Hölttä, P., Heilimo, E., Huhma, H., Kontinen, A., Mertanen, S., Mikkola, P., Paavola, J., Peltonen, P., Semprich, J., Slabunov, A., & Sorjonen-Ward, P., 2012b. The Archaean of the Karelia Province in Finland. Geological Survey of Finland, Special Paper 54, 21–73.

Hölttä, P. & Heilimo, E., 2017. Metamorphic map of Finland. Geological Survey of Finland, Special Paper 60, 77–128.

Huhma, H., Mänttäri, I., Peltonen, P., Kontinen, A., Halkoaho, T., Hanski, E., Hokkanen, T., Hölttä, P., Juopperi, H., Konnunaho, J., Lahaye, Y., Luukkonen, E., Pietikäinen, K., Pulkkinen, A., Sorjonen-Ward, P., Vaasjoki, M., & Whitehouse, M., 2012. The age of the Archaean greenstone belts in Finland. Geological Survey of Finland, Special Paper 54, 74–175.

Ioannou, C., 2020. The Siivikkovaara Ni-Cu-Zn-Pb(-Au) deposit, Kuhmo-Suomussalmi greenstone belt, eastern Finland: Implications for Archean ocean-floor mineralization processes. University of Helsinki, MSc thesis, 78 pp.

Janoušĕk, V., Farrow, C.M., & Erban, V., 2006. Interpretation of Whole-rock Geochemical Data in Igneous Geochemistry: Introducing Geochemical Data Toolkit (GCDkit). Journal of Petrology, 47 (6), 1255-1259. DOI: 10.1093/petrology/egl013.

Jansson, N.F. & Liu, W., 2020. Controls on cobalt and nickel distribution in hydrothermal sulphide deposits in Bergslagen, Sweden - constraints from solubility modelling. GFF, 142 (2), 87–95. DOI: 10.1080/11035897.2020.1751270.

Jensen, L.S., 1976. A New Cation Plot for Classifying Subalkalic Volcanic Rocks. Ontario Division of Mines, Miscellaneous Paper, 66, 22 pp.

Juurela, S., 2013. Final exploration work report Kuhmo – Arola. Boliden Kuhmo Oy, ML2013:000, 15 pp.

Juurela, S., 2017. Final exploration work report Hyrynsalmi – Sika-aho. Boliden Kuhmo Oy, ML2013:0047, 15 pp.

Keays, R.R. & Jowitt, S.M., 2013. The Avebury Ni deposit, Tasmania: A case study of an unconventional nickel deposit. Ore Geology Reviews, 52, 4–17. DOI: 10.1016/j.oregeorev.2012.07.001.

Koljonen, T., ed., 1992. The Geochemical Atlas of Finland, Part 2: Till. Geological Survey of Finland, 230 pp.

Konnunaho, J., Halkoaho, T., Hanski, E., & Törmänen, T., 2015. Komatiite-hosted Ni-Cu-PGE Deposits in Finland. In: Maier, W.D., Lahtinen, R., & O'Brien, H., (eds.), Mineral Deposits of Finland. Elsevier, 93–131.

Konnunaho, J., 2016. Komatiite-hosted Ni-Cu-PGE deposits in Finland: Their characterization, PGE content, and petrogenesis. Geological Survey of Finland, Espoo, 38 pp.

Kullerud, G., Yund, R.A., & Moh, G.H., 1969. Phase relations in the Cu-Fe-S, Cu-Ni-S, and Fe-Ni-S systems. In: Wilson, H.D.B. (ed.), Magmatic Ore Deposits, Society of Exploration Geophysicists, Geophysical Monograph Series, 4, 323-343.

Käpyaho, A., Mänttäri, I., & Huhma, H., 2006. Growth of Archaean crust in the Kuhmo district, eastern Finland: U-Pb and Sm-Nd isotope constraints on plutonic rocks. Precambrian Research, 146, 95-119.

Lahaye, Y. & Arndt, N.T., 1996. Alteration of a Komatiite Flow from Alexo, Ontario, Canada. Journal of Petrology, 37 (6), 1261–1284.

Lauri, L.S., Mikkola, P., & Karinen, T., 2012. Early Paleoproterozoic felsic and mafic magmatism in the Karelian province of the Fennoscandian shield. Lithos, 151, 74–82. DOI: 10.1016/j.lithos.2012.01.013.

Lehtinen, M., 1983. Kuhmon Arolan alueen geologiasta ja nikkeliesiintymästä. University of Turku, MSc thesis, 126 pp.

Lehtonen, E., Heilimo, E., Halkoaho, T., Käpyaho, A., & Hölttä, P., 2016. U-Pb geochronology of Archaean volcanic-sedimentary sequences in the Kuhmo greenstone belt, Karelia Province - Multiphase volcanism from Meso- to Neoarchaean and a Neoarchaean depositional basin? Precambrian Research, 275, 48–69. DOI: 10.1016/j.precamres.2015.12.002.

Lesher, C.M. & Keays, R.R., 2002. Komatiite-associated Ni-Cu-PGE Deposits : Geology, Mineralogy, Geochemistry, and Genesis. Canadian Institute of Mining, Metallurgy and Petroleum, 54, 579–618.

Liu, W., Borg, S.J., Testemale, D., Etschmann, B., Hazemann, J.L., & Brugger, J., 2011. Speciation and thermodynamic properties for cobalt chloride complexes in hydrothermal fluids at 35-440°C and 600bar: An in-situ XAS study. Geochimica et Cosmochimica Acta, 75 (5), 1227–1248. DOI: 10.1016/j.gca.2010.12.002.

Liu, W., Migdisov, A., & Williams-Jones, A., 2012. The stability of aqueous nickel(II) chloride complexes in hydrothermal solutions: Results of UV-Visible spectroscopic experiments. Geochimica et Cosmochimica Acta, 94, 276–290. DOI: 10.1016/j.gca.2012.04.055.

Luukas, J., Kousa, J., Nironen, M., & Vuollo, J., 2017. Major stratigraphic units in the bedrock of Finland, and an approach to tectonostratigraphic division. Geological Survey of Finland, Special Paper 60, 9–40.

Luukkonen, E.J., 1992. Late Archaean and early Proterozoic structural evolution in the Kuhmo-Suomussalmi terrain, eastern Finland. Annales Universitatis Turkuensis, Ser. A.II. Biologica-Geographica-Geologica, 78, 108 pp.

Luukkonen, E., Heino, T., Niskanen, M., & Tenhola, M., 1998. TUTKIMUSTYÖSELOSTUS HYRYNSALMEN KUNNASSA VALTAUSALUEILLA KAIVOLAMPI 1 - 2 (Kaivosrekisteri No 6143/3 ja 6143/2), PUISTOLA1 - 2 (Kaivosrekisteri No 5657/1 ja 6143/1), PAATOLA1 - 2 (Kaivosrekisteri No 5619/1 ja 5619/2), KIVIHARJU 1 - 2 (Kaivosrekisteri No 591686/3 ja 5986/4), SILTAJOKI 1 (Kaivosrekisteri No 5986/2), JOKIPERANAHO 1 - 2 (Kaivosrekisteri No 5656/1 ja 6119/1), RINNEAHO 1 (Kaivosrekisteri No 5657/3) ja HIETANIEMI 1 - 2 (Kaivosrekisteri No 5657/2 ja 5986/1) SUORITETUISTA KULTA- JA NIKKELIMALMITUTKIMUKSISTA VUOSINA 1993 - 1997. Geological Survey of Finland, report M06/4421/-98/1/10, 30 pp.

Luukkonen, E., Halkoaho, T., Hartikainen, A., Heino, T., Niskanen, M., et al., 2002. The activities of the Archean Terrains in Eastern Finland Project (12201 and 210 5000) in

Suomussalmi, Hyrynsalmi, Kuhmo, Nurmes, Rautavaara, Valtimo, Lieksa, Ilomantsi, Kiihtelysvaara, Eno, Kontiolahti, Tohmajärvi and Tuupovaara areas during years 1992–2001. Geological Survey of Finland, report M19/4513/2002/1, 286 pp.

Maier, W.D. & Barnes, S.J., 2004. Pt/Pd and Pd/Ir ratios in mantle-derived magmas: A possible role for mantle metasomatism. South African Journal of Geology, 107 (3), 333–340. DOI: 10.2113/107.3.333.

Maier, W.D., Barnes, S.J., Campbell, I.H., Fiorentini, M.L., Peltonen, P., Barnes, S.J., & Smithies, R.H., 2009. Progressive mixing of meteoritic veneer into the early Earths deep mantle. Nature, 460 (7255), 620–623. DOI: 10.1038/nature08205.

Maier, W.D., Peltonen, P., Halkoaho, T., & Hanski, E., 2013. Geochemistry of komatiites from the Tipasjärvi, Kuhmo, Suomussalmi, Ilomantsi and Tulppio greenstone belts, Finland: Implications for tectonic setting and Ni sulphide prospectivity. Precambrian Research, 228, 63–84. DOI: 10.1016/j.precamres.2012.12.004.

Makkonen, H.V. & Halkoaho, T., 2007. Whole rock analytical data (XRF, REE, PGE) for several Svecofennian (1.9 Ga) and Archaean (2.8 Ga) nickel deposits in eastern Finland. Geological Survey of Finland, report M19/3241/2007/32, 53 pp.

Makkonen, H. V., Halkoaho, T., Konnunaho, J., Rasilainen, K., Kontinen, A., & Eilu, P., 2017. Ni-(Cu-PGE) deposits in Finland – Geology and exploration potential. Ore Geology Reviews, 90, 667–696. DOI: 10.1016/j.oregeorev.2017.06.008.

Mancini, F. & Papunen, H., 1998. Metamorphism of Ni-Cu Sulfides in Mafic-Ultramafic Intrusions: The Svecofennian Sääksjärvi Complex, Southern Finland. Reviews in Economic Geology, 11, 1–14.

Mänttäri, I. & Hölttä, P., 2002. U-Pb dating of zircons and monazites from Archean granulites in Varpaisjärvi, central Finland: Evidence for multiple metamorphism and Neoarchean terrane accretion. Precambrian Research, 118 (1–2), 101–131. DOI: 10.1016/S0301-9268(02)00094-3.

Marshall, B. & Gilligan, L.B., 1987. An introduction to remobilization: Information from ore-body geometry and experimental considerations. Ore Geology Reviews, 2 (1–3), 87–131. DOI: 10.1016/0169-1368(87)90025-4.

Marshall, B. & Gilligan, L.B., 1993. Remobilization, syn-tectonic processes and massive sulphide deposits. Ore Geology Reviews, 8 (1–2), 39–64. DOI: 10.1016/0169-1368(93)90027-V.

Marshall, B., Vokes, F., & Larocque, A., 1998. Regional metamorphic remobilization: upgrading and formation of ore deposits. Reviews in Economic Geology, 11 (1), 19–38.

McDonald, J.A. & Paterson, M.S., 1980. Experimental deformation of nickel sulfide ores and their host rocks, Lunnon Shoot, Karnbalda, Western Australia. Unpublished Report, Australian National University, Canberra, A.C.T., 46 pp.

McQueen, K.G., 1987. Deformation and remobilization in some Western Australian nickel ores. Ore Geology Reviews, 2 (1–3), 269–286. DOI: 10.1016/0169-1368(87)90032-1.

McQueen, K.G., 2005. Ore deposit types and their primary expressions. In: Butt, C.R.M., Cornelius, M., Scott, K.M., & Robertson, I.D.M., Regolith Expression of Australian Ore Systems, 1–14.

Mei, Y., Sherman, D.M., Liu, W., Etschmann, B., Testemale, D., & Brugger, J., 2015. Zinc complexation in chloride-rich hydrothermal fluids (25-600°C): A thermodynamic model derived from ab initio molecular dynamics. Geochimica et Cosmochimica Acta, 150, 265–284. DOI: 10.1016/j.gca.2014.09.023.

Molnár, F., Watkinson, D.H., Jones, P.C., & Gatter, I., 1997. Fluid inclusion evidence for hydrothermal enrichment of magmatic ore at the contact zone of the Ni-Cu-platinum-group element 4b Deposit, Lindsley Mine, Sudbury, Canada. Economic Geology, 92 (6), 674–685.

Molnár, F., Watkinson, D.H., & Jones, P.C., 2001. Multiple hydrothermal processes in footwall units of the North Range, Sudbury Igneous Complex, Canada, and implications for the genesis of vein-type Cu-Ni-PGE deposits. Economic Geology, 96 (7), 1645–1670. DOI: 10.2113/gsecongeo.96.7.1645.

Mookherjee, J.B., 1976. Ores and metamorphism: Temporal and genetic relationships. In: Wolf, K.H. (ed.), Handbook of stratabound and stratiform ore deposits, volume 4. 203–260.

Morton-Thompson, D. & Woods, A.M. (eds.), 1992. Development Geology Reference Manual. American Association of Petroleum Geologists, 550 pp.

Mukwakwami, J., 2012. Structural control of Ni-Cu-PGE ores and mobilization of metals at the Garson mine, Sudbury. PhD Thesis, Laurentian University, Sudbury, Ontario, 246 pp.

Mukwakwami, J., Lafrance, B., Lesher, C.M., Tinkham, D.K., Rayner, N.M., & Ames, D.E., 2014. Deformation, metamorphism, and mobilization of Ni-Cu-PGE sulfide ores at

Garson Mine, Sudbury. Mineralium Deposita, 49 (2), 175–198. DOI: 10.1007/s00126-013-0479-y.

Mutanen, T. & Huhma, H., 2003. The 3.5 Ga Siurua trondhjemite gneiss in the Archaean Pudasjärvi Granulite Belt, northern Finland. Bulletin of the Geological Society of Finland, 75 (1–2), 51–68. DOI: 10.17741/bgsf/75.1-2.004.

Naldrett, A.J., 2004. Magmatic Sulfide Deposits: Geology, Geochemistry and Exploration. Springer, New York. 730 pp.

Nesbitt, R.W., Sun, S.-S., & Purvis, A.C., 1979. Komatiites: Geochemistry and genesis. Canadian Mineralogist, 17, 165–186.

Nyman, M.W., Sheets, R.W., Bodnar, R.J., & A, U.S., 1990. Fluid-inclusion evidence for the physical and chemical conditions associated with intermediate-temperature PGE mineralization at the New Rambler deposit, Southeastern Wyoming. Canadian Mineralogist, 28, 629–638.

Papunen, H., Halkoaho, T., & Luukkonen, E., 2009. Archaean evolution of the Tipasjärvi-Kuhmo-Suomussalmi greenstone complex, Finland. Geological Survey of Finland, Bulletin 403, 68 pp.

Parman, S.W., Grove, T.L., Dann, J.C., & de Wit, M.J., 2004. A subduction origin for komatiites and cratonic lithospheric mantle. South African Journal of Geology, 107 (1–2), 107–118. DOI: 10.2113/107.1-2.107.

Pesquera, A. & Velasco, F., 1993. Ore metamorphism in sulfide mineralizations from the Cinco Villas Massif (Western Pyrenees, Spain). Economic Geology, 88 (2), 266–282. DOI: 10.2113/gsecongeo.88.2.266.

Piirainen, T., 1988. The geology of the Archaean greenstone–granitoid terrain in Kuhmo, eastern Finland. In: Archaean geology of the Fennoscandian Shield. Geological Survey of Finland, Special Paper 4. 39–51.

Pokrovski, G.S., Kara, S., & Roux, J., 2002. Stability and solubility of arsenopyrite, FeAsS, in crustal fluids. Geochimica et Cosmochimica Acta, 66 (13), 2361–2378. DOI: 10.1016/S0016-7037(02)00836-0.

Puustinen, K., Saltikoff, B., & Tontti, M., 1995. Distribution and metallogenic types of nickel deposits in Finland. Geological Survey of Finland, Report of Investigation 132, 38 pp.

Ranta, J.P., Lauri, L.S., Hanski, E., Huhma, H., Lahaye, Y., & Vanhanen, E., 2015. U-Pb and Sm-Nd isotopic constraints on the evolution of the Paleoproterozoic Peräpohja Belt, northern Finland. Precambrian Research, 266, 246–259. DOI: 10.1016/j.precamres.2015.05.018.

Ripley, E.M., Sarkar, A., & Li, C., 2005. Mineralogic and stable isotope studies of hydrothermal alteration at the Jinchuan Ni-Cu deposit, China. Economic Geology, 100 (7), 1349–1361. DOI: 10.2113/gsecongeo.100.7.1349.

Scharrer, M., Kreissl, S., & Markl, G., 2019. The mineralogical variability of hydrothermal native element-arsenide (five-element) associations and the role of physicochemical and kinetic factors concerning sulfur and arsenic. Ore Geology Reviews, 113, 103025. DOI: 10.1016/j.oregeorev.2019.103025.

Seequent Limited, 2019. User Manual for Leapfrog Geo version 5.0, 795 pp.

Slabunov, A.I., Lobach-Zhuchenko, S.B., Bibikova, E. V., Sorjonen-Ward, P., Balagansky, V.V., Volodichev, O.I., Shchipansky, A.A., Svetov, S.A., Chekulaev, V.P., Arestova, N.A., & Stepanov, V.S., 2006. The Archaean nucleus of the Fennoscandian (Baltic) Shield. Geological Society, London, Memoirs, 32, 627–644. DOI: 10.1144/GSL.MEM.2006.035.01.37.

Sorjonen-Ward, P. & Luukkonen, E., 2005. Archean rocks. In: Lehtinen, M., Nurmi, P.A., Rämö, O.T. (eds.), Precambrian Geology of Finland – Key to the Evolution of the Fennoscandian Shield. Elsevier B.V., Amsterdam, 19–99.

Sossi, P.A., Eggins, S.M., Nesbitt, R.W., Nebel, O., Hergt, J.M., Campbell, I.H., O'Neill, H.S.C., Van Kranendonk, M., & Davies, D.H., 2016. Petrogenesis and Geochemistry of Archean Komatiites. Journal of Petrology, 57 (1), 147–184. DOI: 10.1093/petrology/egw004.

Sossi, P.A., Nebel, O., O'Neill, H.S.C., & Moynier, F., 2018. Zinc isotope composition of the Earth and its behaviour during planetary accretion. Chemical Geology, 477, 73–84. DOI: 10.1016/j.chemgeo.2017.12.006.

Spry, P.G., 1998. Sulfidation and Oxidation Haloes as Guides in the Exploration for Metamorphosed Massive Sulfide Ores. Reviews in Economic Geology, 11, 153–166.

Stone, W.E., Beresford, S.W., & Archibald, N.J., 2005. Structural setting and shape analysis of nickel sulfide shoots at the Kambalda dome, Western Australia: Implications for deformation and remobilization. Economic Geology, 100 (7), 1441–1455. DOI: 10.2113/gsecongeo.100.7.1441.

Tao, Z., Liu, B., Guo, K., Guo, N., Li, C., Xia, Y., & Luo, Y., 2021. 3D Primary Geochemical Halo Modeling and Its Application to the Ore Prediction of the Jiama Polymetallic Deposit, Tibet, China. Geofluids, 2021, 13 pp. DOI: 10.1155/2021/6629187.

Tikoff, B. & Greene, D., 1997. Stretching lineations in transpressional shear zones: an example from the Sierra Nevada Batholith, California. Journal of Structural Geology. 19 (1), 29-39.

Tomkins, A.G., Pattison, D.R.M., & Frost, B.R., 2007. On the initiation of metamorphic sulfide anatexis. Journal of Petrology, 48 (3), 511–535. DOI: 10.1093/petrology/egl070.

Tuba, G., Molnár, F., Ames, D.E., Péntek, A., Watkinson, D.H., & Jones, P.C., 2014. Multi-stage hydrothermal processes involved in 'low-sulfide' Cu(-Ni)-PGE mineralization in the footwall of the Sudbury Igneous Complex (Canada): Amy Lake PGE zone, East Range. Mineralium Deposita, 49 (1), 7–47. DOI: 10.1007/s00126-013-0468-1.

Tuisku, P., 1988. Geothermobarometry in the Archaean Kuhmo-Suomussalmi greenstone belt, Eastern Finland. Geological Survey of Finland, Special Paper 4, 171–172.

U.S. Geological Survey, 2001. Mineral Commodity Summaries 2001. U.S. Geological Survey, 192 pp.

U.S. Geological Survey, 2021. Mineral Commodity Summaries 2021. U.S. Geological Survey, 200 pp. DOI: https://doi.org/10.3133/mcs2021.

Le Vaillant, M., 2014. Hydrothermal Remobilisation of Base Metals and Platinum Group Elements Around Komatiite-Hosted Nickel-Sulphide Deposits: Applications To Exploration Methods. PhD Thesis, The University of Western Australia, 642 pp.

Le Vaillant, M., Barnes, S.J., Fiorentini, M.L., Miller, J., McCuaig, T.C., & Mucilli, P., 2015. A hydrothermal Ni-As-PGE geochemical halo around the Miitel komatiite-hosted nickel sulfide deposit, Yilgarn craton, Western Australia. Economic Geology, 110 (2), 505–530. DOI: 10.2113/econgeo.110.2.505.

Le Vaillant, M., Barnes, S.J., Fiorentini, M.L., Santaguida, F., & Törmänen, T., 2016a. Effects of hydrous alteration on the distribution of base metals and platinum group elements within the Kevitsa magmatic nickel sulphide deposit. Ore Geology Reviews, 72, 128–148. DOI: 10.1016/j.oregeorev.2015.06.002.

Le Vaillant, M., Saleem, A., Barnes, S.J., Fiorentini, M.L., Miller, J., et al., 2016b. Hydrothermal remobilisation around a deformed and remobilised komatiite-hosted Ni-Cu-(PGE) deposit, Sarah's Find, Agnew Wiluna greenstone belt, Yilgarn Craton, Western Australia. Mineralium Deposita, 51 (3), 369–388. DOI: 10.1007/s00126-015-0610-3.

Le Vaillant, M., Fiorentini, M.L., & Barnes, S.J., 2016c. Review of lithogeochemical exploration tools for komatiite-hosted Ni-Cu-(PGE) deposits. Journal of Geochemical Exploration, 168, 1–19. DOI: 10.1016/j.gexplo.2016.05.010.

Le Vaillant, M., Fiorentini, M.L., & Barnes, S.J., 2017. Review of predictive and detective exploration tools for magmatic Ni-Cu-(PGE) deposits, with a focus on komatiite-related systems in Western Australia. In: Mondal, S.K. & Griffin, W.L. (eds.), Processes and Ore Deposits of Ultramafic-Mafic Magmas through Space and Time. Elsevier Inc., 47–78. DOI: 10.1016/B978-0-12-811159-8.00003-2.

Viljoen, M. & Viljoen, R., 1969. The geology and geochemistry of the lower ultramafic unit of the Onverwacht group and a proposed new class of igneous rocks. Geological Society of South Africa, Special Publication 2, 55–86.

Vuollo, J. & Huhma, H., 2005. Paleoproterozoic mafic dikes in NE Finland. In: Lehtinen, M., Nurmi, P.A., Rämö, O.T. (eds.), Precambrian Geology of Finland – Key to the Evolution of the Fennoscandian Shield. Elsevier B.V., Amsterdam, 195–236.

Wang, C., Carranza, E.J.M., Zhang, S., Zhang, J., Liu, X., Zhang, D., Sun, X., & Duan, C., 2013. Characterization of primary geochemical haloes for gold exploration at the Huanxiangwa gold deposit, China. Journal of Geochemical Exploration, 124, 40–58. DOI: 10.1016/j.gexplo.2012.07.011.

Watari, T., Nansai, K., & Nakajima, K., 2021. Major metals demand, supply, and environmental impacts to 2100: A critical review. Resources, Conservation and Recycling, 164, 105107. DOI: 10.1016/j.resconrec.2020.105107.

Whitney, D.L. & Evans, B.W., 2010. Abbreviations for names of rock-forming minerals. American Mineralogist, 95 (1), 185–187. DOI: 10.2138/am.2010.3371.

Williams, D.A., Kerr, R.C., & Lesher, C.M., 1998. Emplacement and erosion by Archean komatiite lava flows at Kambalda: Revisited. Journal of Geophysical Research: Solid Earth, 103 (B11), 27533–27549. DOI: 10.1029/97jb03538.

De Wit, M.J., 1998. On Archean granites, greenstones, cratons and tectonics: does the evidence demand a verdict? Precambrian Research, 91 (1–2), 181–226. DOI: 10.1016/S0301-9268(98)00043-6.

Wood, S.A., 2002. The aqueous geochemistry of the platinum-group elements with applications to ore deposits. In: Cabri, L., ed., The geology, geochemistry, mineralogy, mineral beneficiation of the platinum-group elements. Canadian Institute of Mining and Metallurgy, Special Publication 54, 211–249.

Yardley, B.W., 2005. 100th Anniversary Special Paper: Metal concentrations in crustal fluids and their relationship to ore formation. Economic Geology, 100 (4), 613–632.

Appendixes

The Leapfrog Geo 3D-model and the polished thin sections are stored at GTK's office in Kuopio (Viestikatu 7 A, PL 1237, 70211 Kuopio, Finland). The refined drill core log is shown in Appendix 1, the XRF analysis data in Appendixes 2.1–2.6, and the weak leach analysis data in Appendix 3.

Appendix 1. Refined drill core log

HoleID	From (m)	To (m)	Lithology	Alpha angle	Colour	Analysis	Thin section
R306	0	1.5	Soil				
R306	1.5	34.1	Intermediate – felsic volcanic rock	40-50	Light-gray, greenish	x	x
R306	34.1	42.2	Tholeiitic basalt	40	Green, grayish	x	x
R306	42.2	60.3	Komatiite	50	Light-gray, greenish	x	x
R307	0	4	Soil				
R307	4	7.5	Intermediate – felsic volcanic rock	45	Light-gray, greenish		
R307	7.5	23	Tholeiitic basalt	45-55	Green-gray	x	x
R307	23	51	Komatiite	60	Light-gray, greenish		
R310	0	4.5	Soil				
R310	4.5	16.6	Komatiite	25	Light-gray, greenish	x	x
R310	16.6	30	Komatiite	40	Light-gray, greenish		
R310	30	35.25	Tholeiitic basalt	35	Greenish gray, dark		
R310	35.25	43.4	Tholeiitic basalt	40	Greenish gray, dark		
R310	43.4	69.7	Intermediate – felsic volcanic rock	55	Light-gray, some dark	x	x
R310	69.7	107.9	Black schist	35	Dark-gray	x	x
R310	107.9	114.2	Intermediate – felsic volcanic rock	45	Greenish gray, reddish		
R310	114.2	135.9	Komatiite		Light-gray, greenish	x	x
R319	0	4	Soil				
R319	4	15.45	Komatiite		Light-gray, greenish		
R319	15.45	16.3	Tholeiitic basalt		Green-gray		
R319	16.3	17.3	Intermediate – felsic volcanic rock		Light-gray		
R319	17.3	31.2	Tholeiitic basalt	50	Green-gray		
R319	31.2	44.6	Tholeiitic basalt	50	Greenish gray		
R319	44.6	54.9	Intermediate – felsic volcanic rock	60	Light-gray, greenish		
R319	54.9	70.1	Black schist	50	Dark-gray		
R320	0	6.6	Soil				
R320	6.6	10.7	Intermediate – felsic volcanic rock	60	Light-gray, greenish		
R320	10.7	31.7	Komatiite	50	Light-green	x	
R320	31.7	39.4	Tholeiitic basalt	60	Green, grayish		
R320	39.4	73.2	Black schist	50-60	Dark gray	x	x
R336	0	7.9	Soil				
R336	7.9	72.8	Intermediate volcanic conglomerate	60	White-gray, greenish	xxx	xx
R336	72.8	83.4	Komatiite		White-gray, greenish		
R336	83.4	85.2	Intermediate – felsic volcanic rock		Light-gray		
R336	85.2	87.9	Tholeiitic basalt	60	Light-gray, greenish		
R336	87.9	96.6	Komatiitic basalt	65	Greenish gray		
R336	96.6	123	Komatiitic basalt	55	Light-gray, greenish	xx	xx
R336	123	127.9	Black schist		Dark gray		
R345	0	13.6	Soil				

HoleID	From (m)	To (m)	Lithology	Alpha angle	Colour	Analysis	Thin section
R345	13.6	20.6	Intermediate – felsic volcanic rock	40	Light-gray		
R345	20.6	57.7	Komatiite	35	Gray, greenish, white spots	x	
R345	57.7	67.2	Intermediate – felsic volcanic rock	40	Ligh-gray, green increases w/ depth		
R345	67.2	68	Black schist		Dark gray		
R345	68	106.1	Tholeiitic basalt	45	Green, grayish	xx	x
R345	106.1	107.9	Black schist	50	Dark gray		
R346	0	7.1	Soil				
R346	7.1	67	Intermediate volcanic conglomerate	30 -> 50	Green-gray, white kong		
R346	67	70.4	Intermediate – felsic volcanic rock		Light-gray		x
R346	70.4	86.8	Komatiite	30-40	Light-green	x	x
R346	86.8	92.1	Tholeiitic basalt	55	Light-gray to green		
R346	92.1	93.2	Intermediate – felsic volcanic rock				
R346	93.2	100.7	Tholeiitic basalt	55	Light-gray to green	x	x
R346	100.7	110.2	Tholeiitic basalt	60-80	Gray-green		
R346	110.2	113.2	Black schist	60	Dark gray		
R352	0	8	Soil				
R352	8	14.5	Intermediate – felsic volcanic rock	40	Light-gray, rusting		
R352	14.5	22.2	Black schist	50	Dark gray	x	
R352	22.2	24.95	Tholeiitic basalt	70	Light-gray, greenish		
R352	24.95	48.6	Komatiite	30-50	Gray, greenish		
R352	48.6	50	Intermediate – felsic volcanic rock	35	Light-gray		
R352	50	71.3	Tholeiitic basalt	45	Green, grayish	x	x
R355	0	2	Soil				
R355	2	55.4	Intermediate volcanic conglomerate	35	Green, grayish, white kong		
R355	55.4	92.5	Intermediate lapilli tuff	30	Gray, greenish		
R355	92.5	94.9	Intermediate volcanic conglomerate		Green, grayish, white kong		
R355	94.9	121.1	Intermediate lapilli tuff	25	Gray, greenish	x	x
R355	121.1	137.8	Intermediate volcanic conglomerate	30	Green, grayish, white kong		
R355	137.8	146	Intermediate lapilli tuff	35	Gray, greenish		
R355	146	147.4	Intermediate lapilli tuff	30	Light-gray, green, white		
R355	147.4	163.4	Komatiite	40	Gray, greenish	x	
R355	163.4	167.5	Intermediate – felsic volcanic rock		Light-gray, greenish	x	x
R355	167.5	184.7	Komatiitic basalt	45	Green, grayish		
R355	184.7	189.9	Komatiitic basalt	40	Green, grayish	x	x
R372	0	1.2	Soil				
R372	1.2	30.35	Intermediate – felsic volcanic rock	35	Light-gray, greenish	x	x
R372	30.35	35.7	Intermediate volcanic conglomerate	30	Gray-green + white		
R372	35.7	57.7	Intermediate – felsic volcanic rock	35	Light-gray, greenish		
R372	57.7	63	Intermediate volcanic conglomerate	35	Gray-green + white		
R372	63	88	Intermediate – felsic volcanic rock	40	Gray, greenish		
R372	88	94.7	Intermediate volcanic conglomerate	40	Gray-green + white		
R372	94.7	106.9	Intermediate – felsic volcanic rock	40	Gray, greenish	x	x
R372	106.9	121.15	Quartz porphyry	40			
R372	121.15	132.45	Black schist	45	Dark gray/black	x	x

HoleID	From (m)	To (m)	Lithology	Alpha angle	Colour	Analysis	Thin section
R372	132.45	134.55	Intermediate – felsic volcanic rock	50	Light-green + white		
R372	134.55	162.1	Komatiite	40	Light-gray, greenish		
R372	162.1	174.75	Intermediate – felsic volcanic rock	45	Gray, greenish		
R372	174.75	175.8	Black schist	40	Green, black, gray		
R372	175.8	192.1	Komatiitic basalt	50	Light/dark-green, black, grey, white	x	x
R372	192.1	192.25	Black schist	45	Dark gray black		
R372	192.25	193.1	Komatiitic basalt	50	Light/dark-green, black, grey, white		
R373	0	1.2	Soil				
R373	1.2	51	Intermediate – felsic volcanic rock	40	Light-gray, greenish	x	x
R373	51	61.6	Tholeiitic basalt	35	Green, grayish		
R373	61.6	65.2	Intermediate – felsic volcanic rock	40	Light-gray		
R373	65.2	69	Tholeiitic basalt	35	Green, grayish, white layers		
R373	69	96	Intermediate volcanic conglomerate	40	Green + gray-white		
R373	96	159.5	Intermediate lapilli tuff	50	Green + gray-white	x	
R373	159.5	163.3	Intermediate volcanic conglomerate	50	Green + gray-white		
R373	163.3	206.2	Intermediate lapilli tuff	45-50	Green + gray-white	x	x
R373	206.2	223.7	Quartz porphyry		Light-gray	x	x
R373	223.7	245.4	Komatiite	45	Light-gray, greenish		
R373	245.4	263.85	Komatiitic basalt	50	Green + gray-white		
R373	263.85	271.5	Komatiitic basalt	50	Green, white		x
R375	0	3.1	Soil				
R375	3.1	23.45	Intermediate – felsic volcanic rock	30	Light-gray, greenish	x	x
R375	23.45	49.5	Intermediate – felsic volcanic rock	30	Green, grayish	x	x
R375	49.5	77.3	Tholeiitic basalt		Varying shades of green	x	
R375	77.3	79.3	Intermediate – felsic volcanic rock		Gray, greenish		
R375	79.3	84.7	Tholeiitic basalt		Varying shades of green		
R375	84.7	123.5	Intermediate volcanic conglomerate	30	Green + gray-white	x	x
R375	123.5	149.75	Intermediate lapilli tuff	30	Green + gray-white	x	x
R375	149.75	178.3	Intermediate volcanic conglomerate	40	Green + gray-white		
R375	178.3	208.25	Intermediate – felsic volcanic rock	40	Green + gray-white	x	
R375	208.25	209	Intermediate – felsic volcanic rock	40	Light-green + white		
R375	209	236	Komatiite	40	Gray, greenish	x	x
R375	236	249.6	Intermediate – felsic volcanic rock	50	Green, grayish	x	x
R375	249.6	272.7	Komatiitic basalt	50	Green, grayish	x	x
R375	272.7	273.35	Intermediate – felsic volcanic rock	40	Light-gray		
R375	273.35	277	Komatiitic basalt	50	Green, grayish		
R375	277	278	Black schist	45	Dark-gray, black + white		
R375	278	279.1	Intermediate – felsic volcanic rock				
R375	279.1	284.2	Black schist	45	Dark-gray, black + white		

Appendix 2.1. XRF analysis data of Ba, Ce, Cr, Cs, Dy, Er, Eu, Ga, Gd, & Hf

Sample ID	Lithology	Ba	Ce	Cr	Cs	Dy	Er	Eu	Ga	Gd	Hf
		ppm	ppm	ppm	ppm	ppm	ppm	ppm	ppm	ppm	ppm
M52442194R306 35.60-36.10	Tholeiitic basalt	4.6	5.5	130	0.68	3.1	2.14	0.54	6	2.33	0.5
4421/96/R336/89.20-89.50	Undef. Mineralisation	424	29.6	92	n.a.	3.03	1.81	0.86	10	3.79	3.45
4421/95/R310/39.80-40.00	Undef. Mineralisation	406	1.88	2869	n.a.	1.33	0.82	0.33	10	1.14	0.9
4421/96/R346/106.90-107.20	Undef. Mineralisation	472	12.5	3329	n.a.	1.82	1.12	0.42	21	1.65	1.15
4421/96/R336/96.25-96.55	Undef. Mineralisation	650	1.87	3446	n.a.	2.18	1.12	0.27	10	1.49	0.92
4421/96/R346/109.60-109.90	Undef. Mineralisation	214	3.97	2148	n.a.	2.15	1.35	0.34	10	1.56	0.69
4421/95/R310/42.40-42.70	Undef. Mineralisation	416	3.63	3346	n.a.	1.69	0.93	0.35	21	1.39	0.99
4421/95/R319/37.00-37.30	Undef. Mineralisation	141	4.32	2184	n.a.	2.54	1.49	0.48	20	2.16	0.81
4421/95/R319/39.10-39.35	Undef. Mineralisation	261	2.54	2548	n.a.	2.17	1.41	0.45	10	1.87	0.94
4421/95/R319/34.20-34.50	Undef. Mineralisation	308	2.27	3062	n.a.	1.85	0.98	0.4	10	1.36	0.95
4421/96/R336/91.20-91.60	Undef. Mineralisation	351	4.53	2984	n.a.	3.14	1.83	0.49	10	2.4	1.11
M52442196R375 246.40-246.90	Int.–fel. volcanic rock	705	23.4	110	2.43	1.63	1.02	0.65	13.4	2.24	2.8
4421/95/R310/35.50-35.80	Undef. Mineralisation	353	5.07	2271	n.a.	2.22	1.43	0.4	10	2.21	0.75
M52442195R307 22.05-22.70	Tholeiitic basalt	2	5.9	230	0.16	2.38	1.56	0.56	12.4	2.14	1.4
M52442196R352 58.00-58.60	Tholeiitic basalt	1.7	3.2	790	0.08	2.46	1.65	0.49	5.6	1.93	0.4
4421/96/R346/100.70-101.00	Undef. Mineralisation	449	32.8	235	n.a.	3.7	2.38	1.24	22	4.81	4
M52442196R345 38.50-38.90	Komatiite	1.1	0.7	1730	0.11	0.51	0.32	0.22	3.6	0.57	0.3
EJL-95-R319/10.10-10.20	Komatiite	20	14	1853	n.a.	n.a.	n.a.	n.a.	9	n.a.	n.a.
M52442196R375 229.40-229.75	Komatiite	0.7	0.7	2080	0.14	0.83	0.52	0.11	5.4	0.69	0.4
EJL-95-R310/131.70	Komatiite	24	15	2572	n.a.	n.a.	n.a.	n.a.	12	n.a.	n.a.
EJL-95-R310/114.80	Komatiite	21	10	3032	n.a.	n.a.	n.a.	n.a.	8	n.a.	n.a.
R354-196.10-196.70	Komatiite	25	11	1979	n.a.	n.a.	n.a.	n.a.	12	n.a.	n.a.
M52442195R310 12.50-12.80	Komatiite	0.7	1.6	2290	0.2	2.9	1.84	0.16	7.3	1.92	0.6
EJL-95-R315/9	Komatiite	23	15	3068	n.a.	n.a.	n.a.	n.a.	13	n.a.	n.a.
M52442195R310 132.50-132.80	Komatiite	3.1	1.7	2800	0.23	1.29	0.83	0.25	7	1.11	0.6
M52442196R346 84.70-85.20	Komatiite	0.6	1.3	2120	0.19	1.45	0.97	0.19	7.1	1.24	0.6
EJL-95-R318/7.60-7.80	Komatiite	19	16	2366	n.a.	n.a.	n.a.	n.a.	10	n.a.	n.a.
EJL-95-R309/18.40	Komatiite	25	8	1995	n.a.	n.a.	n.a.	n.a.	15	n.a.	n.a.
EJL-95-R310/122.80	Komatiite	24	15	2729	n.a.	n.a.	n.a.	n.a.	12	n.a.	n.a.
M52442195R320 18.25-18.60	Komatiite	0.6	2.4	1640	0.11	1.49	0.86	0.69	6	1.35	0.5
EJL-95-R323/7.85-8.05	Komatiite	23	4	2337	n.a.	n.a.	n.a.	n.a.	6	n.a.	n.a.
EJL-95-R315/51.30	Komatiite	31	1	2605	n.a.	n.a.	n.a.	n.a.	12	n.a.	n.a.
R351-95.20-95.40	Komatiite	22	20	1837	n.a.	n.a.	n.a.	n.a.	8	n.a.	n.a.
M52442194R306 59.80-60.30	Komatiite	0.25	1	2070	0.14	1.2	0.84	0.21	7.2	0.87	0.5
EJL-95-R315/20.50	Komatiite	26	17	2554	n.a.	n.a.	n.a.	n.a.	13	n.a.	n.a.
R352-31.10-31.40	Komatiite	19	14	2043	n.a.	n.a.	n.a.	n.a.	18	n.a.	n.a.
M52442196R355 155.75-156.10	Komatiite	1.4	5.3	2080	0.15	2.37	1.44	0.3	8.4	2.32	0.7
EJL-95-R309/110.75	Komatiite	28	12	2243	n.a.	n.a.	n.a.	n.a.	10	n.a.	n.a.
R351-73.10-73.30	Komatiite	23	15	2000	n.a.	n.a.	n.a.	n.a.	12	n.a.	n.a.
R349-26.70-26.90	Komatiite	22	19	2145	n.a.	n.a.	n.a.	n.a.	15	n.a.	n.a.
M52442196R375 267.45-267.85	Komatiitic basalt	54.2	1.3	1820	0.11	1.41	0.81	0.45	8.1	1.35	0.6
M52442196R346 94.95-95.50	Komatiitic basalt	2.7	1.5	2630	0.3	1.93	1.23	0.23	10.2	1.61	0.8
R352-25.15-25.55	Komatiite	18	19	1745	n.a.	n.a.	n.a.	n.a.	16	n.a.	n.a.
M52442196R336 120.70-121.10	Komatiitic basalt	1.3	2.2	2040	0.04	1.61	1.04	0.32	8.1	1.46	0.7
EJL-95-R320/20.50-20.80	Komatiite	22	14	1656	n.a.	n.a.	n.a.	n.a.	11	n.a.	n.a.
EJL-95-R317/13.55-13.70	Komatiite	34	8	1945	n.a.	n.a.	n.a.	n.a.	17	n.a.	n.a.
EJL-95-R315/21.30-21.60	Tholeiitic basalt	701	0	1236	n.a.	n.a.	n.a.	n.a.	23	n.a.	n.a.
EJL-95-R314/43.00-43.20	Tholeiitic basalt	25	12	558	n.a.	n.a.	n.a.	n.a.	20	n.a.	n.a.
EJL-95-R311/29.70-29.95	Tholeiitic basalt	177	14	1175	n.a.	n.a.	n.a.	n.a.	19	n.a.	n.a.
EJL-95-R311/37.05-37.30	Tholeiitic basalt	498	12	1318	n.a.	n.a.	n.a.	n.a.	24	n.a.	n.a.
EJL-95-R317/40.10-40.30	Komatiite	33	5	1431	n.a.	n.a.	n.a.	n.a.	16	n.a.	n.a.
M52442196R355 189.25-189.65	Komatiitic basalt	87.6	3.7	1820	0.44	2.34	1.48	0.4	10.1	1.82	1
M52442196R345 73.40-74.05	Tholeiitic basalt	103.5	5	960	0.71	3.23	2.08	0.46	12.8	2.51	1.3
M52442196R372 180.35-180.80	Komatiitic basalt	729	12	1670	2.86	1.87	1.06	0.88	10.8	2.67	0.9
EJL-95-R309/120.45	Komatiitic basalt	306	14	1649	n.a.	n.a.	n.a.	n.a.	15	n.a.	n.a.
M52442196R345 102.30-102.70	Tholeiitic basalt	171.5	4.2	1510	0.53	2.94	2.01	0.45	10.4	2.14	1
EJL-95-R318/26.30-26.50	Komatiite	18	18	1071	n.a.	n.a.	n.a.	n.a.	20	n.a.	n.a.
M52442196R375 147.70-148.05	Int. lapilli tuff	286	32	730	2.17	2.8	1.56	0.93	13.9	3.14	2.6
M52442196R336 70.30-70.80	Int. volc. congl.	4.6	34.1	590	0.16	3.42	2	1.23	14.6	3.58	2.8
M52442196R375 123.00-123.35	Int. volc. congl.	288	19.7	700	2.97	2.74	1.73	0.71	13.6	2.66	2.2
EJL-95-R308/12.30-12.60	Int.–fel. volcanic rock	324	12	525	n.a.	n.a.	n.a.	n.a.	19	n.a.	n.a.
M52442196R336 9.95-10.25	Int. volc. congl.	428	27	650	3.94	3.43	2.03	0.85	18.1	3.52	2.8
M52442196R373 99.90-100.35	Int. lapilli tuff	315	36.2	600	3.6	3.67	2.2	1.17	14.1	4.09	3.3
M52442196R375 198.60-199.00	Int.–fel. volcanic rock	368	28.1	630	2.27	2.34	1.38	0.74	14	2.59	2.5
M52442196R373 199.10-199.40	Int. lapilli tuff	453	29.7	580	3.6	3.09	1.84	0.89	13.4	3.46	2.8
M52442196R372 20.30-20.65	Int.–fel. volcanic rock	418	32.7	600	4.28	3.44	2.16	1.05	14.8	3.71	3.2
M52442196R355 100.90-101.20	Int. lapilli tuff	517	31.2	530	4.5	3.03	1.8	0.9	14.7	3.37	3.1
M52442196R336 40.90-41.25	Int. volc. congl.	323	33.4	510	2.87	3.15	1.92	0.91	14.7	3.5	3.1
EJL-95-R316/36.40-36.60	Tholeiitic basalt	36	5	395	n.a.	n.a.	n.a.	n.a.	16	n.a.	n.a.
M52442195R310 51.00-51.65	Tholeiitic basalt	179.5	6.9	420	1.26	2.59	1.69	0.61	12.8	2.47	1.2
EJL-95-R312/17.45-17.75	Int.–fel. volcanic rock	579	16	440	n.a.	n.a.	n.a.	n.a.	26	n.a.	n.a.

Sample ID	Lithology	Ba	Ce	Cr	Cs	Dy	Er	Eu	Ga	Gd	Hf
		ppm	ppm	ppm	ppm	ppm	ppm	ppm	ppm	ppm	ppm
EJL-95-R320/57.50-57.70	Black schist	658	8	290	n.a.	n.a.	n.a.	n.a.	29	n.a.	n.a.
M52442195R320 72.40-72.85	Black schist	166	17.2	260	0.86	1.93	1.16	0.61	11.1	2.13	2.2
EJL-95-R320/7.60-7.90	Tholeiitic basalt	27	15	110	n.a.	n.a.	n.a.	n.a.	26	n.a.	n.a.
M52442196R375 66.25-66.60	Int.–fel. volcanic rock	483	29.9	290	2.25	2.9	1.67	0.99	17.4	3.32	2.3
M52442196R372 99.50-99.80	Int.–fel. volcanic rock	602	29.5	400	3.88	2.96	1.89	0.78	14.2	2.94	2.9
EJL-95-R321/58.50-58.90	Black schist	718	37	357	n.a.	n.a.	n.a.	n.a.	27	n.a.	n.a.
M52442194R306 4.60-5.00	Int.–fel. volcanic rock	217	8.1	540	1.17	3.33	2.21	0.85	16.2	2.92	1.5
M52442196R336 102.40-102.90	Tholeiitic basalt	198	2.6	30	0.95	2.88	1.99	0.44	12.1	2.1	1.2
EJL-95-R309/50.55-50.79	Int.–fel. volcanic rock	510	18	310	n.a.	n.a.	n.a.	n.a.	21	n.a.	n.a.
M52442196R373 9.50-9.95	Int.–fel. volcanic rock	481	42.4	280	5.66	3.09	1.83	0.98	17	3.47	3.9
EJL-95-R323/32.10-32.30	Black schist	414	37	218	n.a.	n.a.	n.a.	n.a.	23	n.a.	n.a.
M52442196R375 40.35-40.65	Int.–fel. volcanic rock	402	35.1	280	3.39	2.72	1.67	0.86	15.3	3.29	3
EJL-95-R319/21.60-21.80	Tholeiitic basalt	25	16	297	n.a.	n.a.	n.a.	n.a.	27	n.a.	n.a.
M52442196R375 10.15-10.50	Int.–fel. volcanic rock	501	31.2	220	4.76	2.28	1.32	0.67	13.9	2.51	3
M52442196R372 129.30-129.65	Black schist	1035	36.7	130	5.34	2.35	1.38	0.61	22.5	2.82	4.4
EJL-95-R322/64.20-64.50	Black schist	456	34	421	n.a.	n.a.	n.a.	n.a.	27	n.a.	n.a.
M52442195R310 87.00-87.60	Black schist	490	39.6	90	2.33	2.36	1.36	0.8	17.7	2.94	3.3
EJL-95-R309/92.80	Black schist	603	47	234	n.a.	n.a.	n.a.	n.a.	26	n.a.	n.a.
EJL-95-R316/40.00-40.20	Komatiitic basalt	36	10	1054	n.a.	n.a.	n.a.	n.a.	13	n.a.	n.a.
M52442196R352 19.10-19.45	Black schist	750	16.8	60	3.47	1.52	0.92	0.41	14.5	1.76	3.1
EJL-95-R313/72.20	Quartz porphyry	1514	68	70	n.a.	n.a.	n.a.	n.a.	29	n.a.	n.a.
M52442196R355 166.50-167.00	Int.–fel. volcanic rock	1220	33.4	40	2.94	1.65	0.94	0.89	18.3	2.47	2.8
M52442196R373 221.90-222.30	Quartz porphyry	1495	47.7	40	4.44	1.14	0.44	0.84	19.3	2.47	3.6
EJL-95-R310/23.60-23.90	Quartz porphyry	3233	65	66	n.a.	n.a.	n.a.	n.a.	28	n.a.	n.a.
EJL-95-R315/65.80	Quartz porphyry	724	48	36	n.a.	n.a.	n.a.	n.a.	17	n.a.	n.a.
EJL-95-R320/44.80-45.10	Quartz porphyry	319	0	59	n.a.	n.a.	n.a.	n.a.	19	n.a.	n.a.
EJL-95-R323/13.10-13.30	Quartz porphyry	1067	0	32	n.a.	n.a.	n.a.	n.a.	19	n.a.	n.a.

Appendix 2.2. XRF analysis data of Ho, La, Lu, Nb, Nd, Pr, Rb, Sm, Sn, & Sr

Sample ID	Lithology	Ho	La	Lu	Nb	Nd	Pr	Rb	Sm	Sn	Sr
		ppm	ppm	ppm	ppm	ppm	ppm	ppm	ppm	ppm	ppm
M52442194R306 35.60-36.10	Tholeiitic basalt	0.69	2.1	0.35	0.7	4.1	0.83	1	1.42	0.5	111
4421/96/R336/89.20-89.50	Undef. Mineralisation	0.62	13.5	0.3	3.78	14.7	3.49	28.2	3.46	10	40
4421/95/R310/39.80-40.00	Undef. Mineralisation	0.27	0.8	0.11	0.7	1.47	0.27	52.7	0.62	10	111
4421/96/R346/106.90-107.20	Undef. Mineralisation	0.39	6.45	0.15	0.85	6.42	1.5	63.3	1.37	10	101
4421/96/R336/96.25-96.55	Undef. Mineralisation	0.38	0.72	0.16	0.85	1.29	0.3	81.3	0.85	10	102
4421/96/R346/109.60-109.90	Undef. Mineralisation	0.45	1.91	0.22	0.49	2.6	0.53	33.8	0.76	10	96
4421/95/R310/42.40-42.70	Undef. Mineralisation	0.34	1.98	0.16	0.81	3.26	0.55	64.7	0.99	10	90
4421/95/R319/37.00-37.30	Undef. Mineralisation	0.53	1.69	0.21	0.62	3.84	0.7	20.1	1.35	10	103
4421/95/R319/39.10-39.35	Undef. Mineralisation	0.46	1.07	0.23	0.69	2.51	0.44	29.7	0.92	10	102
4421/95/R319/34.20-34.50	Undef. Mineralisation	0.35	1.13	0.15	0.71	1.88	0.36	38.2	0.8	10	106
4421/96/R336/91.20-91.60	Undef. Mineralisation	0.61	1.91	0.32	0.75	3.67	0.65	34.8	1.43	10	87
M52442196R375 246.40-246.90	Int.–fel. volcanic rock	0.35	11.3	0.16	3.3	10.8	2.72	51.5	2.39	1	47.2
4421/95/R310/35.50-35.80	Undef. Mineralisation	0.54	2.53	0.2	0.73	3.4	0.7	37.1	1.09	10	79
M52442195R307 22.05-22.70	Tholeiitic basalt	0.47	2.4	0.22	2	4.6	0.93	0.1	1.45	0.5	63.1
M52442196R352 58.00-58.60	Tholeiitic basalt	0.5	1.5	0.25	0.4	2.8	0.51	0.2	1.03	0.5	113
4421/96/R346/100.70-101.00	Undef. Mineralisation	0.79	15.2	0.38	3.2	16.8	4.12	29	4.55	10	86
M52442196R345 38.50-38.90	Komatiite	0.09	0.2	0.04	0.4	0.8	0.14	0.1	0.39	0.5	217
EJL-95-R319/10.10-10.20	Komatiite	n.a.	1	n.a.	1	n.a.	n.a.	2	n.a.	0	231
M52442196R375 229.40-229.75	Komatiite	0.18	0.2	0.08	0.3	0.8	0.11	0.2	0.38	0.5	85.5
EJL-95-R310/131.70	Komatiite	n.a.	8	n.a.	0	n.a.	n.a.	2	n.a.	0	116
EJL-95-R310/114.80	Komatiite	n.a.	14	n.a.	4	n.a.	n.a.	0	n.a.	0	84
R354-196.10-196.70	Komatiite	n.a.	6	n.a.	3	n.a.	n.a.	1	n.a.	0	90
M52442195R310 12.50-12.80	Komatiite	0.59	0.6	0.22	0.6	1.6	0.28	0.2	0.75	0.5	118.5
EJL-95-R315/9	Komatiite	n.a.	3	n.a.	0	n.a.	n.a.	2	n.a.	0	185
M52442195R310 132.50-132.80	Komatiite	0.25	0.6	0.11	0.6	1.8	0.32	0.4	0.71	0.5	150
M52442196R346 84.70-85.20	Komatiite	0.3	0.4	0.11	0.7	1.4	0.24	0.2	0.62	0.5	148
EJL-95-R318/7.60-7.80	Komatiite	n.a.	6	n.a.	3	n.a.	n.a.	3	n.a.	0	12
EJL-95-R309/18.40	Komatiite	n.a.	1	n.a.	3	n.a.	n.a.	0	n.a.	0	184
EJL-95-R310/122.80	Komatiite	n.a.	6	n.a.	3	n.a.	n.a.	5	n.a.	0	94
M52442195R320 18.25-18.60	Komatiite	0.26	0.8	0.1	0.6	2.5	0.46	0.2	0.86	0.5	117
EJL-95-R323/7.85-8.05	Komatiite	n.a.	6	n.a.	3	n.a.	n.a.	4	n.a.	0	134
EJL-95-R315/51.30	Komatiite	n.a.	2	n.a.	0	n.a.	n.a.	2	n.a.	0	135
R351-95.20-95.40	Komatiite	n.a.	0	n.a.	2	n.a.	n.a.	2	n.a.	0	184
M52442194R306 59.80-60.30	Komatiite	0.27	0.3	0.13	0.5	1	0.18	0.1	0.5	0.5	130.5
EJL-95-R315/20.50	Komatiite	n.a.	10	n.a.	3	n.a.	n.a.	2	n.a.	0	84
R352-31.10-31.40	Komatiite	n.a.	16	n.a.	4	n.a.	n.a.	2	n.a.	0	152
M52442196R355 155.75-156.10	Komatiite	0.45	1.8	0.17	1	5	0.99	0.2	1.69	0.5	176.5
EJL-95-R309/110.75	Komatiite	n.a.	2	n.a.	3	n.a.	n.a.	4	n.a.	0	137
R351-73.10-73.30	Komatiite	n.a.	5	n.a.	4	n.a.	n.a.	0	n.a.	0	122
R349-26.70-26.90	Komatiite	n.a.	4	n.a.	3	n.a.	n.a.	0	n.a.	0	152
M52442196R375 267.45-267.85	Komatiitic basalt	0.31	0.5	0.11	0.4	1.4	0.21	3.1	0.7	0.5	85.1

Sample ID	Lithology	Ho	La	Lu	Nb	Nd	Pr	Rb	Sm	Sn	Sr
		ppm	ppm	ppm	ppm	ppm	ppm	ppm	ppm	ppm	ppm
M52442196R346 94.95-95.50	Komatiitic basalt	0.37	0.5	0.16	0.8	1.7	0.29	0.6	0.78	0.5	95.4
R352-25.15-25.55	Komatiite	n.a.	6	n.a.	3	n.a.	n.a.	0	n.a.	0	304
M52442196R336 120.70-121.10	Komatiitic basalt	0.32	0.8	0.13	0.7	2.2	0.41	0.1	0.86	0.5	86.1
EJL-95-R320/20.50-20.80	Komatiite	n.a.	14	n.a.	1	n.a.	n.a.	3	n.a.	0	143
EJL-95-R317/13.55-13.70	Komatiite	n.a.	7	n.a.	3	n.a.	n.a.	3	n.a.	0	26
EJL-95-R315/21.30-21.60	Tholeiitic basalt	n.a.	9	n.a.	2	n.a.	n.a.	52	n.a.	0	40
EJL-95-R314/43.00-43.20	Tholeiitic basalt	n.a.	13	n.a.	3	n.a.	n.a.	2	n.a.	0	99
EJL-95-R311/29.70-29.95	Tholeiitic basalt	n.a.	8	n.a.	2	n.a.	n.a.	19	n.a.	0	94
EJL-95-R311/37.05-37.30	Tholeiitic basalt	n.a.	19	n.a.	4	n.a.	n.a.	48	n.a.	0	22
EJL-95-R317/40.10-40.30	Komatiite	n.a.	9	n.a.	4	n.a.	n.a.	4	n.a.	0	46
M52442196R355 189.25-189.65	Komatiitic basalt	0.46	1.5	0.2	1.2	3.3	0.65	9.3	1.12	0.5	71.7
M52442196R345 73.40-74.05	Tholeiitic basalt	0.65	2	0.32	1.6	4.3	0.85	11.2	1.44	0.5	73.9
M52442196R372 180.35-180.80	Komatiitic basalt	0.34	4.6	0.16	1.3	9.9	2.02	65.9	2.94	1	136
EJL-95-R309/120.45	Komatiitic basalt	n.a.	9	n.a.	1	n.a.	n.a.	82	n.a.	0	164
M52442196R345 102.30-102.70	Tholeiitic basalt	0.62	1.6	0.27	1.3	3.8	0.75	19.3	1.36	0.5	57.6
EJL-95-R318/26.30-26.50	Komatiite	n.a.	14	n.a.	4	n.a.	n.a.	2	n.a.	0	6
M52442196R375 147.70-148.05	Int. lapilli tuff	0.58	15.8	0.24	3.1	15.1	3.67	24.4	3.22	0.5	119
M52442196R336 70.30-70.80	Int. volc. congl.	0.66	18.1	0.29	3.5	17.1	4.35	0.2	3.48	0.5	162
M52442196R375 123.00-123.35	Int. volc. congl.	0.59	9.4	0.26	2.8	9.7	2.33	25.5	2.31	0.5	141.5
EJL-95-R308/12.30-12.60	Int.–fel. volcanic rock	n.a.	27	n.a.	6	n.a.	n.a.	25	n.a.	0	123
M52442196R336 9.95-10.25	Int. volc. congl.	0.65	13.8	0.27	3.9	14.1	3.53	43.9	3.03	1	139
M52442196R373 99.90-100.35	Int. lapilli tuff	0.67	19.1	0.28	5.5	18.4	4.68	29.9	3.78	1	108.5
M52442196R375 198.60-199.00	Int.–fel. volcanic rock	0.49	14.1	0.19	3.4	12.5	3.17	29.6	2.63	0.5	113
M52442196R373 199.10-199.40	Int. lapilli tuff	0.59	15.7	0.26	3.3	15.1	3.84	45.7	3.06	1	180.5
M52442196R372 20.30-20.65	Int.–fel. volcanic rock	0.66	17.3	0.28	3.9	16.6	4.2	43.8	3.43	1	142
M52442196R355 100.90-101.20	Int. lapilli tuff	0.56	16.3	0.26	4.1	15	3.85	57.6	3.08	1	162.5
M52442196R336 40.90-41.25	Int. volc. congl.	0.59	17.7	0.24	4.3	16.3	4.28	35.5	3.33	0.5	118.5
EJL-95-R316/36.40-36.60	Tholeiitic basalt	n.a.	12	n.a.	3	n.a.	n.a.	0	n.a.	0	84
M52442195R310 51.00-51.65	Tholeiitic basalt	0.5	2.7	0.24	1.7	5.6	1.15	33.9	1.7	0.5	168
EJL-95-R312/17.45-17.75	Int.–fel. volcanic rock	n.a.	13	n.a.	6	n.a.	n.a.	61	n.a.	0	114
EJL-95-R320/57.50-57.70	Black schist	n.a.	9	n.a.	7	n.a.	n.a.	135	n.a.	0	130
M52442195R320 72.40-72.85	Black schist	0.35	8.8	0.16	3.4	8.3	2.17	35.6	1.89	<1	85.3
EJL-95-R320/7.60-7.90	Tholeiitic basalt	n.a.	7	n.a.	6	n.a.	n.a.	5	n.a.	0	208
M52442196R375 66.25-66.60	Int.–fel. volcanic rock	0.6	13.3	0.23	4.9	15.7	3.65	27.1	3.49	1	219
M52442196R372 99.50-99.80	Int.–fel. volcanic rock	0.58	16	0.24	3.8	13.9	3.63	54.3	2.78	1	409
EJL-95-R321/58.50-58.90	Black schist	n.a.	28	n.a.	4	n.a.	n.a.	120	n.a.	0	147
M52442194R306 4.60-5.00	Int.–fel. volcanic rock	0.73	3.1	0.33	2.1	6.8	1.3	39.7	2.16	0.5	232
M52442196R336 102.40-102.90	Tholeiitic basalt	0.58	1.1	0.25	1.1	2.3	0.41	24.6	1	0.5	119
EJL-95-R309/50.55-50.79	Int.–fel. volcanic rock	n.a.	23	n.a.	3	n.a.	n.a.	53	n.a.	0	177
M52442196R373 9.50-9.95	Int.–fel. volcanic rock	0.57	23.3	0.25	4.7	18.9	5.13	48.3	3.52	1	212
EJL-95-R323/32.10-32.30	Black schist	n.a.	29	n.a.	2	n.a.	n.a.	61	n.a.	0	113
M52442196R375 40.35-40.65	Int.–fel. volcanic rock	0.56	17.7	0.26	3.8	15.4	3.86	34.1	3.27	0.5	171
EJL-95-R319/21.60-21.80	Tholeiitic basalt	n.a.	14	n.a.	5	n.a.	n.a.	2	n.a.	0	131
M52442196R375 10.15-10.50	Int.–fel. volcanic rock	0.48	16	0.21	3.5	13.4	3.38	43.9	2.52	0.5	207
M52442196R372 129.30-129.65	Black schist	0.43	19.2	0.21	5.7	16	4.42	138	2.97	2	97.6
EJL-95-R322/64.20-64.50	Black schist	n.a.	26	n.a.	6	n.a.	n.a.	81	n.a.	0	128
M52442195R310 87.00-87.60	Black schist	0.43	20.9	0.21	4.1	17.6	4.9	97.5	3.34	1	142.5
EJL-95-R309/92.80	Black schist	n.a.	23	n.a.	5	n.a.	n.a.	83	n.a.	0	117
EJL-95-R316/40.00-40.20	Komatiitic basalt	n.a.	1	n.a.	5	n.a.	n.a.	9	n.a.	0	68
M52442196R352 19.10-19.45	Black schist	0.3	9.2	0.16	3.8	7.8	2.1	92	1.69	1	51.1
EJL-95-R313/72.20	Quartz porphyry	n.a.	32	n.a.	1	n.a.	n.a.	59	n.a.	0	715
M52442196R355 166.50-167.00	Int.–fel. volcanic rock	0.3	17	0.13	3	16.7	4.3	54.2	2.94	1	185
M52442196R373 221.90-222.30	Quartz porphyry	0.18	24.8	0.06	3.1	20.5	5.2	78.9	3.64	1	176
EJL-95-R310/23.60-23.90	Quartz porphyry	n.a.	81	n.a.	2	n.a.	n.a.	84	n.a.	0	158
EJL-95-R315/65.80	Quartz porphyry	n.a.	41	n.a.	5	n.a.	n.a.	72	n.a.	0	41
EJL-95-R320/44.80-45.10	Quartz porphyry	n.a.	17	n.a.	3	n.a.	n.a.	57	n.a.	0	72
EJL-95-R323/13.10-13.30	Quartz porphyry	n.a.	34	n.a.	5	n.a.	n.a.	50	n.a.	0	44

Appendix 2.3. XRF analysis data of Ta, Tb, Th, Tm, U, V, W, Y, Yb, & Zr

Sample ID	Lithology	Ta	Tb	Th	Tm	U	V	W	Y	Yb	Zr
		ppm	ppm	ppm	ppm	ppm	ppm	ppm	ppm	ppm	ppm
M52442194R306 35.60-36.10	Tholeiitic basalt	0.05	0.44	0.39	0.32	0.21	193	0.5	18.1	2.11	23
4421/96/R336/89.20-89.50	Undef. Mineralisation	0.3	0.54	2.93	0.29	0.95	53.3	n.a.	18.5	1.75	115
4421/95/R310/39.80-40.00	Undef. Mineralisation	0.1	0.16	0.25	0.12	0.1	181	n.a.	7.22	0.78	23.7
4421/96/R346/106.90-107.20	Undef. Mineralisation	0.1	0.26	0.25	0.18	0.1	231	n.a.	10.6	1.13	34.7
4421/96/R336/96.25-96.55	Undef. Mineralisation	0.1	0.27	0.25	0.17	0.23	219	n.a.	11.2	1.11	28.5
4421/96/R346/109.60-109.90	Undef. Mineralisation	0.1	0.32	0.25	0.18	0.1	181	n.a.	12.5	1.53	24.6
4421/95/R310/42.40-42.70	Undef. Mineralisation	0.1	0.23	0.25	0.15	0.1	210	n.a.	8.81	0.87	27.9
4421/95/R319/37.00-37.30	Undef. Mineralisation	0.1	0.34	0.25	0.24	0.25	207	n.a.	13.8	1.64	26.2
4421/95/R319/39.10-39.35	Undef. Mineralisation	0.1	0.28	0.25	0.21	0.1	198	n.a.	12.4	1.41	25.5
4421/95/R319/34.20-34.50	Undef. Mineralisation	0.1	0.24	0.25	0.15	0.1	201	n.a.	9.94	1.01	26.1
4421/96/R336/91.20-91.60	Undef. Mineralisation	0.1	0.41	0.25	0.29	0.26	230	n.a.	18.4	2.26	27.7

Sample ID	Lithology	Ta	Tb	Th	Tm	U	V	W	Y	Yb	Zr
		ppm	ppm	ppm	ppm	ppm	ppm	ppm	ppm	ppm	ppm
M52442196R375 246.40-246.90	Int.–fel. volcanic rock	0.4	0.33	3.4	0.14	1.07	81	0.5	9.7	1	101
4421/95/R310/35.50-35.80	Undef. Mineralisation	0.1	0.39	0.25	0.22	0.28	211	n.a.	13.8	1.61	23.5
M52442195R307 22.05-22.70	Tholeiitic basalt	0.05	0.35	0.35	0.21	0.21	241	0.5	12.6	1.55	45
M52442196R352 58.00-58.60	Tholeiitic basalt	0.05	0.35	0.25	0.23	0.16	134	0.5	14	1.66	13
4421/96/R346/100.70-101.00	Undef. Mineralisation	0.36	0.66	3.61	0.37	0.99	128	n.a.	22.5	2.45	132
M52442196R345 38.50-38.90	Komatiite	0.05	0.08	0.06	0.03	0.025	112	0.5	2.2	0.24	9
EJL-95-R319/10.10-10.20	Komatiite	n.a.	n.a.	0	n.a.	0	86	n.a.	2	n.a.	13
M52442196R375 229.40-229.75	Komatiite	0.05	0.14	0.05	0.07	0.025	144	0.5	4.8	0.5	14
EJL-95-R310/131.70	Komatiite	n.a.	n.a.	0	n.a.	0	123	n.a.	7	n.a.	19
EJL-95-R310/114.80	Komatiite	n.a.	n.a.	0	n.a.	0	126	n.a.	5	n.a.	15
R354-196.10-196.70	Komatiite	n.a.	n.a.	0	n.a.	0	127	n.a.	2	n.a.	17
M52442195R310 12.50-12.80	Komatiite	0.05	0.37	0.11	0.24	0.025	189	1	15.5	1.58	20
EJL-95-R315/9	Komatiite	n.a.	n.a.	3	n.a.	0	109	n.a.	3	n.a.	25
M52442195R310 132.50-132.80	Komatiite	0.05	0.2	0.08	0.11	0.025	190	1	6.6	0.74	18
M52442196R346 84.70-85.20	Komatiite	0.05	0.21	0.08	0.13	0.025	185	1	7.5	0.84	19
EJL-95-R318/7.60-7.80	Komatiite	n.a.	n.a.	0	n.a.	0	146	n.a.	9	n.a.	21
EJL-95-R309/18.40	Komatiite	n.a.	n.a.	1	n.a.	0	133	n.a.	2	n.a.	23
EJL-95-R310/122.80	Komatiite	n.a.	n.a.	0	n.a.	1	159	n.a.	3	n.a.	21
M52442195R320 18.25-18.60	Komatiite	0.05	0.21	0.26	0.11	0.07	154	1	7.1	0.72	18
EJL-95-R323/7.85-8.05	Komatiite	n.a.	n.a.	0	n.a.	0	132	n.a.	1	n.a.	16
EJL-95-R315/51.30	Komatiite	n.a.	n.a.	0	n.a.	0	151	n.a.	3	n.a.	22
R351-95.20-95.40	Komatiite	n.a.	n.a.	0	n.a.	0	119	n.a.	7	n.a.	19
M52442194R306 59.80-60.30	Komatiite	0.05	0.16	0.07	0.13	0.025	151	0.5	6.8	0.77	18
EJL-95-R315/20.50	Komatiite	n.a.	n.a.	2	n.a.	0	143	n.a.	7	n.a.	19
R352-31.10-31.40	Komatiite	n.a.	n.a.	0	n.a.	0	148	n.a.	9	n.a.	23
M52442196R355 155.75-156.10	Komatiite	0.05	0.36	0.2	0.19	0.025	211	1	11.7	1.19	21
EJL-95-R309/110.75	Komatiite	n.a.	n.a.	0	n.a.	0	139	n.a.	7	n.a.	13
R351-73.10-73.30	Komatiite	n.a.	n.a.	0	n.a.	0	156	n.a.	8	n.a.	20
R349-26.70-26.90	Komatiite	n.a.	n.a.	0	n.a.	0	158	n.a.	8	n.a.	22
M52442196R375 267.45-267.85	Komatiitic basalt	0.1	0.22	0.07	0.11	0.025	167	0.5	7.9	0.77	20
M52442196R346 94.95-95.50	Komatiitic basalt	0.05	0.28	0.09	0.17	0.025	244	1	10.2	1.13	25
R352-25.15-25.55	Komatiite	n.a.	n.a.	0	n.a.	0	145	n.a.	8	n.a.	26
M52442196R336 120.70-121.10	Komatiitic basalt	0.05	0.24	0.09	0.13	0.025	177	1	8.2	0.9	21
EJL-95-R320/20.50-20.80	Komatiite	n.a.	n.a.	0	n.a.	0	176	n.a.	6	n.a.	29
EJL-95-R317/13.55-13.70	Komatiite	n.a.	n.a.	0	n.a.	0	205	n.a.	11	n.a.	36
EJL-95-R315/21.30-21.60	Tholeiitic basalt	n.a.	n.a.	0	n.a.	0	270	n.a.	15	n.a.	41
EJL-95-R314/43.00-43.20	Tholeiitic basalt	n.a.	n.a.	1	n.a.	1	256	n.a.	28	n.a.	33
EJL-95-R311/29.70-29.95	Tholeiitic basalt	n.a.	n.a.	0	n.a.	0	284	n.a.	16	n.a.	44
EJL-95-R311/37.05-37.30	Tholeiitic basalt	n.a.	n.a.	1	n.a.	0	143	n.a.	13	n.a.	44
EJL-95-R317/40.10-40.30	Komatiite	n.a.	n.a.	0	n.a.	0	200	n.a.	10	n.a.	33
M52442196R355 189.25-189.65	Komatiitic basalt	0.05	0.32	0.14	0.19	0.025	249	0.5	11.8	1.36	28
M52442196R345 73.40-74.05	Tholeiitic basalt	0.05	0.46	0.34	0.31	0.09	272	3	16	2.09	42
M52442196R372 180.35-180.80	Komatiitic basalt	0.1	0.35	0.17	0.14	0.025	287	1	8.3	1.09	28
EJL-95-R309/120.45	Komatiitic basalt	n.a.	n.a.	0	n.a.	0	123	n.a.	6	n.a.	29
M52442196R345 102.30-102.70	Tholeiitic basalt	0.05	0.42	0.16	0.25	0.025	257	0.5	16.3	1.87	31
EJL-95-R318/26.30-26.50	Komatiite	n.a.	n.a.	0	n.a.	0	199	n.a.	12	n.a.	34
M52442196R375 147.70-148.05	Int. lapilli tuff	0.3	0.49	3.93	0.24	1.07	200	2	15.6	1.5	98
M52442196R336 70.30-70.80	Int. volc. congl.	0.2	0.56	5.03	0.28	1.26	206	0.5	16.8	1.89	96
M52442196R375 123.00-123.35	Int. volc. congl.	0.2	0.44	2.72	0.25	0.81	219	1	15.9	1.66	83
EJL-95-R308/12.30-12.60	Int.–fel. volcanic rock	n.a.	n.a.	0	n.a.	0	192	n.a.	16	n.a.	111
M52442196R336 9.95-10.25	Int. volc. congl.	0.3	0.55	3.81	0.28	0.99	278	3	17.6	1.86	101
M52442196R373 99.90-100.35	Int. lapilli tuff	0.4	0.58	4.66	0.27	1.34	195	2	18.1	1.97	114
M52442196R375 198.60-199.00	Int.–fel. volcanic rock	0.3	0.4	3.37	0.2	0.92	169	1	13.2	1.24	101
M52442196R373 199.10-199.40	Int. lapilli tuff	0.2	0.51	4.2	0.26	1.21	189	3	15.6	1.72	102
M52442196R372 20.30-20.65	Int.–fel. volcanic rock	0.3	0.54	4.38	0.28	1.23	193	1	17.5	1.9	113
M52442196R355 100.90-101.20	Int. lapilli tuff	0.3	0.5	4.35	0.24	1.16	190	1	15	1.61	110
M52442196R336 40.90-41.25	Int. volc. congl.	0.3	0.5	4.48	0.24	1.19	172	2	15.8	1.6	118
EJL-95-R316/36.40-36.60	Tholeiitic basalt	n.a.	n.a.	0	n.a.	0	268	n.a.	13	n.a.	42
M52442195R310 51.00-51.65	Tholeiitic basalt	0.05	0.4	0.22	0.22	0.06	240	1	13.3	1.54	38
EJL-95-R312/17.45-17.75	Int.–fel. volcanic rock	n.a.	n.a.	4	n.a.	0	144	n.a.	13	n.a.	115
EJL-95-R320/57.50-57.70	Black schist	n.a.	n.a.	5	n.a.	0	143	n.a.	16	n.a.	105
M52442195R320 72.40-72.85	Black schist	0.2	0.3	3.66	0.16	1.49	85	1	10.4	1.13	76
EJL-95-R320/7.60-7.90	Tholeiitic basalt	n.a.	n.a.	0	n.a.	0	359	n.a.	25	n.a.	77
M52442196R375 66.25-66.60	Int.–fel. volcanic rock	0.3	0.52	2.51	0.24	0.64	186	1	15.9	1.61	84
M52442196R372 99.50-99.80	Int.–fel. volcanic rock	0.3	0.47	4.3	0.25	1.15	162	1	15.9	1.73	106
EJL-95-R321/58.50-58.90	Black schist	n.a.	n.a.	5	n.a.	0	125	n.a.	13	n.a.	131
M52442194R306 4.60-5.00	Int.–fel. volcanic rock	0.1	0.49	0.28	0.32	0.08	316	0.5	17.8	1.99	54
M52442196R336 102.40-102.90	Tholeiitic basalt	0.05	0.4	0.14	0.25	0.025	286	3	14.9	1.74	34
EJL-95-R309/50.55-50.79	Int.–fel. volcanic rock	n.a.	n.a.	3	n.a.	3	159	n.a.	14	n.a.	135
M52442196R373 9.50-9.95	Int.–fel. volcanic rock	0.4	0.49	6.28	0.24	1.93	155	2	16.1	1.64	147
EJL-95-R323/32.10-32.30	Black schist	n.a.	n.a.	4	n.a.	0	102	n.a.	11	n.a.	123
M52442196R375 40.35-40.65	Int.–fel. volcanic rock	0.4	0.47	4.69	0.23	1.2	168	0.5	16.2	1.53	115
EJL-95-R319/21.60-21.80	Tholeiitic basalt	n.a.	n.a.	0	n.a.	0	380	n.a.	25	n.a.	80
M52442196R375 10.15-10.50	Int.–fel. volcanic rock	0.4	0.39	4.37	0.2	1.29	149	1	13.2	1.36	112
M52442196R372 129.30-129.65	Black schist	0.5	0.38	8.45	0.2	2.69	100	1	11.8	1.32	152

Sample ID	Lithology	Ta	Tb	Th	Tm	U	V	W	Y	Yb	Zr
		ppm	ppm	ppm	ppm	ppm	ppm	ppm	ppm	ppm	ppm
EJL-95-R322/64.20-64.50	Black schist	n.a.	n.a.	6	n.a.	0	103	n.a.	10	n.a.	161
M52442195R310 87.00-87.60	Black schist	0.4	0.42	6.48	0.19	1.89	91	1	11.1	1.31	102
EJL-95-R309/92.80	Black schist	n.a.	n.a.	6	n.a.	0	136	n.a.	11	n.a.	137
EJL-95-R316/40.00-40.20	Komatiitic basalt	n.a.	n.a.	0	n.a.	1	249	n.a.	12	n.a.	39
M52442196R352 19.10-19.45	Black schist	0.4	0.27	6.34	0.13	1.91	52	1	8	0.96	100
EJL-95-R313/72.20	Quartz porphyry	n.a.	n.a.	4	n.a.	0	50	n.a.	6	n.a.	156
M52442196R355 166.50-167.00	Int.–fel. volcanic rock	0.2	0.3	2.71	0.12	0.85	124	3	7.8	0.79	98
M52442196R373 221.90-222.30	Quartz porphyry	0.3	0.27	7.14	0.06	1.65	47	0.5	4.9	0.38	126
EJL-95-R310/23.60-23.90	Quartz porphyry	n.a.	n.a.	25	n.a.	0	40	n.a.	7	n.a.	78
EJL-95-R315/65.80	Quartz porphyry	n.a.	n.a.	10	n.a.	0	21	n.a.	8	n.a.	101
EJL-95-R320/44.80-45.10	Quartz porphyry	n.a.	n.a.	19	n.a.	0	29	n.a.	6	n.a.	123
EJL-95-R323/13.10-13.30	Quartz porphyry	n.a.	n.a.	22	n.a.	0	20	n.a.	5	n.a.	121

Appendix 2.4. XRF analysis data of Ag, As, Cd, Co, Cu, Li, Mo, Ni, Pb, & Sc

Sample ID	Lithology	Ag	As	Cd	Co	Cu	Li	Mo	Ni	Pb	Sc
		ppm	ppm	ppm	ppm	ppm	ppm	ppm	ppm	ppm	ppm
M52442194R306 35.60-36.10	Tholeiitic basalt	0.25	10	2.3	536	470	10	0.5	31800	11	57
4421/96/R336/89.20-89.50	Undef. Mineralisation	n.a.	15	n.a.	163	392	n.a.	5	22820	15	12.5
4421/95/R310/39.80-40.00	Undef. Mineralisation	n.a.	15	n.a.	296	142	n.a.	5	16280	15	29.6
4421/96/R346/106.90-107.20	Undef. Mineralisation	n.a.	924	n.a.	259	114	n.a.	5	14750	15	40.1
4421/96/R336/96.25-96.55	Undef. Mineralisation	n.a.	451	n.a.	200	88	n.a.	5	10990	15	37.2
4421/96/R346/109.60-109.90	Undef. Mineralisation	n.a.	1906	n.a.	178	436	n.a.	5	9748	15	37.9
4421/95/R310/42.40-42.70	Undef. Mineralisation	n.a.	1292	n.a.	235	76	n.a.	5	9732	15	36.8
4421/95/R319/37.00-37.30	Undef. Mineralisation	n.a.	69	n.a.	133	70	n.a.	5	9291	15	44.2
4421/95/R319/39.10-39.35	Undef. Mineralisation	n.a.	15	n.a.	141	91	n.a.	5	8119	15	37.2
4421/95/R319/34.20-34.50	Undef. Mineralisation	n.a.	15	n.a.	158	60	n.a.	5	6265	15	33.7
4421/96/R336/91.20-91.60	Undef. Mineralisation	n.a.	202	n.a.	169	26	n.a.	5	4080	15	39.3
M52442196R375 246.40-246.90	Int.–fel. volcanic rock	0.25	2.5	0.25	81	158	20	1	3200	6	13
4421/95/R310/35.50-35.80	Undef. Mineralisation	n.a.	15	n.a.	83.4	24	n.a.	5	3037	15	43.7
M52442195R307 22.05-22.70	Tholeiitic basalt	0.25	2.5	0.6	74	125	30	1	2830	5	33
M52442196R352 58.00-58.60	Tholeiitic basalt	0.25	2.5	1.9	125	408	10	0.5	2460	8	23
4421/96/R346/100.70-101.00	Undef. Mineralisation	n.a.	15	n.a.	104	280	n.a.	5	2169	15	30.2
M52442196R345 38.50-38.90	Komatiite	0.25	125	0.25	88	65	5	1	1780	3	12
EJL-95-R319/10.10-10.20	Komatiite	n.a.	18	n.a.	n.a.	60	n.a.	0	1758	19	21
M52442196R375 229.40-229.75	Komatiite	0.25	21	0.25	96	2	20	0.5	1420	1	19
EJL-95-R310/131.70	Komatiite	n.a.	1	n.a.	n.a.	8	n.a.	0	1387	12	23
EJL-95-R310/114.80	Komatiite	n.a.	20	n.a.	n.a.	49	n.a.	0	1363	19	21
R354-196.10-196.70	Komatiite	n.a.	73	n.a.	n.a.	34	n.a.	0	1350	15	18
M52442195R310 12.50-12.80	Komatiite	0.25	2.5	0.6	86	24	20	0.5	1330	44	21
EJL-95-R315/9	Komatiite	n.a.	0	n.a.	n.a.	22	n.a.	0	1322	22	18
M52442195R310 132.50-132.80	Komatiite	0.25	2.5	0.25	88	34	20	0.5	1250	2	25
M52442196R346 84.70-85.20	Komatiite	0.25	2.5	0.5	80	81	20	0.5	1220	4	21
EJL-95-R318/7.60-7.80	Komatiite	n.a.	2	n.a.	n.a.	5	n.a.	0	1193	13	29
EJL-95-R309/18.40	Komatiite	n.a.	316	n.a.	n.a.	58	n.a.	0	1174	14	27
EJL-95-R310/122.80	Komatiite	n.a.	1	n.a.	n.a.	438	n.a.	0	1163	14	37
M52442195R320 18.25-18.60	Komatiite	0.25	2.5	0.25	74	5	20	0.5	1160	5	18
EJL-95-R323/7.85-8.05	Komatiite	n.a.	118	n.a.	n.a.	37	n.a.	0	1159	12	23
EJL-95-R315/51.30	Komatiite	n.a.	0	n.a.	n.a.	283	n.a.	0	1136	18	28
R351-95.20-95.40	Komatiite	n.a.	1	n.a.	n.a.	48	n.a.	0	1134	15	20
M52442194R306 59.80-60.30	Komatiite	0.25	101	0.5	75	5	20	0.5	1100	2	23
EJL-95-R315/20.50	Komatiite	n.a.	0	n.a.	n.a.	32	n.a.	0	1089	301	28
R352-31.10-31.40	Komatiite	n.a.	83	n.a.	n.a.	90	n.a.	0	1044	17	23
M52442196R355 155.75-156.10	Komatiite	0.25	22	0.6	81	11	20	0.5	1020	4	21
EJL-95-R309/110.75	Komatiite	n.a.	64	n.a.	n.a.	21	n.a.	0	992	19	29
R351-73.10-73.30	Komatiite	n.a.	125	n.a.	n.a.	51	n.a.	0	910	14	25
R349-26.70-26.90	Komatiite	n.a.	59	n.a.	n.a.	26	n.a.	0	869	20	25
M52442196R375 267.45-267.85	Komatiitic basalt	0.25	252	0.25	91	11	30	0.5	845	1	20
M52442196R346 94.95-95.50	Komatiitic basalt	0.25	96	0.7	94	7	50	0.5	778	3	30
R352-25.15-25.55	Komatiite	n.a.	361	n.a.	n.a.	26	n.a.	0	771	17	27
M52442196R336 120.70-121.10	Komatiitic basalt	0.25	218	0.25	64	2	30	0.5	758	2	22
EJL-95-R320/20.50-20.80	Komatiite	n.a.	8	n.a.	n.a.	840	n.a.	0	753	16	26
EJL-95-R317/13.55-13.70	Komatiite	n.a.	0	n.a.	n.a.	128	n.a.	0	664	16	41
EJL-95-R315/21.30-21.60	Tholeiitic basalt	n.a.	139	n.a.	n.a.	194	n.a.	0	614	20	46
EJL-95-R314/43.00-43.20	Tholeiitic basalt	n.a.	57	n.a.	n.a.	114	n.a.	0	612	23	41
EJL-95-R311/29.70-29.95	Tholeiitic basalt	n.a.	4	n.a.	n.a.	30	n.a.	0	534	15	44
EJL-95-R311/37.05-37.30	Tholeiitic basalt	n.a.	136	n.a.	n.a.	104	n.a.	0	530	15	41
EJL-95-R317/40.10-40.30	Komatiite	n.a.	5	n.a.	n.a.	16	n.a.	0	478	20	39
M52442196R355 189.25-189.65	Komatiitic basalt	0.25	31	0.6	64	56	40	1	477	3	32
M52442196R345 73.40-74.05	Tholeiitic basalt	0.25	13	0.6	79	222	30	0.5	438	3	37
M52442196R372 180.35-180.80	Komatiitic basalt	0.25	313	0.6	76	10	10	0.5	419	5	40
EJL-95-R309/120.45	Komatiitic basalt	n.a.	22	n.a.	n.a.	462	n.a.	0	418	22	23
M52442196R345 102.30-102.70	Tholeiitic basalt	0.25	22	0.6	61	51	40	0.5	393	1	42

Sample ID	Lithology	Ag	As	Cd	Co	Cu	Li	Mo	Ni	Pb	Sc
		ppm	ppm	ppm	ppm	ppm	ppm	ppm	ppm	ppm	ppm
EJL-95-R318/26.30-26.50	Komatiite	n.a.	0	n.a.	n.a.	6	n.a.	0	386	18	33
M52442196R375 147.70-148.05	Int. lapilli tuff	0.25	172	0.25	52	73	40	2	306	7	25
M52442196R336 70.30-70.80	Int. volc. congl.	0.25	2.5	0.25	48	92	20	2	302	5	26
M52442196R375 123.00-123.35	Int. volc. congl.	0.25	47	0.25	47	70	40	2	299	5	25
EJL-95-R308/12.30-12.60	Int.–fel. volcanic rock	n.a.	56	n.a.	n.a.	96	n.a.	2	286	19	24
M52442196R336 9.95-10.25	Int. volc. congl.	0.25	107	0.25	51	83	40	1	267	7	30
M52442196R373 99.90-100.35	Int. lapilli tuff	0.25	107	0.25	45	64	40	1	265	7	22
M52442196R375 198.60-199.00	Int.–fel. volcanic rock	0.25	53	0.25	42	49	30	0.5	258	5	20
M52442196R373 199.10-199.40	Int. lapilli tuff	0.25	33	0.25	48	93	30	3	258	7	23
M52442196R372 20.30-20.65	Int.–fel. volcanic rock	0.25	149	0.25	39	84	30	2	256	6	22
M52442196R355 100.90-101.20	Int. lapilli tuff	0.25	92	0.25	43	78	30	1	245	9	21
M52442196R336 40.90-41.25	Int. volc. congl.	0.25	52	0.25	39	57	30	1	231	8	20
EJL-95-R316/36.40-36.60	Tholeiitic basalt	n.a.	36	n.a.	n.a.	135	n.a.	0	220	20	44
M52442195R310 51.00-51.65	Tholeiitic basalt	0.25	102	0.25	49	18	30	0.5	219	2	33
EJL-95-R312/17.45-17.75	Int.–fel. volcanic rock	n.a.	120	n.a.	n.a.	60	n.a.	2	211	20	16
EJL-95-R320/57.50-57.70	Black schist	n.a.	2	n.a.	n.a.	145	n.a.	2	200	26	21
M52442195R320 72.40-72.85	Black schist	<0.5	10	0.5	36	130	30	1	193	8	15
EJL-95-R320/7.60-7.90	Tholeiitic basalt	n.a.	2	n.a.	n.a.	77	n.a.	0	179	20	48
M52442196R375 66.25-66.60	Int.–fel. volcanic rock	0.25	31	0.5	35	0.5	40	1	177	5	21
M52442196R372 99.50-99.80	Int.–fel. volcanic rock	0.25	74	0.25	35	77	20	1	171	4	20
EJL-95-R321/58.50-58.90	Black schist	n.a.	6	n.a.	n.a.	118	n.a.	4	170	21	11
M52442194R306 4.60-5.00	Int.–fel. volcanic rock	0.25	8	0.25	33	91	20	1	164	5	37
M52442196R336 102.40-102.90	Tholeiitic basalt	0.25	34	0.25	44	53	20	0.5	144	3	36
EJL-95-R309/50.55-50.79	Int.–fel. volcanic rock	n.a.	27	n.a.	n.a.	34	n.a.	0	139	17	19
M52442196R373 9.50-9.95	Int.–fel. volcanic rock	0.25	153	0.25	28	65	30	2	136	5	20
EJL-95-R323/32.10-32.30	Black schist	n.a.	5	n.a.	n.a.	57	n.a.	2	132	26	15
M52442196R375 40.35-40.65	Int.–fel. volcanic rock	0.25	2.5	0.25	33	56	30	0.5	121	3	24
EJL-95-R319/21.60-21.80	Tholeiitic basalt	n.a.	0	n.a.	n.a.	40	n.a.	0	118	17	51
M52442196R375 10.15-10.50	Int.–fel. volcanic rock	0.25	35	0.25	27	51	20	1	112	5	20
M52442196R372 129.30-129.65	Black schist	<0.5	<5	<0.5	22	83	20	2	90	6	13
EJL-95-R322/64.20-64.50	Black schist	n.a.	3	n.a.	n.a.	50	n.a.	3	88	20	8
M52442195R310 87.00-87.60	Black schist	<0.5	<5	8.6	27	64	10	3	87	8	16
EJL-95-R309/92.80	Black schist	n.a.	39	n.a.	n.a.	44	n.a.	1	82	18	11
EJL-95-R316/40.00-40.20	Komatiitic basalt	n.a.	4	n.a.	n.a.	49	n.a.	0	68	17	34
M52442196R352 19.10-19.45	Black schist	<0.5	19	<0.5	5	66	10	1	38	3	9
EJL-95-R313/72.20	Quartz porphyry	n.a.	388	n.a.	n.a.	9	n.a.	3	32	23	3
M52442196R355 166.50-167.00	Int.–fel. volcanic rock	0.25	2.5	0.25	20	63	20	0.5	26	4	12
M52442196R373 221.90-222.30	Quartz porphyry	0.25	2.5	0.25	6	9	20	1	26	3	5
EJL-95-R310/23.60-23.90	Quartz porphyry	n.a.	18	n.a.	n.a.	24	n.a.	3	21	77	0
EJL-95-R315/65.80	Quartz porphyry	n.a.	226	n.a.	n.a.	21	n.a.	1	19	28	0
EJL-95-R320/44.80-45.10	Quartz porphyry	n.a.	4	n.a.	n.a.	12	n.a.	1	14	13	0
EJL-95-R323/13.10-13.30	Quartz porphyry	n.a.	16	n.a.	n.a.	7	n.a.	3	9	17	0

Appendix 2.5. XRF analysis data of Tl, Zn, Au, Pt, Pd, Al_2O_3, BaO, CaO, Cr_2O_3, & FeOtot

Sample ID	Lithology	Tl	Zn	Au	Pt	Pd	Al2O3	BaO	CaO	Cr2O3	FeOtot
		ppm	ppm	ppb	ppb	ppb	%	%	%	%	%
M52442194R306 35.60-36.10	Tholeiitic basalt	5	287	702	3.7	1.1	3.85	0.01	12.45	0.02	26.45
4421/96/R336/89.20-89.50	Undef. Mineralisation	n.a.	359	6.61	0.38	2.77	8.69	n.a.	1.66	0.01	28.90
4421/95/R310/39.80-40.00	Undef. Mineralisation	n.a.	1113	5.07	14.9	13.7	10.2	n.a.	4.95	0.42	12.10
4421/96/R346/106.90-107.20	Undef. Mineralisation	n.a.	466	9.24	16.2	16.3	11.6	n.a.	4.1	0.49	10.10
4421/96/R336/96.25-96.55	Undef. Mineralisation	n.a.	322	7.38	16.7	15.5	11.4	n.a.	5.32	0.5	7.90
4421/96/R346/109.60-109.90	Undef. Mineralisation	n.a.	301	13.9	9.12	12	7.6	n.a.	7.51	0.31	17.90
4421/95/R310/42.40-42.70	Undef. Mineralisation	n.a.	463	22	17	17.8	11.4	n.a.	4.4	0.49	8.00
4421/95/R319/37.00-37.30	Undef. Mineralisation	n.a.	478	11	12	11.6	8.48	n.a.	7.86	0.32	11.30
4421/95/R319/39.10-39.35	Undef. Mineralisation	n.a.	404	3.3	13.3	11.8	9.37	n.a.	5.63	0.37	11.60
4421/95/R319/34.20-34.50	Undef. Mineralisation	n.a.	607	2.47	14.2	13.8	10.5	n.a.	5.21	0.45	8.50
4421/96/R336/91.20-91.60	Undef. Mineralisation	n.a.	510	6.23	15	16.1	10	n.a.	5.96	0.44	13.10
M52442196R375 246.40-246.90	Int.–fel. volcanic rock	5	126	5	2	1.8	12.54	0.08	0.3	0.02	11.14
4421/95/R310/35.50-35.80	Undef. Mineralisation	n.a.	361	1.38	12.1	12.1	8.22	n.a.	6.34	0.33	12.00
M52442195R307 22.05-22.70	Tholeiitic basalt	5	207	187	18.6	12.9	13.21	0.005	3.81	0.04	16.63
M52442196R352 58.00-58.60	Tholeiitic basalt	5	311	23	5	5.4	3.68	0.005	9.61	0.11	30.55
4421/96/R346/100.70-101.00	Undef. Mineralisation	n.a.	225	5.38	1.59	1.66	10.3	n.a.	6.74	0.03	25.70
M52442196R345 38.50-38.90	Komatiite	5	38	1	5.1	5	3.18	0.005	9.96	0.23	6.08
EJL-95-R319/10.10-10.20	Komatiite	n.a.	69	n.a.	n.a.	n.a.	3.54	n.a.	9.38	n.a.	6.62
M52442196R375 229.40-229.75	Komatiite	5	94	2	7.9	7.4	5.36	0.005	4.48	0.29	8.42
EJL-95-R310/131.70	Komatiite	n.a.	101	n.a.	n.a.	n.a.	6.34	n.a.	6.43	n.a.	8.62
EJL-95-R310/114.80	Komatiite	n.a.	270	n.a.	n.a.	n.a.	6.38	n.a.	4.37	n.a.	9.63
R354-196.10-196.70	Komatiite	n.a.	125	n.a.	n.a.	n.a.	5.93	n.a.	3.43	n.a.	9.36
M52442195R310 12.50-12.80	Komatiite	5	123	2	9.6	9.3	6.58	0.005	5.04	0.32	9.30
EJL-95-R315/9	Komatiite	n.a.	83	n.a.	n.a.	n.a.	6.04	n.a.	4.8	n.a.	9.09

Sample ID	Lithology	Tl	Zn	Au	Pt	Pd	Al2O3	BaO	CaO	Cr2O3	FeOtot
		ppm	ppm	ppb	ppb	ppb	%	%	%	%	%
M52442195R310 132.50-132.80	Komatiite	5	99	2	12.8	10.5	7.02	0.005	8.85	0.38	9.33
M52442196R346 84.70-85.20	Komatiite	5	101	5	8.4	7.4	6.08	0.005	6.29	0.28	8.99
EJL-95-R318/7.60-7.80	Komatiite	n.a.	83	n.a.	n.a.	n.a.	6.82	n.a.	8.29	n.a.	8.94
EJL-95-R309/18.40	Komatiite	n.a.	95	n.a.	n.a.	n.a.	6.37	n.a.	8.94	n.a.	8.54
EJL-95-R310/122.80	Komatiite	n.a.	153	n.a.	n.a.	n.a.	8.33	n.a.	8.39	n.a.	10.71
M52442195R320 18.25-18.60	Komatiite	5	80	0.5	7.1	6.2	5.58	0.005	6.96	0.23	8.42
EJL-95-R323/7.85-8.05	Komatiite	n.a.	151	n.a.	n.a.	n.a.	6.35	n.a.	5.03	n.a.	8.55
EJL-95-R315/51.30	Komatiite	n.a.	69	n.a.	n.a.	n.a.	7.49	n.a.	7.77	n.a.	9.54
R351-95.20-95.40	Komatiite	n.a.	102	n.a.	n.a.	n.a.	5.44	n.a.	7.58	n.a.	8.48
M52442194R306 59.80-60.30	Komatiite	5	126	0.5	9.5	8.6	6.77	0.005	6.51	0.29	9.45
EJL-95-R315/20.50	Komatiite	n.a.	69	n.a.	n.a.	n.a.	7.27	n.a.	8.47	n.a.	9.09
R352-31.10-31.40	Komatiite	n.a.	119	n.a.	n.a.	n.a.	6.73	n.a.	8.02	n.a.	9.27
M52442196R355 155.75-156.10	Komatiite	5	82	2	9.1	8.2	7.42	0.005	7.17	0.27	9.82
EJL-95-R309/110.75	Komatiite	n.a.	115	n.a.	n.a.	n.a.	6.57	n.a.	7.93	n.a.	8.76
R351-73.10-73.30	Komatiite	n.a.	157	n.a.	n.a.	n.a.	7.07	n.a.	6.59	n.a.	9.18
R349-26.70-26.90	Komatiite	n.a.	97	n.a.	n.a.	n.a.	7.26	n.a.	7.61	n.a.	9.72
M52442196R375 267.45-267.85	Komatiitic basalt	5	109	13	9.6	9.2	6.61	0.005	12.85	0.24	8.33
M52442196R346 94.95-95.50	Komatiitic basalt	5	167	1	14	14.2	8.52	0.005	7.05	0.37	11.14
R352-25.15-25.55	Komatiite	n.a.	129	n.a.	n.a.	n.a.	6.47	n.a.	12.6	n.a.	8.93
M52442196R336 120.70-121.10	Komatiitic basalt	5	178	5	10	10.8	7.58	0.005	11.1	0.29	8.19
EJL-95-R320/20.50-20.80	Komatiite	n.a.	96	n.a.	n.a.	n.a.	8.13	n.a.	7.05	n.a.	5.07
EJL-95-R317/13.55-13.70	Komatiite	n.a.	104	n.a.	n.a.	n.a.	11	n.a.	6.3	n.a.	10.26
EJL-95-R315/21.30-21.60	Tholeiitic basalt	n.a.	122	n.a.	n.a.	n.a.	14.2	n.a.	1.44	n.a.	12.33
EJL-95-R314/43.00-43.20	Tholeiitic basalt	n.a.	115	n.a.	n.a.	n.a.	10.6	n.a.	9.79	n.a.	19.35
EJL-95-R311/29.70-29.95	Tholeiitic basalt	n.a.	98	n.a.	n.a.	n.a.	14.5	n.a.	1.97	n.a.	11.70
EJL-95-R311/37.05-37.30	Tholeiitic basalt	n.a.	110	n.a.	n.a.	n.a.	15.1	n.a.	0.021	n.a.	14.40
EJL-95-R317/40.10-40.30	Komatiite	n.a.	105	n.a.	n.a.	n.a.	9.17	n.a.	8.81	n.a.	10.17
M52442196R355 189.25-189.65	Komatiitic basalt	5	115	26	14.7	12.4	9.81	0.01	8.23	0.24	8.47
M52442196R345 73.40-74.05	Tholeiitic basalt	5	158	7	14.3	12.1	12.62	0.01	5.27	0.13	10.94
M52442196R372 180.35-180.80	Komatiitic basalt	5	73	1	15.9	14.3	10.66	0.09	15.45	0.22	8.30
EJL-95-R309/120.45	Komatiitic basalt	n.a.	72	n.a.	n.a.	n.a.	9.77	n.a.	7.89	n.a.	9.18
M52442196R345 102.30-102.70	Tholeiitic basalt	5	120	3	18.3	15.6	12.44	0.02	5.49	0.24	13.66
EJL-95-R318/26.30-26.50	Komatiite	n.a.	91	n.a.	n.a.	n.a.	10.3	n.a.	5.02	n.a.	10.71
M52442196R375 147.70-148.05	Int. lapilli tuff	5	110	81	5	4.6	12.18	0.04	2.87	0.1	8.13
M52442196R336 70.30-70.80	Int. volc. congl.	5	81	5	4.6	4.9	13.53	0.005	3.7	0.08	8.40
M52442196R375 123.00-123.35	Int. volc. congl.	5	103	35	6.2	5.4	12.2	0.03	5.04	0.09	9.19
EJL-95-R308/12.30-12.60	Int.–fel. volcanic rock	n.a.	127	n.a.	n.a.	n.a.	12.8	n.a.	1.98	n.a.	6.99
M52442196R336 9.95-10.25	Int. volc. congl.	5	113	107	4.8	4.6	14.3	0.05	2.38	0.08	9.61
M52442196R373 99.90-100.35	Int. lapilli tuff	5	99	40	4.4	4.5	12.28	0.04	2.3	0.08	7.95
M52442196R375 198.60-199.00	Int.–fel. volcanic rock	5	99	6	4.5	4.4	12.52	0.05	2	0.08	6.68
M52442196R373 199.10-199.40	Int. lapilli tuff	5	104	7	4.6	4.5	12.34	0.06	2.81	0.08	7.45
M52442196R372 20.30-20.65	Int.–fel. volcanic rock	5	94	7	4.1	4.2	12.28	0.05	3.11	0.07	6.61
M52442196R355 100.90-101.20	Int. lapilli tuff	5	86	3	3.8	3.7	13.09	0.06	3.14	0.07	5.95
M52442196R336 40.90-41.25	Int. volc. congl.	5	105	15	3.9	3.8	13.23	0.04	1.39	0.07	6.02
EJL-95-R316/36.40-36.60	Tholeiitic basalt	n.a.	116	n.a.	n.a.	n.a.	15.3	n.a.	9.78	n.a.	6.91
M52442195R310 51.00-51.65	Tholeiitic basalt	5	65	3	15.7	12.5	13.78	0.03	10.2	0.06	7.40
EJL-95-R312/17.45-17.75	Int.–fel. volcanic rock	n.a.	83	n.a.	n.a.	n.a.	14.3	n.a.	2.2	n.a.	5.07
EJL-95-R320/57.50-57.70	Black schist	n.a.	1240	n.a.	n.a.	n.a.	16.2	n.a.	0.43	n.a.	8.01
M52442195R320 72.40-72.85	Black schist	<10	173	17	2.6	2.4	9.88	0.03	3.79	0.04	12.83
EJL-95-R320/7.60-7.90	Tholeiitic basalt	n.a.	76	n.a.	n.a.	n.a.	14.8	n.a.	6.61	n.a.	8.39
M52442196R375 66.25-66.60	Int.–fel. volcanic rock	5	107	1	1.1	1.3	14.26	0.05	8.32	0.04	10.60
M52442196R372 99.50-99.80	Int.–fel. volcanic rock	5	94	7	3.1	3	12.26	0.07	4.97	0.05	6.13
EJL-95-R321/58.50-58.90	Black schist	n.a.	48	n.a.	n.a.	n.a.	16	n.a.	0.816	n.a.	5.91
M52442194R306 4.60-5.00	Int.–fel. volcanic rock	5	62	3	19	13.7	17	0.03	7.73	0.07	5.65
M52442196R336 102.40-102.90	Tholeiitic basalt	5	114	1	8	5	12.53	0.03	7.15	0.005	8.16
EJL-95-R309/50.55-50.79	Int.–fel. volcanic rock	n.a.	77	n.a.	n.a.	n.a.	13.7	n.a.	2.05	n.a.	5.29
M52442196R373 9.50-9.95	Int.–fel. volcanic rock	5	76	3	2.1	2.4	14.33	0.05	1.48	0.04	6.41
EJL-95-R323/32.10-32.30	Black schist	n.a.	96	n.a.	n.a.	n.a.	14.4	n.a.	1.77	n.a.	8.13
M52442196R375 40.35-40.65	Int.–fel. volcanic rock	5	106	1	3	3.5	14.62	0.05	2.34	0.04	9.34
EJL-95-R319/21.60-21.80	Tholeiitic basalt	n.a.	146	n.a.	n.a.	n.a.	14.6	n.a.	4.33	n.a.	13.77
M52442196R375 10.15-10.50	Int.–fel. volcanic rock	5	52	13	2.1	2.3	12.88	0.06	2.19	0.03	5.18
M52442196R372 129.30-129.65	Black schist	<10	32	8	1.4	1.6	16.07	0.11	1.08	0.02	3.74
EJL-95-R322/64.20-64.50	Black schist	n.a.	40	n.a.	n.a.	n.a.	16.7	n.a.	0.396	n.a.	4.28
M52442195R310 87.00-87.60	Black schist	<10	953	10	1.2	1.5	15.11	0.07	1.78	0.01	5.01
EJL-95-R309/92.80	Black schist	n.a.	37	n.a.	n.a.	n.a.	17.1	n.a.	1.05	n.a.	3.98
EJL-95-R316/40.00-40.20	Komatiitic basalt	n.a.	108	n.a.	n.a.	n.a.	12.8	n.a.	5.68	n.a.	12.15
M52442196R352 19.10-19.45	Black schist	<10	30	4	0.7	1.5	13.38	0.1	0.06	0.01	3.59
EJL-95-R313/72.20	Quartz porphyry	n.a.	32	n.a.	n.a.	n.a.	15	n.a.	0.003	n.a.	1.75
M52442196R355 166.50-167.00	Int.–fel. volcanic rock	5	87	2	0.1	0.3	16.16	0.15	4.62	0.005	5.01
M52442196R373 221.90-222.30	Quartz porphyry	5	44	39	0.2	0.4	15.34	0.17	1.46	0.005	2.52
EJL-95-R310/23.60-23.90	Quartz porphyry	n.a.	27	n.a.	n.a.	n.a.	15.2	n.a.	0.107	n.a.	0.22
EJL-95-R315/65.80	Quartz porphyry	n.a.	24	n.a.	n.a.	n.a.	11.1	n.a.	0.095	n.a.	0.47
EJL-95-R320/44.80-45.10	Quartz porphyry	n.a.	19	n.a.	n.a.	n.a.	9.97	n.a.	0.462	n.a.	0.99
EJL-95-R323/13.10-13.30	Quartz porphyry	n.a.	1	n.a.	n.a.	n.a.	9.56	n.a.	0.035	n.a.	0.25

Appendix 2.6. XRF analysis data of K_2O, MgO, MnO, Na_2O, P_2O_5, S, SiO_2, SrO, & TiO_2

Sample ID	Lithology	K2O	MgO	MnO	Na2O	P2O5	S	SiO2	SrO	TiO2
		%	%	%	%	%	%	%	%	%
M52442194R306 35.60-36.10	Tholeiitic basalt	0.01	6.49	0.85	0.06	0.03	7.88	19.23	0.01	0.18
4421/96/R336/89.20-89.50	Undef. Mineralisation	1.02	2.51	0.262	0.58	0.073	10.37	40.6	n.a.	0.391
4421/95/R310/39.80-40.00	Undef. Mineralisation	1.62	2.88	0.171	3.02	0.029	5.25	50.4	n.a.	0.592
4421/96/R346/106.90-107.20	Undef. Mineralisation	1.84	3.39	0.209	2.3	0.036	3.19	54	n.a.	0.672
4421/96/R336/96.25-96.55	Undef. Mineralisation	2.69	3.44	0.198	1.21	0.04	2.48	55.6	n.a.	0.675
4421/96/R346/109.60-109.90	Undef. Mineralisation	0.975	4.92	0.385	1.1	0.031	6.11	40.5	n.a.	0.443
4421/95/R310/42.40-42.70	Undef. Mineralisation	2.1	3.43	0.162	1.82	0.036	2.01	57.1	n.a.	0.676
4421/95/R319/37.00-37.30	Undef. Mineralisation	0.585	4.94	0.373	2.43	0.033	2.08	48.1	n.a.	0.506
4421/95/R319/39.10-39.35	Undef. Mineralisation	0.82	3.68	0.318	3.28	0.035	3.69	52	n.a.	0.539
4421/95/R319/34.20-34.50	Undef. Mineralisation	1.18	4.1	0.224	3.07	0.034	2.05	55.4	n.a.	0.61
4421/96/R336/91.20-91.60	Undef. Mineralisation	0.909	4.14	0.517	0.94	0.035	0.43	52.4	n.a.	0.601
M52442196R375 246.40-246.90	Int.–fel. volcanic rock	1.91	2.69	0.06	1.34	0.06	3.004	63.28	0.01	0.37
4421/95/R310/35.50-35.80	Undef. Mineralisation	1.29	4.8	0.584	0.0337	0.039	1.1	52.7	n.a.	0.483
M52442195R307 22.05-22.70	Tholeiitic basalt	0.01	4.15	0.46	2.76	0.07	2.124	48.08	0.01	0.8
M52442196R352 58.00-58.60	Tholeiitic basalt	0.005	6.31	1.96	0.005	0.01	1.872	18.53	0.01	0.2
4421/96/R346/100.70-101.00	Undef. Mineralisation	0.931	7.1	0.615	0.21	0.034	5.27	25.7	n.a.	0.399
M52442196R345 38.50-38.90	Komatiite	0.005	25.4	0.16	0.005	0.01	0.268	34.78	0.02	0.18
EJL-95-R319/10.10-10.20	Komatiite	0.001	25.7	0.188	0	0.014	0.183	35.9	n.a.	0.197
M52442196R375 229.40-229.75	Komatiite	0.005	24	0.1	0.01	0.02	0.002	44.38	0.01	0.29
EJL-95-R310/131.70	Komatiite	0.01	23.5	0.158	0	0.02	0.004	43.3	n.a.	0.279
EJL-95-R310/114.80	Komatiite	0.002	23.5	0.129	0	0.02	0.116	44.1	n.a.	0.27
R354-196.10-196.70	Komatiite	0	23.9	0.101	0	0.026	0.071	43.5	n.a.	0.307
M52442195R310 12.50-12.80	Komatiite	0.005	24	0.14	0.02	0.02	0.036	41.26	0.02	0.4
EJL-95-R315/9	Komatiite	0.002	26	0.138	0	0.023	0.02	41	n.a.	0.288
M52442195R310 132.50-132.80	Komatiite	0.01	22.6	0.21	0.05	0.02	0.004	41.09	0.02	0.35
M52442196R346 84.70-85.20	Komatiite	0.005	23	0.17	0.01	0.02	0.008	39.03	0.01	0.36
EJL-95-R318/7.60-7.80	Komatiite	0.01	21.4	0.18	0	0.022	0.001	45.5	n.a.	0.317
EJL-95-R309/18.40	Komatiite	0	18.9	0.247	0	0.026	0.129	37.2	n.a.	0.319
EJL-95-R310/122.80	Komatiite	0.006	20.8	0.187	0	0.026	0.149	40.1	n.a.	0.358
M52442195R320 18.25-18.60	Komatiite	0.005	20.7	0.13	0.01	0.02	0.002	42.02	0.01	0.29
EJL-95-R323/7.85-8.05	Komatiite	0.004	22.6	0.123	0	0.024	0.045	40.6	n.a.	0.27
EJL-95-R315/51.30	Komatiite	0.012	22.1	0.175	0	0.022	0.034	39.1	n.a.	0.738
R351-95.20-95.40	Komatiite	0	22.1	0.182	0	0.024	0.005	37.5	n.a.	0.279
M52442194R306 59.80-60.30	Komatiite	0.005	20.7	0.14	0.005	0.02	0.028	39.87	0.01	0.36
EJL-95-R315/20.50	Komatiite	0.025	21.7	0.166	0.02	0.031	0.007	43	n.a.	0.298
R352-31.10-31.40	Komatiite	0	18.4	0.118	0	0.026	0.154	38.6	n.a.	0.367
M52442196R355 155.75-156.10	Komatiite	0.005	21.9	0.16	0.01	0.02	0.012	37.03	0.02	0.38
EJL-95-R309/110.75	Komatiite	0.008	19.8	0.164	0	0.026	0.041	38.5	n.a.	0.263
R351-73.10-73.30	Komatiite	0	21.8	0.101	0	0.028	0.212	37.9	n.a.	0.365
R349-26.70-26.90	Komatiite	0	18.5	0.12	0	0.027	0.057	37.6	n.a.	0.419
M52442196R375 267.45-267.85	Komatiitic basalt	0.09	12.1	0.27	0.22	0.02	0.02	36.15	0.01	0.38
M52442196R346 94.95-95.50	Komatiitic basalt	0.01	8.99	0.34	0.01	0.03	0.008	49.79	0.01	0.5
R352-25.15-25.55	Komatiite	0	14.4	0.23	0	0.024	0.078	32.1	n.a.	0.365
M52442196R336 120.70-121.10	Komatiitic basalt	0.005	13.8	0.19	0.005	0.02	0.016	37.36	0.01	0.39
EJL-95-R320/20.50-20.80	Komatiite	0.004	19.5	0.075	0	0.031	0.104	36.7	n.a.	0.419
EJL-95-R317/13.55-13.70	Komatiite	0.021	17.2	0.174	1.56	0.039	0.004	45.1	n.a.	0.519
EJL-95-R315/21.30-21.60	Tholeiitic basalt	1.75	5.78	0.214	0.13	0.056	0.569	55.6	n.a.	0.687
EJL-95-R314/43.00-43.20	Tholeiitic basalt	0.003	4.86	0.557	0	0.041	0.255	34.5	n.a.	0.546
EJL-95-R311/29.70-29.95	Tholeiitic basalt	0.631	6.15	0.297	1.99	0.054	0.05	54.3	n.a.	0.713
EJL-95-R311/37.05-37.30	Tholeiitic basalt	1.6	5.88	0.133	0.02	0.009	0.287	55	n.a.	0.737
EJL-95-R317/40.10-40.30	Komatiite	0.014	15.8	0.192	0	0.036	0.003	43.6	n.a.	0.474
M52442196R355 189.25-189.65	Komatiitic basalt	0.26	11.15	0.15	0.77	0.03	0.004	43.8	0.01	0.5
M52442196R345 73.40-74.05	Tholeiitic basalt	0.37	8.36	0.2	1.92	0.05	0.424	47.39	0.01	0.59
M52442196R372 180.35-180.80	Komatiitic basalt	2.2	8.93	0.34	0.77	0.02	0.028	26.97	0.01	0.53
EJL-95-R309/120.45	Komatiitic basalt	1.37	13.9	0.157	1.75	0.029	0.132	37.9	n.a.	0.449
M52442196R345 102.30-102.70	Tholeiitic basalt	0.64	5.69	0.39	0.46	0.04	0.056	49.1	0.01	0.63
EJL-95-R318/26.30-26.50	Komatiite	0.009	18.7	0.159	0	0.043	0	45.1	n.a.	0.496
M52442196R375 147.70-148.05	Int. lapilli tuff	0.72	5.54	0.18	2.06	0.09	0.736	60.06	0.02	0.7
M52442196R336 70.30-70.80	Int. volc. congl.	0.02	4.54	0.12	4.35	0.12	0.588	57.38	0.02	0.7
M52442196R375 123.00-123.35	Int. volc. congl.	0.8	5.7	0.24	2.08	0.1	0.544	53.74	0.02	0.69
EJL-95-R308/12.30-12.60	Int.–fel. volcanic rock	0.836	4.95	0.081	2.27	0.104	0.418	63.5	n.a.	0.701
M52442196R336 9.95-10.25	Int. volc. congl.	1.14	4.99	0.15	2.01	0.1	1.152	56.84	0.01	0.76
M52442196R373 99.90-100.35	Int. lapilli tuff	0.82	5.2	0.13	2.35	0.1	0.804	60.55	0.01	0.71
M52442196R375 198.60-199.00	Int.–fel. volcanic rock	0.94	4.75	0.1	2.14	0.08	0.264	65.39	0.01	0.64
M52442196R373 199.10-199.40	Int. lapilli tuff	1.39	4.31	0.11	1.5	0.09	0.568	62.83	0.02	0.69
M52442196R372 20.30-20.65	Int.–fel. volcanic rock	1.22	4.52	0.12	1.75	0.1	0.408	62.7	0.02	0.67
M52442196R355 100.90-101.20	Int. lapilli tuff	1.7	4.28	0.09	1.62	0.09	0.368	62.5	0.02	0.68
M52442196R336 40.90-41.25	Int. volc. congl.	1.03	4.09	0.08	2.73	0.1	0.256	65.94	0.01	0.68
EJL-95-R316/36.40-36.60	Tholeiitic basalt	0.048	5.51	0.163	3.8	0.053	0.1	46.5	n.a.	0.724

Sample ID	Lithology	K2O	MgO	MnO	Na2O	P2O5	S	SiO2	SrO	TiO2
		%	%	%	%	%	%	%	%	%
M52442195R310 51.00-51.65	Tholeiitic basalt	1.02	5.38	0.21	1.92	0.05	0.108	45.79	0.02	0.68
EJL-95-R312/17.45-17.75	Int.–fel. volcanic rock	1.79	4.05	0.074	2.22	0.112	0.142	64.6	n.a.	0.631
EJL-95-R320/57.50-57.70	Black schist	3.83	1.24	0.081	0.99	0.078	2.97	59.5	n.a.	0.475
M52442195R320 72.40-72.85	Black schist	1.12	3.18	0.14	1.32	0.07	3.7	57.96	0.01	0.31
EJL-95-R320/7.60-7.90	Tholeiitic basalt	0.037	4.14	0.162	5.75	0.107	0.186	50.7	n.a.	1.26
M52442196R375 66.25-66.60	Int.–fel. volcanic rock	0.83	3.89	0.2	2.64	0.13	0.002	47.21	0.03	1.07
M52442196R372 99.50-99.80	Int.–fel. volcanic rock	1.67	2.79	0.11	1.9	0.1	0.4	61.78	0.04	0.58
EJL-95-R321/58.50-58.90	Black schist	3.69	0.95	0.057	1.52	0.125	3.02	64.5	n.a.	0.517
M52442194R306 4.60-5.00	Int.–fel. volcanic rock	1.06	2.31	0.18	2.73	0.07	0.072	55.21	0.03	0.82
M52442196R336 102.40-102.90	Tholeiitic basalt	0.79	6.29	0.18	3.18	0.05	0.24	46.92	0.01	0.75
EJL-95-R309/50.55-50.79	Int.–fel. volcanic rock	1.58	3.53	0.1	2.57	0.109	0.195	65.6	n.a.	0.68
M52442196R373 9.50-9.95	Int.–fel. volcanic rock	1.49	2.41	0.08	2.29	0.08	0.448	65.77	0.03	0.67
EJL-95-R323/32.10-32.30	Black schist	2.04	1.88	0.114	2.59	0.11	2.04	61.1	n.a.	0.427
M52442196R375 40.35-40.65	Int.–fel. volcanic rock	1.18	2.52	0.17	2.54	0.12	0.268	61.25	0.02	0.68
EJL-95-R319/21.60-21.80	Tholeiitic basalt	0.012	6.93	0.155	2.82	0.095	0.074	46.5	n.a.	1.22
M52442196R375 10.15-10.50	Int.–fel. volcanic rock	1.46	1.93	0.1	2.26	0.09	0.308	67.85	0.03	0.63
M52442196R372 129.30-129.65	Black schist	4.12	1.62	0.02	1.07	0.1	1.144	65.79	0.01	0.44
EJL-95-R322/64.20-64.50	Black schist	2.68	0.96	0.035	3.77	0.158	1.26	67.9	n.a.	0.522
M52442195R310 87.00-87.60	Black schist	3.16	1.7	0.06	2.19	0.08	1.744	62.92	0.02	0.37
EJL-95-R309/92.80	Black schist	2.8	0.65	0.036	4	0.127	1.35	66.8	n.a.	0.622
EJL-95-R316/40.00-40.20	Komatiitic basalt	0.121	12.3	0.248	0.39	0.048	0.015	42.3	n.a.	0.637
M52442196R352 19.10-19.45	Black schist	3.51	1.34	0.01	0.19	0.05	0.004	73.37	0.01	0.33
EJL-95-R313/72.20	Quartz porphyry	1.98	1.16	0.066	5.04	0.152	0.067	68.8	n.a.	0.335
M52442196R355 166.50-167.00	Int.–fel. volcanic rock	1.92	3.32	0.1	3.83	0.14	0.548	57.34	0.02	0.45
M52442196R373 221.90-222.30	Quartz porphyry	2.89	1.28	0.02	2.94	0.14	0.088	68.8	0.02	0.34
EJL-95-R310/23.60-23.90	Quartz porphyry	4.73	0.04	0.009	1.49	0.064	0.018	76.8	n.a.	0.304
EJL-95-R315/65.80	Quartz porphyry	2.62	0.21	0.006	0.93	0.019	0.162	83	n.a.	0.173
EJL-95-R320/44.80-45.10	Quartz porphyry	1.69	0.47	0.023	2.02	0.021	0.078	82.6	n.a.	0.181
EJL-95-R323/13.10-13.30	Quartz porphyry	2.36	0.17	0.009	0.6	0.022	0	85.5	n.a.	0.157

Appendix 3. Weak leach analysis data of Ni, Cu, Co, S, & Cr

HOLE-ID	From	To	Ni	Cu	Co	S	Cr	Ni/Cu	Nisf
	m	m	ppm	ppm	ppm	%	ppm		wt%
R310	28.4	29.4	480	41	58	0.01	1500	11.65854	
R310	29.4	30.4	760	2	76	0.01	1800	382.5	
R310	30.4	31.4	580	67	62	0.01	1200	8.686567	
R310	31.4	32.4	730	111	90	0.01	2600	6.594594	
R310	32.4	33.4	840	30	85	0.01	2300	28.16667	
R310	33.4	34.4	1010	20	117	0.01	1900	50.5	
R310	34.4	35.4	4810	102	117	3	1100	47.15686	6.093
R310	35.4	36.4	4820	74	163	1.63	2500	65.13513	11.237
R310	36.4	37.4	11300	84	209	1.69	1800	134.5238	25.408
R310	37.4	38.4	13500	98	209	3.9	2600	137.7551	13.154
R310	38.4	39.4	11500	75	221	3.06	1300	153.3333	14.281
R310	39.4	40.4	15200	136	303	5.22	600	111.7647	11.065
R310	40.4	41.4	11300	131	267	4.22	790	86.25954	10.175
R310	41.4	42.4	11400	118	247	2.89	980	96.61017	14.99
R310	42.4	43.4	7260	199	180	5.57	900	36.48241	4.953
R310	43.4	44.4	540	57	34	0.06	200	9.526316	
R310	44.4	45.4	140	102	43	1.15	120	1.323529	
R310	45.4	46.4	160	78	45	0.03	130	2.089744	
R310	46.4	47.5	190	87	39	0.26	130	2.195402	
R310	47.5	48.25	50	33	18	0.01	100	1.424242	
R310	48.25	49.25	200	78	54	0.01	450	2.564103	
R310	49.25	50.25	170	90	55	0.01	400	1.888889	
R310	50.25	51.25	260	39	59	0.01	350	6.589744	
R310	51.25	52.25	260	131	64	1.17	610	1.954198	
R310	52.25	53.25	410	96	69	0.01	1200	4.291667	
R310	53.25	54.25	430	63	70	0.11	1200	6.746032	
R310	54.25	55.25	710	48	85	0.01	2100	14.79167	
R310	55.25	56.25	700	99	96	0.01	2300	7.080808	
R310	56.25	57.25	500	254	78	0.01	1900	1.968504	
R310	57.25	58.25	1000	6	87	0.01	3100	166.6667	
R310	58.25	59.25	580	39	76	0.01	2700	14.92308	
R310	59.25	60.6	520	80	77	0.01	1900	6.4875	
R310	60.6	61.6	290	299	62	0.58	560	0.976589	
R310	61.6	62.6	440	94	67	0.01	1000	4.723404	

HOLE-ID	From	To	Ni	Cu	Co	S	Cr	Ni/Cu	Nisf
	m	m	ppm	ppm	ppm	%	ppm		wt%
R310	62.6	63.6	510	116	82	0.01	780	4.37069	
R310	63.6	64.6	480	97	92	0.01	780	4.907217	
R310	64.6	65.6	450	164	76	0.01	780	2.762195	
R310	65.6	66.6	400	119	64	0.01	780	3.361345	
R310	66.6	67.6	430	121	77	0.01	710	3.545455	
R310	67.6	68.6	450	85	82	0.01	700	5.305882	
R310	68.6	69.7	470	80	70	0.49	1000	5.9125	
R310	69.7	70.9	160	95	32	1.72	160	1.736842	
R310	70.9	71.9	50	23	9	0.07	59	2.043478	
R310	71.9	72.9	80	27	16	0.48	92	2.888889	
R310	72.9	73.9	50	18	13	0.4	72	2.944444	
R310	73.9	74.9	90	34	18	0.84	100	2.617647	
R310	74.9	75.9	80	52	24	1.33	100	1.596154	
R310	75.9	76.9	160	109	40	2.88	140	1.431193	
R310	76.9	77.9	130	95	34	2.38	160	1.357895	
R310	77.9	78.9	170	135	42	2.6	190	1.266667	
R310	78.9	79.9	100	61	20	1.08	130	1.672131	
R310	79.9	80.9	60	30	13	0.65	59	1.9	
R310	80.9	81.9	130	96	34	2.33	100	1.34375	
R310	81.9	82.9	100	90	30	2.13	92	1.122222	
R310	82.9	83.9	100	89	31	2.23	87	1.101124	
R310	83.9	84.9	100	93	35	2.39	97	1.107527	
R310	84.9	86.9	100	93	37	2.46	90	1.096774	
R310	86.9	87.9	150	120	50	2.96	110	1.216667	
R310	87.9	88.9	130	88	37	2.37	110	1.488636	
R310	88.9	89.9	120	100	34	2.6	120	1.2	
R310	89.9	90.9	90	74	25	2.1	120	1.22973	
R310	90.9	91.9	80	67	25	1.72	160	1.253731	
R310	91.9	92.9	130	61	28	1.77	180	2.04918	
R310	92.9	93.9	170	68	37	2.23	210	2.558824	
R310	93.9	94.9	190	80	42	2.33	220	2.425	
R310	94.9	95.9	230	82	48	2.16	320	2.743902	
R310	95.9	96.9	170	60	30	1.48	230	2.8	
R310	96.9	97.9	170	66	36	1.88	280	2.530303	
R310	97.9	99.7	210	83	86	3.11	230	2.566265	
R310	99.7	100.7	140	84	35	2.31	160	1.619048	
R310	100.7	101.7	120	74	32	1.89	120	1.594595	
R310	101.7	102.7	120	61	30	1.76	150	1.901639	
R310	102.7	103.7	120	70	32	2.04	130	1.7	
R310	103.7	104.7	130	64	33	1.98	170	1.953125	
R310	104.7	105.7	150	87	41	3.08	180	1.701149	
R310	105.7	106.7	70	56	25	1.56	130	1.339286	
R310	106.7	107.7	120	67	32	2.27	140	1.820896	
R310	107.7	108.7	70	76	28	2.88	120	0.881579	
R310	108.7	109.7	120	107	35	3.75	94	1.102804	
R310	109.7	110.7	140	118	40	3.97	110	1.220339	
R310	110.7	111.7	190	125	49	4.12	180	1.528	
R310	111.7	112.7	270	104	55	3.08	490	2.625	
R310	112.7	113.7	30	24	10	0.36	66	1.125	
R310	113.7	114.7	400	78	37	0.23	1100	5.153846	
R310	114.7	115.7	520	33	58	0.01	1700	15.63636	
R319	24.6	25.6	140	68	53	0.06	330	2.088235	
R319	25.6	26.6	100	16	44	0.02	250	6.5	
R319	26.6	27.6	90	34	47	0.07	240	2.794118	
R319	27.6	28.6	220	33	55	0.02	190	6.727273	
R319	28.6	30.2	720	151	90	0.44	2200	4.735099	
R319	30.2	31.5	2600	60	82	1.79	1600	43.33333	
R319	31.5	33	18800	284	234	10.3	480	66.19718	6.936
R319	33	34.5	6060	111	140	3.67	410	54.59459	6.275
R319	34.5	35.5	6180	62	175	1.98	1700	99.67742	11.861
R319	35.5	36.5	17700	112	276	3.78	1300	158.0357	17.794
R319	36.5	37.5	10500	104	203	2.98	1600	100.9615	13.389
R319	37.5	38.5	12800	126	219	4.73	880	101.5873	10.283
R319	38.5	39.5	8540	101	183	4.42	990	84.55446	7.342
R319	39.5	40.5	3590	67	135	2.11	4800	53.58209	6.465
R319	40.5	41.8	1300	99	53	2.01	690	13.13131	

HOLE-ID	From	To	Ni	Cu	Co	S	Cr	Ni/Cu	Nisf
	m	m	ppm	ppm	ppm	%	ppm		wt%
R319	41.8	42.8	560	31	70	0.18	1300	17.93548	
R319	42.8	44.4	430	17	48	0.01	690	25.47059	
R319	44.4	45.4	200	81	48	0.25	400	2.419753	
R319	45.4	46.4	140	152	47	0.66	230	0.927632	
R319	46.4	47.4	280	75	54	0.38	640	3.733333	
R319	47.4	48.4	230	48	53	0.28	550	4.854167	
R319	48.4	49.4	380	35	59	0.1	1700	10.8	
R319	49.4	50.4	710	39	83	0.14	3700	18.30769	
R319	50.4	51.4	340	97	51	0.25	1400	3.556701	
R319	51.4	53	410	48	69	0.21	1200	8.541667	
R319	53	54	520	59	78	0.3	550	8.881356	
R319	54	55	420	84	64	0.82	730	5.011905	
R319	55	56	210	168	58	2.57	160	1.220238	
R319	56	57.9	50	41	18	0.68	83	1.317073	
R319	57.9	60.8	90	100	35	2.01	110	0.95	
R319	60.8	61.75	110	132	42	2.66	120	0.863636	
R319	61.75	63	60	46	19	0.92	110	1.347826	
R319	63	64.3	90	58	26	1.45	96	1.482759	
R319	64.3	65.5	140	80	38	2.48	130	1.8	
R319	65.5	66.3	80	60	26	1.51	110	1.366667	
R319	66.3	67.7	120	96	36	2.5	120	1.270833	
R319	67.7	68.7	140	66	23	1.2	150	2.075758	
R319	68.7	70.1	90	41	21	0.93	100	2.292683	
R336	7.9	8.9	240	93	50	0.4	347	2.580645	
R336	14.6	15.6	240	89	48	0.77	320	2.674157	
R336	19.6	20.6	240	78	48	0.79	394	3.115385	
R336	24.6	25.6	290	75	56	0.08	369	3.866667	
R336	29.6	30.6	260	71	38	0.33	351	3.605634	
R336	34.6	35.6	230	82	40	0.29	324	2.829268	
R336	39.6	40.6	280	129	43	0.51	384	2.170543	
R336	44.6	45.6	210	76	37	0.08	338	2.736842	
R336	49.6	50.6	230	68	41	0.05	375	3.382353	
R336	54.6	55.6	230	80	44	0.61	311	2.8875	
R336	83.4	84.4	40	130	20	0.82	46	0.3	
R336	84.4	85.2	40	67	16	0.51	22	0.537314	
R336	85.2	86.2	730	104	99	0.42	1840	7.009615	
R336	86.2	87.2	700	64	71	0.07	2310	10.92188	
R336	87.2	87.9	600	32	68	0.08	1940	18.65625	
R336	87.9	88.9	10400	155	126	6.55	445	67.09677	6.034
R336	88.9	89.9	18200	364	183	7.8	187	50	8.867
R336	89.9	90.9	5650	108	100	1.82	1490	52.31482	11.797
R336	90.9	91.9	4020	50	182	0.5	1990	80.4	30.552
R336	91.9	92.9	3920	85	161	0.42	2010	46.11765	35.467
R336	92.9	93.9	980	128	73	0.28	963	7.671875	13.3
R336	93.9	95.2	2160	151	88	0.79	973	14.30464	10.39
R336	95.2	96.2	3220	235	118	3.92	216	13.70213	3.121
R336	96.2	96.6	6630	83	167	1.59	539	79.87952	15.845
R336	96.6	97.6	480	25	81	0.1	866	19.28	
R336	97.6	98.6	700	31	55	0.19	955	22.6129	
R346	67.4	68.4	50	45	10	0.49	40	1.155556	
R346	68.4	69.4	90	260	42	3.08	54	0.357692	
R346	69.4	70.4	100	241	43	3.06	93	0.423237	
R346	86.8	88.1	80	114	50	0.48	102	0.72807	
R346	88.1	89.1	70	378	45	1.57	135	0.187831	
R346	89.1	90.1	60	271	47	1.23	33	0.217712	
R346	90.1	91.1	60	92	44	0.34	47	0.684783	
R346	91.1	92.1	220	58	43	0.13	430	3.724138	
R346	92.1	93.2	40	243	24	0.14	47	0.168724	
R346	93.2	94.2	640	51	76	0.12	2230	12.52941	
R346	94.2	95.2	680	31	90	0.03	2230	22.06452	
R346	95.2	96.2	650	49	84	0.02	2190	13.34694	
R346	96.2	97.2	620	38	76	0.03	1950	16.31579	
R346	97.2	98.2	680	39	82	0.06	1850	17.35897	
R346	98.2	99.2	790	32	108	0.11	2060	24.84375	
R346	99.2	100	490	33	29	0.19	1540	14.72727	
R346	100	101	1160	157	65	2	1720	7.388535	

HOLE-ID	From	To	Ni	Cu	Co	S	Cr	Ni/Cu	Nisf
	m	m	ppm	ppm	ppm	%	ppm		wt%
R346	101	101.6	5720	704	269	8.24	82	8.125	2.638
R346	101.6	102.6	3560	106	126	2.17	1290	33.58491	6.234
R346	102.6	103.6	5400	174	172	3.82	1420	31.03448	5.372
R346	103.6	104.6	8400	107	238	3.05	762	78.50467	10.466
R346	104.6	105.6	7690	95	205	2.27	1080	80.94736	12.873
R346	105.6	106.6	8990	87	190	2.33	1290	103.3333	14.662
R346	106.6	107.6	11900	182	320	3.42	1210	65.38461	13.222
R346	107.6	108.6	7730	185	148	3.59	1550	41.78378	8.182
R346	108.6	109.6	8960	130	163	2.74	1300	68.92308	12.426
R346	109.6	110.2	11700	375	669	4.9	826	31.2	9.073
R346	110.2	111.7	1990	151	37	2.38	181	13.17881	
R346	111.7	113.2	90	38	18	0.45	41	2.421053	